

DISCOVERY OF SMALL-MOLECULE MODULATORS OF THE RNA-BINDING PROTEINS LIN28 AND RNASE L

Dissertation

For achievement of the academic degree of
Doctor in Natural Sciences
(Dr. rer. nat.)

Submitted to
Faculty of Chemistry and Chemical Biology
TU Dortmund University

by

Lydia Borgelt, M.Sc.

Born in Lippstadt

Dortmund, 2023

1st Examiner: Prof. Dr. Dr. h.c. Herbert Waldmann

2nd Examiner: Prof. Dr. Hannes Mutschler

Supervisor: Dr. Peng Wu

The work described in this thesis was performed under the supervision of Dr. Peng Wu and the formal supervision of Prof. Dr. Dr. h.c. Herbert Waldmann at the Chemical Genomics Centre of the Max Planck Society, the Max Planck Institute of Molecular Physiology, and the Faculty of Chemistry and Chemical Biology at TU Dortmund University in Dortmund.

Results presented in this thesis contributed to the following publications:

Borgelt, Lydia; Huang, Fubao; Hohnen, Lisa; Qiu, Xiaqiu; Goebel, Georg L.; Hommen, Pascal; Wu, Peng. Spirocyclic Chromenopyrazole Inhibitors Disrupting the Interaction between the RNA-binding protein LIN28 and Let-7. *ChemBioChem* e202300168 (2023).

Borgelt, Lydia; Haacke, Neele; Lampe, Philipp; Qiu, Xiaqiu; Gasper, Raphael; Schiller, Damian; Hwang, Jimin; Sievers, Sonja, Wu, Peng. Small-molecule screening of ribonuclease L binders for RNA degradation. *Biomed. Pharmacother.* **154**, 113589 (2022).

Borgelt, Lydia; Li, Fu; Hommen, Pascal; Lampe, Philipp; Hwang, Jimin; Goebel, Georg L.; Sievers, Sonja; Wu, Peng. Trisubstituted Pyrrolinones as Small-Molecule Inhibitors Disrupting the Protein–RNA Interaction of LIN28 and *Let-7*. *ACS Med. Chem. Lett.* **12**, 893–898 (2021).

Borgelt, Lydia; Hohnen, Lisa; Pallesen, Jakob S.; Hommen, Pascal; Goebel, Georg L.; Bosica, Francesco; O'Mahony, Gavin, Wu, Peng. *N*-Biphenyl Pyrrolinones and Dibenzofuran Analogues as RNA-Binding Protein LIN28 Inhibitors Disrupting the LIN28–*Let-7* Interaction. (2023) *Submitted*.

Hwang, Jimin; Haacke, Neele; **Borgelt, Lydia**; Qiu, Xiaqiu; Gasper, Raphael; Wu, Peng. Rational design and evaluation of 2-((pyrrol-2-yl)methylene)thiophen-4-ones as RNase L inhibitors. *Eur. J. Med. Chem.* **256**, 115439 (2023).

Hommen, Pascal; Hwang, Jimin; Huang, Fubao; **Borgelt, Lydia**; Hohnen, Lisa; Wu, Peng. Chromenopyrazole–peptide conjugates as small-molecule based inhibitors disrupting the protein–RNA interaction of LIN28–*let-7*. *ChemBioChem* e202300376 (2023).

Hwang, Jimin; Qiu, Xiaqiu; **Borgelt, Lydia**; Haacke, Neele; Kanis, Laurin; Petroulia, Stavroula; Gasper, Raphael; Schiller, Damian; Lampe, Philipp; Sievers, Sonja; Imig, Jochen; Wu, Peng. Synthesis and evaluation of RNase L-binding 2-aminothiophenes as anticancer agents. *Bioorg. Med. Chem.* **58**, 116653 (2022).

The work of the author also contributed to the following publications during the PhD studies:

Borgelt, Lydia; Wu, Peng. Targeting ribonucleases with small molecules and bifunctional molecules. *ACS Chem. Biol.* (2023), doi: 10.1021/acscchembio.3c00191.

Goebel, Georg L; Hohnen, Lisa; **Borgelt, Lydia**; Hommen, Pascal; Qiu, Xiaqiu; Lightfoot, Helen; Wu, Peng. Small molecules with tetrahydroquinoline-containing Povarov scaffolds as inhibitors disrupting the Protein–RNA interaction of LIN28–*let-7*. *Eur. J. Med. Chem.* **228**, 114014 (2022).

Hwang, Jimin, **Borgelt, Lydia** & Wu, Peng. Multicomponent Petasis Reaction for the Synthesis of Functionalized 2-Aminothiophenes and Thienodiazepines. *ACS Comb. Sci.* **22**, 495–499 (2020).

Results displayed in this dissertation can also be found in the following Master theses:

L. Hohnen, “Assay development and biological evaluation of small-molecule inhibitors targeting the protein-RNA interaction of LIN28 and *let-7*”, Master Thesis, **2021**.

N. Haacke, “Targeting the latent ribonuclease by small-molecule modulators”, Master Thesis, **2022**.

Acknowledgments

I am sincerely thankful for the opportunity to pursue my Ph.D. at the CGC in Dortmund. The time spent at the CGC has been instrumental in my intellectual and personal growth. I am very grateful to all the individuals who played a role in enabling the success of the projects and making the entire journey memorable and enjoyable.

First and foremost, I would like to thank Dr. Peng Wu for providing me with the opportunity to work on a diverse set of fascinating RNA-binding proteins. I am grateful for his constant guidance, fruitful discussions, and support. I appreciate the level of independence I was granted during my work, as it supported me in fostering my self-confidence and growth as a researcher. Dr. Peng Wu's trust in my abilities and constant support enabled the success of my Ph.D., and for that, I am genuinely thankful.

Second, I would also like to express my appreciation to Prof. Dr. Dr. h.c. Herbert Waldmann for establishing the Chemical Genomics Centre and taking over his role as the first examiner of this thesis.

Moreover, I thank Prof. Dr. Hannes Mutschler for taking the responsibility as the second examiner of this thesis.

I am grateful to Prof. Dr. Andrea Musacchio and Prof. Dr. Daniel Summerer for being on my Thesis Advisory Committee. They both initiated fruitful discussions, and I acknowledge their constructive feedback throughout my Ph.D.

I would especially like to thank the talented Chemists involved in the synthesis of the numerous molecules evaluated in this work. These inspiring scientists include Dr. Pascal Hommen, Dr. Jimin Hwang, Dr. Fubao Huang, Georg Goebel, and Mao Jiang, along with their students. I appreciate that their synthesis of the diverse set of compounds found in this work was crucial to the success of the research.

Special thanks go to my exceptional Master's students, Lisa Hohnen and Neele Haacke. Seeing and supporting their growth as scientists have been a pleasure, and I appreciate their motivation and dedication to the research projects. Additionally, I am thankful for our time together in the lab, it has been truly enjoyable.

Further, I am grateful to all the co-authors involved in the publications that resulted from this work for their contributions.

I would like to acknowledge the Compound Management and Screening Center (COMAS), especially Dr. Sonja Sievers and Dr. Philipp Lampe, for conducting the small-molecule

screenings from this work and for the fruitful discussions and suggestions on the screening assays.

I also thank the facilities of the MPI for their support, explanations, and measurements. I want to thank Dr. Raphael Gasper-Schönenbrücher and Petra Geue for their explanations of biophysical devices and sharing knowledge on protein crystallography. I appreciate the PCF for providing media, proteases, and insect cell lines, and Dr. Petra Janning and her team for discussions on, and measurements of proteomics samples.

I would like to thank Prof. Robert H. Silverman for providing 2'-5'A. Dr. Gavin O'Mahony from AstraZeneca is acknowledged for the fruitful cooperation on the trisubstituted pyrrolinone project.

I am deeply grateful for the opportunity to be a member of the International Max Planck Research School for Living Matter, which has not only provided me with the chance to attend international conferences but also offered beneficial workshops that have contributed significantly to my development as a researcher and beyond. I would like to thank the coordinators, Dr. Lucia Sironi and Christa Hornemann, who organized the excellent graduate program with passion and expertise and trusted and supported us in organizing our Symposium.

I want to thank current and former members of the Peng Wu group, the CGC, and the Department of Chemical Biology at the MPI of Molecular Physiology for providing a great working atmosphere, and Dr. Debora Bruzzese and Birgit Apprecht for coordinating and supporting the CGC. I especially thank Kim, Stefan, Joseph, Jen-Yao, Rachel, and Jessica for scientific and non-scientific discussions and support.

Dr. Peng Wu is again acknowledged for proofreading, as well as Julia Kotschy, Kim Wendrich and Jen-Yao Chang. Your feedback was very helpful.

Last but not least, I would like to thank my parents, my sister and my partner for their constant support.

Table of Contents

Abstract.....	1
Zusammenfassung	3
1 Introduction.....	5
1.1 RNA-binding proteins.....	5
1.2 The miRNA-binding protein LIN28	6
1.2.1 miRNAs	8
1.2.2 The miRNA family <i>let-7</i>	9
1.2.3 The protein LIN28 regulates <i>let-7</i> biogenesis.....	10
1.2.4 LIN28 as a target in medicinal chemistry.....	13
1.2.5 Targeting of regulators of the LIN28 pathway.....	19
1.3 The OAS–RNase L pathway	19
1.3.1 Ribonuclease L is a central regulator of the innate antiviral response	19
1.3.2 Ribonuclease L as a target of small-molecule drugs	23
1.3.3 OAS in the RNase L-mediated innate immune response	26
2 Aim of this thesis.....	29
3 Material and methods	31
3.1 Material.....	31
3.1.1 Lists of used materials	31
3.2 Methods.....	38
3.2.1 General procedures	38
3.2.2 Methods for the identification and evaluation of LIN28 inhibitors.....	41
3.2.3 Methods for the identification and evaluation of RNase L modulators	46
3.2.4 Methods for the identification and evaluation of OAS1 activators	51
4 Results and discussion	55
4.1 Discovery and biochemical evaluation of inhibitors of the LIN28– <i>let-7</i> interaction ..	55
4.1.1 Purification of recombinant LIN28A.....	55
4.1.2 Screening-based discovery.....	56
4.1.3 Scaffold-based approach.....	70

4.1.4	Conclusions from the screening- and scaffold-based approaches.....	79
4.2	Discovery and biochemical evaluation of modulators of the RNase L–OAS pathway	80
4.2.1	Purification of recombinant RNase L.....	80
4.2.2	Discovery of RNase L activators using a screening-based approach.....	81
4.2.3	Evaluation of 2-aminothiophenes as RNase L activators.....	90
4.2.4	Preliminary evaluation of biphenylthiophenes as RNase L binders.....	93
4.2.5	Evaluation of rationally designed 2-((pyrrol-2-yl)methylene)thiophen-4-ones as RNase L inhibitors.....	95
4.2.6	Conclusions from targeting RNase L with small-molecule modulators.....	101
4.2.7	Discovery of OAS1 activators.....	102
5	Conclusions and perspectives.....	110
6	References.....	112
7	Abbreviations.....	124
8	Appendix.....	128
8.1	Plasmid maps.....	128
8.2	Supplementary figures.....	136

Abstract

RNA-binding proteins (RBPs) regulate all aspects of RNA biology and metabolism and are emerging targets for the development of molecular probe compounds and therapeutics for various diseases. While oligonucleotide-based and peptide-based strategies have been applied to modulate RNAs and protein–RNA interactions, efficient RBP-targeting strategies utilizing small molecules, which bear inherent merits in comparison with other chemotypes, remain obscure. In this thesis, I studied small-molecule-based strategies to target three different RBPs, the oncogenic miRNA-binding protein LIN28, the antiviral ssRNA-cleaving protein RNase L and the associated dsRNA-binding protein OAS.

LIN28, which negatively regulates *let-7* miRNAs that downregulate the translation of numerous oncogenic proteins, is overexpressed in many human cancers and is a driver of tumor progression and metastasis. Thus, LIN28 inhibition via small molecules is a promising strategy for the development of cancer therapeutics. Reported LIN28 inhibitors suffer from poor inhibitory potency, insufficient characterization of mechanism of action, limited structure-activity relationship, and poor cellular activity. This work employed a screening-based and a scaffold-based approach for the identification of LIN28 inhibitors with new scaffolds and improved potency. In the former approach, trisubstituted pyrrolinones were identified as LIN28 inhibitors via a fluorescence polarization assay-based screening. The most active pyrrolinone **41** increased the expression levels of mature *let-7* in LIN28-expressing cells. A following structure-activity relationship study revealed biphenyl compounds, such as **85**, that showed a more potent effect in inducing *let-7* maturation. In the latter approach, a spirocyclization strategy was applied based on the chromenopyrazole scaffold of reported LIN28 inhibitors to increase the LIN28-inhibitory potency induced by the rigidity of the spirocyclic scaffold. The identified and well-characterized inhibitors are worthy starting points for the development of anticancer drugs and LIN28-targeting chemical probes.

The dsRNA-cleaving protein RNase L and the ssRNA-binding protein OAS are key enzymes in the human antiviral innate immune response. OAS detects foreign dsRNA upon viral infection, leading to OAS activation and production of the second messenger 2'-5'A. The binding of 2'-5'A to RNase L leads to RNase L dimerization and activation. The RNase L dimer then cleaves ssRNAs resulting in a global translational arrest and a cellular antiviral state. Small-molecule activators of OAS and RNase L are thus promising candidates for the development of broad-spectrum antiviral therapeutics. Furthermore, RNase L activators are useful components to build bifunctional RNase L recruiters to achieve proximity-induced targeted degradation of RNAs. In this work, robust assays for the screening and validation of OAS and RNase L activators were developed and used for the discovery of small-molecule

Abstract

modulators. While the identification of OAS and RNase L activators proved to be challenging, potential RNase L binders were identified. Additionally, a rational design approach led to the discovery of thiophenones as RNase L inhibitors that showed more potent inhibitory potency than reported RNase L inhibitors that target the nucleotide-binding pocket of RNase L.

Collectively, the results of this thesis demonstrate the feasibility targeting RBPs using a variety of small-molecule-based strategies. Screening- and scaffold-based approaches enabled the identification of modulators with new scaffolds and improved potency in targeting RBPs. The established assays, the identified compounds, and the optimization strategies presented in this work will be useful for the future development of small molecules targeting RBPs.

Zusammenfassung

RNA-bindende Proteine (RBPs) regulieren alle Aspekte der RNA-Biologie und des RNA-Stoffwechsels und sind aufstrebende Zielproteine für die Entwicklung molekularer Sonden und Therapeutika für verschiedene Krankheiten. Während oligonukleotid- und peptidbasierte Strategien bereits zur Modulation von RNAs und Protein-RNA-Interaktionen angewandt wurden, sind effiziente RBP-Targeting-Strategien unter Verwendung niedermolekularer Verbindungen noch nicht bekannt. In dieser Arbeit wurden Modulatoren dreier verschiedener RBPs studiert. Die untersuchten Zielproteine waren das onkogene miRNA-bindende Protein LIN28, das antivirale ssRNA-spaltende Protein RNase L sowie das damit verbundene dsRNA-bindende Protein OAS.

LIN28 ist ein negativer Regulator von *let-7* miRNAs, welche die Translation zahlreicher onkogener Proteine herunterregulieren. LIN28 liegt in vielen menschlichen Krebsarten überexprimiert vor und ist eine treibende Kraft der Tumorprogression und Metastasierung. Daher ist die Inhibition von LIN28 durch niedermolekulare Verbindungen eine vielversprechende Strategie für die Entwicklung von Krebstherapeutika. Bisher bekannte LIN28-Inhibitoren weisen eine geringe Aktivität, eine unzureichende Charakterisierung des Wirkmechanismus, eine begrenzte Struktur-Aktivitäts-Beziehung und eine niedrige zelluläre Aktivität auf. In dieser Arbeit wurden ein Screening-basierter und ein Scaffold-basierter Ansatz zur Identifizierung von LIN28-Inhibitoren mit neuen Gerüststrukturen und verbesserter Wirksamkeit angewendet. Im ersten Ansatz konnten trisubstituierte Pyrrolinone als LIN28-Inhibitoren durch ein Fluoreszenzpolarisationsscreening identifiziert werden. Das aktivste Pyrrolinon **41** erhöhte die Expressionslevel von gereifter *let-7* miRNA in LIN28-exprimierenden Krebszellen. Eine darauffolgende Struktur-Aktivitäts-Beziehungsstudie ergab, dass Verbindung **85** eine noch stärkere Induktion der *let-7*-Reifung hervorrufen konnte. Im zweiten Ansatz wurde eine Spirozyklisierungsstrategie angewendet, die auf dem Chromenopyrazolscaffold bekannter LIN28-Inhibitoren basiert. Durch die Rigidität des spirozyklischen Moleküls wurde die LIN28-inhibitorische Potenz erhöht. Die identifizierten und gut charakterisierten Inhibitoren sind wertvolle Ausgangspunkte für die Entwicklung von Krebsmedikamenten und chemischen Sonden gegen LIN28.

Das dsRNA-spaltende Protein RNase L und das ssRNA-bindende Protein OAS sind Schlüsselenzyme der humanen angeborenen antiviralen Immunantwort. OAS erkennt im Falle einer Virusinfektion vorliegende fremde dsRNA, was zur Aktivierung von OAS und zur Produktion des Botenstoffs 2'-5'A führt, der wiederum die Dimerisierung und Aktivierung von RNase L hervorruft. Das RNase-L-Dimer spaltet dann ssRNA, was einen globalen Translationsstopp und einen antiviralen Zellzustand hervorruft. Niedermolekulare Aktivatoren

Zusammenfassung

von OAS und RNase L sind daher vielversprechende Kandidaten für die Entwicklung von antiviralen Therapeutika mit breitem Wirkungsspektrum. Darüber hinaus könnten RNase-L-Aktivatoren als Bestandteile bifunktioneller RNase-L-rekrutierender Moleküle dienen, die RNase L in die Nähe einer Ziel-RNA bringen, um einen gezielten Abbau von RNAs zu erreichen. In dieser Arbeit wurden robuste Assays für das Screening und die Validierung von OAS- und RNase-L-Aktivatoren entwickelt, und für die Entdeckung von niedermolekularen Modulatoren verwendet. Während sich die Identifizierung von OAS- und RNase L-Aktivatoren als herausfordernd erwies, konnten potenzielle RNase L-bindende Moleküle identifiziert werden. Darüber hinaus führte ein molekularer Designansatz zur Entdeckung von RNase-L-inhibierenden Thiophenonen, die eine höhere inhibitorische Aktivität als bisher bekannte RNase L-Inhibitoren, welche die RNase L Nukleotidbindetasche adressieren, aufwiesen.

Diese Arbeit zeigt, dass es möglich ist, RBPs mit einer Vielzahl von Strategien, welche auf niedermolekularen Verbindungen basieren, zu inhibieren. Screening- und Scaffold-basierte Ansätze ermöglichten die Identifizierung von RBP-Modulatoren mit neuen Gerüststrukturen und verbesserter Aktivität. Die in dieser Arbeit etablierten Assays, Verbindungen und Substanzoptimierungsstrategien werden für die zukünftige Entwicklung von niedermolekularen Verbindungen, die auf RBPs abzielen, nützlich sein.

1 Introduction

1.1 RNA-binding proteins

The central dogma of molecular biology describes that genetic information is stored as deoxyribonucleic acid (DNA) before transcription to ribonucleic acids (RNAs), which are then translated into proteins as functional units.¹ Remarkably, proteome analysis and identification of conserved sequences among species revealed that less than two percent of the human genome is translated to proteins.^{2,3} At the same time, three-quarters of the human genome is transcribed into RNA, as found by the Encyclopedia of DNA Elements (ENCODE) project.⁴ RNAs that are not translated to protein and thus are not messenger RNAs (mRNAs) are termed non-coding RNAs and are functional units within cellular pathways. Their functions range from regulation of transcription, posttranscriptional modulation of mRNA, regulation of translation and control of chromatin dynamics.⁵ Due to these essential cellular functions, (non-coding) RNAs are emerging targets in chemical biology and medicinal chemistry.^{6,7} RNAs do not exist without interaction partners within cells and are highly regulated. Interactions with RNA-binding proteins (RBPs) affect the functions of RNAs and all aspects of RNA metabolism ranging from biogenesis to degradation of RNAs. The diverse interaction network between RNA and RBPs offers new opportunities for interference in RNA-dependent pathways by chemical entities.⁸

RBPs recently emerged as potential drug targets for the development of therapeutics for various diseases.⁹ A census of RBPs led to the detection of more than 1500 RBPs which are encoded by 7.5% of all human protein-coding genes.¹⁰ More than 500 human RBPs that bind to coding mRNA were identified, half of which contain a classified RNA-binding domain, while the other half are likely non-canonical RBPs.^{8,11,12} Canonical RNA-binding proteins usually consist of several RNA-binding domains that each have a relatively low affinity to RNA and, in some cases, poor sequence specificity. For these, sufficient specificity and affinity for binding to defined RNA targets is achieved by domain clustering. Examples of canonical RNA-binding domains are the zinc finger domain, the S1 domain, or the highly abundant RNA-recognition motif.¹³ RNA-binding domains form diverse interactions with RNA, including hydrophobic interactions with nucleotides, salt bridges to the RNA backbone, hydrogen bonds between amino acid residues and bases, and shape complementarity.^{13,14} The interactions of RBPs and RNA are involved in diverse functions such as regulation of immune biology, mRNA transportation, and miRNA regulation and thus have implications in various diseases. About 150 RBPs are linked to human diseases such as autoimmune diseases, cancer, and neurodegenerative diseases.^{10,15,16} Two-thirds of the disease-related RBPs are binders of non-coding RNA.¹⁰ Due to the close association with pathology and human diseases, modulation

of RBP activity is a promising strategy for the development of therapeutics. However, RBPs are challenging targets to be addressed by small molecules since they do not harbor classical small-molecule binding pockets, and many RBPs contain unstructured domains. Nevertheless, several RBP- and protein–RNA interaction-targeting small molecules were recently discovered, and proteome-wide screenings of protein ligandability identified addressable lysine- and tyrosine residues and fragment binding sites in RBPs.^{9,17} Examples of RBPs that have been addressed by small molecules are the mRNA-stabilizing proteins ELAV1, MSI1/2, and IGF2BP1/2, mRNA translation regulators eIF4A and eIF4G, and proteins implicated in mRNA methylation such as METTL3 and YTHDF1/2.^{9,16–18} These reported RBP-targeting small molecules indicate that targeting RBPs could offer new opportunities to tackle a variety of diseases. Besides small molecules, RNA-binding proteins could be addressed with oligonucleotides or related analogues. However, intracellular bioavailability and stability are limiting factors for oligonucleotides due to size and charge. Additionally, toxicity and immunogenicity issues still hamper the success of oligonucleotides as drugs.^{19–21} In contrast, small molecules have inherent advantages such as being orally available and having sufficient membrane permeability, and thus are a favorable chemotype for RBP targeting.²² This thesis studied three RNA-binding proteins as small-molecule targets: microRNA (miRNA)-binding protein LIN28, single-stranded RNA (ssRNA)-cleaving protein RNase L and the double-stranded RNA (dsRNA)-binding protein OAS1.

1.2 The miRNA-binding protein LIN28

The miRNA-binding protein Lin28 is one of the best-studied RBPs. Lin28 was discovered as a temporal regulator of early development in the nematode *Caenorhabditis elegans* in 1984.²³ In mammals, LIN28 is highly expressed during embryonic development and influences body patterning. Mice embryos overexpressing LIN28 showed increased caudal vertebrae number and tail bud proliferation and expression but also perinatal lethality due to incomplete lung development.^{24,25} While active in early development, LIN28 expression is downregulated in most differentiated tissues, except for skeletal and cardiac muscle and reproduction-related organs like the hypothalamus, ovary, and testis.^{26,27} Single nucleotide polymorphisms in the *LIN28* gene were correlated with the timing of the onset of puberty.²⁷ On the cellular level, LIN28 was discovered as a pluripotency factor that, together with NANOG, OCT4, and SOX2, reprograms cells creating induced pluripotent stem cells.^{28,29} The reprogramming process is accelerated by LIN28, leading to an increased cell proliferation rate.³⁰ As a regulator of proliferation, LIN28 is active during cell growth but inhibited at high cell densities. LIN28 downregulation is triggered by cell-contact inhibition and mediated by sequestration of LIN28 from the cytoplasm as a consequence of interaction with phosphorylated Merlin.³¹

Introduction

In humans, pluripotency is regulated by two LIN28 isoforms, 23 kDa LIN28A and 27 kDa protein LIN28B. Both consist of an *N*-terminal cold shock domain (CSD) and a *C*-terminal zinc knuckle domain (ZKD).³² LIN28B has an extended *C*-terminal acidic stretch and a nuclear and nucleolar localization signal (Figure 1).^{33,34} Consequently, LIN28B is mainly located in the nucleoli and LIN28A was described to be primarily in the cytoplasm, although it was suggested to be able to shuttle to and from the nucleus.^{34,35} The unique combination of the two conventional RNA-binding domains CSD and ZKD makes LIN28 a canonical RBP. The CSD is a β -barrel folded from five antiparallel β -strands. Its name is derived from the first discovered CSD-containing protein, cold shock protein A, which was identified to be highly expressed in *Escherichia coli* upon temperature reduction to 15 °C.^{36,37} The ZKD of LIN28 consists of two zinc knuckle-type (CCHC-type) zinc-finger motifs, each containing a zinc ion coordinated by three cysteines and one histidine residue.³⁸ Both domains are involved in nucleic acid binding. The main target of LIN28 is the miRNA *let-7*, a non-coding tumor suppressive RNA, which is described in more detail in section 1.2.2. Besides binding to *let-7*, LIN28 was reported to bind to mRNA, ribosomal RNA (rRNA), and DNA.^{39–42} LIN28A binds to transcription bubbles of active DNA promoters and recruits the DNA demethylase Tet1. As a result, transcription is directly modulated via DNA methylation modification or removal.³⁹ Research on the interaction of LIN28 with mRNA revealed several thousand target RNAs, with enrichment for a GGAGA consensus sequence found in a study using crosslinking immunoprecipitation followed by high-throughput sequencing.⁴² It was reported that mRNA binding by LIN28 directly influences protein translation and depends on the interaction with helicases and RBPs.^{42–44} The most abundant mRNA targets of LIN28 are its own mRNA, implicating self-regulation, mRNAs of other RBPs, and cell cycle regulators.⁴¹ Moreover, regulation of metabolic enzymes via LIN28–mRNA binding with implications in glucose metabolism was reported.^{45,46} Another suggested function of mRNA and rRNA binding of LIN28 is the sequestration of LIN28 from the cytosol, reducing its local active concentration and influencing the ability to bind to target miRNAs.⁴⁰ Although LIN28 was reported to bind to many coding RNAs, its leading reported interaction partner are *let-7* miRNAs.

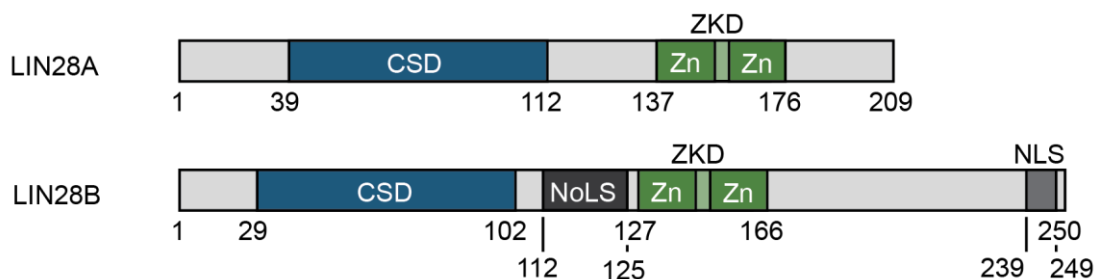


Figure 1. Schematic structure of the LIN28 isoforms LIN28A and LIN28B.⁴⁷

1.2.1 miRNAs

MicroRNAs (miRNAs) are small non-coding RNAs, and their length was reported to be about 22 nucleotides.⁴⁸ More than 1,900 human gene loci coding for miRNAs are annotated in the miRNA database miRbase.⁴⁹ Biogenesis of miRNAs occurs via a distinct process conserved for most miRNAs (Figure 2). First, they are transcribed by RNA polymerase II as 5'-capped and 3' poly(A)-tailed primary transcript miRNAs (pri-miRNAs).^{50,51} The pri-miRNAs consist of at least one hairpin structure with an imperfectly base-paired stem with a length of ~33 base pairs (bp) and a terminal loop at one end and flanking single-stranded RNA segments at the other end of the stem. The unpaired flanking region is essential for the recognition by the microprocessor complex formed by DROSHA and DGCR8.⁵² The RNase III enzyme DROSHA cleaves the pri-miRNA at a distance of 11 bp from the unpaired region, leaving a one to four nucleotide long 3'-overhang.⁵²⁻⁵⁴ The cleavage product termed precursor miRNA (pre-miRNA) has a length of 60-70 nucleotides.⁵⁴ The structural elements of pre-miRNA are recognized by Exportin-5 which then exports the pre-miRNA together with the GTP bound GTPase RAN to the cytosol.^{53,55,56} Pre-miRNA is specifically recognized by the endonuclease DICER, which acts as a molecular ruler and cleaves both strands of the base-paired stem, leaving a fragment of ~22 nucleotide length.^{57,58} One of the two strands from the cleaved stem serves as the mature miRNA, which is loaded to the RNA-induced silencing complex (RISC), mediated by DICER and the protein TARBP2 and Argonaute (AGO) family proteins.⁵⁹ The RISC is the functional unit of miRNAs that repress mRNAs by binding to complementary, 2-8 nucleotides long seed sequences usually located in the 3' untranslated region of mRNAs.⁶⁰ Silencing of target mRNA is achieved by the recruitment of mRNA decapping and deadenylating enzymes followed by exonucleases that degrade the mRNA.⁶¹

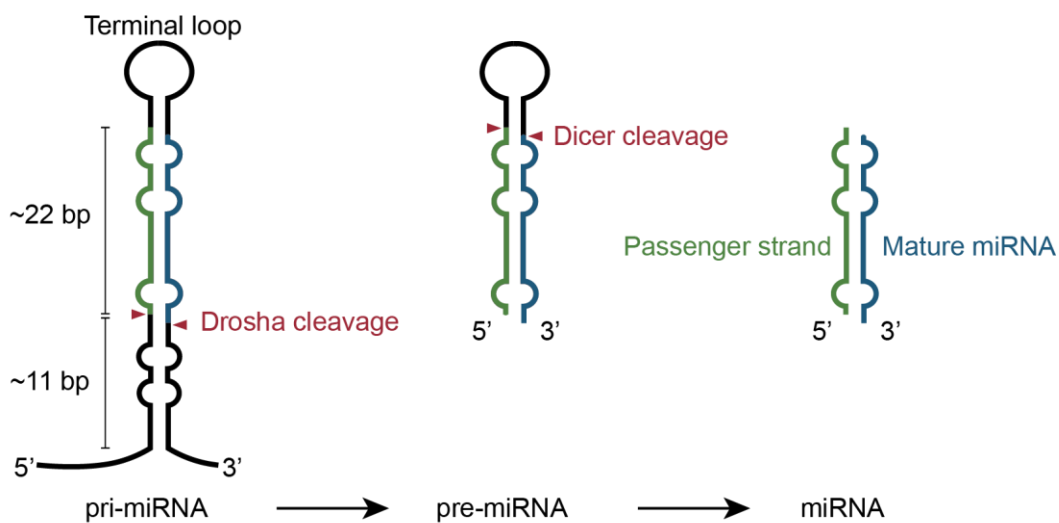


Figure 2: Structure and biogenesis of miRNAs through processing by Drosha and Dicer.⁶²

Target mRNAs of miRNAs can be identified by *in silico* prediction considering miRNA and mRNA sequences or experimentally, for example, by AGO-RNA immunoprecipitation.^{63,64} On average 606 target genes per miRNA were predicted in humans, leading to a considerable amount of mRNAs regulated by miRNAs.⁶⁵ Alterations in miRNA expression and regulation are associated with diseases such as cancer and neurodevelopmental disorders.^{66,67} One miRNA family that was implicated in cancer is the LIN28 target *let-7*.⁶⁸

1.2.2 The miRNA family *let-7*

Similar to LIN28, lethal-7 (*let-7*) miRNA was discovered in *C. elegans* in the year 2000 as one of the first described miRNAs.⁶⁹ Its biogenesis follows the canonical miRNA biogenesis pathway described before (Figure 4A). A total of 12 *let-7* family members were identified in humans (*let-7a-1*, *let-7a-2*, *let-7a-3*, *let-7b*, *let-7c*, *let-7d*, *let-7e*, *let-7f-1*, *let-7f-2*, *let-7g*, *let-7i* and *miR-98*).⁷⁰ While the *pri-let-7* sequences differ among the 12 *let-7* members since they are transcribed from distinct gene loci, the mature sequences only differ in 9 *let-7* isoforms, indicated by different letters in the nomenclature (Figure 3).⁷¹ Nevertheless, the mature sequence of *let-7* and its function in development are conserved among species.⁷²

The major negative regulator of *let-7* is the RBP LIN28 and the outcome of *let-7* overexpression is generally the opposite of the effect of high LIN28 levels. *Let-7* is mainly present in differentiated cells and tissues. The miRNA functions as a repressor of cell proliferation, and is thus considered a tumor suppressor.⁷³⁻⁷⁷ Numerous target mRNAs of the *let-7* miRNA displaying perfect base pairing in at least the conserved seed region of the *let-7* family were identified (Figure 3).⁷¹ Among the repressed genes are cell cycle progression regulators such as cyclin D, cyclin-dependent kinase 6 (CDK6), and M-phase inducer phosphatase 1 (CDC25A), explaining the effect of *let-7* on proliferation.⁷³ Another target class of *let-7* contains mRNAs of transcription factors such as Myc proto-oncogene protein (MYC) and Zinc finger and BTB domain-containing protein 16 (ZBTB16), which in turn regulate cell proliferation and differentiation.^{73,78,79} One thoroughly characterized target of *let-7* is the oncogene RAS, a GTPase and central controller of cell growth.^{75,80} Taken together, the mRNA targets of *let-7* reveal its role as a master regulator of cell proliferation and differentiation. As a result, downregulation of *let-7* is often observed in less differentiated cancer cells proliferating abnormally.⁸¹⁻⁸³

Introduction

Consensus	U	GAGGUAG	UAGGUUGUAUAGUU
<i>let-7a-1</i>	U	GAGGUAG	UAGGUUGUAUAGUU
<i>let-7a-2</i>	U	GAGGUAG	UAGGUUGUAUAGUU
<i>let-7a-3</i>	U	GAGGUAG	UAGGUUGUAUAGUU
<i>let-7b</i>	U	GAGGUAG	UAGGUUGUGUGGUU
<i>let-7c</i>	U	GAGGUAG	UAGGUUGUAUGGUU
<i>let-7d</i>	A	GAGGUAG	UAGGUUGCAUAGUU
<i>let-7e</i>	U	GAGGUAG	GAGGUUGUAUAGUU
<i>let-7f-1</i>	U	GAGGUAG	UAGAUGUAUAGUU
<i>let-7f-2</i>	U	GAGGUAG	UAGAUGUAUAGUU
<i>let-7g</i>	U	GAGGUAG	UAGUUGUACAGUU
<i>let-7i</i>	U	GAGGUAG	UAGUUGUGUGUU
<i>mir-98</i>	U	GAGGUAG	UAAGUUGUAUUGUU

Seed

Figure 3. Sequences of mature *homo sapiens let-7* family members. Seed binding sequences are colored in blue, and mismatches to the consensus sequence are shown in red.⁷¹

1.2.3 The protein LIN28 regulates *let-7* biogenesis

Most reported functions of LIN28 and *let-7* are tightly connected to their mutual interaction. LIN28 binds to *pri-* and *pre-let-7* in the stem-loop region termed pre-element (preE) of the unprocessed miRNA and thereby shields the RNA from cleavage by Drosha and Dicer (Figure 4B).⁸⁴ While LIN28A and LIN28B are specific for the *let-7* miRNA family when tested against a panel of 72 pre-miRNAs, *let-7* miRNAs interact with multiple proteins in pull-down experiments.⁸⁵ Both the CSD and ZKD of LIN28 bind to *let-7*. A 15 amino acid long flexible linker connecting the two RNA-binding domains allows promiscuous binding with different *let-7* family members (Figure 4D).³² Consequently, the RNA-binding domains of LIN28 recognize specific sequences of *let-7*, separated by a variable number of non-bound nucleotides.⁸⁶ The ZKD binds to a conserved 5'-GGAG-3' consensus sequence in the terminal loop of *pre-let-7*.^{32,86} Only *pre-let-7a-3* does not contain the GGAG motif but bears an AUGGG sequence instead, leading to a weaker interaction.^{38,87} Dicer cleaves *let-7* a few nucleotides downstream from the GGAG motif, for example four nucleotides in case of *pre-let-7f-1*, but cannot access the cleavage site if LIN28 is bound.^{49,84}

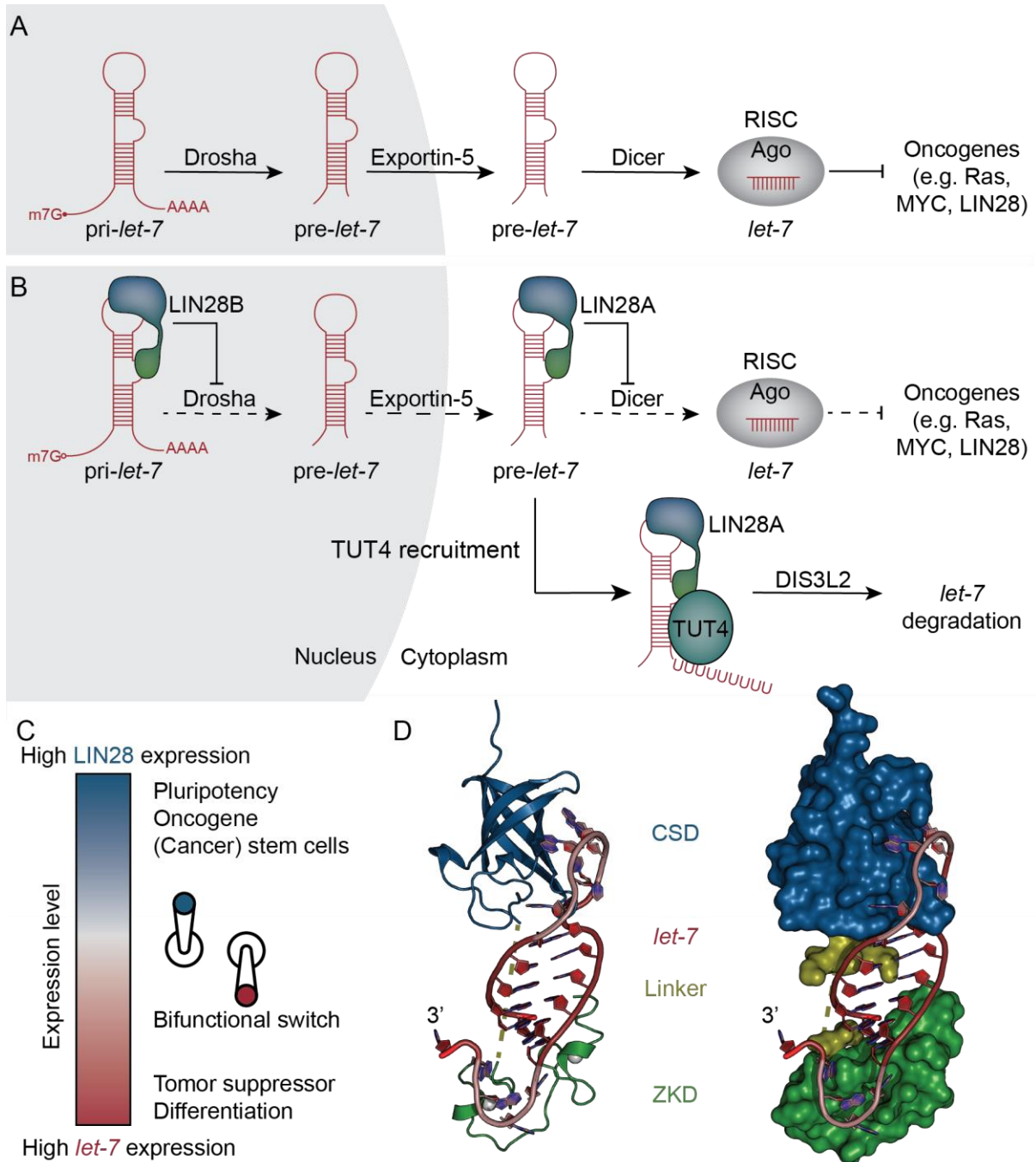


Figure 4. (A) Biogenesis pathway of *let-7* and (B) inhibition mechanisms by LIN28 and TUT4. LIN28 inhibits the processing of *pri-* and *pre-let-7* by Drosha and Dicer and recruits TUT4 for oligouridylation as a signal for the degradation of *let-7*. (C) LIN28 and *let-7* act as a bifunctional switch regulating differentiation and tumorigenicity of cells. (D) Structure of LIN28A in complex with a truncated *let-7-f1* pre-element as ribbon (left) and surface (right) representation (PDB 5UDZ).⁸⁸ The CSD is colored in blue, the ZKD in green, the linker was partially unresolved in the crystal structure and is shown in yellow and indicated as a dashed line, zinc ions are depicted in grey, and the *let-7* RNA is shown in red. CSD-binding consensus sequence UGAU and ZKD binding sequence GGAG are shown in light red.

Introduction

The target of the CSD is a loop structure with a less conserved sequence. Efforts in trying to identify a consensus CSD-binding motif have been reported from different groups. For instance, Sliz and colleagues proposed an NNGAYNNN (Y = pyrimidine; N = any base) CSD binding motif based on several crystal structures, while Heinemann and colleagues identified binding pyrimidine-rich to 7- to 9-mers with a GUNNUNN consensus sequence in biochemical assays.^{32,84} However, a photoactivatable-ribonucleoside-enhanced crosslinking and immunoprecipitation (PAR-CLIP) experiment using individual protein domains could not reproduce the aforementioned CSD-binding RNA motifs.⁸⁹ Later, Zhang and colleagues proposed a (U)GAU RNA motif for CSD binding based on CLIP (cross-linking and immunoprecipitation) data of more than 10,000 LIN28 binding sites on mRNA and the authors distinguished *let-7* family members containing the CSD binding sequence (CSD⁺) and *let-7* isoforms that do not harbor the (U)GAU motif (CSD⁻). The findings were supported by different affinities of CSD⁺ and CSD⁻ miRNAs to the CSD in biochemical assays.⁹⁰

The ZKD mediates an additional mechanism of *let-7* regulation specific to the LIN28A isoform. It recruits terminal uridylyltransferase TUT4 and potentially also TUT7, which oligouridylate the 3'-end of *pre-let-7* (Figure 4B).^{34,86,88,91} The transferases are 185 and 171 kDa proteins, respectively, consisting of an N-terminal LIN28-interacting module and a C-terminal catalytic terminal uridylyltransferase domain.^{92,93} Without the presence of LIN28, the TUT enzymes catalyze the UTP-dependent transfer of one nucleotide to *pre-let-7* miRNA, facilitating Dicer processing due to the formation of an optimal Dicer cleavage site.^{93,94} The ZKD of LIN28 forms a ternary complex with the LIN28 interacting module of TUT4, thereby switching enzyme activity from monouridylation to processive oligouridylation.^{86,88,93,95} Oligouridylation is a signal for degradation of the *let-7* miRNA by the 3'-5' exonuclease DIS3L2 (DIS3-like exonuclease 2).⁹⁶ DIS3L2 specifically recognizes the oligouridyl tail, which binds to a funnel-like structure leading to the exonuclease's active site. The polyuridyl tail is degraded processively, followed by the rest of the miRNA.⁹⁷ LIN28B, in contrast, was suggested to function independently from TUT4 and possibly inhibits *let-7* maturation by sequestration of *pri-let-7* in the nucleolus.³⁴ Both LIN28 isoforms were additionally suggested to indirectly regulate all cellular miRNAs due to influencing free *let-7* levels, which in turn scavenge a limited amount of available Argonaute protein. Low-abundance miRNAs can only bind Argonaute if *let-7* is present at low levels because of binding by LIN28.⁹⁸ Taken together, LIN28 can regulate *let-7* through direct binding, restraining its localization to specific cellular compartments, and recruitment of degrading enzymes. Interestingly, the mRNA of LIN28 is also a target of mature *let-7* miRNA leading to the inhibition of LIN28 translation. Together, both molecules form a bistable switch leading to the predominant expression of either LIN28 or *let-7* (Figure 4C).⁹⁹ The switch generally decides if the cells are in a pluripotent state (high LIN28 condition) or differentiated

(high *let-7*).¹⁰⁰ Dysregulation of this bistable switch is relevant in diseases such as cancer. LIN28 overexpression was detected in ~15% of human tumors and cancer cell lines with downregulation of *let-7* family miRNAs and, thus, upregulation of *let-7* targets.¹⁰¹ The targets of LIN28 and *let-7* together influence all ten hallmarks of cancer proposed in 2011 and also modulate the 2022 proposed hallmark of nonmutational epigenetic reprogramming via regulation of TET1 activity.^{39,102–104} The central role of LIN28 in cancer is underlined by the observation that LIN28 expression is a biomarker for cancer stem cells which are dedifferentiated cells that allow the regrowth of tumors out of a limited number of cells.^{101,105} Cancer stem cells are often resistant to chemotherapy, and accordingly, LIN28 overexpression is generally associated with metastasis and poor prognosis.^{101,102,106–108} Owing to the different mechanisms in which LIN28A and LIN28B act on *let-7*, both are overexpressed in different kinds of tumors. While, for example, HER2-positive breast cancers typically have high expression of LIN28A, LIN28B was found overexpressed in triple-negative breast cancers.³⁴ Inhibition of LIN28 by siRNA in human xenograft tumor models in mice led to reduced tumor size, indicating that the interaction of LIN28 and *let-7* is a promising target for cancer therapy.³⁴

1.2.4 LIN28 as a target in medicinal chemistry

Since the RBP LIN28 is a well-validated oncogene, LIN28 inhibitors have great potential as starting points for anticancer drug development. Additionally, selective LIN28 inhibitors are sought-after as chemical probes to increase understanding of the functions of LIN28 by perturbation of its cellular pathways.^{109–111} Knowledge of the LIN28 biology suggests the usage of *let-7* as a LIN28 inhibitor. Indeed, delivery of *let-7* to mouse tumor models led to tumor reduction.¹¹² Chemically modified *let-7* was studied as LIN28 inhibitor by Mirna Therapeutics, Inc. and reported recently by Segal *et al.*^{21,102} The latter report used hydrophobically modified *let-7b*, which was directly taken up by cancer cells and led to LIN28 silencing *in vitro*. *In vivo*, localization to targeted lung tumors was found, although most of the molecules were detected in the clearance organs of the studied mice.²¹ Therapeutic miRNAs generally display problems such as toxicity, poor bioavailability in the targeted tissue, degradation, and activation of the immune response.²¹ A more advanced oligonucleotide-based approach to target LIN28 developed proteolysis-targeting chimeras (PROTACs) against the RBP.¹¹³ PROTACs are bifunctional molecules with a protein of interest-binding moiety linked to an E3-ligase recruiting molecule. The chimera induces the formation of a ternary complex in which the E3-ligase catalyzes ubiquitination of the targeted protein, serving as a signal for protein degradation.¹¹⁴ The RNA-PROTAC ORN3P₁ (**1**) contained 2'-O-methoxymethyl-modified ribonucleotides with a ZKD-binding sequence (5'-AGGAGAU-3') conjugated to a peptide that recruits the E3-ligase

Introduction

von Hippel-Lindau (VHL). The bifunctional molecules were cell-permeable and induced 50% degradation of LIN28 at a concentration of 2 μM (Figure 6).¹¹³

In contrast to oligonucleotide drugs, small molecules have the potential to lead to more stable molecules with lower immunogenicity and oral bioavailability. The first small-molecule inhibitors of the RBP LIN28 were reported in 2016.^{115–117} All LIN28 inhibitors to date originate from screenings of small-molecule libraries using a wide range of different methods (Figure 5 and Figure 6).^{115–122} Most small-molecule screenings were performed using fluorescence-based technologies, which allow high throughput and miniaturization and do not require any washing steps.^{115–120} For example, Roos *et al.* reported a Förster resonance energy transfer (FRET) assay using cell lysate containing fluorescent protein EGFP-fused LIN28, which was incubated with quencher-coupled *let-7* RNA. An inhibitor disrupting the complex formation of LIN28 and *let-7* would lead to a detectable fluorescent signal. Out of 16,000 compounds, triazolopyridazine C1632 (**2**) was identified as a LIN28 inhibitor. The molecule was validated in an enzyme-linked immunosorbent assay (ELISA), revealing a half-maximal inhibitory concentration (IC_{50}) of 8 μM . In cellular assays, upregulation of mature *let-7* levels were measured by qPCR.¹¹⁵ However, the effects in the qPCR could not be reproduced by Dong and colleagues.¹²² Although off-target binding to bromodomains with micromolar affinities and the benzodiazepine receptor were reported, C1632 (**2**) was used in several studies as a LIN28 chemical probe.^{109–111} Treatment with C1632 (**2**) reduced expression of *let-7* target PD-L1 restoring antitumor immunity *in vivo*.¹¹⁰ Further, C1632 (**2**) was suggested to modulate lipid homeostasis via LIN28 inhibition and was even shown to reduce replication of severe acute respiratory syndrome coronavirus 2 (SARS-CoV-2) and inflammation via downregulation of pro-inflammatory *let-7* targets.^{109,111} A sophisticated FRET assay by Lim *et al.* used a probe created by the coupling of a Cy3-fluorophore to an unnatural amino acid incorporated into the flexible linker of LIN28. Again, quencher-labeled miRNA was used as a fluorescence acceptor. Screening of 4,500 small molecules led to the discovery of chromenopyrazole SB1301 (**3**) with an IC_{50} of 4 μM . The inhibitor was validated in an orthogonal electrophoretic mobility shift assay (EMSA) and shown to bind to the CSD by surface plasmon resonance (SPR) and differential scanning fluorimetry (DSF). In cells, the molecule was active at 20–40 μM concentrations increasing levels of mature *let-7*, decreasing *let-7* target proteins as shown by western blot, and also active in a luciferase assay.¹¹⁶ A follow-up study employed the same assay to screen another library of 8,400 molecules identifying KCB3602 (**4**) (IC_{50} 4.8 μM) and derivatives. Binding to LIN28A was shown in SPR, and the compound induced upregulation of *let-7* while downregulating *let-7* target proteins.¹¹⁹

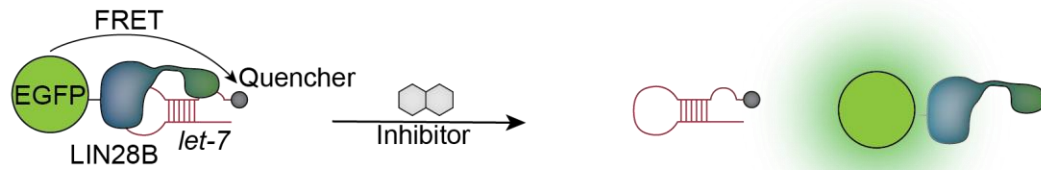
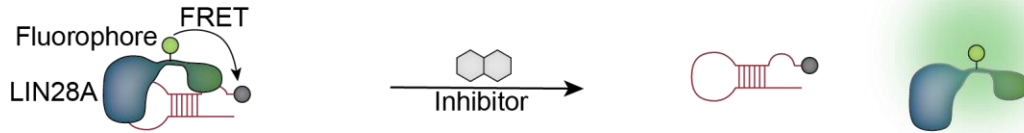
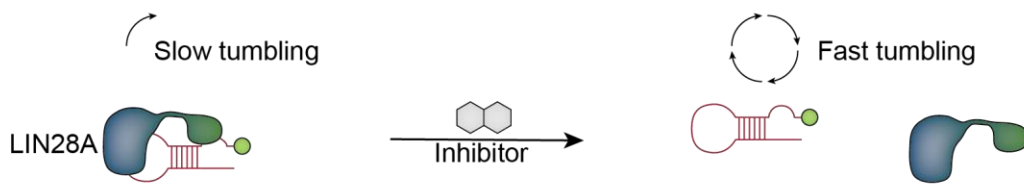
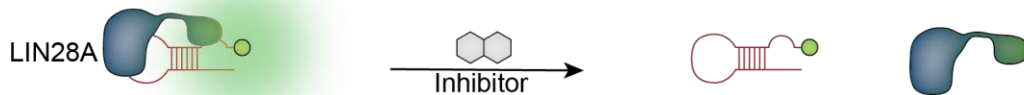
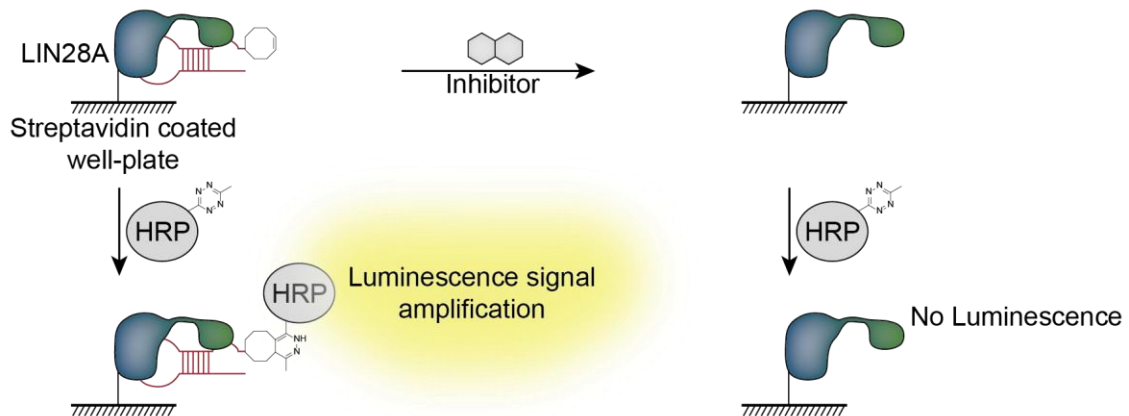
A FRET assay, Roos *et al.*B FRET assay, Lim *et al.*C FP assay, Wang *et al.*, Lightfoot *et al.*D FI assay, Byun *et al.*E cat-ELCCA, Lorenz *et al.*

Figure 5. Principles of reported assays screening for LIN28 inhibitors. (A) FRET assay using EGFP-LIN28B fusion protein and quencher labeled *let-7*.¹¹⁵ (B) FRET assay using site-specific chemical fluorophore labeling of LIN28A and quencher labeled *let-7*.^{116,119} (C) FP assay using fluorophore-labeled *let-7*.^{117,118} (D) FI assay using proximity-induced changes in fluorescence of a fluorophore connected to *let-7*.¹²⁰ (E) Catalytic enzyme-linked click chemistry assay employing immobilized LIN28 incubated with 5'-*trans*-cyclooctene modified *let-7* and further with methyl tetrazine-labeled horseradish peroxidase.¹²¹ EGFP, enhanced green fluorescent protein; FI, fluorescence intensity; cat-ELCCA, catalytic enzyme-linked click chemistry assay; HRP, horseradish peroxidase.

Introduction

While FRET requires a fluorophore–quencher pair, only a single fluorophore is needed in fluorescence polarization assays. Free dye-labeled precursor *let-7* RNA tumbles more rapidly in solution than LIN28-bound RNA. As an effect, after excitation with plane-polarized light, the fluorophore's emission that is linked to unbound RNA will be more depolarized than that of protein-bound fluorescently labeled miRNA. A fluorescence polarization (FP) assay was developed by Lightfoot *et al.* and led to the identification of the low-micromolar LIN28 inhibitors aurintricarboxylic acid (**5**) (IC_{50} 1.2 μ M), 6-hydroxy-DL-DOPA (**6**) (IC_{50} 7.1 μ M), Reactive blue 4 (**7**) (IC_{50} 10.8 μ M) and SB/ZW/0062 (**8**) (IC_{50} 4.7 μ M). The molecules were validated by EMSA and a DICER cleavage assay in which DICER-processing of *pre-let-7* in the presence of LIN28 was restored by 6-hydroxy-DL-DOPA (**6**) and SB/ZW/0062 (**8**). No cellular assays were performed with these screening hits.¹¹⁷ Cellular assays were conducted by Wang *et al.* after employing an FP assay screening more than 100,000 compounds discovering DAQ-B1 (**9**) (IC_{50} 1 μ M), BVT-948 (**10**) (IC_{50} 3.5 μ M), gossypol (**11**) (IC_{50} 1.6 μ M), TPEN (**12**) (IC_{50} 2.5 μ M), LI20 (**13**) (IC_{50} 5.7 μ M) and LI71 (**14**) (IC_{50} 7 μ M) as primary hit inhibitors of the LIN28–*let-7* interaction. TPEN targets the ZKD, while LI71 interacts with the CSD, as shown by NMR.¹¹⁸ The latter small molecule upregulated *let-7* maturation as measured by qPCR, which an independent group reproduced later.^{118,122} Controversially, despite being a CSD binder, LI71 (**14**) was active in EMSA and FP that used only the ZKD of LIN28.¹²² Recently, Byun *et al.* recognized that not only fluorescence polarization but also fluorescence intensity (FI) of fluorophores coupled to *pre-let-7* is influenced by LIN28 binding. TAMRA fluorescence signal increased upon complex formation. An FI assay based on that observation was used for a library screening, and KCB170522 (**15**) (IC_{50} 9.6 μ M) and luteolin (**16**) (IC_{50} 2.4 μ M) were identified as LIN28 inhibitors. EMSA, qPCR, and western blot of LIN28 target proteins validated the hits. Luteolin (**16**) showed poor activity in cells, while KCB170522 was active at a concentration of 20 μ M.¹²⁰ A recent study by Radaeva *et al.* used the FP assay only as a secondary assay after an extensive *in silico* screening. Ultimately, Ln7 (**17**) (IC_{50} 45 μ M), Ln15 (**18**) (IC_{50} 9 μ M), and Ln115 (**19**) (IC_{50} 21 μ M) were reported as LIN28 ZKD inhibitors and validated by biolayer interferometry (BLI), qPCR of mature *let-7* and western blot of *let-7* target proteins.¹²² A non-fluorescent screening assay, termed catalytic enzyme-linked click chemistry assay (cat-ELCCA), was developed by Garner and colleagues. The assay uses LIN28, which is immobilized on a microtiter plate followed by incubation with *pre-let-7* modified at the 5'-end with *trans*-cyclooctene. Inhibitors would prevent the binding of *let-7* to LIN28 at this step. Then, methyl tetrazine-labeled horseradish peroxidase is added to the microtiter plate to induce a click-reaction with cyclooctene. A washing step before the detection of the chemiluminescence signal ensures that the small molecules do not interfere with binding. The molecules discovered by cat-ELCCA, CCG-233094 (**20**), and CCG-234459 (**21**) with IC_{50} values of

Introduction

8.3 μM and 10.3 μM , respectively, were both based on the same scaffold. The compounds were active in an orthogonal EMSA assay, but no cellular assays were reported.¹²¹ Taken together, multiple studies reported inhibitors of LIN28, but no so far identified compound reached submicromolar activity, and especially potency in cellular assays, if determined, remained low. Reported inhibitors suffer from limited characterization since the targeted protein domain is only known for a few inhibitors. No co-crystal structure of LIN28 with a small molecule was reported and therefore the exact binding mode of the compounds remains unknown. Structural binding information would be helpful to confirm the binding of the inhibitors and investigate the interactions between LIN28 and its inhibitor in detail. This could reveal possible sites of modifications and allow a rational structural design approach to improve the inhibitors. Further, a potentially solvent-exposed site could be determined based on a structure to attach a linker to design bifunctional molecules such as PROTACs. Structure-activity relationship (SAR) investigation, which generally informs about the mechanism of action of compounds and enables improvement of activities, was only reported for a few LIN28 inhibitors so far. The ZKD interactors TPEN (**12**), Ln115 (**19**), CCG-234459 (**20**) and CCG-233094 (**21**) harbor symmetrical electron pair-donating structural motifs, which potentially act as metal complexors of the bivalent zinc ions of the ZKD.^{117,121,122} Selectivity of the compounds for LIN28 was determined for C1632 (**2**), which also binds to bromodomains with low micromolar affinity and to the benzodiazepine receptor.¹¹⁵ Thus, improved small-molecule inhibitors of LIN28 need to be discovered by screenings and extended SAR investigation need to be performed.

Introduction

MOE-RNA

Peptide

AGGAGAU-(linker)-C[Ahx]LA[Hyp]YI

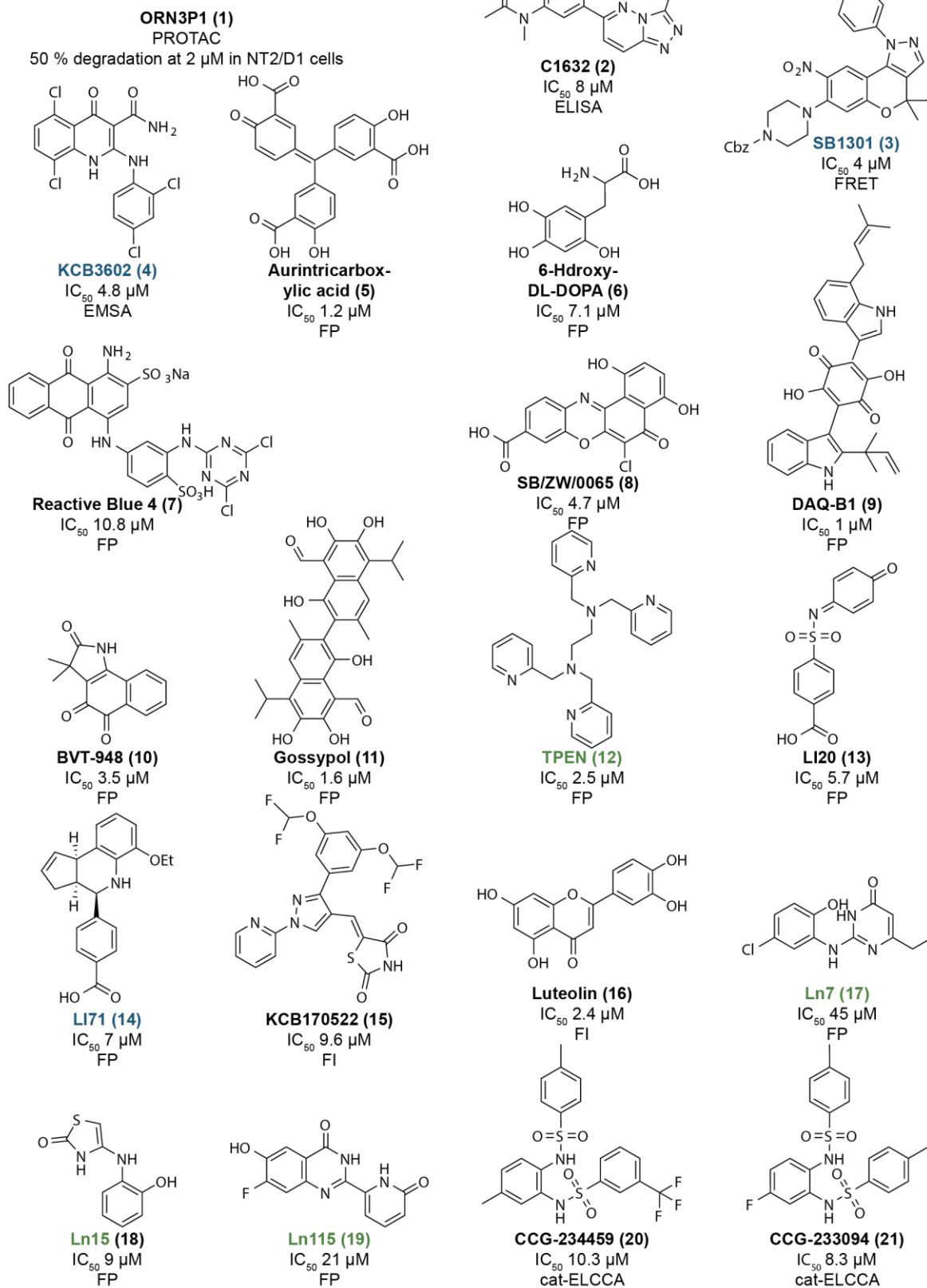


Figure 6. Reported inhibitors of LIN28. Listed are their reported IC_{50} values together with the tested assay. In case of the PROTAC molecule, the degradation activity is listed. Blue compound names indicate CSD binders, and green font indicates ZKD binders. Compounds with black fonts indicate unclear mechanisms of inhibition. MOE, 2'-O-methoxyethyl; [Ahx], 6-(Fmoc-amino)hexanoic acid; [Hyp], L-hydroxyproline.^{113,115-122}

1.2.5 Targeting of regulators of the LIN28 pathway

It is noteworthy to mention that apart from LIN28, also its interactors were studied as targets in medicinal chemistry, with an effect on *let-7* maturation.^{123–126} A nanobody inhibiting the interaction of LIN28A and TUT4 was shown to prevent the uridylation of *let-7*, which proves that the protein-protein interaction might be a potential target for therapeutics.¹²³ One small-molecule screening for inhibitors of TUT4 enzyme activity was reported using a biochemical assay that detects the uridylation side-product inorganic phosphate in a luminescent readout. Aurothioglucose hydrate was the only hit molecule that was active *in vitro* and in cellular assays measuring the uridylation of *let-7*. However, mature *let-7* levels were not affected by the molecule.¹²⁴ Cinkornpumin *et al.* reported a cellular assay based screening of 36,480 compounds to identify modulators of mature *let-7* levels without focusing solely on LIN28 inhibition. A luciferase assay was designed employing Renilla luciferase fused to eight *let-7* target sequences so that luciferase expression would be reduced by mature miRNA binding to the 3'-untranslated region of Renilla luciferase mRNA. The identified hit molecule reduced *let-7* target mRNA levels. Small-molecule target identification suggested Phosphodiesterase 10 A as the target of the screening hit, linking cyclic-AMP signaling to *let-7* biogenesis.¹²⁵ Another medicinal chemistry approach targeting the LIN28 pathway used small oligonucleotides directly targeting *let-7*. The 2'-O methyl modified 'looptomirs' inhibited the binding of LIN28 to *let-7* by binding to the pre-miRNA stem-loop without impairing Dicer processing. The oligoribonucleotides displayed low nanomolar activities *in vitro* and reduced expression of the *let-7* target LIN28B *in cellulo*. However, the abovementioned disadvantages of oligonucleotides as potential therapeutic agents applied here accordingly.¹²⁶

1.3 The OAS–RNase L pathway

The OAS-RNase L pathway plays an important role in the human innate immune response. It allows immune detection of foreign double-stranded RNA in the cytoplasm of cells and activates an antiviral cellular state by inducing RNA cleavage via ribonuclease L (RNase L).

1.3.1 Ribonuclease L is a central regulator of the innate antiviral response

The 2'-5'-A-dependent ribonuclease (RNase L) pathway is activated upon viral infection of mammalian cells. The ribonuclease (RNase) is constitutively expressed in nearly all cell types in an inactive state.¹²⁷ RNase L signaling is triggered by the occurrence of double-stranded RNA (dsRNA), which is recognized as a pathogen-associated molecular pattern (PAMP) by 2'-5'-oligoadenylate synthetases (OAS). Double-stranded RNAs are usually not present in mammalian cells but exist as replicative intermediates of RNA viruses after infection.^{128,129} Binding of dsRNA to OAS induces a conformational change and thus activates the synthetases, which produce 5'-phosphorylated 2'-5'-linked oligoadenylates (2'-5'A) out of ATP

Introduction

(Figure 7A).¹³⁰ The 2'-5'-linkage is rarely observed in nature, and the sole known function of the second messenger 2'-5'A is the activation of RNase L.^{131,132} Most detected 2'-5'A molecules are trimeric and bind to RNase L in a one-to-one ratio inducing dimerization or oligomerization of the 83.5 kDa RNase L protein.¹³³⁻¹³⁶ The 2'-5'A-bound dimer of RNase L is the active state which cleaves single-stranded RNA (ssRNA) at rather unspecific UN^N (whereas N stands for any base and “^” indicates the cleavage site) consensus motifs (Figure 7B).^{135,137,138} After cleavage, a 5'-OH group and a 2'-3'-cyclic phosphate are left at the RNA products' ends, characteristic of nucleases without metal ions in the catalytic site.^{139,140} This is caused by the cleavage mechanism in which the 2'-OH of the ssRNA serves as a nucleophile.¹⁴⁰

The substrates of RNase L are virtually all types of RNA. Cleavage of viral RNA, mRNA, ribosomal RNA (rRNA), circular RNA (circRNA), transfer RNA (tRNA), and mitochondrial mRNA was reported.^{127,137,141,142} While ribosomes remain functional after cleavage, degradation of mRNA by RNase L causes a global translational arrest of the cells, and an antiviral state is induced.^{137,138,143} While most mRNAs are downregulated by 2'-5'A-mediated decay, specific mRNAs of interferon-induced antiviral proteins, such as interferons, are resistant to the effect of RNase L and still translated, mediating the antiviral state of the cell.¹⁴⁴⁻¹⁴⁶ RNase L cleavage products were reported to activate downstream signaling via MDA5 and RIG-I, ultimately leading to the expression of interferons.¹⁴⁷ Interferons are secretory proteins activated by the innate and acquired immune response that initiate the expression of interferon-stimulated genes, such as OAS, thus amplifying antiviral signaling.^{148,149} Further downstream effects of the 2'-5'A-mediated response are inhibition of mRNA export from the nucleus, inflammasome activation, and induction of apoptosis.^{139,143,150-152} Additionally, activation of RNase L was reported to induce the formation of RNase L-dependent bodies with unknown functions, which are characteristic assemblies of ribonucleoprotein complexes different from stress granules.^{153,154} The RNase L-dependent bodies consist of non-translated mRNA fragments and RNA-binding proteins.¹⁵⁴

Introduction

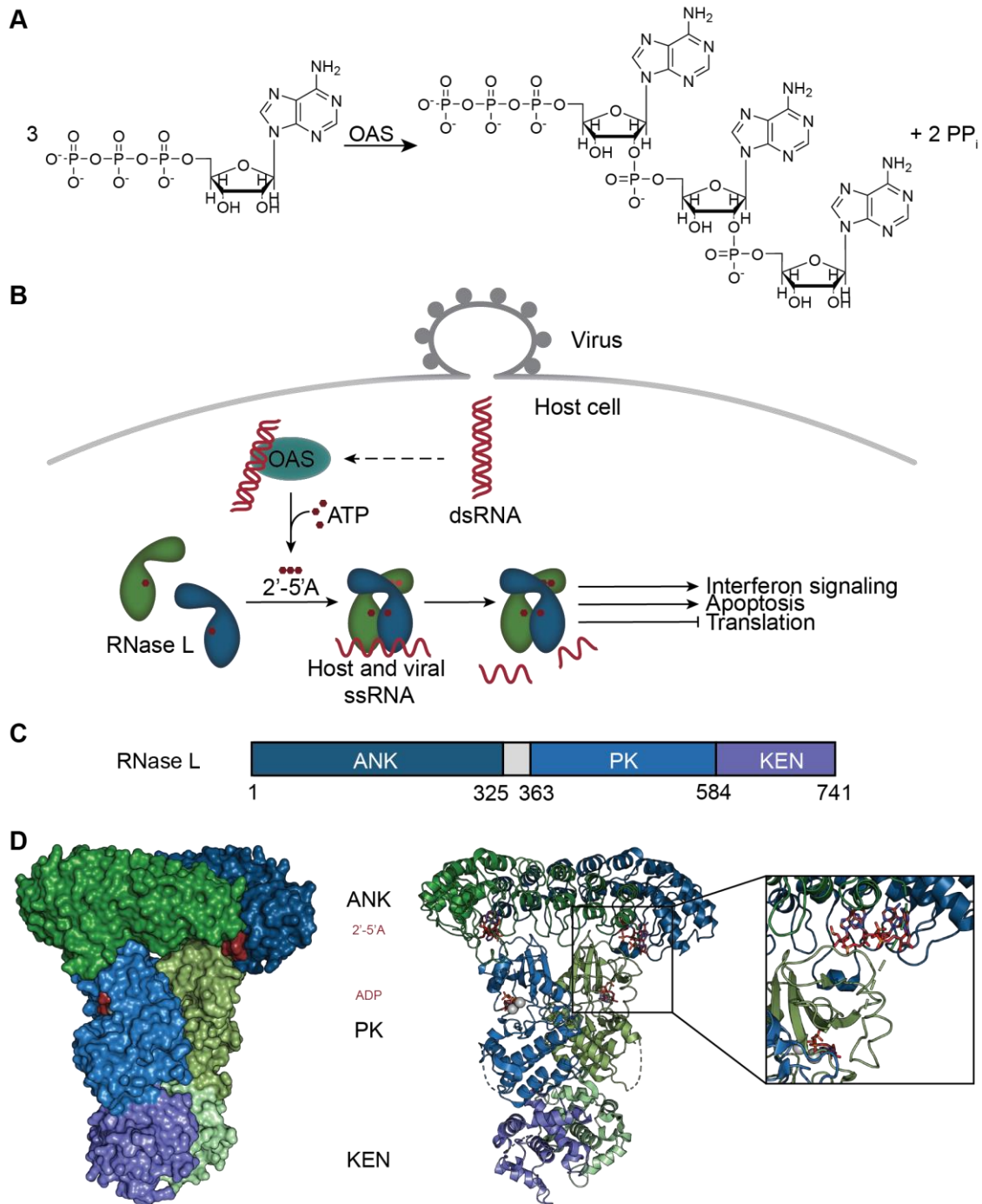


Figure 7: (A) OAS catalyzes the reaction of ATP molecules to 2'-5'-A. This example shows the reaction to the most active trimeric form of 2'-5'-A. (B) 2'-5'-A-mediated decay pathway. Viral dsRNA activates OAS to produce RNase L-activating 2'-5'-A. Active dimerized RNase L cleaves host and viral ssRNA to induce interferon signaling, apoptosis and a global translational arrest. (C) Schematic structure of RNase L consisting of ankyrin repeat domain (ANK), pseudokinase domain (PK) and kinase extension nuclease domain (KEN). (D) Structure of RNase L (PDB 4OAV; one protomer is shown in green, the other protomer is depicted in blue, the individual domains are shown in different shades of blue or green, 2'-5'-A and nucleotide are shown in red). Left: surface representation of dimeric RNase L, center: cartoon representation of RNase L dimer, right: zoom on 2'-5'-A which binds at the interface of the ANK of both protomers and the PK domain.¹³⁵

Introduction

RNase L, the central regulator of the 2'-5'A-mediated decay pathway, is built up out of three domains, an *N*-terminal ankyrin repeat domain (ANK), a pseudokinase domain (PK), and a C-terminal kinase-extension nuclease domain (KEN, Figure 7C).^{134,135} Crystal structures of the RNase L dimer and monomeric and dimeric ANK were reported giving insights into the mechanism of action of RNase L (Figure 7D).^{133–135,155} Active RNase L is a crossed homodimer with interaction surfaces between all three domains. The ANK consists of nine ankyrin repeats, of which repeats 2-4 are involved in 2'-5'A sensing.^{134,135} No significant structural changes of the ANK domain were observed upon 2'-5'A binding.¹³³ The N-lobe of the PK of the interacting protomer provides the rest of the 2'-5'A binding pocket.^{134,135,155} The PK lacks catalytic function and carries a DFD motif instead of the kinase-typical DFG motif in the regulatory activation loop.¹³⁵ Nevertheless, ATP and ADP bind to the two-magnesium ion-containing active site of the PK. Both, as well as non-hydrolyzable ATP analogs, have the same effect on RNase activity, and the nucleotide-bound RNase L has a rigid closed kinase conformation comparable to the structure of the active state of kinases.^{134,135} Although the RNase is only active when 2'-5'A is present and nucleotides are bound in both PKs, the differences in the structures of RNase L with and without nucleotide bound were marginal (RMSD 0.5 Å).¹³⁴ Conclusively, the PK was suggested to serve mainly as a scaffold for dimerization.¹³⁵ The KEN is linked to the PK via a rigid connection. Both protomers are required to allow the binding and cleavage of a single RNA substrate at the interface by a metal-independent cleavage mechanism.¹³⁴ One protomer interacts specifically with a U nucleotide via histidine 672; the other protomer catalyzes RNA cleavage of the scissile bond after the nucleotide adjacent to the U using its histidine 672 residue. Mutation of both of the histidine 672 residues consequently leads to an inactive ribonuclease, while the RNase L dimer with only one missing histidine in the active site remains active.¹³⁵ The metal-free RNase domain connected to a kinase is a unique protein fold only observed in RNase L and serine/threonine-protein kinase and endoribonuclease IRE1, which, however, carries an active kinase domain.¹³³ Further mechanistic studies revealed that 2'-5'A-binding is necessary for dimerization and activation of RNase L, while the presence of ATP or ADP is only necessary for activation, but not for dimerization.¹³⁴ The 5'-phosphate group of 2'-5'A is essential for activity, but exchange to a phosphonate is tolerated.¹⁵⁶ 2'-5'A binds RNase L with a K_D of 40 pM, and the high affinity is explained by the interaction of every functional group of the 2'-5'A trimer with RNase L, making 2'-5'A a potent RNase L regulator.^{134,157,158}

Host proteins such as 2'phosphodiesterase degrading 2'-5'A regulate the 2'-5'A mediated decay pathway in the cells.¹⁵⁹ Additionally, the protein ABCE1, also known as RNase L inhibitor, was reported to bind RNase L directly, thereby inhibiting RNase L activity.¹⁶⁰ A critical upstream regulator of the double-stranded RNA response is ADAR1, an enzyme that

catalyzes the deamination of adenosine, producing inosine. The effect of RNA modification by ADAR1 is the destabilization of dsRNA, reducing OAS1 activation. It was shown that ADAR1 knockout lethality is rescued by simultaneous knockout of RNase L, hinting towards RNase L-mediated apoptosis in the absence of ADAR1.¹⁶¹ The importance of the 2'-5'-mediated decay in host defense is underlined by the fact that viruses evolved diverse mechanisms to evade the RNase L-mediated innate immune response. Examples of viral evasion include proteins that reduce levels of dsRNA thereby limiting OAS activation, proteins that bind to RNase L inhibiting dimerization, proteins masking RNA, RNAs that inhibit RNase activity, and 2',5'-phosphodiesterases degrading 2'-5'A.¹⁶²

1.3.2 Ribonuclease L as a target of small-molecule drugs

RNase L activation is important in host defense against viral infection, and thus small-molecule RNase L activators have the potential to be developed into antiviral therapeutics. Besides, mutations in the *RNASE L* gene were associated with hereditary prostate cancer, and RNase L activation reduces the formation of cancer metastases, rendering RNase L a potential target for anticancer drugs.^{163,164} Another disease in which upregulation of RNase L activity was observed, together with the abundance of a cleaved RNase L species, is chronic fatigue syndrome (CFS).^{165,166} However, insufficient scientific evidence exists to assign RNase L dysregulation as a cause for CFS.¹⁶⁷ Until now, two screenings for the identification of RNase L activators have been reported.^{157,168} The first employed a FRET-probe consisting of an RNA sequence from respiratory syncytial virus labeled with a fluorophore-quencher pair at both ends. While fluorescence is quenched when the RNA is intact, RNase L activation and subsequent cleavage of RNA lead to a fluorescent signal. Screening of 30,000 small molecules identified thiophenone C1 (**22**) and thienopyrimidinone C2 (**23**) with half-maximal effective concentrations (EC₅₀) of 26 and 22 μM, respectively.¹⁵⁷ During SAR evaluation of C1 (**22**) and C2 (**23**), C1 (**22**) was improved to C1-3 (**24**) with 48% cleavage activity when assayed at a concentration of 130 μM and normalized to cleavage induced by 100 nM 2'-5'A. C2 (**23**) was reported to induce -37% cleavage when compared to 2'-5'A and DMSO, and modifications could not improve activity above that of DMSO.¹⁶⁹ Recently, screening of a DNA-encoded library identified DEL-2 (**25**) as an RNase L binder. A FRET assay suggested activating potency by the molecule (Figure 8).¹⁶⁸

Due to the moderate substrate-sequence specificity of RNase L and its ubiquitous expression in nearly all tissues, RNase L could be used as a biomolecular tool for degradation of any RNA of interest. Bifunctional molecules could be employed to induce proximity between an RNA of interest on the one side, and the RNase on the other side. Silverman and co-workers first published such an approach in 1993 using an antisense oligonucleotide coupled to 2'-5'A. The

Introduction

oligonucleotide specifically binds to an HIV-RNA, and the 2'-5'A recruits and activates RNase L leading to specific degradation of the HIV RNA in cell-free assays.¹⁷⁵

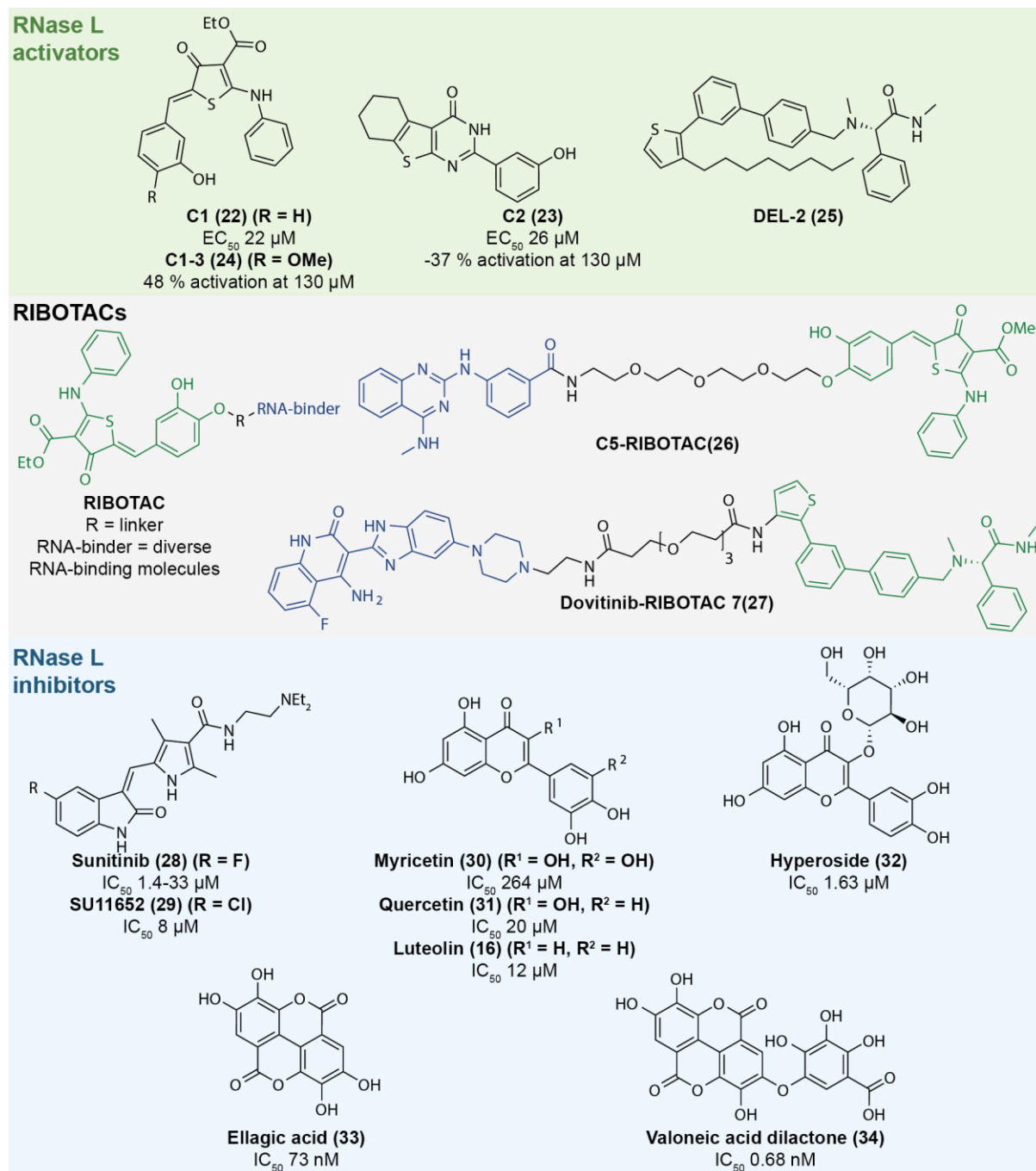


Figure 8: Reported RNase L activators, general structure and examples of Ribonuclease targeting chimeras (RIBOTACs) and RNase L inhibitors.^{157,168-174}

The concept was further advanced by Disney and colleagues using a dimeric small-molecule miRNA binder coupled to 2'-5'A to degrade *miR-96*, and the molecules were termed ribonuclease targeting chimeras (RIBOTACs).¹⁷⁶ Then, the RNase L recruiting moiety was exchanged to small-molecules C1-3 (**24**) or DEL-2 (**25**) and used to target RNAs such as *miR-*

21 (e.g. Dovitinib-RIBOTAC **7** (**27**)), reducing pre-miR-21 levels and metastasis formation in a tumor mouse model.^{168,169,177} Further targets of RIBOTACS were an oncogenic *miR-17*, *miR-18a*, and *miR-20a* cluster, mRNA of quiescin sulfhydryl oxidase 1 isoform a, a G4C2 RNA repeat associated with amyotrophic lateral sclerosis and frontotemporal dementia, and the SARS-CoV-2 attenuator hairpin (C5-RIBOTAC (**26**), Figure 8).^{168–170,178–180} Also RNA-binders that do not bind to functional binding sites of the nucleic acids were shown to be potential starting points for RIBOTACs degrading pre-miR-155, and MYC and JUN mRNA.¹⁸¹ Additional to RIBOTACS recruiting RNase L, bifunctional RNA-degrading molecules were also created using moieties that chemically cleave RNA, such as bleomycin and imidazole.^{169,182–184}

In addition to RNase L activators that are highly sought-after as drugs and tool compounds, inhibitors of RNase L could prove to be useful. The RNase L pathway is implicated in the genetic neurodevelopmental and inflammatory disease Aicardi-Goutières syndrome (AGS) through mutations of the *ADAR1* gene, leading to an increased presence of dsRNA and thus activation of RNase L.^{161,174} Most reported RNase L inhibitors known to date target the PK domain (Figure 8). The first reported PK-binding RNase L inhibitor was sunitinib (**28**), an FDA-approved tyrosine kinase inhibitor targeting vascular endothelial growth factor receptor (IC₅₀ 4 nM) and other kinases relevant in cancer.¹⁸⁵ When assayed against RNase L, IC₅₀ values ranged from 1.4 to 33 μM, and the antitumor effect of oncolytic viruses was enhanced by sunitinib (**28**).^{171,172,186} The kinase inhibitor was co-crystallized with RNase L proving binding to the PK domain and implicating dimer destabilization as the mode of action.¹⁸⁶ A four-fold increase in activity was observed with sunitinib (**28**) analog SU11652 (**29**), in which the fluorine residue was exchanged for chlorine.¹⁸⁶ Flavonoids such as myricetin (**30**), quercetin (**31**), and luteolin (**16**) (which also showed up in a screening for LIN28 inhibitors, see above) inhibit RNase L with IC₅₀ values of 264 μM, 20 μM, and 12 μM, respectively, and they were shown to bind to the PK domain.^{172,173} A myricetin (**30**) analog, hyperoside (**32**), showed an improved activity against RNase L (IC₅₀ 1.6 μM). However, no effect in intact cells was observed.¹⁷³ The stated IC₅₀ values for flavonoids were determined in the absence of competitively binding ATP or ADP although it was reported that nucleotide binding is necessary for RNase L activation in the first place.¹³⁴ Screening of 500 known kinase inhibitors showed that ellagic acid (**33**) and its derivative valoneic acid dilactone (**34**) inhibit RNase L in biochemical assays with nucleotide presence, with IC₅₀ values of 73 nM and 0.68 nM, respectively. Both molecules did not bind competitively to ATP, and their mode of action is not understood yet. When used at low micromolar concentrations, the phenolic small-molecule RNase L inhibitors reduced RNase L-mediated rRNA cleavage in cells.¹⁷⁴

In conclusion, there are few reported RNase L activators and inhibitors with moderate potency and limited characterization of their mode of inhibition. While RNase L activators are mainly

used and characterized as components of RIBOTACs that successfully induce the degradation of targeted RNAs, reported RNase L kinase inhibitors suffer from low selectivity or low cellular activity. Thus, the discovery of novel RNase L modulators is of high interest. Apart from targeting RNase L, the 2'-5'A-mediated decay pathway could also be addressed via modulation of OAS.

1.3.3 OAS in the RNase L-mediated innate immune response

OAS is the immediate upstream regulator of RNase L, and synthesizes 2'-5'A out of ATP upon dsRNA sensing. Three active OAS proteins exist in humans: OAS1, consisting of one polymerase beta-like nucleotidyl transferase domain (OAS domain); OAS2, harboring two consecutive domains of the same fold; and OAS3, consisting of three domains. Additionally, OASL is an inactive protein with one OAS domain and two ubiquitin-like domains (UBL).^{187,188} Furthermore, different isoforms of OAS1, OAS2 and OASL are generated by alternative splicing.¹⁸⁹ Although the active OAS2 and OAS3 consist of multiple OAS domains, only the C-terminal OAS domain of each protein is catalytically active (Figure 9A). The inactive domains contribute to RNA binding.¹⁸⁷ In OAS3, the three domains form a linear arrangement allowing for longer RNA sequences to bind when compared to OAS2 and OAS1.¹⁹⁰ Consequentially, OAS1 is activated by shorter dsRNAs of more than 17 base pairs in length, OAS2 senses dsRNA of medium length and OAS3 is activated by the longest RNA species of at least 50 base pairs.^{187,188} Each individual OAS domain is formed of an N-terminal and a C-terminal lobe that are connected by a flexible hinge region (Figure 9B).¹³⁰ Upon RNA binding, a conformational change is induced, reducing the angle between the two lobes and thus narrowing the catalytic site of OAS. As a consequence, crucial catalytic residues are brought into close proximity to the substrate.^{130,191} The catalytic center of OAS carries two magnesium ions that are coordinated by three catalytic triad aspartate residues. The bivalent ions allow coordination of the donor ATP substrates phosphate groups facilitating the nucleophilic attack of the acceptor molecules (ATP or 2'-5'A) 2' oxygen on the donor phosphate.^{130,191,192} Additionally to the influence of the length of RNA sequences, studies tried to evaluate the dependency of OAS activation on the RNA sequence. Crystal structures revealed that mostly the phosphate and the 2'-OH of the dsRNA backbone interact with a surface of OAS1, whose RNA-binding site makes it a non-canonical RBP. For OAS1, only one G nucleotide residue is specifically recognized via hydrogen bond formation with the protein.^{130,191} The activating consensus sequence for OAS1, WWN9WG (where W is A or U, and N is any nucleotide), was not supported by all studies, and the sequence specificity of OAS2 and 3 was not studied until now.^{193,194} The ability to form a 2'-5' linkage between nucleotides is very uncommon in human cells and only observed for OAS1 and the dsDNA sensing cytosolic immune sensor cyclic GMP-AMP synthase (cGAS) which is structurally similar to OAS.^{162,195}

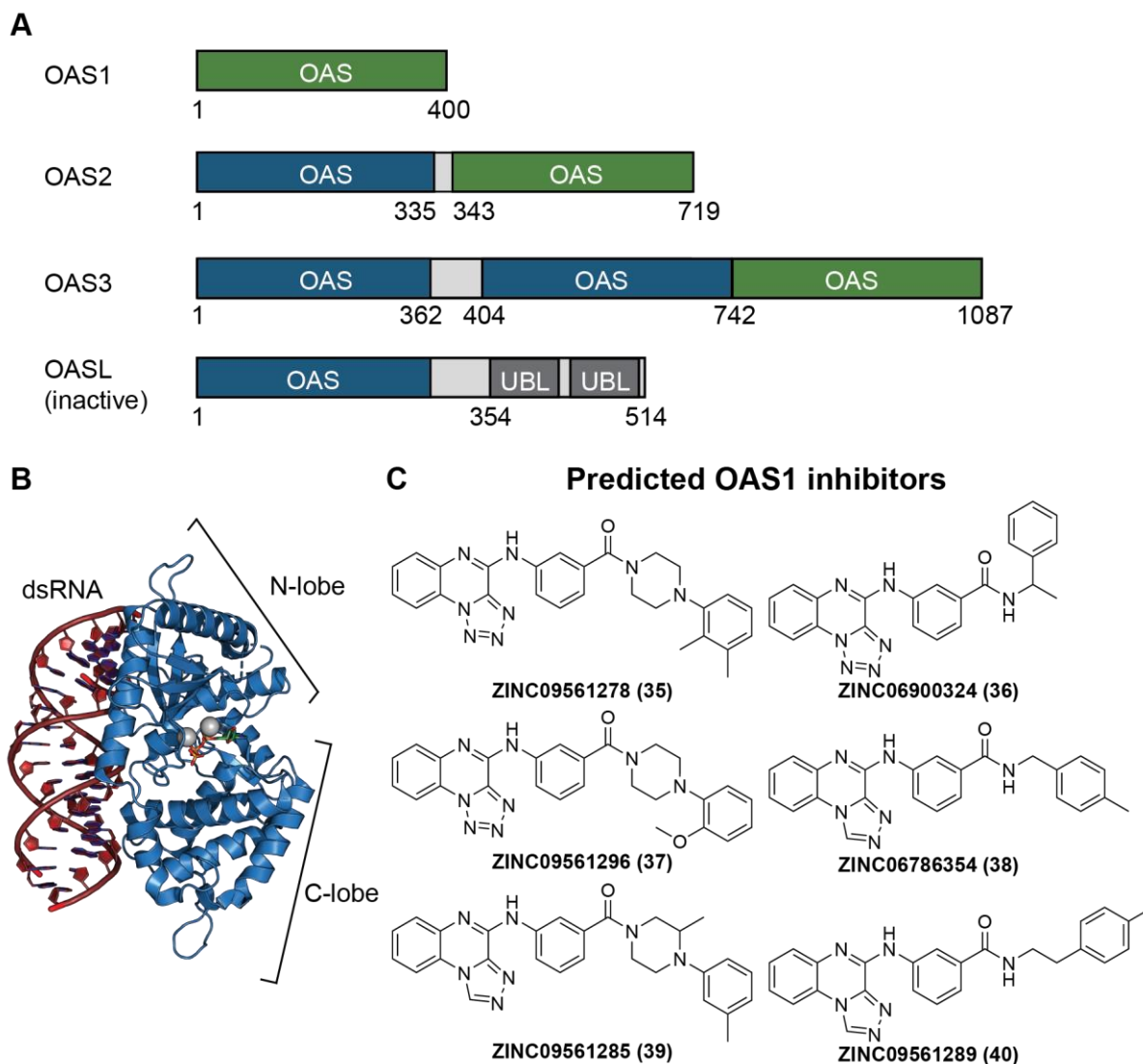


Figure 9: (A) Schematic structure of the three active OAS isoforms and of catalytically inactive OASL. Green indicates the active, C-terminal OAS domains, blue domains are able to bind RNA, but do not synthesize 2'-5'A. (B) Crystal structure of RNA-bound OAS1 (PDB 4IG8). The activating dsRNA is shown in red, the OAS protein as blue cartoon. A nucleotide (green) is bound in the catalytic site coordinated by two magnesium ions (grey) between the N-lobe and the C-lobe of OAS1.¹⁹¹ (C) *In silico* predicted OAS1 inhibiting molecules.¹⁹⁶

Similar to RNase L, modulation of OAS1 with small molecules could potentially be useful to study and treat autoimmune diseases, inflammatory diseases or cancer. For example, OAS mediates resistance mechanisms against oncolytic viruses used in cancer therapy and upregulation of OAS was found in autoimmune diseases.¹⁹⁷⁻¹⁹⁹ OAS1 inhibition was reported using divalent metal ions in biochemical assays.²⁰⁰ *In silico* prediction of OAS1 inhibiting molecules resulted compounds **35-40** that share a quinoxaline scaffold and were not experimentally validated (Figure 9C).¹⁹⁶ OAS activators in contrast could potentially boost antiviral immunity during infections. In fact, during SARS-CoV2 infection, a prenylated OAS1 isoform was found to protect patients against severe COVID-19 outcomes.^{201,202} An activator

Introduction

of OAS1 is rintatolimod (ampligen) which is a mismatched dsRNA (poly I: poly C12U) targeting toll-like receptor 3 but also OAS1.^{203,204} Rintatolimod is tested in clinical trials against CFS and post-COVID conditions (clinical trial identifier NCT05592418).²⁰⁴ Discovery of novel OAS1 activators will be of great interest given the positive effect of OAS1 activation against viral diseases and a potential involvement in CFS.

2 Aim of this thesis

RBPs are essential regulators of coding and non-coding RNAs and as such are prime targets for the modulation of all aspects of RNA biology by small molecules. Dysregulation of RBP-containing pathways often induces or promotes disease relevant phenotypes, such as cancer or autoimmune diseases. Consequently, discovery of RBP-targeting molecules could lead to therapeutics that treat a diverse set of diseases. Furthermore, RBP-targeting small-molecule probes would enable to study RNA biology and related pathways involving protein–RNA interactions in unprecedented level. The aim of this work is to discover small-molecule modulators of three such RBPs influencing different RNA species: the miRNA-binding protein LIN28, the ssRNA-cleaving protein RNase L and the dsRNA-binding protein OAS.

In the first part, the oncogenic protein LIN28 was addressed, which is a negative regulator of the miRNA *let-7* that represses the mRNAs of a broad variety of oncogenic proteins. LIN28 is overexpressed in approximately 15% of human cancers and plays a central role in cancer progression which is associated with poor prognosis. To date, several small-molecule LIN28 inhibitors were discovered using a variety of screening methods. However, the majority of the reported small molecules were not well characterized for their mode of action, their structure-activity relationship was not clear, and most molecules showed poor cellular activities. The potency of the most active LIN28 inhibitors reported in biochemical assays is in the low micromolar range. Improvement of the potency *in vitro* or *in cellulo* could advance the development of LIN28-targeting small molecules. Thus, this part of the work aimed to develop LIN28 inhibitors with improved potency based on a scaffold-based approach, and identify novel LIN28-inhibiting small molecules using a screening-based approach.

The second part focused on targeting crucial RBPs of the OAS–RNase L antiviral pathway that is an important part of the human innate antiviral immune response. OAS is activated by dsRNA upon virus infection, triggering OAS-mediated enzymatic synthesis of the unique second messenger 2'-5'A which in turn binds and activates RNase L. Activated RNase L dimers recognize and cleave host and viral RNA, leading to an antiviral state of the infected cell and eventually apoptosis. Small-molecule activators of RNase L and OAS could therefore serve as potential antiviral therapeutics. Moreover, RNase L activators were used as building blocks of bifunctional molecules recruiting RNase L to achieve targeted degradation of a wide range of RNAs of interest, enabled by the low RNA-sequence specificity of RNase L. So far, very limited examples of RNase L activators were reported with poor activity that is less than 10,000-fold than that of natural activator 2'-5'A and no small-molecule activator of OAS is known. Thus, this part of the work aims to identify novel RNase L and OAS activators via screening-based and scaffold-based approaches. Concomitantly, RNase L inhibitors could be

Aim of this thesis

studied as starting points for the development of therapeutics against autoimmune diseases. Consequently, an accompanying aim of this part is the evaluation of rationally designed RNase L inhibitors.

3 Material and methods

3.1 Material

3.1.1 Lists of used materials

3.1.1.1 Chemical reagents and compounds

In this thesis, compounds synthesized by Dr. Pascal Hommen (compounds **3**, **41**, **42**, **65-70**, **88-108**, **124-130**), Dr. Jimin Hwang (compounds **22**, **24**, **28**, **121**, **123**, **131**, **168-207**, **213-248**), Dr. Fubao Huang (compounds **120**, **122**, **132-135**), Georg Goebel (compounds **109-119**), Mao Jiang (compounds **208-212**), and their students were used. These molecules were produced at the Chemical Genomics Centre of the Max Planck Society in Dortmund. Compounds **43-64**, **71-75**, **136-167** and **249-252** were provided by the Compound Management and Screening Center (COMAS) Dortmund. Molecules **76-87** were provided by Dr. Gavin O'Mahony (Astra Zeneca).

Table 1: Commercial chemicals used in this work.

Chemical	Supplier
4-amino-3-hydroxynaphthalene-1-sulfonic acid	Thermo Fisher Scientific Inc.
Acetonitrile	Thermo Fisher Scientific Inc.
Acrylamide/Bis solution 30% (37.5:1)	AppliChem GmbH
Acrylamide/Bis solution 40% (19:1)	SERVA Electrophoresis GmbH
Ammonium molybdate tetrahydrate	Sigma-Aldrich Chemie GmbH
Ampicillin	Gerbu Biotechnik GmbH
APS	Sigma-Aldrich Chemie GmbH
ATP	Carl Roth GmbH + Co. KG
Biocytin	Sigma-Aldrich Chemie GmbH
Bis-Tris	Fisher Scientific GmbH
Bromophenol blue	AppliChem GmbH
BSA fraction V	Sigma-Aldrich Chemie GmbH
Chloroacetamide	Fisher Scientific GmbH
Color protein standard	New England Biolabs Inc.
cOmplete protease inhibitor EDTA free	Thermo Fisher Scientific Inc.
Coomassie Blue R-250	US Biological
DEPC	AppliChem GmbH
DMSO	Th. Geyer GmbH & Co. KG
DNase I	Roche Diagnostics Deutschland GmbH
Dpnl	New England Biolabs Inc.
DTT	Gerbu Biotechnik GmbH
EDTA	MP Biomedicals
EMPORE octadecyl C18 disks	Sigma-Aldrich Chemie GmbH
Ethanol	Thermo Fisher Scientific Inc.

Material and methods

Ethanolamine	Sigma-Aldrich Chemie GmbH
Ethidium bromide	Carl Roth GmbH + Co. KG
EZ-Link Sulfo NHS-LC-LC-Biotin	Thermo Fisher Scientific Inc.
Formic acid	VWR International GmbH
Gene ruler 1 kb DNA ladder	Thermo Fisher Scientific Inc.
GeneJuice transfection reagent	Sigma-Aldrich Chemie GmbH
Glycerol	Gerbu Biotechnik GmbH
Glycin	Carl Roth GmbH + Co. KG
Glyoxal	Sigma-Aldrich Chemie GmbH
H ₂ SO ₄	Carl Roth GmbH + Co. KG
HEPES	Gerbu Biotechnik GmbH
Hydrochloric acid	Carl Roth GmbH + Co. KG
Imidazole	Sigma-Aldrich Chemie GmbH
IPTG	Carl Roth GmbH + Co. KG
Isopropanol	Thermo Fisher Scientific Inc.
KCl	Thermo Fisher Scientific Inc.
L-Glutathione, reduced	Sigma-Aldrich
Lipofectamine 2000	Thermo Fisher Scientific Inc.
Lys-C	Promega Corporation
Lysozyme	Sigma-Aldrich Chemie GmbH
Methanol	Thermo Fisher Scientific Inc.
MgCl ₂	Sigma-Aldrich Chemie GmbH
Milk powder	Carl Roth GmbH + Co. KG
NaCl	VWR International GmbH
NaH ₂ PO ₄	Carl Roth GmbH + Co. KG
NP-40	Sigma-Aldrich Chemie GmbH
Phusion polymerase	New England Biolabs Inc.
PIPES	Sigma-Aldrich Chemie GmbH
PMSF	Sigma-Aldrich Chemie GmbH
Poly(I:C)	Bio-Techne
Propidium iodide	BioVision
Recombinant RNase Inhibitor	Takara Bio Europe
Roti®-GelStain	Carl Roth GmbH + Co. KG
SDS	Carl Roth GmbH + Co. KG
Sigma Fast Protease Inhibitor Cocktail	Sigma-Aldrich Chemie GmbH
Sodium metabisulfite	Thermo Fisher Scientific Inc.
Sodium sulfite	Thermo Fisher Scientific Inc.
SYBR green II	Thermo Fisher Scientific Inc.
T4 DNA polymerase	New England Biolabs Inc.
TCEP	Carl Roth GmbH + Co. KG

Material and methods

TEMED	Sigma-Aldrich Chemie GmbH
TFA	Thermo Fisher Scientific Inc.
Triethanolamine	Fisher Scientific GmbH
Tris	Carl Roth GmbH + Co. KG
Triton X-100	Arcos Organics
Trypsin	Sigma-Aldrich Chemie GmbH
Tween-20	SERVA Electrophoresis GmbH
UltraPure Agarose	Thermo Fisher Scientific Inc.
Urea	Alfa Aesar GmbH & Co KG,
ZnCl ₂	Sigma-Aldrich Chemie GmbH
β-mercaptoethanol	SERVA Electrophoresis GmbH

3.1.1.2 Buffers and solutions

Table 2: Common buffers used in this work.

Buffer name	Composition
5x Sample buffer	0.25 M Tris-HCl, pH 6.8, 0.5 M DTT, 50% (v/v) glycerol, 10% (w/v) SDS, 0.25% (w/v) bromophenol blue
BPTE (10x)	3% (w/v) PIPES free acid, 6% (w/v) Bis-Tris free base, 10 mM EDTA, pH 7
Coomassie staining solution	0.03% (w/v) Coomassie Blue R-250, 44% EtOH (v/v), 12% (v/v) AcOH
RIPA	150 mM NaCl, 1% (v/v) NP-40, 0.5% (w/v) sodium deoxycholate, 0.1% (w/v) SDS, DNase I, cOmplete protease inhibitor EDTA free
Separating buffer	1.5 M Tris-HCl, pH 8.8, 0.4% SDS
Stacking buffer	0.5 M Tris-HCl, pH 6.8, 0.4% SDS
TAE (1x)	40 mM Tris, 20 mM acetic acid, 1 mM EDTA, pH8
TBE (1x)	89 mM Tris, 89 mM boric acid, 2 mM EDTA, pH 8
TBS-T	20 mM Tris (pH 7.6), 150 mM NaCl, 0.05% Tween-20

3.1.1.3 Cell lines

Table 3: Cell lines used in this work.

Name	Description	Culture conditions	Supplier
HEK293T	Human epithelial kidney	DMEM, 10% FBS, antibiotic-antimycotic solution, 5% CO ₂ , 37 °C	ATCC, CRL-3216
HeLa	Human cervix carcinoma	DMEM, 10% FBS, antibiotic-antimycotic solution, 5% CO ₂ , 37 °C	DSMZ, German Collection of Microorganisms and Cell Cultures, DSMZ no. ACC 57
High five	Insect cells	Sf-900 III SFM	PCF Dortmund
JAR	Human choriocarcinoma	RPMI-1640, 15% FBS, antibiotic-antimycotic solution; 5% CO ₂ , 37 °C	DSMZ, German Collection of Microorganisms and Cell Cultures, DSMZ no. ACC 462
K-562	Human chronic myelogenous leukemia	RPMI-1640, 10% FBS, 5% CO ₂ , 37 °C	CLS
Sf9	Insect cells	Sf-900 III SFM	PCF Dortmund

Material and methods

3.1.1.4 Bacterial strains

Table 4: Bacterial strains used in this work.

Name	Genotype
<i>Escherichia coli</i> BL21(DE3)	F ⁻ <i>ompT hsdS_B</i> (<i>r_B</i> ⁻ , <i>m_B</i> ⁻) <i>gal dcm</i> (DE3)
<i>Escherichia coli</i> DH10EmBacY	F ⁻ <i>mcrA</i> Δ(<i>mrr-hsdRMS-mcrBC</i>) Φ80 <i>lacZ</i> ΔM15 Δ <i>lacX74 recA1 endA1 araD139</i> Δ(<i>ara, leu</i>)7697 <i>galU galK λ rpsL nupG</i> /bMON14272yfp+/pMON7124
<i>Escherichia coli</i> Top10F'	F' ⁺ { <i>lacI</i> ^q Tn10(Tet ^R)} <i>mcrA</i> Δ(<i>mrr-hsdRMS-mcrBC</i>) φ80 <i>lacZ</i> ΔM15 Δ <i>lacX74 recA1 araD139</i> Δ(<i>ara-leu</i>) 7697 <i>galU galK rpsL endA1 nupG</i>

3.1.1.5 Media

Table 5: Ingredients non-commercial media used in this work.

Name	Ingredients
LB-medium	1% (w/v) tryptone, 0.5% (w/v) yeast extract, 1% (w/v) NaCl, pH 7.4
SOC-medium	2% (w/v) tryptone, 0.5% (w/v) yeast extract, 0.058% (w/v) NaCl, 0.019% (w/v) KCl, 0.203% (w/v) MgCl ₂ × 6 H ₂ O, 0.246% (w/v) MgSO ₄ × 7 H ₂ O, 4% (w/v) 50% (w/w) glucose
LB-agar plates	1% (w/v) tryptone, 0.5% (w/v) yeast extract, 1% (w/v) NaCl, 1.5% (w/v) bacto agar, pH 7.4

3.1.1.6 Antibodies

Table 6: Antibodies, suppliers and corresponding dilutions as used within this work.

Antigen	Origin	Supplier	Dilution	Product number
c-Myc	Rabbit	Cell signaling technology	1:1000	#5605
GAPDH	Mouse	Thermo fisher / invitrogen	3 µg/mL	AM4300
Histone H3	Rabbit	activemotif	0.1-1 µg/mL	AB_2793771
Histone H3K27me3	Rabbit	activemotif	0.5-2 µg/mL	AB_2561020
Histone H3K9me3	Rabbit	activemotif	1:1000-1:5000	AB_2532132
LIN28A	Rabbit	Abgent	1:100	AP11549a
Mouse-HRP	Sheep	Cytiva	1:5000	NXA931-1ML
Rabbit HRP	Goat	Bioss Antibodies	1:1000	bs-0295G-HRP
Ras	Rabbit	Cell signaling technology	1:1000	#3965
RNase L	Rabbit	abcam	1:10000	EPR15894/ab191392

3.1.1.7 RNAs

Table 7: Sequences of RNAs used in this work.

Name	Experiment	Sequence (5' to 3')	Supplier
RNA-1	LIN28 FP	GGGGUAGUGAUUUUACCCUGUUUAGGAGAU-FAM	IDT
RNA-2	LIN28 EMSA	GGGGUAGUGAUUUUACCCUGUUUAGGAGAU-Cy3	IDT
RNA-3	MST	Cy5-UUAGGGUCACACCCACCACUGGGAGAUAA	
RNA-4	RNase L FRET	FAM-UUAUCAAAUUCUUUUUUGCCCCAUUUUUUUUGGU- Black Hole Quencher-1	IDT
RNA-5	optimized RNase L FRET	Alexa Fluor 647-CCA UUU UUU UGG-Iowa Black Quencher RQ	IDT
RNA-6	RNase L cleavage assay	Cy3-CCCACCCACCUUCCACCCACCCACCC CACCC	IDT
RNA-7	OAS1 FP and EMSA	GGCUUUUGACCUUUAUGC	IDT
RNA-8	OAS1 FP and EMSA	GCAUAAAAGGUCAAAAGCC-FAM	IDT

3.1.1.8 Plasmids

Table 8: List of plasmids used in this work. All plasmid maps are shown in section 8.1.

Name	Backbone	Insert
pET19a-His-TEV-LIN28A(16-187)	pET19a	LIN28A(16-187)
pET19a-His-TEV-LIN28A(16-126)	pET19a	LIN28A(16-126)
pET19a_His-TEV-LIN28(16-126E89A)	pET19a	LIN28A(16-126)E89A
pMAL_His-MBP-LIN28B(24-111)	pMAL	LIN28B(24-111)
pET19a_His-TEV-XtrLIN28B(27-114)	pET19a	<i>X. tropicalis</i> Lin28B(27-114)
pET19a-His-TEV-RNaseL	pET19a	RNase L
pFastBacHTb-his6-RNaseL	pFastBacHTb	RNase L
pFastBacHTb-His6-SUMO-TEV-OAS1	pFastBacHTb	OAS1

3.1.1.9 Commercial kits

Table 9: Commercially available kits used in this work.

Name	Supplier
E.Z.N.A.® Cycle Pure Kit	Omega Bio-tek Inc.
E.Z.N.A.® Gel Extraction Kit	Omega Bio-tek Inc.
Kinase-Glo Max Luminescent Kinase Assay	Promega Corporation
MycoAlert Mycoplasma detection kit	Lonza Group AG
Pierce BCA Protein Assay Kit	Thermo Fisher Scientific Inc.
Pierce Coomassie Protein Assay Kit	Thermo Fisher Scientific Inc.
Q5 Site-Directed Mutagenesis Kit	New England Biolabs
QIAprep Spin Miniprep Kit	Qiagen N.V.
RNase-Free Dnase Set	Qiagen N.V.
RNeasy Mini Kit	Qiagen N.V.
TaqMan microRNA assays, Assay IDs: 001093, 000377, 002282	Applied Biosystems, Thermo FisherScientific Inc.
TaqMan microRNA Reverse Transcription Kit	Applied Biosystems, Thermo FisherScientific Inc.

3.1.1.10 Laboratory devices

Table 10: Laboratory devices used in this work.

Instrument name	Description	Supplier
Avanti J-26XP	Centrifuge	Beckmann Coulter GmbH
Centrifuge 5424	Centrifuge	Eppendorf SE
Centrifuge 5427R	Centrifuge	Eppendorf SE
Centrifuge 5804R	Centrifuge	Eppendorf SE
CFX Connect Real-Time PCR System	qPCR cycler	Bio-Rad Laboratories Inc.
ChemiDoc MP	Gel imager	Bio-Rad Laboratories Inc.
EnVision	Plate reader	PerkinElmer Inc.
Fisherbrand Sonic Dismembrator FB-705	Sonicator	Thermo Fisher Scientific Inc.
Galaxy 170S	CO ₂ Incubator	Eppendorf SE
Incucyte ZOOM	Life cell analysis system	Sartorius AG
Innova 42	Incubation shaker	New Brunswick Scientific
Innova 4430	Incubation shaker	New Brunswick Scientific
Invitrogen Countess	Automated cell counter	Thermo Fisher Scientific Inc.
Monolith Nt.115	MST	NanoTemper Technologies GmbH
NanoDrop 2000 c	Spectrophotometer	Thermo Fisher Scientific Inc.
NanoTemper Prometheus NT.48	NanoDSF	NanoTemper Technologies GmbH
Octet Red384	BLI	Sartorius AG
Optima MAX-TL	Ultracentrifuge	Beckmann Coulter GmbH
Paradigm	Plate reader	Molecular Devices, LLC.
Personal Cycler	PCR Cycler	Biometra GmbH
PowerPac HC	Power supply	Bio-Rad Laboratories Inc.
Prometheus NT.48	Nano differential scanning fluorimetry device	NanoTemper Technologies GmbH
Refeyn TwoMP	Mass Photometer	Refeyn
Scanlaf Mars 1200	Laminar flow cabinet	LaboGene A/S
Tecan Spark	Plate reader	Tecan Group AG
Thermomixer comfort	Thermoblock	Eppendorf SE

3.1.1.11 Consumables

Table 11: Consumables used in this work.

Item	Supplier
1.5 mL Tubes	Eppendorf SE
2 mL Tubes	Eppendorf SE
96 well plates (353075)	Corning BV
Äkta Prime	GE Healthcare
Amersham ECL Western Blotting Detection Reagent	Cytiva

Material and methods

Amicon Ultra-15, MWCO 3 kDa	Merck KGaA
Amicon Ultra-15, MWCO 30 kDa	Merck KGaA
Antibiotic-antimycotic solution (100x)	Sigma-Aldrich Chemie GmbH
Cell scraper 16 cm	SARSTEDT AG & Co. KG
Corning 3824 384 well plate	Corning BV
Corning 4514 384 well plate	Corning BV
Countess Cell Counting Chamber Slides	Thermo Fisher Scientific Inc.
DMEM, high glucose	Thermo Fisher Scientific Inc.
DPBS 1X w/o calcium and magnesium	Corning BV
DynaMag-2 Magnet	Thermo Fisher Scientific Inc.
ECL Substrate Kit (Ultra High Sensitivity)	Abcam Netherlands B.V.
Eppendorf Research plus pipettes (1000 µL, 200 µL, 100 µL, 20 µL, 10 µL, 2 µL variable volume)	Eppendorf SE
FBS	Life Technologies GmbH
Filter membranes, nitrocellulose 0.22 µm	Merck KGaA
Filtropur S 0.22 µm	SARSTEDT AG & Co. KG
Filtropur S 0.45 µm	SARSTEDT AG & Co. KG
GeneRuler 1 kb DNA ladder	Thermo Fisher Scientific Inc.
High Load Superdex 75 pg 16/600	GE Healthcare
High Load Superdex 75 pg 16/600	GE Healthcare
HisTrap Column	GE Healthcare
HiTrap Heparin HP Column	Cytiva
Mini Trans-Blot Cell	Bio-Rad Laboratories Inc.
Mini-PROTEAN Tetra Cell	Bio-Rad Laboratories Inc.
Mini-PROTEAN Tetra Vertical Electrophoresis Cell	Bio-Rad Laboratories Inc.
Monolith NT.115 Standard Treated Capillaries	NanoTemper Technologies GmbH
NHS activated magnetic Sepharose	Fisher Scientific GmbH
NHS Mag Sepharose	Fisher Scientific GmbH
Nitrocellulose Membrane, 0.45 µm, 30 cm x 3.5 m	Thermo Fisher Scientific Inc.
Octet SA Biosensors	Sartorius AG
Opti-MEM Reduced Serum Medium	Thermo Fisher Scientific Inc.
PBS	Thermo Fisher Scientific Inc.
Phusion® High-Fidelity DNA Polymerase	New England Biolabs Inc.
Ponceau S staining solution	Thermo Fisher Scientific Inc.
PowerPac HC	Bio-Rad Laboratories Inc.
Powerpette Plus	VWR International GmbH
Prometheus Standard Capillaries	NanoTemper Technologies GmbH
Protein LoBind Tubes	Eppendorf SE
RNase away	VWR International GmbH
RNase free water	MACHEREY-NAGEL GmbH & Co. KG,
RPML-1640	Sigma-Aldrich Chemie GmbH
SafeSeal Tips Professional 10 µl	Biozym Scientific GmbH
SafeSeal Tips Professional 1250 µL	Biozym Scientific GmbH
SafeSeal Tips Professional 200 µl	Biozym Scientific GmbH
Serological pipettes 1 mL	SARSTEDT AG & Co. KG
Serological pipettes 10 mL	SARSTEDT AG & Co. KG
Serological pipettes 25 mL	SARSTEDT AG & Co. KG
Serological pipettes 5 mL	SARSTEDT AG & Co. KG
Serological pipettes 50 mL	SARSTEDT AG & Co. KG

Material and methods

Sf-900 III SFM	Thermo Fisher Scientific Inc.
Slide-A-Lyzer 3.5K	Thermo Fisher Scientific Inc.
Spectra/Por Dialysis Tubing 3.5 kD	Thermo Fisher Scientific Inc.
Streptavidin (SA) Biosensors	Sartorius AG
Sub-Cell GT Cell	Bio-Rad Laboratories Inc.
TaqMan Universal Master Mix II with UNG	Applied Biosystems, Thermo FisherScientific Inc.
Tissue Culture Dish, 100 mm, Standard surface	SARSTEDT AG & Co. KG
Trypsin-EDTA solution	Sigma-Aldrich Chemie GmbH

3.1.1.12 Software

Table 12: Software used in this work.

Name	Description	Supplier
Adobe Illustrator 2023	Vector graphics	Adobe
Bio-Rad CFX Manager 3.1	qPCR analysis	Bio-Rad Laboratories Inc.
Chem3D 20.1	Ligand energy minimization	PerkinElmer Inc.
ChemDraw	Chemical analysis and visualization	PerkinElmer Inc.
Excel	Data analysis and visualization	Microsoft Corporation
Graph Pad Prism 9	Data analysis and visualization	GraphPad Software
Image Lab	Image analysis	Bio-Rad Laboratories Inc.
IncuCyte® ZOOM 2018A	Image analysis	Sartorius
Origin 2019b	Data analysis and visualization	OriginLab Corporation
PyMOL	Protein structure analysis and visualization	Schrödinger LLC.
Quattro Workflow	Compound screening analysis	Quattro Research GmbH
Schrödinger Maestro 12.3	Docking	Schrödinger LLC.

3.2 Methods

3.2.1 General procedures

3.2.1.1 Cloning of plasmids

In general, proteins and protein domains of interest were subcloned to vectors of choice using sequence and ligation-independent cloning (SLIC)²⁰⁵. Plasmids were either digested with restriction enzymes or linearized by PCR using Phusion polymerase, followed by analysis on a 1% agarose gel and gel purification using an E.Z.N.A. gel extraction kit. Inserts were amplified by polymerase chain reaction (PCR) using Phusion polymerase and appropriate primers (purchased from Sigma-Aldrich) as described by the manufacturer of the polymerase, followed by purification using a cycle pure kit. The concentration of linearized plasmid and insert was determined using a nanodrop. A total of 100 ng plasmid were mixed with two times molar excess of insert and 1 μ L of NEB2.1 buffer in a total volume of 10 μ L on ice. Then, 0.4 μ L T4 DNA polymerase was added and the reaction was incubated at room temperature

for four minutes, followed by incubation on ice for ten minutes. Half of the volume was transformed into chemically competent *E. coli* Top10F' cells. Single colonies were transferred into 5 mL LB medium containing antibiotics to which the used plasmids contained resistance genes and incubated for 16 h at 37 °C and 180 rpm. Plasmids were isolated using QIAprep Spin Miniprep Kit and sequenced by sanger sequencing to verify insertion of the desired insert. The sequencing service was provided by Microsynth Seqlab GmbH.

3.2.1.2 Transformation of plasmids

Plasmids were transformed into chemically competent *E. coli* cells using heat shock. Competent cells (50 µL) were incubated with plasmid (1-5 µL) on ice for 20 minutes. Then, the suspension was heated to 42 °C for 60 s and cooled down on ice for five minutes. After addition of 200 µL SOC medium, the cells were incubated at 37 °C and 300 rpm shaking for one hour and plated on LB agar plates containing an appropriate antibiotic under sterile conditions.

3.2.1.3 Site-directed mutagenesis

Site-directed mutagenesis was used to add mutations, insertions, or deletions to plasmids. The Q5 Site-Directed Mutagenesis Kit (New England Biolabs) was used according to the manufacturers protocol. Plasmid sequence was confirmed by sanger sequencing using the service of Microsynth Seqlab GmbH.

3.2.1.4 RNA assays

All experiments containing RNA were performed under RNA-, RNase-, and DNase-free conditions. Pipettes and tables were cleaned using RNase away. Buffers were prepared using RNase-free ultrapure water that was treated with 0.1% (v/v) DEPC for 12 h at 37 °C prior to autoclaving at least two times. RNA stock solutions were diluted in commercially available RNase-free water, and certified RNase-, RNA- and DNA-free pipette tips and reaction tubes were used.

3.2.1.5 SDS-PAGE

Sodium dodecyl sulfate-polyacrylamide gel electrophoresis (SDS-PAGE) was used to analyze protein identity and purity during protein purifications and as part of western blot procedures. Gels were hand-casted with a final acrylamide concentration of 15% or 18%. The latter concentration was used to analyze proteins with a molecular weight of less than 12 kDa. Gels consisted of a separating gel and a stacking gel containing 4% acrylamide. The following recipe was used for gel preparation (Table 13):

Table 13: Recipe for SDS-PAGE, volumes for casting six gels.

Ingredient	Stacking gel (4%)	Separating gel (15%)	Separating gel (18%)
Acrylamide/bis (30%)	2.25 mL	15 mL	18 mL
Ultrapure H ₂ O	8.85 mL	7.25 mL	4.25 mL
Separating / Stacking buffer	3.75 mL	7.5 mL	7.5 mL
APS (10% w/v)	150 µL	250 µL	250 µL
TEMED	15 µL	25 µL	25 µL

Samples were diluted in 5x sample buffer and applied to the gel. Gels were run at 50 V for 10 minutes, followed by 180 V until the bromophenol blue reached the end of the gel. Then, gels were stained using a staining solution and destained in 10% (v/v) acetic acid. Gel documentation was done using the ChemiDoc MP.

3.2.1.6 Western blot

Western blot was performed using wet transfer. Proteins separated by SDS-PAGE were transferred to a 0.45 µM nitrocellulose membrane in buffer containing 20% (w/v) methanol, 25 mM Tris-HCl (pH 8.3), and 192 mM glycine. If proteins larger than 80 kDa were probed, 0.1% SDS was added to the buffer. Proteins were transferred at 4 °C for either 16 h at 30 V or 2 h at 70 V. The membrane was washed twice with TBS-T for five minutes, followed by staining with Ponceau S for 10 minutes. After imaging using the ChemiDoc MP system, the membrane was washed with TBS-T for five minutes and blocked with 5% (w/v) milk powder in TBS-T for 1 h. Then, the membrane was cut, and each part was probed with indicated primary antibody at 4 °C overnight. Antibodies were diluted in 5% BSA in TBS-T. After three subsequent washes with TBS-T for five minutes, each membrane was treated with the recommended dilution of secondary antibody for one hour at room temperature, followed again by three washes with TBS-T for five minutes. The chemiluminescent signal was developed by incubation with ECL western blotting detection reagent or ECL substrate kit (ultra-high sensitivity) according to the manufacturers' descriptions. Chemiluminescent and colorimetric images were recorded using ChemiDoc MP.

3.2.1.7 Insect cell culture

Insect cell lines HighFive and Sf9, kindly provided by the protein chemistry facility (MPI Dortmund), were cultured in Sf-900 III SFM and handled under aseptic conditions using a laminar flow cabinet and sterile material. Cells were grown at 27 °C and 110 rpm. Insect cells were subcultured regularly by counting the cells with an automated cell counter and determining their viability by staining with 0.4% trypan blue solution in a 1:1 dilution. High five cells were split to a density of 0.2×10⁶ cells/mL every three days or 0.15×10⁶ cells/mL every

four days. Sf9 cells were diluted to 0.8×10^6 cells/mL every two days or 0.5×10^6 cells/mL every three days.

3.2.1.8 Cell culture methods

All mammalian cells were handled under sterile conditions using a laminar-flow cabinet. Cells were cultured in a humidified atmosphere at 37 °C and 5% CO₂. Subculturing of cells was initiated before the cells reached confluency by removing the old medium, washing the adherent cells with PBS, and treatment with Trypsin/EDTA for 3 minutes. Then, cells were detached and suspended by adding growth medium and diluted into a new cell culture vessel containing fresh medium. In 10 cm dishes, 10 mL of medium was used. For the seeding of cells, cells were counted using a Countess Automated Cell counter and diluted to the desired cell density. Cells were analyzed on a regular basis for mycoplasma contamination using the MycoAlert Mycoplasma detection kit according to the manufacturers protocol.

3.2.2 Methods for the identification and evaluation of LIN28 inhibitors

3.2.2.1 Expression and purification of LIN28 protein

Constructs of hexahistidine (His₆)-tagged LIN28A or LIN28B were cloned as described above and transformed into *E. coli* BL21(DE3). Cells were incubated in LB-medium at 37 °C and 180 rpm until the optical density at 600 nm (OD₆₀₀) reached a value between 0.5 and 0.8. The suspension was cooled to 18 °C and induced with 300 μM IPTG before further incubation at 18 °C and 180 rpm for 18 h. After harvesting by centrifugation, the bacterial pellet was resuspended in lysis buffer containing 50 mM NaH₂PO₄, pH 8, 300 mM NaCl, and 0.1 mM PMSF and lysed using sonication (amplitude 55%, 5 s on, 5 s off, 5 min total). Centrifugation was used to clear the lysate at 60,000 xg for 1 h. The supernatant was applied onto a HisTrap column, and the column was washed with buffer containing 50 mM NaH₂PO₄, pH 8, 300 mM NaCl, and 5% glycerol. After a wash with 25 mM imidazole, the protein was eluted using an imidazole gradient with up to 0.5 M imidazole over a length of 200 mL. The affinity-tag was cleaved using His₆-TEV protease overnight while dialyzing against a buffer containing 50 mM NaH₂PO₄, pH 8, 300 mM NaCl, and 5% glycerol. Another round of immobilized nickel affinity chromatography was performed to remove the protease and unspecific binders by collecting the protein of interest in the flow-through. Crystallization constructs were further purified using a Heparin column after dialysis against 20 mM Bis-tris (pH 6.5) with 1 mM DTT. Elution of the protein from the Heparin column was done with a gradient of up to 1 M NaCl in 20 mM Bis-tris (pH 6.5). All protein constructs were concentrated and further purified by gel filtration using a High Load Superdex 75 pg 16/600 column equilibrated with buffer (30 mM NaH₂PO₄, pH 7.5, 50 mM NaCl, 5% glycerol, 2 mM β-ME). The purified protein was concentrated and stored at -80 °C until further use. Protein concentration was determined using NanoDrop.

3.2.2.2 Fluorescence polarization assay

The assay was adapted from Wang *et al.*¹¹⁸ Low-volume black polystyrene 384 well plates (Corning 4514) were used to perform IC₅₀ measurements in triplicates. Purified LIN28A(16-187) was used at a final concentration of 200 nM and was incubated with varied concentrations of compounds or unlabeled RNA-1 for 30 min in FP assay buffer (20 mM Tris, pH 7, 100 mM NaCl, 5 mM MgCl₂, 2 mM glutathione (reduced), 0.1% NP-40). FAM-labeled FP-probe (RNA-1) using the sequence of *mus musculus* preE-*let-7f-1* was added with a final concentration of 2 nM. Incubation was performed at room temperature, and detection was done using a TECAN Spark plate reader using a monochromator. Data were analyzed and visualized with GraphPad Prism.

3.2.2.3 Small-molecule screening

LIN28 inhibitor screening was conducted by the Compound Management and Screening Center of the Max Planck Institute of Molecular Physiology. Compounds were used at 30 μM in FP assay buffer, and 40 μM LIN28A(16-187) and 2 nM RNA-1 were used. Pipetting of compounds was done automatically with an ECHO 520 liquid handler, and protein and RNA were subsequently dispensed using a multidrop dispenser with a 30-minute incubation in between both additions. After 15 minutes, fluorescence polarization was detected on an EnVision plate reader, and total fluorescence was measured on a Paradigm plate reader. Every plate contained a reaction without compound as positive control and a reaction without protein as a negative control. Data were analyzed using the software Quattro Workflow.

3.2.2.4 Electrophoretic mobility shift assay

The EMSA was adapted from Lim *et al.*¹¹⁶ LIN28A(16-187), 5 U recombinant RNase inhibitor, and compound were incubated in EMSA reaction buffer containing 50 mM Tris (pH 7.5), 100 mM NaCl, 10 mM β-ME, 50 μM ZnCl₂, 2% DMSO, 0.01% Tween-20 and 12% glycerol for two hours. Then, RNA-2 (Cy-3 labeled *m. musculus* preE-*let-7f-1*) was added with a final concentration of 5 nM and a final LIN28A concentration of 10 nM in 50 μL total reaction volume. After 15 min, 10 μL of each reaction was analyzed on a non-denaturing PAGE. Gels contained 1× TAE, 5.2% acrylamide/bis (or 10% if only the LIN28 CSD was used), and ultrapure water, and polymerization was initiated by the addition of APS and TEMED. Gels were pre-run at 220 V for 1 h at 4 °C before loading and for one hour at 4 °C and 220 V after loading using 0.25× TAE as a running buffer. The fluorescence signal was detected using a ChemiDoc with an exposure time of 120 s. Band intensities F were determined using ImageLab or ImageJ, and inhibition rates I were calculated by the following equations normalizing to only RNA and only complex controls:

Material and methods

$$F_{\text{rel}}(x) = \frac{F_{\text{RNA}}(x)}{F_{\text{complex}}(x)} \quad (1)$$

$$I(x) = \frac{F_{\text{rel}}(x) - F_{\text{rel}}(\text{complex})}{F_{\text{rel}}(\text{RNA}) - F_{\text{rel}}(\text{complex})} \cdot 100\% \quad (2)$$

3.2.2.5 Thermal shift assay

A thermal shift assay was performed by nano-differential scanning fluorimetry (nanoDSF) at a NanoTemper Prometheus, applying a temperature gradient from 20 °C to 90 °C with an increase rate of 1 °C per minute. The excitation power was set to 50-60%. During each experiment, 30 µM protein was diluted in 30 mM NaH₂PO₄, 50 mM NaCl, 1 mM MgCl₂, and 50 µM ZnCl₂ at pH 8, and the compound was added to final concentrations between 100 µM and 0.78 µM. The temperature gradient was started after 45 minutes of incubation time at room temperature, and measurements were taken using standard capillaries. Intrinsic tryptophan fluorescence was recorded, and the ratio of fluorescence at 350 nm to that at 330 nm was determined. Calculations of the first derivative and the inflection point of the melting curve were performed using the software of the device.

3.2.2.6 qPCR

Human choriocarcinoma cells JAR²⁰⁶ were seeded in either 24- or 6-well plates and treated with compound at a final DMSO concentration of 0.5% for 24 h. Treatments were performed in three biological replicates. Cells were lysed, and RNA was extracted using the RNeasy Mini kit. The RNA concentration was determined by NanoDrop, and a total amount of 20 ng RNA was used for reverse transcription, followed by qPCR. The TaqMan microRNA Reverse Transcription Kit and TaqMan Universal Master Mix II with UNG were used according to the manufacturers protocols. The qPCR was performed and monitored in a CFX Connect Real-Time PCR System. TaqMan microRNA assays from Applied Biosystems were used (Assay IDs: 001093, 001973, 000377, 002282, 002221, 002283) monitoring mature *let-7* levels, while U6 snRNA served as a control and samples treated with DMSO were used for normalization using the 2^{-ΔΔCT} method.²⁰⁷

3.2.2.7 Cellular thermal shift assay

A cellular thermal shift assay (CETSA) was performed generally following the method as described by Reckzeh *et al.*²⁰⁸ JAR cells were grown in four 100 mm dishes to approximately 90% confluency and detached with 1.5 mL trypsin per dish. After incubation for 2 min on ice, cells were washed with ice-cold PBS three times by centrifugation at 350 ×g for 2 minutes, followed by resuspension in 25 mL buffer. After the last wash and centrifugation, cells were resuspended in ice-cold lysis buffer (0.4% (v/v) NP-40 in PBS) and lysed by a freeze-thaw procedure. Cells were frozen in liquid nitrogen and thawed on ice subsequently four times.

Lysates were centrifuged for 60 min at 20000 \times g and 4 °C. The supernatant was kept, and the protein concentration was determined by BCA assay according to the manufacturers protocol. The lysate was diluted to 2.5 mg/mL total protein concentration, split into two portions of 1.4 mL, and one portion was treated with 100 μ M compound in DMSO while the other was treated with an equal amount of DMSO. After incubation for 15 minutes at room temperature, each sample was split into 120 μ L portions which were incubated at different temperatures individually in a thermocycler with a temperature gradient for three minutes. Denatured proteins were removed by ultracentrifugation at 100000 \times g and 4 °C for 20 minutes, and supernatants were analysed by western blot using LIN28 antibody as described in 3.2.1.6.

3.2.2.8 Microscale thermophoresis

Compound **41** was titrated in PBS supplemented with 0.05% Tween-20 and 5% DMSO producing 16 different concentrations. Then, Cy5-labeled preE-*let-7a-1* (RNA-3) was diluted in PBS buffer containing 0.05% Tween-20 to a concentration of 40 nM. Equal volumes of both solutions were mixed and loaded into Monolith NT.115 Standard Treated Capillaries. Microscale thermophoresis (MST) measurements were performed using a Monolith Nt.115 and analyzed using the software of the device.

3.2.2.9 Thermal shift assay of *let-7*

PreE-*let-7f-1* (unlabeled RNA-1) was annealed at a concentration of 2 μ M in buffer containing 10 mM Tris, pH 7.5, 50 mM NaCl and 1 mM EDTA. Annealing was achieved by heating to 95 °C for 3 min followed by cooling down to 20 °C over the course of 2 hours. Then, the RNA (final concentration 1 μ M) was mixed with 6x SYBR green II and 60 μ M **41** in PBS. The RNA was gradually heated to 90 °C with a rate of 1 °C per minute in a CFX Connect Real-Time PCR System while reading out the fluorescent signal. The data was analyzed using the software of the device.

3.2.2.10 Biolayer interferometry

Biolayer interferometry (BLI) was employed for direct binding assays. The cold shock domain of LIN28 (LIN28 16-126) was biotinylated using EZ-Link Sulfo NHS-LC-LC-Biotin for two hours on ice according to the manufacturers protocol to achieve labeling of one biotin per protein molecule. Excess biotin reagent was removed by dialysis against buffer (20 mM HEPES pH 7.5, 150 mM NaCl, 1 mM MgCl₂), and the protein concentration was determined using NanoDrop. Then, the protein was immobilized on streptavidin (SA) biosensors that were pre-equilibrated in buffer (20 mM HEPES pH 7.5, 150 mM NaCl, 1 mM MgCl₂, 0.05% Tween 20, 1% DMSO and 0.3 mg/mL BSA). Compound association was measured in concentrations ranging from 100 μ M to 0 μ M after a baseline recording. Dissociation was recorded in buffer. Measurements were performed on an Octet Red384 instrument using 384 well plates with a

total sample volume of 50 μ L. Data analysis was performed using the software of the device with double referencing to sensors loaded with 10 μ g/mL biocytin instead of protein and sensors immersed in buffer instead of compound. The DMSO concentration was constant in all wells.

3.2.2.11 DNA EMSA

LIN28 binding to double-stranded RNA was assayed by EMSA, adapted from Zeng *et al.*³⁹ DNA strands were annealed in a 1:1 mixture by heating to 95 °C followed by slowly cooling to 25 °C over at least 45 min and further cooling to 4 °C leading to 50 μ M annealed DNA. The annealing buffer was made of 10 mM Tris (pH 7.5), 50 mM NaCl and 1 mM EDTA. The fluorophore-labeled antisense strand with the sequence Cy3-CTGGGTTTCAGCACCATTTTTTGCGCCAGAAG was annealed with either DNA of the following sequence to form a mutant dsDNA: CTTCTGGCGCTGTCCATGGTGCTGAACCCAG or a sequence with an insertion to form a DNA bubble: CTTCTGGCGCTGTCCATCACAAGGTGCTGAACCCAG. The used sequences were described in literature before.³⁹ Next, EMSA reactions were set up in a buffer containing 25 mM HEPES (pH 8.0) 50 mM KCl, 0.1% (v/v) Triton X-100, 2 mM MgAc₂, 3 mM DTT, 50 ng/ μ l poly I:C and 5% (v/v) glycerol. Compounds were incubated with LIN28A(16-187) for 2 h before the addition of DNA to achieve final concentrations of 40 nM protein and 5 nM DNA. After further incubation for 30 minutes, a 5.2% TAE-PAGE was run in 0.25xTAE buffer as described in 3.2.2.4. Gels were run for 40 min before imaging for 120 s using a ChemiDoc MP in the Cy3 fluorescence mode.

3.2.2.12 Docking

The docking was performed by Georg Goebel at the Chemical Genomics Centre in Dortmund. **135** was docked to the preE-*let-7* binding site of the LIN28A CSD from the crystal structure with the PDB code 5UDZ.⁸⁸ The software Schrödinger Maestro 12.3 was used. The ligand **135** was prepared by energy minimization by MM2 with PerkinElmer Chem3D 20.1. Then, the ligand preparation module was used to generate chemical states and the LIN28A conformation was prepared by the protein preparation module, including hydrogen addition, water molecule removal and energy minimization. Binding sites were generated by removal of miRNA fragments, using the grid generation model and remaining fragments of *let-7*. **135** was docked with the glide dock module and results were judged by small-molecule orientations, interactions, docking scores and solvent exposure patterns.

3.2.2.13 Crystallography

LIN28B(24-111) and *Xenopus tropicalis* Lin28B(27-114) were purified as described in 3.2.2.1. Immediately after the gel filtration, screenings with numerous conditions using the sitting drop

were set up at 4 °C. Each drop contained 100 nL reservoir solution and 100 nL protein solution or protein solution preincubated with compound. Additional fine screens were performed varying concentrations of precipitant, salt and pH values, starting with the reported conditions. For LIN28B, 2 M ammonium sulfate, 0.2 M NaCl and 0.1 M MES, pH 6.5 was used as a starting condition and crystals were grown at 4 °C. For *X. tropicalis* Lin28B, 2.5 M sodium acetate and 0.1 M HEPES, pH 7.0 was used as the initial condition for fine screening and the crystals were grown at 20 °C.

3.2.2.14 Western Blot

JAR cells were seeded in either 6-well plates (5×10^5 cells/well) or 100 mm dishes (8×10^5 cells/well), incubated overnight and treated with compound with a final DMSO concentration of 0.5% DMSO. After 24 h, cells were washed with ice-cold DPBS and lysed with ice-cold RIPA buffer (200 μ L for 6-well plate, 700 μ L for 100 mm dish). The adherent cells were detached using a cell scraper and transferred to a pre-cooled 1.5 mL tube. After incubation for 30 min on ice, the lysate was cleared by centrifugation for 30 min at 21000 $\times g$ and 4 °C. The supernatant was pipetted into a fresh tube, and the total protein concentration was determined using BCA assay according to the manufacturers protocol. If the protein concentration allowed, a total of 20-30 μ g protein with the same concentration used for every sample was separated by SDS-PAGE. Without gel staining, protein levels were analyzed according to the general procedure for western blots described above (3.2.1.6). Antibodies were used, as shown in 3.1.1.6.

3.2.2.15 Incucyte antiproliferation assay

In order to monitor the effect of compounds on the proliferation efficiency of cells, 5000 JAR cells per well were seeded into a 96-well plate (Corning). After 24 h, the medium was replaced with medium containing compounds with varied concentrations and a constant final DMSO concentration of 0.7% (v/v), and propidium iodide stain was added with a final concentration of 1 μ g/mL. Cells were monitored by automated microscopy in an Incucyte Zoom over 72 h after treatment taking two images per well every two hours in phase-contrast and red fluorescence channel. Treatments were done in triplicates. Data were analyzed using the software of the machine. Data visualization was done with GraphPad Prism.

3.2.3 Methods for the identification and evaluation of RNase L modulators

3.2.3.1 Expression and purification of RNase L

The human RNase L gene was cloned to pET19a plasmid. The plasmid was transformed into *E. coli* BL21(DE3) cells. Cells were grown overnight in 100 mL LB medium a 5 L expression culture was inoculated with the 100 mL culture. Bacteria were incubated at 180 rpm and 37 °C until an OD₆₀₀ of 0.6-0.8 was reached. Expression was induced with 300 μ M IPTG and

Material and methods

performed for 18 h at 18 °C and 180 rpm. After harvesting at 5000 ×g and 4 °C, cells were resuspended in cold lysis buffer (25 mM Tris, pH 7.4, 50 mM KCl, 5 mM MgCl₂, 10% glycerol, 0.1 mM PMSF, SIGMAFAST™ Protease Inhibitor Cocktail, DNase I) and lysed by sonication on ice (amplitude 55%, 5 s on, 5 s off, 5 min total). As a next step, the lysate was cleared by centrifugation at 60000 ×g for 1 h at 4 °C, filtered using a 0.45 µm syringe filter, and applied to an immobilized nickel affinity chromatography column. Equilibration and washing of the column were done using buffer A containing 25 mM Tris, pH 7.4, 50 mM KCl, 5 mM MgCl₂, and 10% glycerol, and the protein was eluted from the column after a wash with 25 mM imidazole. Elution was performed with a gradient of imidazole ramping up to 500 mM. Imidazole was removed from the protein solution by dialysis against buffer A (MWCO 3500), during which the His₆-tag of the protein was cleaved using His₆-TEV-protease. The protease, the protein tag, and unspecific binders were removed during reverse immobilized nickel affinity chromatography, and the flow-through and wash fractions were collected. The protein was concentrated (MWCO 30k, 4 °C, 4000 ×g) and further purified by gel filtration using a High Load Superdex 75 pg 16/600 column. The column was equilibrated and ran with buffer containing 25 mM Tris, pH 7.4, 50 mM KCl, 5 mM MgCl₂, 0.025 mM ATP, 7 mM β-mercaptoethanol, and 10% glycerol. SDS-PAGE was used to identify fractions containing pure protein of interest. These fractions were pooled, concentrated, snap-frozen in liquid nitrogen, and stored at -80 °C until further use. The protein concentration was determined using Pierce Coomassie Protein Assay Kit. For the detection of RNase L inhibitors, the protein was expressed and purified from insect cells, comparable to the methods described in 3.2.4.1 and in this section. The gel filtration was performed without ATP in the buffer.

3.2.3.2 FRET assay for the detection of RNase L activators

A Förster resonance energy transfer (FRET) assay, adapted from Thakur *et al.* and further optimized, was performed in FRET buffer (25 mM Tris pH 7.4, 100 mM KCl, 10 mM MgCl₂, 2 mM L-glutathione (reduced), 2.5 µM ATP).²⁰⁹ Assays were set up in a 384 well plate format in black plates with non-binding surface (Corning 4514) with a total reaction volume of 20 µL. Final concentrations were 50 nM RNase L and 10 nM original FRET probe (RNA-4) or 50 nM optimized FRET probe (RNA-5) with 5 nM recombinant RNase L. Compounds, or 2'-5'A were titrated at indicated final concentrations. Validation experiments with single-dose of compounds were performed with additional 0.1% (v/v) NP-40 in the assay buffer. A Tecan Spark was used to read out fluorescence signal. For dose-response measurements, EC₅₀ values were determined using GraphPad Prism.

3.2.3.3 FRET assay used in screening

Small-molecule screening to identify RNase L activators was performed by the Compound Management and Screening Center of the Max Planck Institute of Molecular Physiology. Compounds were screened at 30 μ M concentration with 0.5 nM RNase L and 10 nM RNA-5 in FRET buffer. The signal was detected on an Envision plate reader. For the identification of false-positive hits, the assay was repeated without RNase L enzyme.

3.2.3.4 FRET assay for the detection of RNase L inhibitors

The FRET assay for the detection of RNase L inhibitors was set up similarly to the assay for the detection of activators as described in 3.2.3.2. 0.5 nM 2'-5'A was added to each reaction and incubated for 5 minutes on ice with 5 nM RNase L protein in FRET buffer without ATP with additional 0.1% NP-40. Then, compounds were added to the mixture together with ATP at a final concentration of 50 μ M followed by incubation for 30 min on ice. RNA-5 was added with a final concentration of 50 nM. After 120 min incubation, fluorescence intensity (F) was detected on a TECAN Spark plate reader. Inhibition rates (I) were calculated by the following equation

$$I = \left(1 - \frac{(F_{\text{compound}} - F_{\text{DMSO}})}{F_{2'-5'A} - F_{\text{DMSO}}} \right) \cdot 100\% \quad (3)$$

and half maximal inhibitory concentrations were determined by fitting using GraphPad Prism.

3.2.3.5 RNA gel electrophoresis cleavage assay for the detection RNase L activators

A gel-electrophoresis-based cleavage assay was performed to detect cleavage of RNA by RNase L. Reactions were set up in buffer containing 25 mM Tris, pH 7.4, 100 mM KCl, 10 mM MgCl₂, 7 mM β -mercaptoethanol and 50 μ M ATP. Purified RNase L protein (final concentration 60 nM) was incubated with indicated concentrations of 2'-5'A or compound for 120 min at room temperature. Then, an RNA cleavage assay probe (RNA-6) was added to the mixture with a final concentration of 30 nM, followed by further incubation for 30 minutes, protected from light. Loading buffer (40% (v/v) glycerol, 15% (v/v) 10 \times TBE) was added, and 5 μ L of the reaction was applied to a 15% denaturing polyacrylamide gel. The gel was run for 45 min before loading samples in 1 \times TBE buffer and pockets were washed using a syringe before loading. Then, the gel was run with samples for 25 min in 60 $^{\circ}$ C prewarmed 1 \times TBE buffer at 250 V in the dark. The signal was detected using ChemiDoc MP with 2 minutes of exposure. The gel was cast using 8 M ultrapure urea, 15% (v/v) acrylamide (40%, 19:1), and a final concentration of 1 \times TBE buffer. Polymerization was initiated with APS and TEMED. Band intensities were determined with ImageLab software.

3.2.3.6 RNA gel electrophoresis cleavage assay for the detection of RNase L inhibitors

Reactions were set up containing 60 nM recombinant RNase L and 2 nM 2'-5'A in buffer containing 25 mM Tris, pH 7.4, 100 mM KCl, 10 mM MgCl₂, 7 mM β-mercaptoethanol and 50 μM ATP. Then, compound was added for 30 min, followed by the addition of 30 nM RNA-6 for 30 min in the dark. Samples were separated by denaturing urea PAGE as described in 3.2.3.5.

3.2.3.7 NanoDSF of RNase L

Samples were prepared in buffer containing 25 mM HEPES, pH 7.4, 100 mM KCl, 10 mM MgCl₂, and 2.5 μM ATP, and RNase L was used at a concentration of 3 μM. Protein was incubated with 60 μM compound or 1.75 μM 2'-5'A for 50 minutes at room temperature before measurement. Samples were loaded into standard capillaries. A heat ramp from 20 °C to 90 °C was applied with a slope of 1 °C per minute and data was analyzed using the software of the used device, a NanoTemper Prometheus NT.48.

3.2.3.8 Mass photometry

Mass photometry measurements were performed with buffer containing 25 mM Tris, pH 7.4, 100 mM KCl, 10 mM MgCl₂, and 2.5 μM ATP. The buffer was filtered before use with a 0.22 μM syringe filter. A Refeyn TwoMP was calibrated with 100 nM BSA (monomer and dimer) and 100 nM Thyroglobulin diluted tenfold in measurement buffer. Buffer was used for focusing, and 500 nM RNase L was incubated on ice with 1 μM 2'-5'A for 30 min before tenfold dilution in the buffer droplet for measurement. Binding events were recorded and analyzed by the software of the device.

3.2.3.9 Biolayer interferometry for the evaluation of RNase L binders

Biolayer interferometry was measured using an OctetRed384 instrument in a 384-well plate format (50 μL per well). First, purified recombinant RNase L was biotinylated using EZ-Link Sulfo NHS-LC-LC-Biotin according to the manufacturers protocol with a calculated labeling ratio of one biotin per protein macromolecule. Excess reagent was removed during dialysis (MWCO 3500) against buffer containing 20 mM HEPES (pH 7.5), 150 mM NaCl and 1 mM MgCl₂ overnight at 4 °C. The protein concentration was determined, and the ideal loading concentration of protein was tested in a loading control experiment. Then, RNase L was immobilized on streptavidin (SA) biosensors pre-equilibrated in assay buffer (20 mM HEPES, pH 7.5, 150 mM NaCl, 1 mM MgCl₂, 0.05% Tween-20, 1% DMSO and 0.3 mg/mL BSA). Measurements consisted of baseline recording, association, and dissociation measurements in buffer, buffer containing compound (0-100 μM), and buffer, respectively. The DMSO concentration was kept constant in all wells. A control measurement was performed with

biosensors loaded with 10 µg/mL biocytin, and data were analyzed by double referencing using the software of the device. Data were visualized using GraphPad Prism.

3.2.3.10 Pull-down

NHS-activated magnetic beads (25 µL per non-binding tube) were equilibrated with 500 µL ice-cold 1 mM HCl. The liquid was replaced with 500 µL compound (**226**, **247**, or **248**) or 1% DMSO in a buffer containing 0.15 M triethanolamine, 0.5 M NaCl, pH 8.3, and incubated for 90 minutes. Then, the beads were quenched with three consecutive washes with 500 µL buffer block A (0.5 M ethanolamine, 0.5 M NaCl, pH 8.3) followed by buffer block B (0.1 M sodium acetate, 0.5 M NaCl, pH4). Beads were washed with 500 µL lysis buffer (50 mM PIPES (pH 7.4), 50 mM NaCl, 5 mM MgCl₂, 5 mM EGTA, 0.1% NP-40, 0.1% Triton X-100, 0.1% Tween-20, 0.1% β-mercaptoethanol, Sigma Fast protease inhibitors) and incubated with 500 µL K-562 cell lysate with a protein concentration of 1.8 mg/mL. The lysate was prepared before from cultured cells by washing with PBS twice before the addition of lysis buffer. The beads were incubated with lysate overnight at 4 °C and washed twice for 10 min with lysis buffer without β-mercaptoethanol and protease inhibitors but with 75 mM MgCl₂. Proteins were reduced, alkylated, and digested on the beads. First, 50 µL buffer containing 8 M urea, 50 mM Tris, pH 7.5, and 1 mM DTT was added to the beads for 30 minutes at room temperature with shaking at 350 rpm. Chloroacetamide was added to a final concentration of 5 mM to each sample and incubated for a further 30 min under shaking at room temperature. Then, the proteins were digested with 1 µg Lys-C each for 1 h at 37 °C and 350 rpm. The supernatant was removed, and proteins were further digested with 165 µL of 1 µg Trypsin in 50 mM Tris, pH 7.5 for 1 h at 350 rpm and 37 °C. Both digestions were pooled and incubated overnight with additional 2 µg trypsin at 37 °C and 350 rpm. The reaction was quenched with 20 µL of 10% TFA. Peptides were desalted using C18 disks in 200 µL pipette tips. Tips were prepared by subsequent washes with 100 µL methanol, 100 µL elution buffer (80% acetonitrile, 0.1% formic acid), and two times 100 µL 0.1% formic acid. Peptides were loaded on the tip, washed with 100 µL 0.1% formic acid, and eluted with two times 20 µL elution buffer. Samples were dried in a vacuum concentrator at 30 °C and analyzed by nano HPLC-MS/MS at the HRMS facility of the MPI Dortmund. Protein identification was performed by computational comparison to a database of the human reference genome and quantified with label-free quantification using MaxQuant, performed by the HRMS facility of the MPI Dortmund.

3.2.3.11 Ribosomal RNA cleavage assay

First, RNase L expression was evaluated in HEK293T, JAR, and HeLa cell lines by western blot to identify which cell line was suitable for experiments targeting RNase L. All cells were grown in 100 mm dishes to near confluency, washed with ice-cold PBS and lysed with 1 mL ice-cold lysis buffer (150 mM NaCl, 1% NP-40, 50 mM Tris-HCl, pH8, SigmaFast Protease

inhibitors). Cells were detached using a cell scraper and kept at 4 °C under constant agitation in a fresh microcentrifuge tube. Lysates were cleared at 12000 ×g for 20 min at 4 °C, and supernatants were transferred into fresh vessels. Protein concentration was determined by BCA assay following the manufacturers protocol and 20 µg total protein were separated by SDS-PAGE and analyzed by western blot as described in 3.2.1.5 and 3.2.1.6. HeLa cells were found to express RNase L and used for the rRNA cleavage assay. Cells were seeded in 6-well plates at 1×10⁵ cells per well, cultured for 24 hours and treated with compound or DMSO. Every well contained 0.5% (v/v) DMSO in total. After four hours, cells were transfected with 2 µg/mL poly I:C using Lipofectamine 2000 according to the manufacturers protocol. Culturing was continued for four hours before extraction of total RNA using the RNeasy Mini Kit. The total RNA concentration was measured by NanoDrop, and equal amounts of RNA were glyoxylated by adding 5 µL glyoxal mix (60% (v/v) DMSO, 8% (v/v) glyoxal, 12% (v/v) 10× BPTE, 4.8% (v/v) glycerol, 20 µg/mL ethidium bromide) to the RNA in a total sample volume of 20 µL. Gene ruler 1 kb DNA ladder was also glyoxylated, and a volume of 2 µL was used. The reactions were heated to 55 °C for one hour, and 18 µL were separated using a stain-free 1.2% agarose gel prepared with 1× BPTE buffer. The gel was run at 80 V in 1× BPTE buffer for 90 min, and fluorescence was detected using a ChemiDoc MP. Band intensities were analyzed with ImageLab.

3.2.3.12 Western Blot

Cells were cultured in 100 mm dishes, washed with DPBS and lysed with 700 µL ice-cold RIPA buffer. After scraping the cells, the lysate was cleared by centrifugation for 30 min at 21000 ×g and 4 °C. The concentration of the protein was measured by BCA assay and equal amounts of protein were separated by SDS-PAGE. RNase L expression was detected following the general procedure described above (3.2.1.6). Antibodies were used, as listed in 3.1.1.6.

3.2.4 Methods for the identification and evaluation of OAS1 activators

3.2.4.1 Expression of OAS1 protein

His₆-SUMO-TEV-OAS1 was subcloned into pFastBacHT plasmid by SLIC and expressed in insect cells following the Bac-to-Bac baculovirus expression system user guide. The plasmid was transformed into *E. coli* DH10EmBacY cells and plated onto LB-agar plates containing 50 µg/mL kanamycin, 10 µg/mL tetracycline, 10 µg/mL gentamicin, 40 µg/mL IPTG and 100 µg/mL 5-bromo-4-chloro-3-indolyl-β-D-galactopyranoside. Positive, white clones were selected by blue/white selection, and the bacmid was isolated from a 6 mL overnight culture in LB-medium with 50 µg/mL kanamycin, 10 µg/mL tetracycline, and 10 µg/mL gentamicin. Cells were resuspended in 300 µL buffer P1 and lysed with 300 µL buffer P2 from the QIAprep Spin Miniprep Kit, 300 µL neutralization buffer was added, and the liquid was centrifuged for

Material and methods

10 min at 14000 \times g. The supernatant was transferred into a new tube and centrifuged again before the addition of 700 μ L isopropanol and another centrifugation for 10 min at 14000 \times g. The pellet was washed twice with 200 μ L and 50 μ L 70% ethanol and dried under sterile conditions, followed by resuspension in 42 μ L sterile water. The bacmid was transfected to Sf9 insect cells by addition of 10 μ L bacmid and 8 μ L gene juice transfection agent to 250 mL insect cell medium followed by dropwise addition to $1 \cdot 10^6$ SF-9 cells per well, which were seeded in a 6-well plate before. After three days incubation at 27 °C, the cells were resuspended and added to $1 \cdot 10^6$ cells grown adherently in a 100 mm dish. Sf9-cells were incubated for four days at 27 °C to allow the virus to replicate, and cells were resuspended and harvested by centrifugation at 100 \times g for 5 min. The virus was filtered using particle-free filtration and stored at 4 °C with 10% FBS. The virus was amplified using 250 μ L virus in 50 mL cells at a density of $2 \cdot 10^6$ cells per mL. The cells were cultured at 27 °C and 110 rpm. After four days, the virus was harvested by centrifugation at 100 \times g for 5 min, filtered to remove remaining cells, and stored with 10% FBS at 4°C. The protein was expressed in 200 mL HighFive cells with a density of $2 \cdot 10^6$ cells per mL by addition of 0.5% (v/v) baculovirus. Expression was performed for 72 h while shaking at 110 rpm and 27 °C. Cells were harvested by centrifugation at 2000 \times g for 10 minutes.

3.2.4.2 Purification of OAS1 protein

To purify the OAS1 protein, the cell pellet was resuspended in a buffer containing 20 mM HEPES (pH 7.4), 300 mM NaCl, 5 mM $MgCl_2$, 10% (v/v) glycerol, 0.1 mM PMSF, lysozyme, DNase I, and Sigma Fast protease inhibitors. Cells were lysed by sonication (amplitude 35%, 5 s on, 5 s off), and the lysate was cleared by centrifugation at 60000 \times g for 60 min. The supernatant was applied on an immobilized nickel affinity chromatography column equilibrated with buffer A containing 20 mM HEPES (pH 7.4), 300 mM NaCl, 5 mM $MgCl_2$, and 10% (v/v) glycerol. The column was washed with buffer A, followed by buffer A containing 2.5 mM imidazole. Proteins were eluted with a gradient containing up to 500 mM imidazole. Fractions were analyzed by SDS-PAGE, and fractions harboring the target protein were merged and dialyzed overnight with the addition of 1 mL TEV protease against buffer A. Protease was eliminated by reverse immobilized nickel affinity chromatography and the fractions containing the target protein were concentrated (MWCO 10K) and applied to a High Load Superdex 75 pg 16/600 column equilibrated with gel filtration buffer (50 mM Tris (pH 8), pH 8, 100 mM NaCl, 3 mM TCEP, 10% (v/v) glycerol). The protein was purified by gel filtration, and fractions were analyzed by SDS-PAGE. Fractions containing OAS1 were merged, concentrated, snap-frozen in liquid nitrogen, and stored at -80 °C until further use. Protein identity was confirmed by LC/MS.

3.2.4.3 Enzymatic synthesis of 2'-5'A

A total of 6 mg polyinosinic acid was annealed with 15 mg polycytidylic acid agarose in 2 mL buffer containing 10 mM HEPES (pH 7.5), 50 mM KCl, 10 mM MgCl₂, 7 mM β-mercaptoethanol and 10% glycerol. Annealing was performed at 37 °C for one hour. Then, the beads were spun down at 500 ×g for 5 min at 4 °C and washed with 10 mL buffer followed by centrifugation at 500 ×g for 5 min at 4 °C. The washing was repeated two more times. Then, the immobilized poly I:C was incubated with 0.18 mg purified OAS1 in a total volume of 100 μL at 4 °C under constant agitation. Excess protein was removed by washing for three times as described before. Synthesis of 2'-5' was induced by resuspension of the immobilized enzyme in 2 mL buffer with additional 4 mM ATP. The mixture was incubated at 37 °C for two hours shaking with a speed of 500 rpm. The crude 2'-5'A solution was isolated by centrifugation (10,000 ×g, 5 min) and the supernatant was analyzed for its ability to activate RNase L using the FRET assay described in section 3.2.3.2.

3.2.4.4 Mass photometry of OAS1

Mass photometry of OAS1 was measured as described for RNase L in section 3.2.3.8. The working concentration of OAS1 was 39 nM and the buffer did not contain ATP. A tenfold excess of annealed RNA-7 and RNA-8 was used for OAS-1 binding

3.2.4.5 FRET assay for the detection of OAS1 activators

The OAS1 FRET assay setup was similar to the FRET assay described in 3.2.3.2. Buffer contained 25 mM Tris (pH 7.4) 100 mM KCl, 10 mM MgCl₂, 7 mM β-mercaptoethanol and 5 mM ATP. Assays were performed in 384 well format using black non-binding plates (Corning 4514) with an assay volume of 20 μL. The final concentrations after optimization were 50 nM RNA-5, 5 nM RNase L and 100 nM OAS1. Poly I:C was used as a positive control at indicated concentrations. Fluorescence signal was read using a TECAN Spark plate reader. Data were analyzed using GraphPad Prism.

3.2.4.6 Small-molecule screening of OAS1 activators

Small-molecule screening was performed by the Compound Management and Screening Center of the Max Planck Institute of Molecular Physiology, generally as described in 3.2.4.5. An Envision plate reader was used for the readout. Results were compared to RNase L FRET assay screening and the assay without RNase L as described in 3.2.3.3.

3.2.4.7 Pyrophosphate assay

A pyrophosphate assay was performed similarly to the description by Conn and colleagues.²¹⁰ Samples were incubated in a buffer containing 20 mM Tris (pH 7.4), 7 mM MgCl₂, 1 mM DTT, 10 mM NaCl, and 1.5 mM ATP. Each reaction contained 300 nM recombinant OAS protein and either 30 μM compound or 20 μg/mL poly I:C. Reaction volumes were 150 μL. The

solutions were incubated at 37 °C, and 10 µL aliquots were taken after 0, 5, 10, 20, 40, 60, 90, and 120 min. Each aliquot was immediately transferred into 2.5 µL quenching buffer (250 mM EDTA, pH 8) in a transparent 96-well plate. Subsequently, 10 µL detection reagent (2.5% (w/v) ammonium molybdate tetrahydrate in 2.5 M H₂SO₄), 10 µL reducing agent (0.5 M β-mercaptoethanol), and 4 µL fresh, sterile filtered Eikonogen reagent (13 mM 4-amino-3-hydroxynaphthalene-1-sulfonic acid, 25 mM sodium sulfite, 963 mM sodium meta-bisulfite) were added to the plate. Wells were filled with water to 100 µL, and absorbance was measured at a wavelength of 580 nm using a TECAN Spark plate reader.

3.2.4.8 Kinase-Glo assay for the detection of ATP levels

ATP-concentration in OAS-1 reactions was detected using Kinase-Glo Max Luminescent Kinase Assay. Reactions were set up in buffer containing 25 mM Tris (pH 7.4), 100 mM KCl, 10 mM MgCl₂, 7 mM β-mercaptoethanol, and 10 µM ATP. Each reaction of 10 µL contained a dilution series of compound or poly I:C and 100 nM recombinant OAS1. After 120 min incubation, 10 µL kinase glo reagent was added to the reaction in white polystyrene 384 well plates with non-binding surface (Corning 3824). After ten minutes of incubation, luminescence was measured using a TECAN Spark plate reader with an integration time of 1 s.

3.2.4.9 Fluorescence polarization assay to investigate OAS–RNA interaction

RNA (RNA-7 and RNA-8, 200 µM each) was annealed in buffer containing 10 mM Tris (pH 8), 50 mM NaCl and 1 mM EDTA by heating to 95 °C for 2 min followed by slowly cooling to room temperature over 45 min. Then, recombinant OAS1 was titrated in assay buffer containing 25 mM Tris (pH 8), 100 mM KCl, 10 mM MgCl₂, and 7 mM β-mercaptoethanol in black non-binding 384-well plates (Corning 4514). Annealed RNA was added to a final concentration of 5 nM and an assay volume of 20 µM. Fluorescence anisotropy was measured using a TECAN Spark plate reader and analyzed using GraphPad Prism.

3.2.4.10 Electrophoretic mobility shift assay of OAS1

RNA-7 was annealed with RNA-8 as described in 3.2.4.9. 5 nM RNA was incubated with varied concentrations of OAS1 protein in buffer containing 25 mM Tris (pH 8), 100 mM KCl, 10 mM MgCl₂, 7 mM β-mercaptoethanol, 0.01% (v/v) Tween-20 and 12% (v/v) glycerol for 30 min at room temperature in the dark. Then, 10 µL of each sample were separated by a non-denaturing 5.2% polyacrylamide gel in 0.25× TAE buffer as described in 3.2.2.4.

4 Results and discussion

4.1 Discovery and biochemical evaluation of inhibitors of the LIN28–*let-7* interaction

Parts of this section were done in cooperation with Philipp Lampe (COMAS) or Georg L. Goebel or were part of the Master thesis of Lisa Hohnen. Contributions are indicated below the respective Figures and Tables.

Inhibitors of the LIN28–*let-7* interaction could serve as candidates for the development of anticancer therapeutics, and they could further be used as chemical probes to improve the understanding of the pathways and mechanisms in which the RNA- and DNA-binding protein LIN28 is involved. The central role of LIN28 suggests a reverse chemical genetics approach, starting with the knowledge that perturbation of LIN28 in tumor cells will affect *let-7* expression and, eventually, tumor cell proliferation. In this work, inhibition of the interaction of LIN28 and *let-7* was thus assayed in biochemical assays and later validated in cells. Two general strategies were applied: a screening-based discovery and a scaffold-based approach. The screening-based approach required an assay allowing for medium to high throughput, while the scaffold-based approach, starting with a known LIN28 inhibitor, allowed for assays with reduced throughput, owing to a smaller number of compounds generated during the approach.

4.1.1 Purification of recombinant LIN28A

For the development of biochemical assays, the LIN28 protein was first purified. Due to its cytosolic localization, the LIN28 isoform LIN28A is likely more ligandable than its nuclear and nucleolar homolog LIN28B. Thus, LIN28A was selected to be used for the identification of LIN28 inhibitors, and a construct containing its folded domains were recombinantly produced from *E. coli*. A purification procedure was established and performed in three steps: immobilized nickel affinity chromatography (Figure 10A), protease cleavage of the His₆-tag and reverse immobilized nickel affinity chromatography (Figure 10B), and a final gel filtration (Figure 10C). The desired protein was well overexpressed and represented the main component of the solution already after the first nickel column. Cleavage of the tag is well detectable in the SDS-PAGE, and His₆-TEV protease, as well as other unspecific binding proteins, were separated from the protein of interest in the reverse immobilized nickel affinity chromatography (Figure 10B). Removal of the tag reduces its potential interference in the biochemical assays. The gel filtration allowed the separation of LIN28A from further larger proteins and aggregates. Peak 2 in Figure 10C was pooled and contained LIN28A with sufficient purity. The cold shock domain of LIN28A was purified accordingly, and high purity was achieved. The chromatogram and SDS-PAGE of the final gel filtration are shown in Figure S1A.

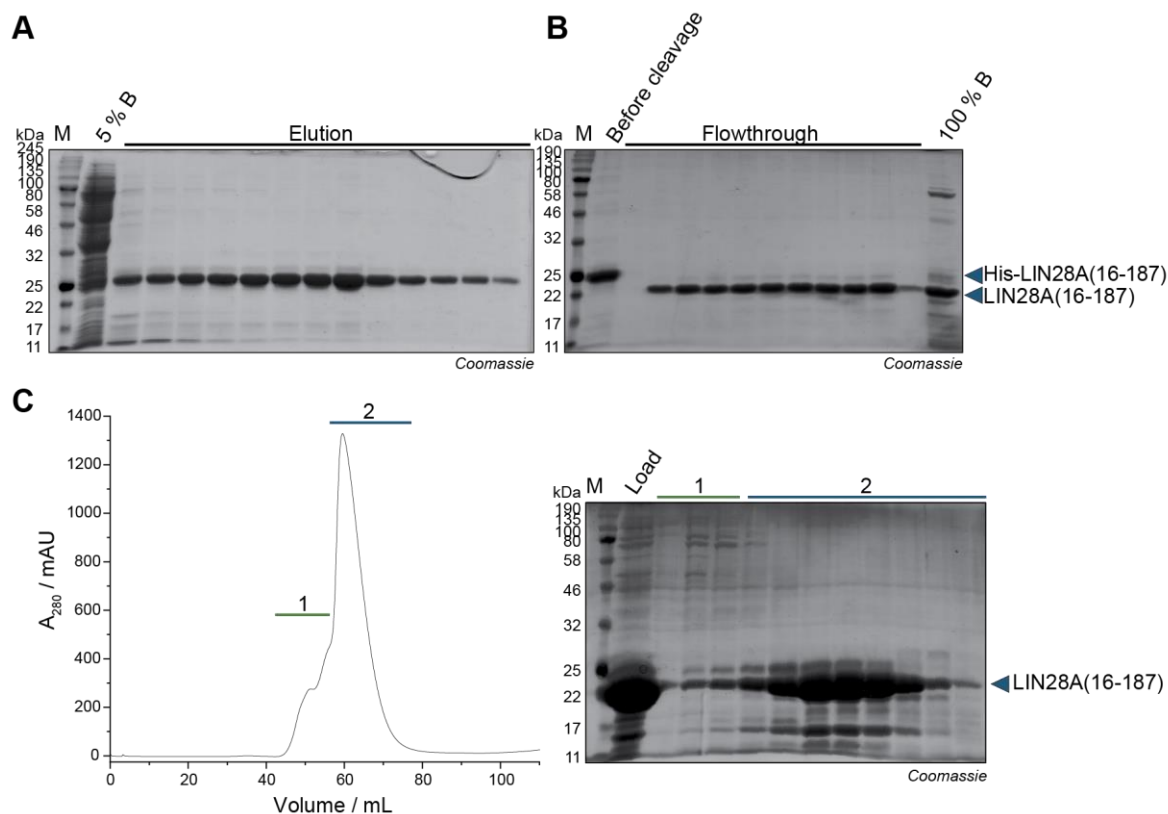


Figure 10: Purification of LIN28A(16-187). (A) SDS-PAGE of immobilized nickel affinity chromatography column. (B) SDS-PAGE of reverse immobilized nickel affinity chromatography column. (C) Chromatogram and SDS-PAGE of gel filtration. The void volume peak is labeled with 1, the LIN28A main peak is labeled with 2.

4.1.2 Screening-based discovery

Results from this section were published as “Trisubstituted Pyrrolinones as Small-Molecule Inhibitors Disrupting the Protein–RNA Interaction of LIN28 and Let-7” and submitted as *N-Biphenyl Pyrrolinones and Dibenzofuran Analogues as RNA-Binding Protein LIN28 Inhibitors Disrupting the LIN28–Let-7 Interaction*.²¹¹

The screening-based approach was designed for the discovery of novel small-molecule LIN28A inhibitors. The goal was to screen a diverse compound library with a medium-to-high-throughput assay to identify hits that could potentially bind to LIN28A or *let-7*. As a next step, assays orthogonal to the screening setup were established to verify the molecules’ inhibitory activity and elucidate their mode of action. Since a drug discovery approach starting with a biochemical assay does not account for potential binding of identified molecules to other proteins or targets and does not experimentally test membrane permeability, the inhibitors were further validated for their activity in cellular assays.

4.1.2.1 Fluorescence polarization assay for the identification of inhibitors of the LIN28–*let-7* interaction

A fluorescence polarization (FP) assay was established for the screening of inhibitors of the interaction of LIN28A and *let-7* allowing for medium to high throughput. The assay employed a FAM-fluorophore labeled *let-7* pre-element, which is the part of the pre-miRNA that naturally interacts with LIN28A. The FP is read-out after excitation of the fluorophore and expected to increase upon binding of LIN28A to the RNA. However, disruption of the protein–RNA interaction by an inhibitor will reduce the FP, due to the presence of free *let-7* in the assay solution (Figure 11A). Indeed, titration of recombinant LIN28A(16-187) to the RNA probe led to a dose-dependent increase of the FP (Figure 11B) and 50% of the signal was reached at a concentration of 12 nM LIN28. Unlabeled preE-*let-7* RNA and the reported LIN28 inhibitor SB1301 (**3**) were used as positive controls, with IC_{50} values of 4 nM and 48 μ M, respectively (Figure 11C, D). The tested IC_{50} values for both controls were consistent with the reported values. Thus, the established assay was used for small-molecule screening.

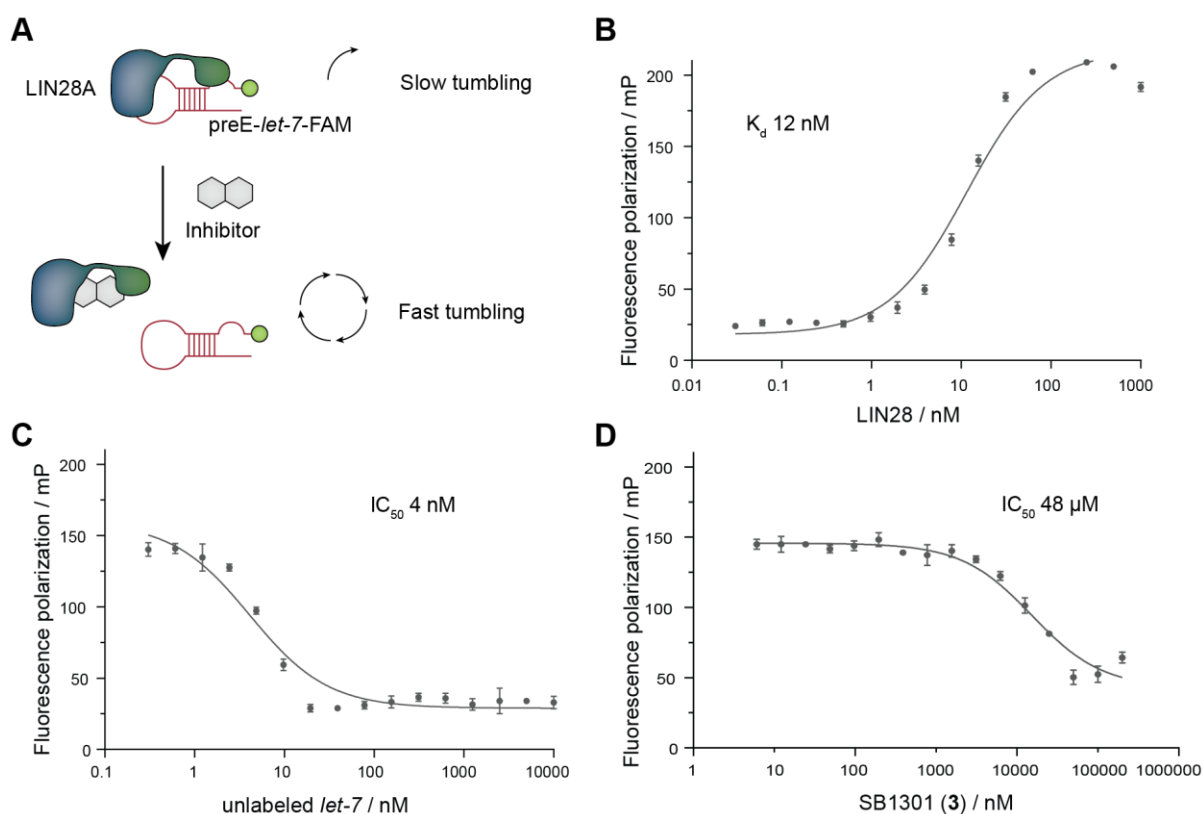


Figure 11: FP assay optimization. (A) Schematic representation of the FP assay for the identification of inhibitors of the LIN28–*let-7* interaction. (B) Change of FP signal upon titration of recombinant LIN28A to fluorophore-labeled preE-*let-7*. (C) FP-signal decreases upon the addition of unlabeled *let-7* to the complex of LIN28A and preE-*let-7*-FAM. (D) Titration of reported LIN28 inhibitor SB1301 (**3**) to LIN28A–preE-*let-7*-FAM complex measuring FP-signal. All experiments were performed in triplicates. The error bars indicate the standard deviation (SD).

4.1.2.2 LIN28–*let-7* inhibitor screening

A small-molecule library containing ~15,000 natural-product-inspired compounds was screened at a concentration of 30 μM using the established FP assay. Unlabeled preE-*let-7* served as the positive control, and Z'-factors were determined to be above 0.76, revealing robustness of the screening assay with sufficient separation between positive and negative controls. Hit molecules were selected based on their inhibitory activity (> 50% inhibition), their purity measured by LC-MS (>85%), and their total fluorescence intensity (Figure 12A). Molecules showing more than 300% fluorescence intensity of that of FAM-labeled RNA were excluded due to autofluorescence interfering with the assay readout, as fluorescent molecules will tumble fast in solution and are expected to produce a low FP. Collectively, based on the selection criteria, a total of six heterocyclic small molecules were identified as hits for further evaluation, of which the trisubstituted pyrrolinone **41** showed reproducible inhibition in the low micromolar range (IC_{50} 15 μM) when tested in dose-response FP assay. The in-house resynthesized molecule showed consistent inhibitory activity (Figure 12A, B).

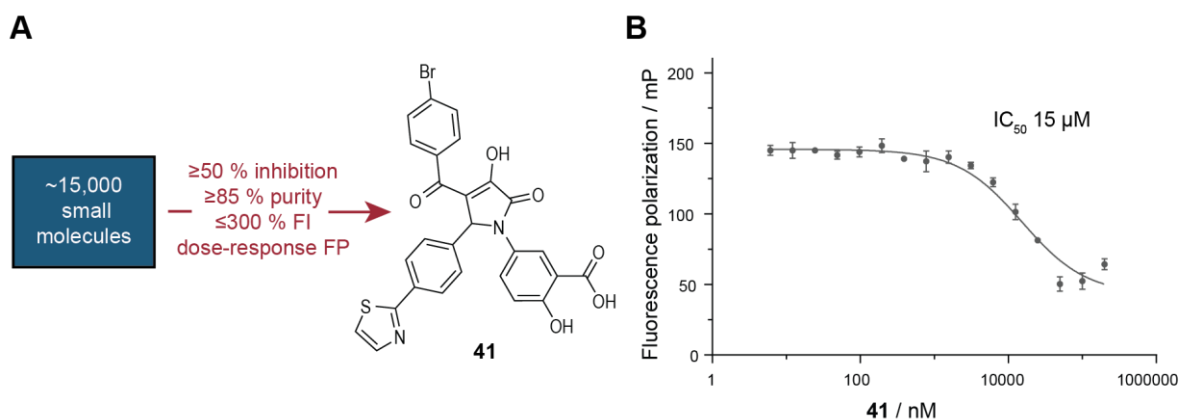


Figure 12: Screening for the identification of LIN28 inhibitors. (A) Schematic representation of the primary screening pipeline and structure of the hit **41**. The screening was performed by Dr. Philipp Lampe, COMAS. (B) Dose-response FP curve of **41**. The experiment was performed in triplicates. The error bars indicate the SD.

4.1.2.3 Hit validation

An orthogonal EMSA was developed to visualize the separation of preE-*let-7f-1* and its complex with LIN28 in a native PAGE due to the difference in size. Detection of the RNA was enabled by fluorophore labeling. The addition of **41** inhibited the interaction of LIN28A and *let-7* in a dose-dependent manner, with ~50% inhibition at 40 μM , supporting the hypothesis that **41** inhibits the LIN28–*let-7* interaction (Figure 13A). Both the FP assay and EMSA are competitive assays that do not reveal information on whether the small molecule binds to the RBP or the RNA. Thus, a thermal shift assay was performed by nanoDSF, measuring the melting of a protein via the detection of changes in intrinsic tryptophan fluorescence during unfolding of the protein. Binding of a small molecule to the protein would lead to its stabilization

Results and discussion

and thus a positive shift in melting temperature T_m . The purified CSD of LIN28A was incubated with varied concentrations of **41** or the inactive pyrrolinone **42** (see section 4.1.2.5). The global minima of the first derivatives of the melting curves indicated the melting temperature of the CSD, which was dose-dependently shifted upon small-molecule binding by **41**. The maximum shift was 1.6 °C at a concentration of 50 μM indicating stabilization of the protein by the compound. In contrast, the inactive compound **42** induces a maximum shift of only 0.6 °C. (Figure 13B).

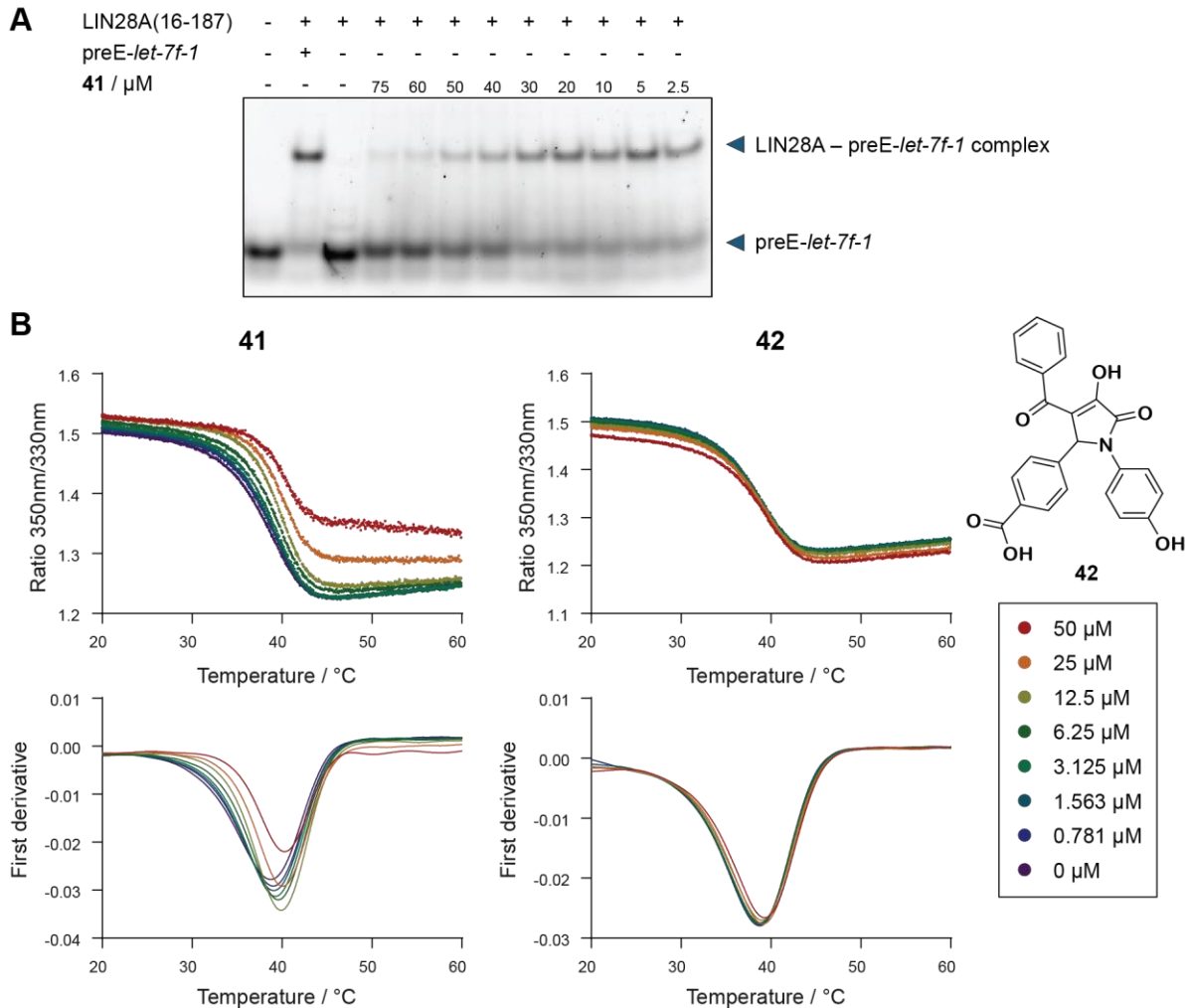


Figure 13: Orthogonal validation assays for inhibitors of the LIN28–*let-7* interaction. (A) Dose-dependent EMSA of **41**. (B) Dose-dependent thermal shift assay of the LIN28A CSD measured by nanoDSF. **41** (left) and **42** as a control molecule lacking a salicylic acid (right) were tested. The graphs depict the melting curve measuring intrinsic protein fluorescence (top) and the first derivatives (bottom).

4.1.2.4 Cellular assays

Cellular assays were performed using the human choriocarcinoma cell line JAR, endogenously expressing LIN28A. A twofold upregulation of the levels of mature *let-7* family miRNAs *let-7a* and *let-7g* was observed upon the treatment with 5 μM or 20 μM **41**, suggesting inhibition of the *let-7*-maturation inhibitor LIN28 (Figure 14A). In order to attribute the observed effect to **41**-mediated inhibition of LIN28A, a cellular thermal shift assay (CETSA) was performed. Melting of LIN28 protein was detected by western blot after clearing the lysate from proteins that aggregated due to heating. No major difference was observed between incubation with **41** and DMSO (Figure 14B). However, minor differences in melting temperature cannot be detected in CETSA due to the large steps between the analyzed temperatures. In nanoDSF, the melting temperature was shifted by up to 1.6 $^{\circ}\text{C}$ by **41**, which might be too low for observation in CETSA. Thus, the direct interaction of **41** with LIN28 in JAR cells cannot be excluded.

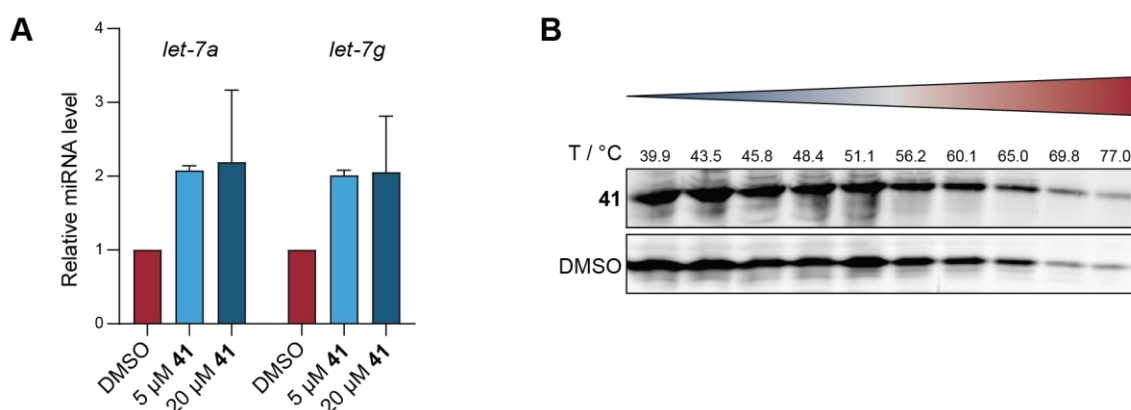


Figure 14: Cellular assays of **41**. (A) Relative levels of mature miRNA *let-7a* and *let-7g* were measured by qPCR after the treatment of JAR cells with **41**. The experiment was performed in three biological replicates. The error bars indicate the SD. (B) CETSA detecting melting of LIN28A in JAR-cell lysate treated with 100 μM **41** or DMSO.

4.1.2.5 SAR of trisubstituted pyrrolinones as LIN28 inhibitors

To investigate the structural feature required for potent inhibition of LIN28, the structure-activity relationship (SAR) based on the trisubstituted pyrrolinone scaffold of **41** was elucidated. A total of 29 trisubstituted pyrrolinones analog to **41** were tested in the FP assay (Table 14). Additionally, five pyrazoles with a bicyclic core scaffold obtained by cyclization of the pyrrolinones were assayed (Table 15). The best performing pyrrolinones were **41**, **43**, **44**, **68**, **69**, and **70**. All six compounds with IC_{50} values below 20 μM contained a salicylic acid moiety in the 1-position of the pyrrolinone core, with the R^3 being a carboxylic acid and the R^4 being a hydroxy group. Exchange of both substituents, as done in **65** when compared to **41**, rendered the molecule inactive, highlighting the crucial role of the salicylic acid. Interestingly, **59** and **67** were both moderately active, despite not carrying a salicylic acid. This indicated

Results and discussion

that more modifications were tolerated by the molecule, such as the exchange of the carboxylic acid to a nitro group as in **67**, suggesting that further modifications in the 1-position of the pyrrolinone core should be evaluated. Generally, changes in the 4-position of the pyrrolinone were tolerated with 4-methoxyphenyl or 4-bromophenyl substituents, furan-2-yl (**69**) or 3,4-dimethoxyphenyl (**70**). The latter substitution leads to a compound that is equally potent as **41**. Assayed substituents of the 5-position of the pyrrolinone core were thiazol-2-yl and carboxylic acid, as well as a nitro group. Thiazol-2-yl and carboxylic acid were both generally tolerated, with no obvious difference. Further investigations on the influence of the 5-position on the inhibitory activity of trisubstituted pyrrolinones were necessary. All investigated bicyclic pyrazoles were inactive at the tested concentrations of up to 30 μ M (Table 15).

The importance of the salicylic acid moiety at the 1-position of the pyrrolinone core was highlighted by the SAR but also underlined by the nanoDSF experiment in which **42** without the salicylic acid was inactive when compared to **41** (Figure 13B). The negatively charged substituent might mimic the negative charge of the RNA and thus replace its binding to LIN28. At the *let-7*-interaction interface, the LIN28 CSD generally carries a positive charge mediated by multiple lysine and arginine residues (Figure 19). However, carboxylic acids are associated with reduced cellular bioavailability and metabolic toxicity, which is a concern for cellular and *in vivo* applications.

Results and discussion

Table 14: Half-maximal inhibitory activities of trisubstituted pyrrolinones measured in FP-assay.

Compound	R ¹	R ²	R ³	R ⁴	IC ₅₀ / μM ^a
41	4-bromophenyl	thiazol-2-yl	COOH	OH	5 ^b
42	phenyl	COOH	H	OH	>100 ^{b,c}
43	phenyl	thiazol-2-yl	COOH	OH	12 ^b
44	phenyl	COOH	COOH	OH	6 ^b
45	phenyl	COOH	COOH	H	>100 ^{b,c}
46	phenyl	COOH	H	COOH	>100 ^{b,c}
47	4-methoxyphenyl	NO ₂	COOH	H	>100 ^{b,c}
48	4-methoxyphenyl	NO ₂	H	COOH	>100 ^{b,c}
49	4-methoxyphenyl	COOH	COOH	OH	30-40 ^{b,c}
50	4-methoxyphenyl	COOH	COOH	H	>100 ^{b,c}
51	4-methoxyphenyl	COOH	H	COOH	>100 ^{b,c}
52	4-methoxyphenyl	COOH	1 <i>H</i> -tetrazol-5-yl	H	>100 ^{b,c}
53	4-bromophenyl	NO ₂	COOH	H	>100 ^{b,c}
54	4-bromophenyl	NO ₂	1 <i>H</i> -tetrazol-5-yl	H	>100 ^{b,c}
55	4-bromophenyl	COOH	COOH	OH	30-40 ^{b,c}
56	4-bromophenyl	COOH	COOH	H	>100 ^{b,c}
57	4-bromophenyl	COOH	H	COOH	>100 ^{b,c}
58	4-bromophenyl	COOH	1 <i>H</i> -tetrazol-5-yl	H	>100 ^{b,c}
59	phenyl	thiazol-2-yl	COOH	H	30-40 ^{b,c}
60	phenyl	thiazol-2-yl	1 <i>H</i> -tetrazol-5-yl	H	>100 ^{b,c}
61	4-bromophenyl	thiazol-2-yl	H	COOH	>100 ^{b,c}
62	4-methoxyphenyl	thiazol-2-yl	COOH	H	>100 ^{b,c}
63	4-methoxyphenyl	thiazol-2-yl	1 <i>H</i> -tetrazol-5-yl	H	>100 ^{b,c}
64	4-bromophenyl	thiazol-2-yl	COOH	H	>100 ^{b,c}
65	4-bromophenyl	thiazol-2-yl	OH	COOH	>100 ^{b,c}
66	4-bromophenyl	thiazol-2-yl	H	OH	>100 ^{b,c}
67	phenyl	thiazol-2-yl	NO ₂	OH	41 ^b
68	phenyl	COOH	OH	COOH	16 ^b
69	furan-2-yl	thiazol-2-yl	COOH	OH	5 ^b
70	3,4-dimethoxyphenyl	thiazol-2-yl	COOH	OH	12 ^b

^aAll IC₅₀ values were tested in quadruplicate. ^bDetermined by Dr. Philipp Lampe, COMAS. ^cExtrapolated based on IC₅₀ curves.

Results and discussion

Table 15: Half-maximal inhibitory activities of trisubstituted pyrazoles measured in FP-assay.

Compound	R ¹	R ²	R ³	IC ₅₀ / μM ^a
71	NO ₂	COOH	OH	>100
72	NO ₂	H	COOH	>100
73	NO ₂	H	methoxyphenylcarbamoyl	>100
74	Br	COOH	OH	>100
75	NO ₂	H	benzylcarbamoyl	>100

^aAll samples were tested in quadruplicates. IC₅₀ range was extrapolated based on FP-assay curves. The assay was performed by Dr. Philipp Lampe, COMAS.

Recently, trisubstituted pyrrolinones lacking the hydroxy group at the pyrrolinone core when compared to **41**, were reported as a RNA-binding chemotype, identified in a fluorescent dye displacement screening.¹⁸¹ Consequently, the binding of hit compound **41** to preE-*let-7* RNA was evaluated to clarify whether the compound also binds to *let-7*. Compound **41** did not show any detectable binding in microscale thermophoresis (MST) when assayed against Cy5-labeled preE-*let-7a-1* (Figure 15A). Furthermore, the melting temperature of preE-*let-7f-1* was not significantly shifted upon incubation of the RNA with **41** at 60 μM. Taken together, both experiments suggested that **41** inhibited the LIN28-*let-7* interaction by binding to LIN28 instead of the structured element of the *let-7* miRNA.

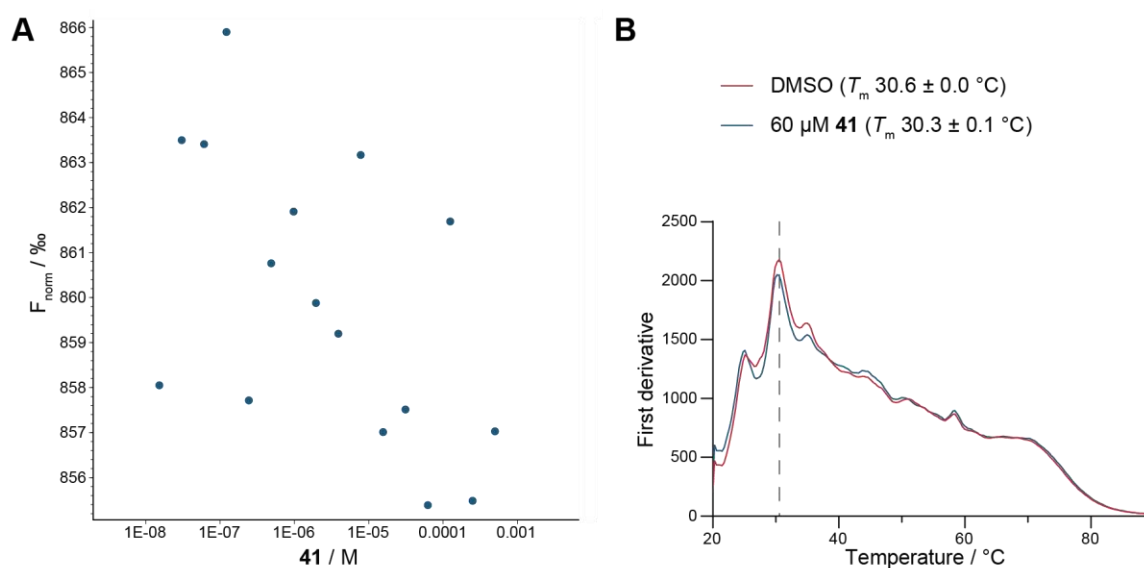


Figure 15: Evaluation of *let-7*-binding with **41**. (A) MST measuring the binding of **41** to Cy5-labeled preE-*let-7a-1*. Representative data from three independent replicates. (B) First derivative of melting curve of preE-*let-7f-1* incubated with **41** (60 μM) or DMSO. Average melting temperatures and SD were determined from triplicates.

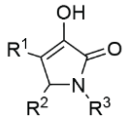
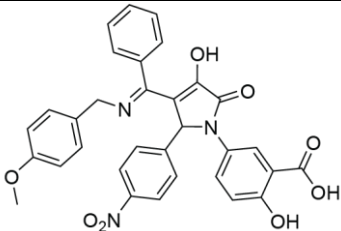
Results and discussion

Trisubstituted pyrrolinones were previously identified as stabilizers of the protein–protein interaction (PPI) of plant 14-3-3 proteins and a plant plasma membrane H⁺-ATPase (PMA2). The two most active PPI stabilizers were the screening hit PPI-1 (**76**) (R¹ = phenyl, R² = NO₂, R³ = COOH and R⁴ = OH) with an EC₅₀ of ~100 μM and a pyrazole derivative (**71**).²¹² The most potent LIN28 inhibitors, **41** and **44**, showed less than 30% and less than 10% of the activity of PPI-1 (**76**) when assayed for PPI stabilization, respectively.²¹² This indicated a distinct SAR for PPI stabilization and LIN28 inhibition. Based on our first SAR results, PPI-1 (**76**) and 61 derivatives were screened via EMSA at a concentration of 75 μM for their potency against LIN28. While PPI-1 (**76**) was inactive despite carrying a salicylic acid, eleven active compounds with more than 60% inhibition were identified and evaluated in dose-response EMSA (Table 16, Figure S2).

The newly identified LIN28 inhibitors gave insights into the SAR of the trisubstituted pyrrolinones. The assayed molecules were either modified in the 1-, 4-, or 5-position of the pyrrolinone core when compared to PPI-1 (**76**). In contrast to the first SAR study, multiple compounds carrying the salicylic acid moiety were inactive, revealing that the negatively charged moiety is insufficient for activity. In general, the 4-position allowed for multiple different substituents to render the molecule active, while in the 5-position, nitrogen-containing heterocycles seemed to be beneficial. Interestingly, two molecules without salicylic acid in the 1-position of the pyrrolinone core inhibited the LIN28–*let-7* interaction. Due to the known drawbacks of carboxylic acids, such as metabolic toxicity and low membrane permeability, molecules without the salicylic acid moiety are of high interest for the development of therapeutic LIN28 inhibitors.²¹³ **85**, carrying a biphenyl substituent at the 1-position, was resynthesized in-house and showed an IC₅₀ in the range of 30 μM (Figure 16A, B). BLI and nanoDSF indicated the binding of the compound to the CSD of LIN28A, and the detected shift in melting temperature was higher than that of **41**, indicating an increased potency (Figure 16C, Table 17). The influence of the stereochemical configuration on potency was assayed in nanoDSF and EMSA (Table 17, Figure S2). In both assays, the (*R*)-enantiomer was more active than the (*S*)-enantiomer, however, with only slight differences (IC₅₀ 24 μM and 37 μM, respectively) which did not suggest that the stereochemistry played a significant role.

Results and discussion

Table 16: Trisubstituted pyrrolinones with more than 60% activity identified from a collection of 62 molecules. Structures of the inactive molecules are not disclosed.

				
Com- pound	R ¹	R ²	R ³	Inhibition at 75 μM /% ^a
PPI-1 (76)	benzoyl	4-nitrophenyl	3-carboxy-4-hydroxyphenyl	<5
77	4-methyl-benzoyl	4-nitrophenyl	3-carboxy-4-hydroxyphenyl	66
78	picolinoyl	4-nitrophenyl	3-carboxy-4-hydroxyphenyl	>99
79	thiazol-2-yl	4-nitrophenyl	3-carboxy-4-hydroxyphenyl	65
80	benzoyl	1 <i>H</i> -benzo[d][1,2,3]triazol-5-yl	3-carboxy-4-hydroxyphenyl	95
81	benzoyl	1 <i>H</i> -indazol-6-yl	3-carboxy-4-hydroxyphenyl	71
82	benzoyl	1-methyl-1 <i>H</i> -benzo[d][1,2,3]triazol-5-yl	3-carboxy-4-hydroxyphenyl	70
83	benzoyl	isoquinolin-6-yl	3-carboxy-4-hydroxyphenyl	>99
84	benzoyl	4-aminophenyl	3-carboxy-4-hydroxyphenyl	84
85	benzoyl	4-nitrophenyl	(1,1'-biphenyl)-3-yl	84
86	benzoyl	4-nitrophenyl	3-phenylpropyl	77
Com- pound	Structure			Inhibition at 75 μM /% ^a
87				>99

^aThe experiment was performed by Lisa Hohnen as part of her Master thesis.

Results and discussion

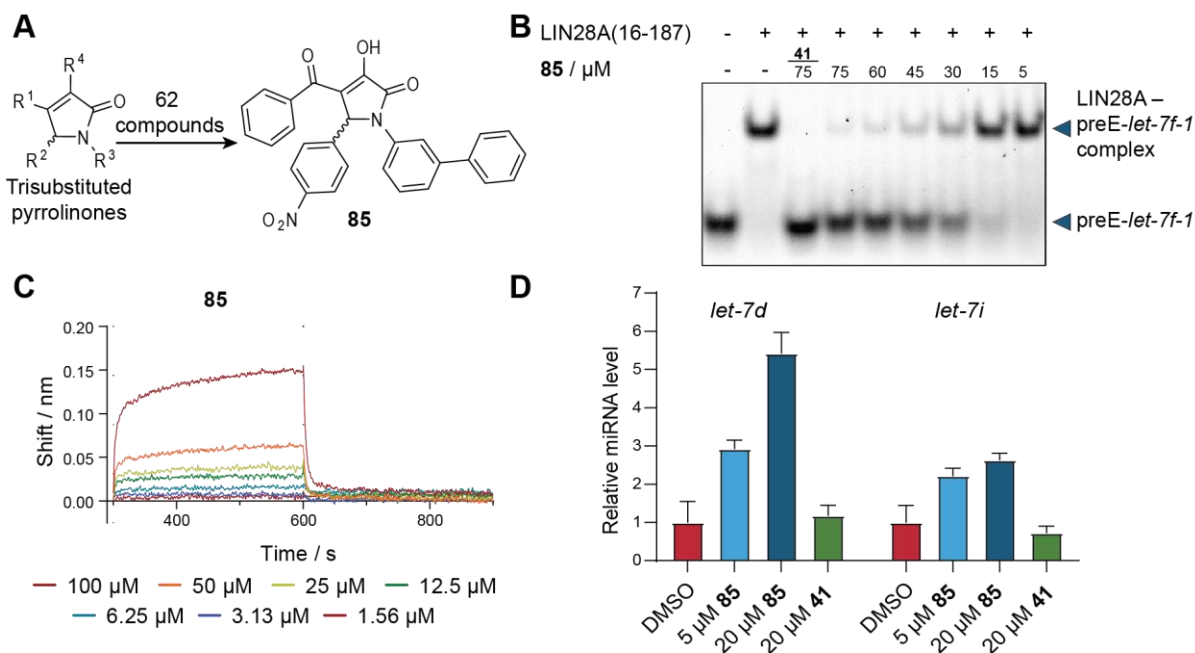


Figure 16: (A) Extended SAR evaluation of 62 trisubstituted pyrrolinones led to the identification of biphenyl-substituted compound **85** as a LIN28 inhibitor. (B) Dose-dependent EMSA of **85**. The experiment was performed by Lisa Hohnen as part of her Master thesis. (C) BLI of **85** binding to the LIN28A CSD. The data represents three independent replicates. (D) Changes of relative mature miRNA *let-7d* and *let-7i* levels upon treatment with **85** or **41** compared to DMSO measured by qPCR. The experiment was performed in three independent biological replicates. The error bars indicate the SD.

A qPCR assay performed in JAR cells measuring levels of mature *let-7d* and *let-7i* revealed a more than five-fold increase of *let-7d*, and a more than two-fold increase of *let-7i* after treatment with 20 μM **85** (Figure 16D). For these two *let-7* family members, **41** did not induce any significant change. Improved membrane permeability of **85** could possibly explain the significant increase of mature *let-7d* levels. However, LIN28-independent effects influencing mature *let-7* levels could not be excluded.

Table 17: Shift of melting temperature of LIN28A CSD induced by trisubstituted pyrrolinones.

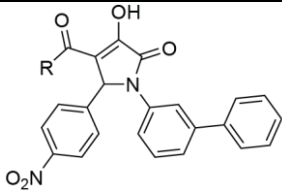
Compound (75 μM)	LIN28A CSD $\Delta T_m / ^\circ\text{C}^a$
41	1.75 ± 0.07
78	0.38 ± 0.06
80	0.85 ± 0.02
82	0.44 ± 0.09
83	1.15 ± 0.08
85R	1.90 ± 0.10
85S	1.88 ± 0.02

^aMeasured by Lisa Hohnen as part of her Master thesis. The experiment was performed in triplicates. The SD is indicated.

Results and discussion

A co-crystal structure of 14-3-3, an interacting peptide, and PPI-1 (**76**) revealed a metal-chelating mechanism of action involving the hydroxy group of the pyrrolinone core and the carbonyl oxygen at the 4-substituent. Chelation of a magnesium ion at the interaction site of the protein was described to benefit the potency of the compound instead of contributing to a pan-assay interference mechanism.²¹⁴ A metal-chelating mode of action is unlikely for LIN28 inhibition by trisubstituted pyrrolinones due to the observation that **87** was active against LIN28, although it was designed to act on 14-3-3 in a metal-independent mechanism.²¹⁴ Furthermore, **85** bound to the LIN28 CSD, which does not carry any metal ions, as shown by BLI and nanoDSF. Based on the findings that **85** was active in orthogonal biophysical and cellular assays, the effect of modifications of the benzoyl group was explored (Table 18).

Table 18: Analogs of **85** modified in the 4-position of the pyrrolinone core and their potency in EMSA.



Compound	R	Inhibition at 75 μ M /% ^a
88	cyclohexyl	49
89	cyclopropyl	<5
90	cyclobutyl	8
91	furan-2-yl	87
92	5-methylfuran-2-yl	83
93	1-methyl-1 <i>H</i> -pyrrol-2-yl	75
94	thiazol-2-yl	8
95	4-(trifluoromethyl)phenyl	40
96	4-fluoro-2-hydroxyphenyl	<5
97	4-(methylsulfonyl)phenyl	<5
98	3,4,-dimethoxyphenyl	<5
99	4-bromophenyl	73
100	4-methoxyphenyl	87
101	4-fluorophenyl	76
102	2-fluorophenyl	98
103	3-hydroxy-4-nitrophenyl	49

^aThe experiment was performed by Lisa Hohnen as part of her Master thesis.

In general, it seemed that five-membered heterocyclic substituents with hydrogen bond acceptors (**91-93**) or phenyl residues with hydrogen bond acceptors in *ortho*- or *para*-position (**99-102**) are beneficial for potency while cycloalkyls residues decreased LIN28 inhibition. The observed trends were generally supported by dose-dependent EMSAs (Figure S3). Rigidification of the biphenyl moiety was achieved by the formation of dibenzofuran

Results and discussion

substituents (Table 19). In theory, these molecules have a lower conformational entropy penalty when binding to a protein and carry an additional hydrogen bond acceptor. Overall, the dibenzofuran-3-yl substituted pyrrolinones displayed higher inhibitory activity than that of the dibenzofuran-2-yl substituted compounds. Dose-dependent EMSA validated **109** and **113** as the most potent small molecules of this series.

Six further rigidified spirocyclic pyrrolinones were inactive in EMSA and thus not evaluated further (Table 20). Based on the observation that pyrrolinones substituted at the 1-position of the core with biphenyl or dibenzofuranyl instead of a salicylic acid moiety were active, it would be interesting to see whether parallel modifications in the 4-position, beyond the scope in this work or modifications in the 5-position could increase potency. Relevant substituents in the 5-position would be those of compounds **80-84**, which switched the inactive PPI-1 (**76**) to inhibitors of LIN28. Nevertheless, this work showed that it is possible to exchange the salicylic acid of the identified trisubstituted pyrrolinones to aromatic groups without substantially losing *in vitro* potency while gaining activity *in cellulo*.

Table 19: Dibenzofuranyl substituted pyrrolinones and their potency against LIN28 in EMSA.

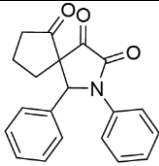
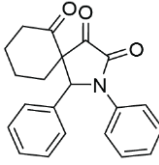
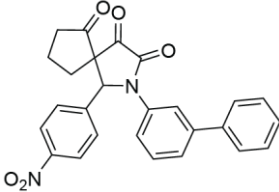
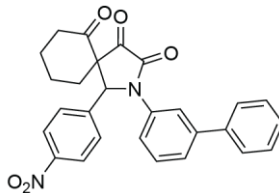
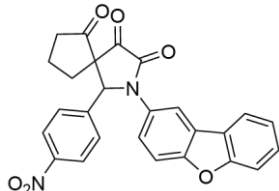
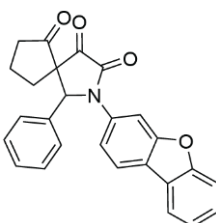
Compound	R	Inhibition at 75 μ M /% ^a
104	phenyl	94
105	4-bromophenyl	53
106	4-methoxyphenyl	74
107	4-fluorophenyl	60
108	furan-2-yl	90

Compound	R	Inhibition at 75 μ M /% ^a
109	phenyl	97
110	4-bromophenyl	86
111	4-methoxyphenyl	87
112	4-fluorophenyl	93
113	furan-2-yl	95

^aThe experiment was performed by Lisa Hohnen as part of her Master thesis.

Results and discussion

Table 20: Spirocyclic pyrrolinones and their potency in EMSA.

Compound	Structure	Inhibition at 75 μ M /% ^a
114		<5
115		<5
116		<5
117		<5
118		<5
119		<5

^aThe experiment was performed by Lisa Hohnen as part of her Master thesis.

4.1.3 Scaffold-based approach

Results from this section were published as “Spirocyclic Chromenopyrazole Inhibitors Disrupting the Interaction between the RNA-binding protein LIN28 and Let-7” and as “Chromenopyrazole–peptide conjugates as small-molecule based inhibitors disrupting the protein–RNA interaction of LIN28–let-7”.^{215,216}

Besides the identification of trisubstituted pyrrolinones as LIN28 inhibitors from a screening-based approach followed by SAR evaluation, reported LIN28 inhibitors were used as the starting point for structural modification and optimization efforts used in the scaffold-based approach. Although multiple LIN28 inhibitors were reported, most were only poorly validated or characterized for their mode of action and cellular potency. Two of the best-characterized compounds are the tetrahydroquinoline LI71 and the chromenopyrazole SB1301 (**3**).^{116,118} We found that LI71 could only be modified to a limited extent while retaining activity.²¹⁷ In contrast, SB1301 (**3**) harbors a chromenopyrazole scaffold that could be modified at multiple positions, and evaluated for the relevant SAR.

4.1.3.1 SAR of chromenopyrazole LIN28 inhibitors

The effect of modifications of SB1301 (**3**) in three different positions was explored (Table 21). Modifications of the carboxylic acid revealed that the exchange of the 4-carboxyphenyl to 3-carboxyphenyl (**120**) or 4-sulphoxyphenyl (**121**) was tolerated, while 2-carboxyphenyl (**122**) reduced activity by more than 50%. Removal of the carboxylic acid (**124**, **125**) resulted in a complete loss of activity, underlining its importance for the potency of chromenopyrazoles against LIN28. Modifications of R¹ primarily produced inactive molecules; only a piperidin-1-yl group (**129**) retained activity. Reduction of the nitro group (R²) to amine (**130**) reduced activity to 25% and removal of the nitro group led to a complete loss of activity (**131**).

Results and discussion

Table 21: Structures and inhibitory activities of chromenopyrazoles in EMSA.

Compound	R ¹	R ²	R ³	Inhibition at 75 μM /%
SB1301 (3) ^c	4-((benzyloxy)carbonyl) piperazin-1-yl	NO ₂	4-carboxyphenyl	100 ^a
SB-9 (120) ^c	4-((benzyloxy)carbonyl) piperazin-1-yl	NO ₂	3-carboxyphenyl	93 ^a
121	4-((benzyloxy)carbonyl) piperazin-1-yl	NO ₂	4-sulfoxyphenyl	98 ^a
122	4-((benzyloxy)carbonyl) piperazin-1-yl	NO ₂	2-carboxyphenyl	36 ^a
123	4-((benzyloxy)carbonyl) piperazin-1-yl	NO ₂	4-sulfoxyphenyl	98 ^a
SB-4 (124) ^c	4-((benzyloxy)carbonyl) piperazin-1-yl	NO ₂	phenyl	<5 ^{a,b}
SB-6 (125) ^c	4-((benzyloxy)carbonyl) piperazin-1-yl	NO ₂	benzyl	<5 ^{a,b}
126	F	NO ₂	4-carboxyphenyl	<5 ^{a,b}
127	morpholino	NO ₂	4-carboxyphenyl	<5 ^{a,b}
128	piperazin-1-yl	NO ₂	4-carboxyphenyl	<5 ^{a,b}
129	piperidin-1-yl	NO ₂	4-carboxyphenyl	95 ^a
130	4-((benzyloxy)carbonyl) piperazin-1-yl	NH ₂	4-carboxyphenyl	25 ^a
131	4-((benzyloxy)carbonyl) piperazin-1-yl	H	4-carboxyphenyl	<5 ^{a,b}

^aThe assay was performed by Lisa Hohnen as part of her Master thesis. ^bMeasured in EMSA as part of this thesis.

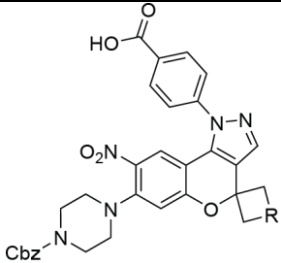
^cPreviously reported by Lim *et al.*¹¹⁶

The above described three modified positions were shown to be important for activity and only limited changes were allowed while retaining potency, so an additional position involving a spiroization strategy at the *gem*-methyl fragment was explored. Four spirochromenopyrazoles were assayed, in which the *gem*-dimethyl group was cyclized to four- (**132**), five- (**133**), or six-membered rings (**134**), as well as an *N*-Bn-piperidine (**135**). In theory, spirocyclic compounds are molecularly more drug-like than their non-spirocyclic counterparts owing to their high content of sp³-hybridized carbon atoms.^{218,219} Simultaneously, functional groups can potentially be locked in favorable positions by the rigid, three-dimensional spirocyclic scaffold

Results and discussion

with the potential to improve the molecules' potency, and its absorption, distribution, metabolism, and excretion (ADME), when used as a therapeutic drug.^{218,220} The inhibitory activity and IC₅₀ values of the four molecules were determined in EMSA, and the compounds were further evaluated for their stabilizing effect on the LIN28A CSD (Table 22, Figure 17). All investigated molecules were active in EMSA at 75 μM and **134** and **135** displayed a lower IC₅₀ than that of SB1301 (**3**), although the differences in the IC₅₀ values were marginal. Compound **133** was less active at 75 μM, which is in line with a higher IC₅₀ value, and a very low shift observed in nanoDSF. The compounds **132** and **135** stabilized the CSD to a similar extent as SB1301 (**3**), while **134** induced a higher temperature shift of 2.0 °C. Thus, the three molecules **132**, **134** and **135** seemed to be equally potent or even more active than SB1301 (**3**) in the biochemical assays.

Table 22: Structures of spirochromenopyrazoles and SB1301 (**3**) and their respective activities in EMSA and nanoDSF against LIN28A.



Compound	R	Inhibition at 75 μM /% ^a	IC ₅₀ / μM ^b	LIN28A CSD ΔT _m / °C ^c
SB1301 (3)	-	97	10 ± 7	1.3 ± 0.1
132	CH ₂	99	11 ± 3	1.1 ± 0.2
133	C ₂ H ₄	77	15 ± 3	0.3 ± 0.3
134	C ₃ H ₆	99	7 ± 3	2.0 ± 0.1
135	CH ₂ NBnCH ₂	100	5 ± 4	1.0 ± 0.1

^aMeasured by EMSA, normalized to free Cy3-*let-7*. The assay was performed by Lisa Hohnen as part of her Master thesis. ^bMeasured by EMSA and listed ± SD calculated from three replicates. The assay was performed by Lisa Hohnen as part of her Master thesis. ^cMeasured by nanoDSF and listed ± SD calculated from three replicates. The assay was performed by Lisa Hohnen as part of her Master thesis.

Results and discussion

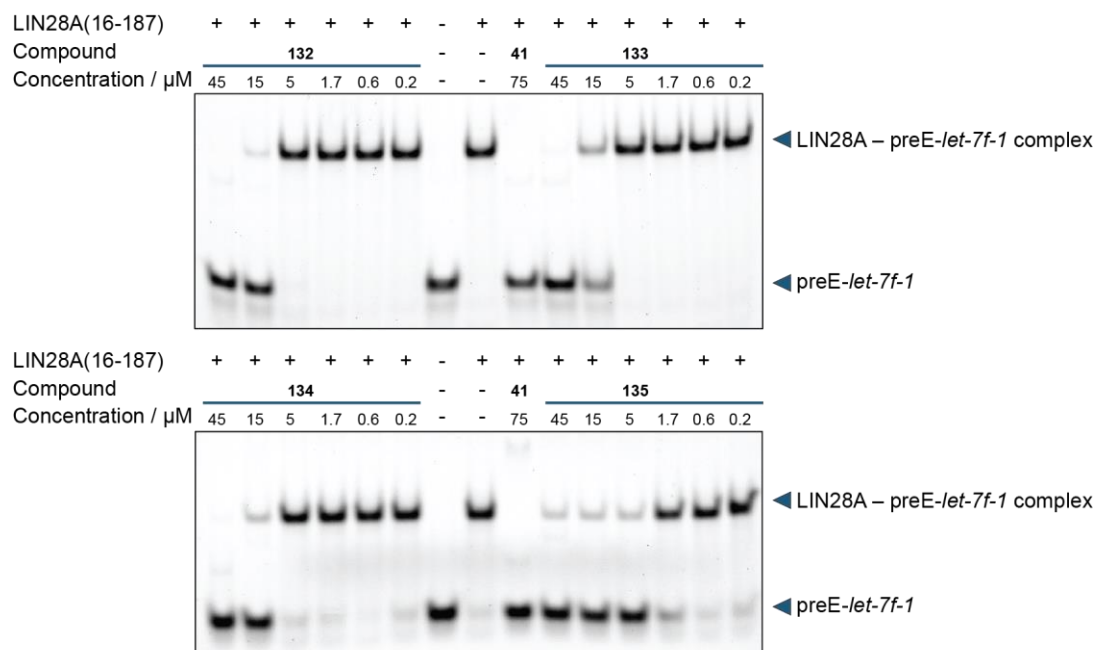


Figure 17: Dose-dependent EMSA of spirochromenopyrazoles **132**, **133**, **134** and **135**. The experiment was performed by Lisa Hohnen as part of her Master thesis.

4.1.3.2 Validation of spirochromenopyrazoles in orthogonal assays

The best-performing chromenopyrazoles, namely the spirochromenopyrazoles **134** and **135**, were further evaluated in orthogonal assays to verify their potency in comparison with that of SB1301 (**3**). BLI revealed that SB1301 (**3**) displayed a fast association and dissociation to the LIN28A CSD with a dose-dependent increase of the wavelength shift (Figure 18). The negative control **124**, that does not bear a carboxylic acid, induced a barely detectable signal. In comparison, **134** and **135** showed a higher signal with slower binding and unbinding kinetics than SB1301 (**3**). While **135** did not allow accurate fitting, the K_D of **134** was estimated to be $39 \pm 2 \mu\text{M}$.

Results and discussion

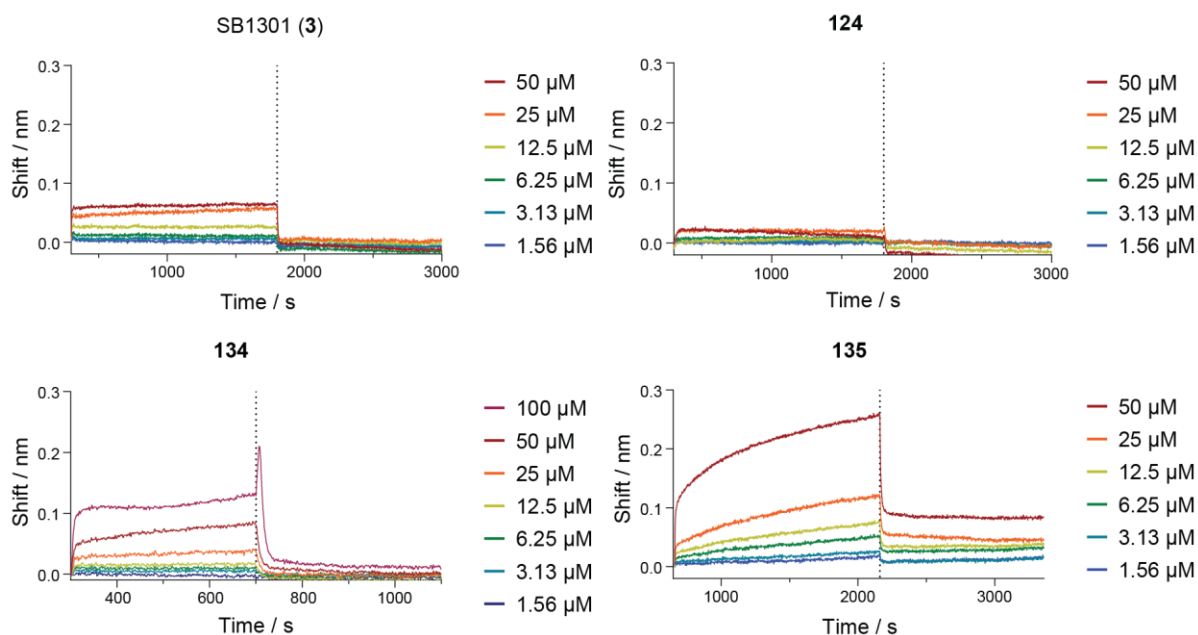


Figure 18: BLI of chromenopyrazoles SB1301 (**3**) and **124**, and spirochromenopyrazoles **134** and **135**. The data is representative for three replicates.

The inhibitory activity of **135** was additionally evaluated against LIN28 binding to mismatched double-stranded DNA, mimicking the active transcription bubbles to which LIN28 was reported to bind, leading to the recruitment of TET1 and epigenetic changes that regulate gene expression.³⁹ Compound **135** dose-dependently inhibited the DNA–LIN28 complex at low micromolar concentrations (Figure 19A). The binding mode of **135** to the LIN28A CSD was explored considering the hypothesis that spirocyclization is able to add interaction sites and lock functional groups in favorable positions. Molecular docking of **135** to the CSD predicted binding to the surface pocket of LIN28 at the positively charged site, in which part of the preE-*let-7* hairpin (5U-6A-14U-15A, numbers as in PDB 5UDZ) binds (Figure 19B).⁸⁸ The importance of the carboxylic acid and the nitro group observed in the SAR was underlined by hydrogen bond interactions to arginine 50 and valine 49, respectively (Figure 19C). The terminal benzene ring of the Cbz-group formed a cation- π interaction with arginine 120. Compound **135**, as compared to SB1301 (**3**), was predicted to form an additional hydrogen bond to glutamic acid residue 89 and hydrophobic interactions with lysine 45 via the spirocyclic moiety. To test if the added interactions of **135** to the CSD influenced binding and selectivity, the mutant protein in which glutamic acid 89 was mutated to alanine was expressed and purified (Figure S1B). EMSA revealed that SB1301 (**3**) was able to inhibit the interaction of the LIN28A CSD (E89A) with preE-*let-7*. At the same time, **135** completely lost its activity, potentially due to the exchange of the favorable hydrogen bond to glutamic acid 89 to an unfavorable interaction (Figure 19D). A more accurate experiment to visualize the interaction of LIN28 and a small molecule is the co-crystallization of the protein and small molecule,

followed by X-ray structure determination. Until now, structures of LIN28 without interacting RNA were only solved of human and *Xenopus tropicalis* Lin28B.⁸⁴ Thus, constructs of human LIN28B, *X. tropicalis* Lin28B, and a construct of LIN28A with domain borders corresponding that of LIN28B were purified and used to screen numerous crystallization conditions with and without **135** (Figure 19E, Figure S1C, D). Since the CSDs of LIN28A and LIN28B only differ in amino acids that are not involved in RNA-binding, it was hypothesized that both would similarly interact with *let-7* competitive compounds (Figure 19E). The only obtained protein crystals (**135** crystallized alone in several conditions) were those of LIN28B and *X. tropicalis* Lin28B at the reported conditions (Figure 19F).⁸⁴ Co-crystallization of LIN28B with **135** at these conditions did not lead to the incorporation of the compound, no additional electron density was detected. The larger crystals of human LIN28B were used for soaking of **135** (and **41**, and **85**). Soaking was performed for six hours, the maximum time that was possible before the crystals dissolved. However, X-ray measurements and structure determination did not show additional electron densities corresponding to the compounds, although resolutions of up to ~1.4 Å were achieved.

Soaking is likely hampered by the comparative large size of **135** relative to the CSD, since **135** carries ~7% of the molecular weight of the LIN28B CSD. During soaking, the compound needs to enter the crystal lattice, which is less likely with increasing size of the molecule. On top of that, the small molecules bind to a surface pocket of LIN28 instead of a deep pocket. The protein surface is often involved in crystal-contact formation, prohibiting simultaneous interaction of the protein surface with a compound. Thus, co-crystallization is, in general, the more promising approach for LIN28 with small molecules when compared to soaking, although it also did not succeed in this project since no favorable crystallization conditions were identified. Despite not being able to confirm the docking mode by X-ray crystallography, it would be interesting to evaluate molecules with H-bond acceptors in a similar position as the *N*-Bn substituent in **135** to potentially further increase the potency.

Results and discussion

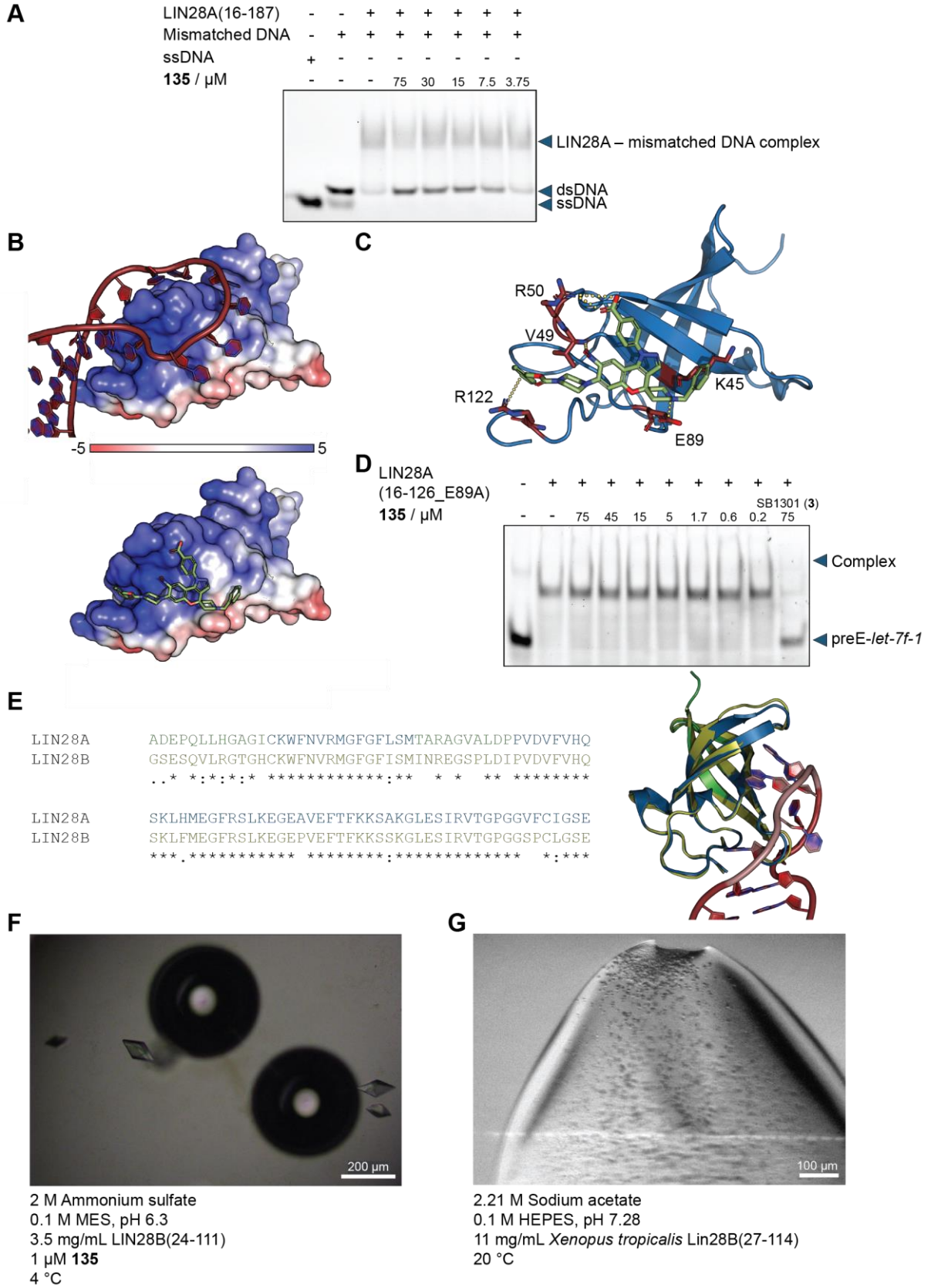


Figure 19: Validation of **135** binding to the LIN28A CSD. (A) EMSA testing binding of LIN28 to mismatched dsDNA and inhibition of the complex by **135**. The data is representative from three replicates. (B) Charge surface representation of LIN28A CSD in complex with preE-*let-7*, depicted in red (PDB 5UDZ, top)⁸⁸ and docking of **135**

Results and discussion

(green) to the LIN28 CSD (bottom). The docking was performed by Georg L. Goebel. (C) Cartoon representation of the LIN28A CSD (PDB 5UDZ, blue) in complex with **135** (green) docked into the structure. Important interacting amino acids are shown in red. The docking was performed by Georg L. Goebel. (D) EMSA testing the effect of **135** and SB1301 (**3**) on LIN28A(E89A) binding to preE-*let-7*. The data is representative for three replicates. (E) Sequence (left) and structure alignment of the part with the solved crystal structure of LIN28B (yellow, PDB 4A4I)⁸⁴ with the respective sequence of LIN28A (blue, PDB 3TS0).³² The asterisks highlight identical amino acids. Less conserved regions of LIN28A compared to LIN28B are shown in green. The pre-miRNA is depicted in red. (F) Crystals of LIN28B(24-111). The measurement revealed that **135** was not present in the crystal structure. (G) Crystals of *X. tropicalis* LIN28B(27-114).

4.1.3.3 Evaluation of chromenopyrazoles as LIN28 inhibitors in cellular assays

As a next step, the effect of **134** and **135** was evaluated in cellular assays. Based on the reported influence of LIN28 on histone methylation in mouse pluripotent stem cells, we measured histone methylation upon compound treatment by western blot (Figure 20A).²⁹ No changes in histone methylation levels were observed, presumably because of different histone methylation levels between mouse pluripotent stem cells and JAR cells. *Let-7*-family members *let-7a* and *let-7g* were upregulated upon treatment with **135**, with a stronger effect than with SB1301 (**3**), supporting the hypothesis that the spirocyclic moiety improves potency (Figure 20B). The *let-7* target genes MYC and Ras were downregulated by ~50% and ~25% after treatment with 20 μ M **135**, respectively (Figure 20C, D). Additionally, **134** and **135** completely inhibited cell proliferation of LIN28 expressing JAR cells at concentrations of 50 μ M and 25 μ M, respectively, while cells were still growing similar to DMSO treated cells after treatment with 25 μ M SB1301 (**3**) and at a decreased rate when 50 μ M was used (Figure 20E-H). Overall, biochemical and cellular assays suggest that the spirocyclization strategy led to more potent three-dimensional compounds that improved the selectivity of chromenopyrazoles. On top of that, the spirocyclic fragment offers an amenable position for linker attachment for the development of potential bifunctional molecules in the future.

Results and discussion

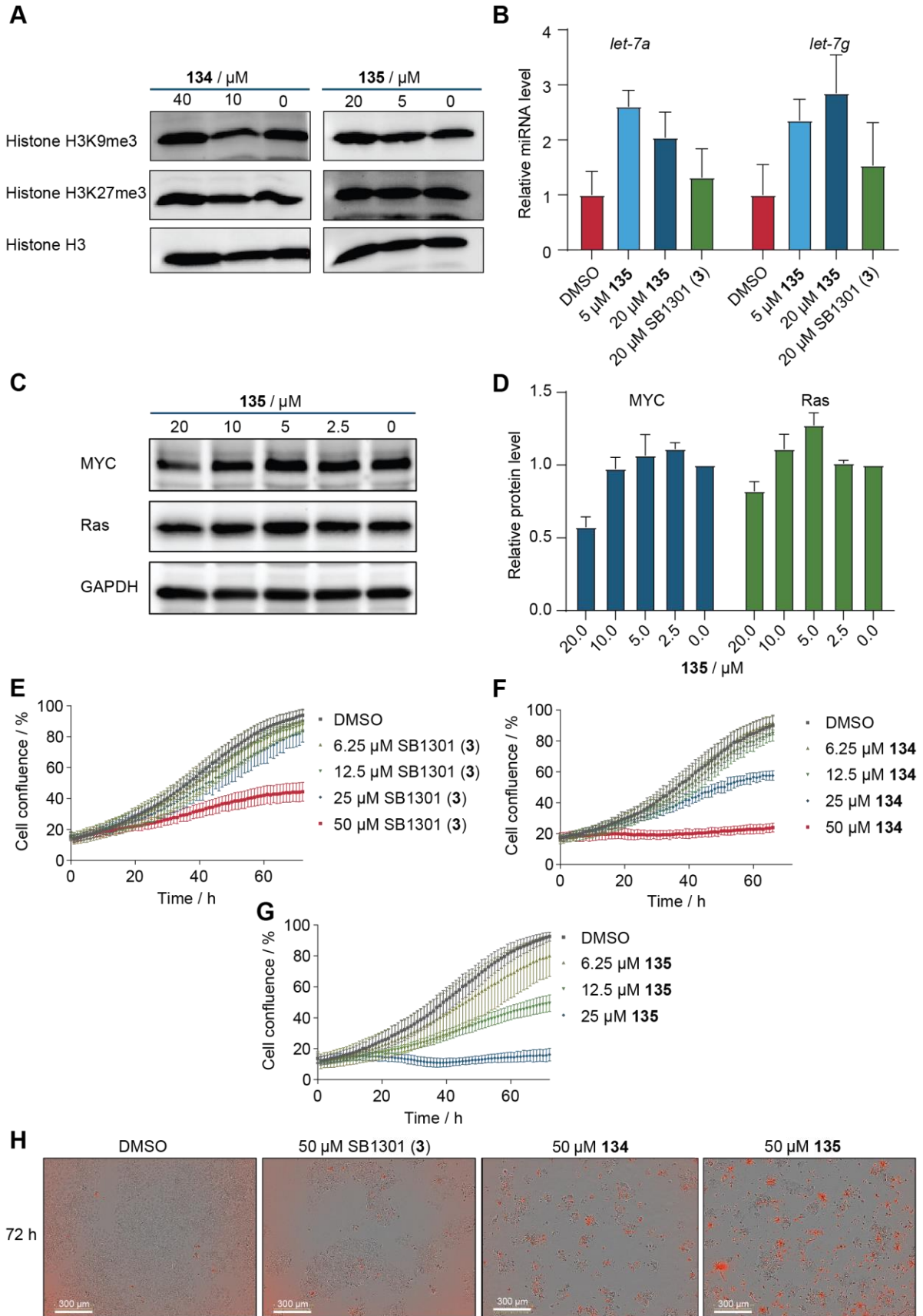


Figure 20: Cellular assays evaluating spirochromenopyrazoles. (A) Western blot measuring histone methylation in JAR cells upon treatment with compounds. The data is representative from two biological replicates. (B) Relative

Results and discussion

levels of mature miRNA *let-7a* and *let-7g* upon treatment with **135** or SB1301 (**3**). The data was calculated from three biological replicates. (C) Western blot measuring levels of *let-7* target proteins MYC and Ras after treatment with **135**. The data is representative from two replicates. The experiment was performed by Lisa Hohnen as part of her Master thesis. (D) Quantification of protein levels as shown in (C) normalized to GAPDH. The data is averaged from two biological replicates. The experiment was performed by Lisa Hohnen as part of her Master thesis. (E) Change of cell confluence of JAR cells upon treatment with SB1301 (**3**) during 72 h. The data is averaged from three replicates and two images each. The experiment was performed by Lisa Hohnen as part of her Master thesis. (F) Change of cell confluence of JAR cells upon treatment with **134** during 72 h. The data is averaged from three replicates and two images each. (G) Change of cell confluence of JAR cells upon treatment with **135** during 72 h. The data is averaged from three replicates and two images each. The experiment was performed by Lisa Hohnen as part of her Master thesis. (H) Microscope images of JAR cells after 72 h treatment with compounds or DMSO. Apoptotic cells are stained with propidium iodide. The images of cells treated with DMSO, SB1301 (**3**), and **135** were recorded by Lisa Hohnen as part of her Master thesis. (B), (D-G) The error bars indicate the SD.

4.1.4 Conclusions from the screening- and scaffold-based approaches

Using the screening- and scaffold-based approaches, **41** was identified as a new LIN28 inhibitor. The SAR based on the trisubstituted pyrrolinone scaffold of **41** and the chromenopyrazole scaffold of the reported inhibitor SB1301 (**3**) was explored. In both molecules, the presence and position of a carboxylic acid proved to be essential for potency. A similar observation was made for the CSD-binding tetrahydroquinoline LI71. It was shown by our study that LI71 required to carry a carboxylic acid to be active against LIN28.²¹⁷ The negatively charged substituent might be important to mimic the charge of the RNA backbone and interact with the positively charged *let-7* binding site of LIN28. In light of these findings, we identified compound **85** in this project, that lacked a carboxylic acid but retained activity against LIN28. Although the potency of **85** was not significantly higher in comparison with that of the carboxylic acid-containing molecules, it showed improved cellular activity. This is likely due to an improved cell permeability originating from the exchange of the salicylic acid by a biphenyl substituent. However, this hypothesis needs to be further supported by experimental data on membrane permeability.

The fact that all LIN28 inhibitors reported to date did not show nanomolar potency hampers the development of probes or drugs based on the concept of LIN28–*let-7* interaction disruption. Challenges in improving the binding affinity of the small -molecule inhibitors lie in the competition with the high-affinity natural ligand *let-7* miRNA and the absence of a deep, and well-defined pocket that could be utilized for small-molecule binding. The interaction of LIN28 and *let-7* involves multiple surface interactions, comparable to PPIs where only shallow pockets are present. A feasible approach could be the linkage of a CSD-binding and a ZKD-targeting compound to form a bifunctional molecule that cooperatively targets both domains simultaneously. This could possibly increase the affinity of the molecule to the protein and add specificity for LIN28, which is the only human protein consisting of both CSD and ZKD.

4.2 Discovery and biochemical evaluation of modulators of the RNase L–OAS pathway

Parts of this section were done in cooperation with Philipp Lampe, COMAS, or part of the Master thesis of Neele Haacke. The contributions are indicated below each Figure or Table.

The OAS–RNase L antiviral pathway is a central regulator of the innate immune response, and as such an interesting target for chemical modulators that activate or inhibit RNase L or OAS. RNase L and OAS-modulating compounds could be either developed into broad-spectrum antiviral drugs, used to study or treat autoimmune diseases, or employed as molecular tools. Recently, the development of RIBOTACs, bifunctional molecules recruiting RNase L for targeted degradation of ligandable RNAs, revealed the application potential of RNase L binders beyond the classical small-molecule scope. Novel RNase L modulators and binders could broaden the scope of the approach. This work used screening- and scaffold-based approaches in search for new RNase L activators, inhibitors and binders, as well as small-molecule activators of OAS1.

4.2.1 Purification of recombinant RNase L

To develop RNase L assays, full-length RNase L was first recombinantly expressed and purified from *E. coli*. The purification strategy included immobilized nickel affinity chromatography (Figure 21A), cleavage of the His₆-tag, reverse nickel affinity chromatography (Figure 21B), and final gel filtration (Figure 21C). Although the expression level of RNase L was not very high, and protein precipitated during dialysis, the protein was relatively pure after two immobilized nickel affinity chromatography columns, and sufficient purity was obtained after gel filtration. The second peak of the gel filtration was combined and used for RNase L-based assays.

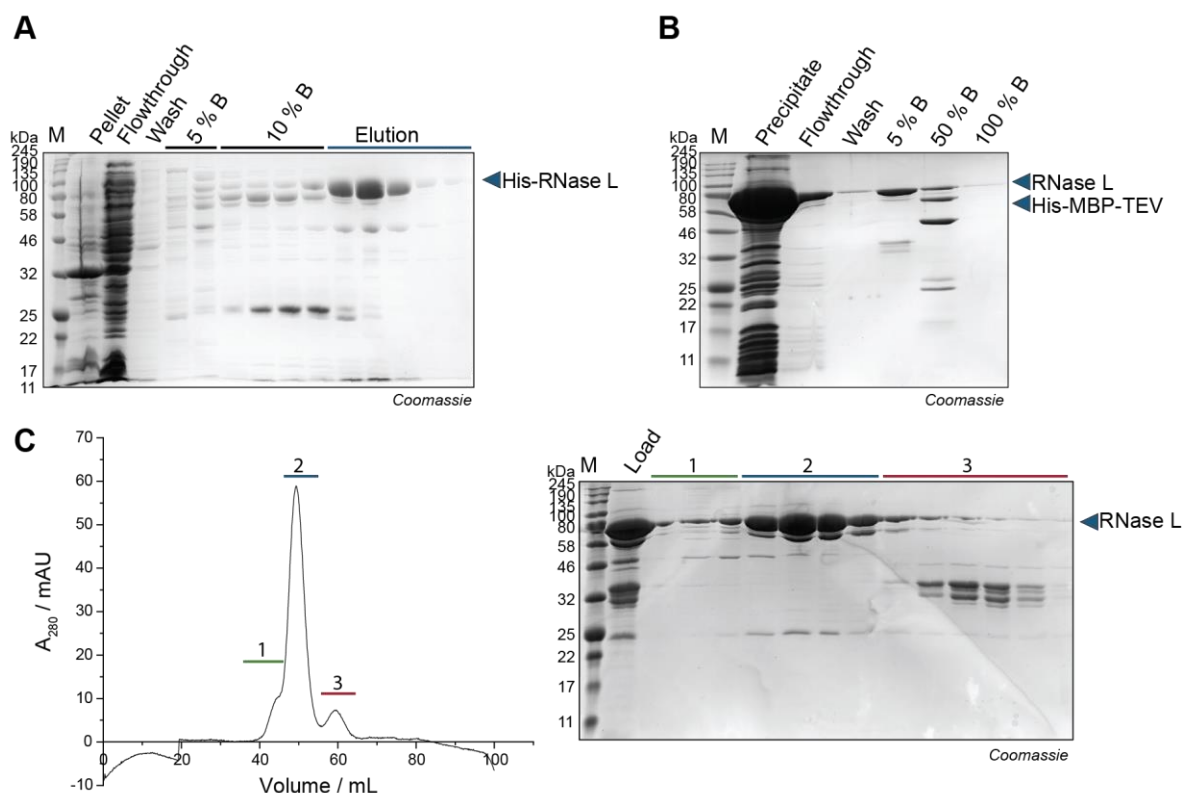


Figure 21: Purification of RNase L from *E. coli*. (A) SDS-PAGE of immobilized nickel affinity chromatography column. (B) SDS-PAGE of reverse immobilized nickel affinity chromatography column. (C) Chromatogram and SDS-PAGE of gel filtration. In the chromatogram and SDS-PAGE, the void-volume peak is labeled with 1, the main RNase L-containing peak is labeled with 2 and a third peak is labeled with 3.

4.2.2 Discovery of RNase L activators using a screening-based approach

Results from this section were published as “Small-molecule screening of ribonuclease L binders for RNA degradation”.²²¹

Activators of RNase induce the antiviral 2'-5'A-mediated decay pathway leading to a global translational arrest, an antiviral state of the cell, and eventually apoptosis. As such, they could be used as antiviral agents working similarly to the natural activator 2'-5'A. Furthermore, such as small molecule C1-3 (**24**), they could be used as building blocks to develop a new generation of RIBOTACs. Currently, the most potent known small-molecule RNase L activators are less than 10,000-fold active as 2'-5'A judged by *in vitro* EC_{50} values, underlining the need for the discovery of novel RNase L activators.¹⁵⁷ In this work, a screening was performed to identify RNase L activators using a FRET assay. Further, analogs of C1-3 (**24**) were studied for their ability to activate RNase L.

4.2.2.1 Optimization of a FRET assay to detect RNase L activators

In order to screen for small-molecule RNase L activators, the recombinantly purified RNase L was used in a FRET assay. Activation of RNase L leads to its dimerization and cleavage of RNA, preferably after UU dinucleotides. First, an RNA probe derived from respiratory syncytial virus genomic RNA that contained multiple RNase L cleavage sites was used. The RNA-probe was labeled at both ends with a FAM-fluorophore and a quencher, as used in reported methods (Figure 22A, B).^{157,169,209} The fluorescence is quenched in the intact probe. Cleavage of the RNA by RNase L increases the distance between the fluorophore and quencher, resulting in an increase of the fluorescent signal. The natural RNase L activator 2'-5'A, kindly provided by Prof. Robert H. Silverman's group, was used as a positive control. The corresponding LC-MS analysis of the crude 2'-5'A mixture enzymatically synthesized from 4 mM ATP is shown in Figure S4 and was used to calculate the concentration of active, trimeric 2'-5'A in the mixture. Later, 2'-5'A was also produced during this work (see 4.2.7.2). Titration of 2'-5'A in the FRET assay resulted in a dose-dependent fluorescence signal increase (Figure 22E). The fluorophore was then exchanged to Alexa 647 to reduce the number of false-positive, autofluorescent hits, which interfere less with red-shifted fluorophores (Figure 22C).²²² However, background fluorescence occurred even without or with very low concentrations of 2'-5' A (Figure 22F). Thus, the RNA probe was shortened from 33 to 12 bases to allow more efficient quenching (Figure 22D), and the used RNase concentration was reduced. These optimizations led to a very low background fluorescence, an improvement of the signal-to-noise ratio by more than five-fold compared to the FAM-labeled probe and more than ten-fold compared to the Alexa-647-labeled 33-mer RNA, and a stable signal over at least 180 minutes (Figure 22G).

The determined EC_{50} was 0.1 nM, which is comparable to the reported value of 0.5 nM.¹⁵⁷ While compound fluorescence of reported RNase L activators C1 (**22**), C2 (**23**), and C1-3 (**24**) was observed during measurements without RNase L or RNA probe in the FAM-channel, no such signal was detected in the fluorescence range of the Alexa 647. This supports the hypothesis that compounds interfere less with red-shifted dyes.²²² Taken together, our robust FRET assay showed a high signal-to-noise ratio and a stable signal, and an expected EC_{50} value for positive control 2'-5'A.

Results and discussion

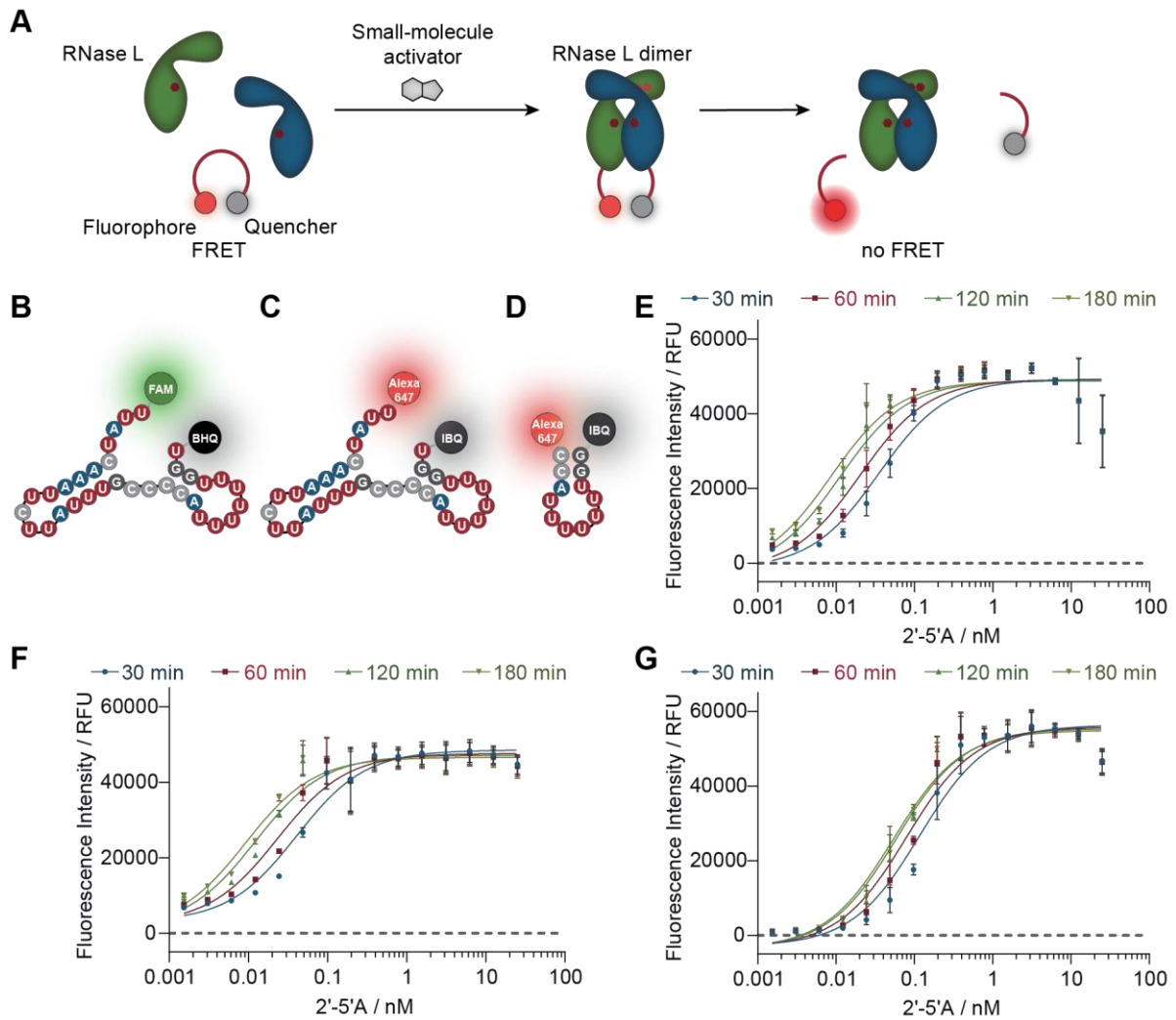


Figure 22: FRET assay for the detection of RNase L activators. (A) Schematic representation of the assay principle. RNase L cleaves a small RNA probe upon activation resulting in a fluorescent signal. (B) The predicted fold of 33-mer FRET probe labeled with FAM. The predicted fold of 33-mer FRET probe labeled with Alexa 647. The predicted fold of the short 12-mer FRET probe labeled with Alexa 647. RNA-folds were predicted using the *RNAfold* Server (<http://rna.tbi.univie.ac.at>, opened on 19.06.2023). (E) Increase of fluorescence intensity upon incubation of RNase L with 2'-5'A and the FAM-labeled FRET probe. (F) Dose-dependent increase of fluorescence upon incubation of RNase L with 2'-5'A and the Alexa 647-labeled 33-mer FRET probe. (G) FRET assay using the 12-mer Alexa 647 FRET probe, RNase L, and natural activator 2'-5'A. The FRET assays were performed in triplicates. The error bars indicate the SD.

4.2.2.2 Small-molecule screening

The optimized assay was reformatted to 1536-well plates, and the concentrations of RNase L and RNA were further reduced to allow higher screening efficiency. Approximately 240,000 molecules were initially screened at a single dose of 30 μ M. The 2'-5'A (0.5 nM) served as the positive control and samples without 2'-5'A were used as a negative control, resulting in a Z'-factor of 0.62. The 439 hits that induced fluorescence by at least 5% were additionally tested in a counter assay without the target RNase to remove molecules whose fluorescence

Results and discussion

increase was not caused by RNase L-mediated RNA cleavage. A total of 62 hit molecules with at least twofold induction in the assay with RNase L compared to the counter assay and at least 10% induction of RNase L were identified as hits, which translated to an extremely low hit rate of less than 0.03% (Figure 23A). Interestingly, diphenylmethanimine **159** induced a 25-fold higher signal when assayed with RNase L than without enzyme, and its analog **160** was also identified as a hit. However, the latter small molecule was autofluorescent as it showed a 150% fluorescence signal in the counter assay. The hit molecules were evaluated in dose-response FRET, and 32 molecules were selected for further evaluation in orthogonal assays based on their dose-response activity and inspection of their structural features (Figure 23B, Figure 24A). The compounds were then re-evaluated in the optimized assay without reduced probe concentration, which in theory, reduced interference of fluorescent compounds. The hit molecules were tested at a concentration of 130 μM to avoid missing weak activators, the same concentration that was used to evaluate RNase L activator C1-3 (**24**) in the reported study (Figure 24B).¹⁶⁹ The compounds with the highest induction were assayed in dose-response and compared to the fluorescence of the molecules in buffer (Figure S5). All three compounds, **138**, **154**, and **157** seemed autofluorescent at the evaluated conditions.

Results and discussion

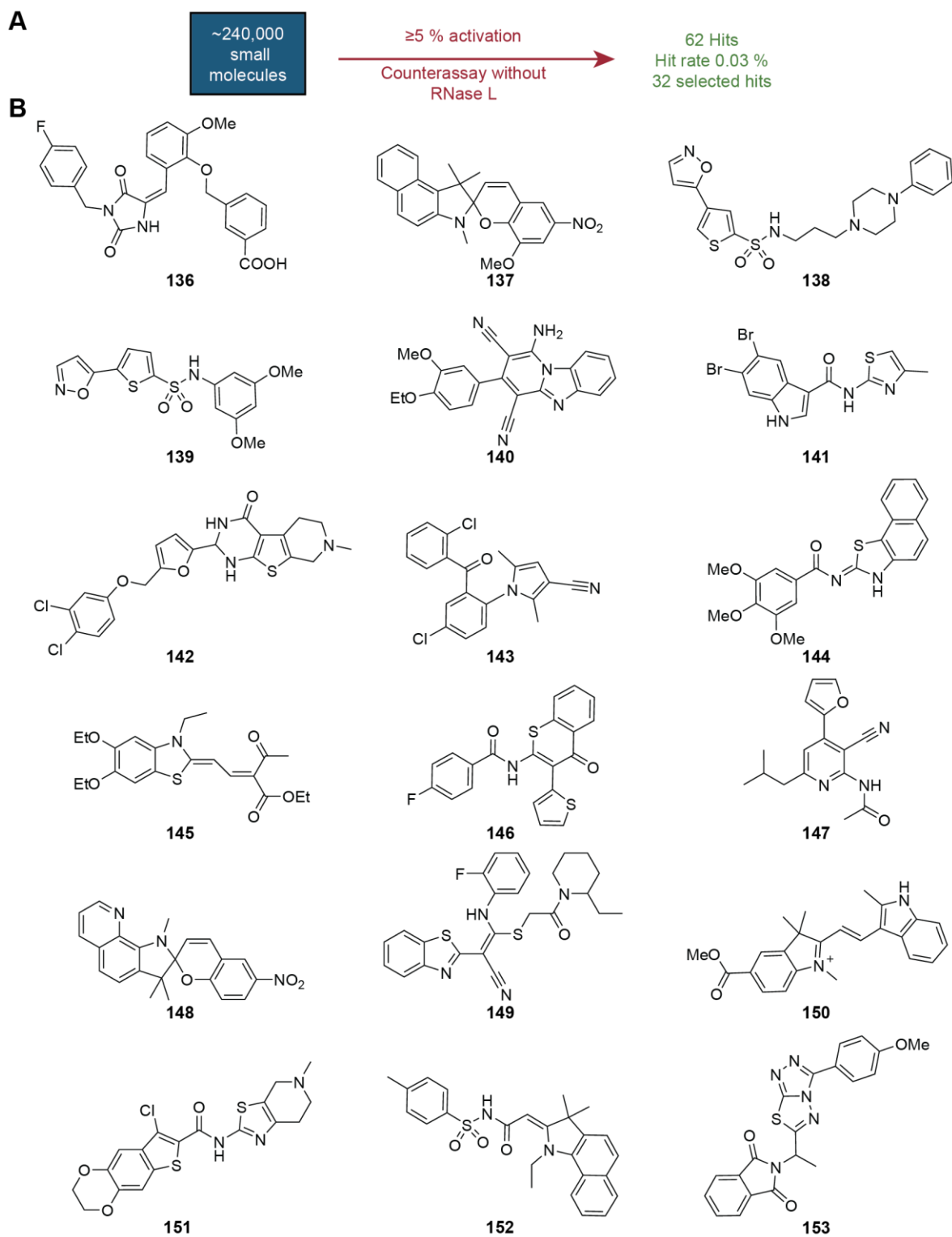


Figure 23: RNase L activator screening. The screening was performed by Dr. Philipp Lampe, COMAS. (A) Summarizing overview of the screening. (B) Structures 18 of 32 selected hits. The remaining compounds are shown in Figure 24.

Results and discussion

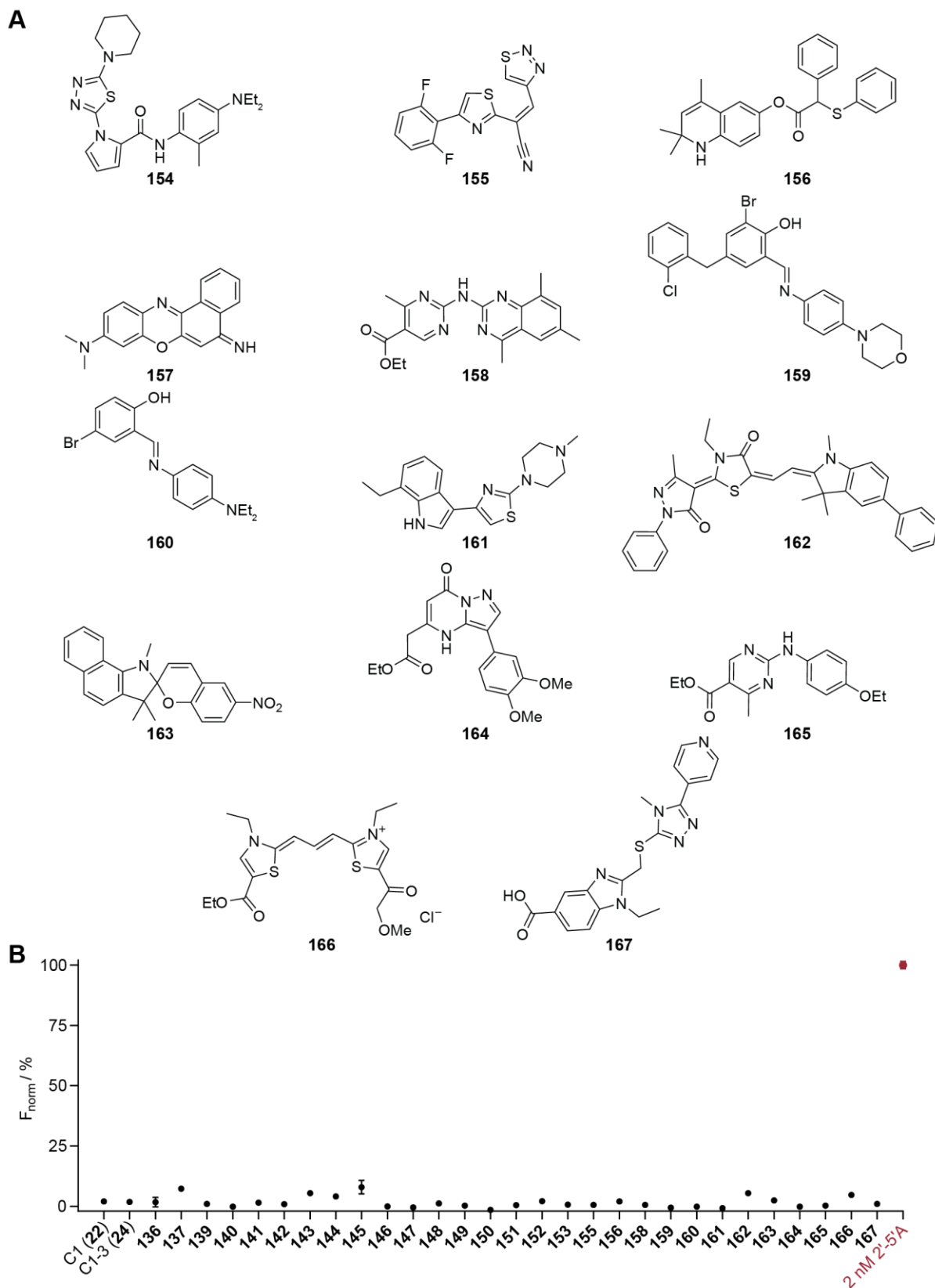


Figure 24: (A) Structures 14 of 32 selected hits. The remaining compounds are shown in Figure 23. (B) Normalized fluorescence: induced by selected hits and reported RNase L activators, measured at 130 μM . The experiment was performed in triplicates. The error bars indicate the SD. The assay was performed by Neele Haacke as part of her Master thesis.

4.2.2.3 Orthogonal assays for hit validation

The molecules were evaluated in orthogonal assays to verify if their activity could be attributed to autofluorescence or if they were able to activate RNase L. First, a fluorescently labeled, linear RNA probe was designed to contain a defined RNase L cleavage site (Figure 25A). RNase L was incubated with the positive control 2'-5'A, which dose-dependently induced RNase L activation and thus RNA cleavage. The cleaved RNA was then separated from the full-length probe by denaturing PAGE (Figure 25B). An EC₅₀ of approximately 0.1 nM was observed, consistently with the value from the FRET assay. The 32 screening hit molecules were evaluated in the RNA cleavage assay (Figure 25C). While 2 nM 2'-5'A activated RNase L to cleave the RNA-probe to near completeness, the compounds only induced cleavage of less than 6% of 2'-5'A, despite used at a high concentration of 130 μM. The small molecules **166** and **167** were fluorescent in the Cy3-channel. While **166**, structurally similar to the Cy3-dye, did not migrate through the gel but remained in the well, small molecule **167** showed a migration pattern comparable to that of the cleaved RNA. The intact RNA intensity was very similar to that of the control without an activator. Thus, induction of RNA cleavage by **167** was excluded. Then, the compounds were evaluated for their ability to stabilize RNase L in a thermal shift assay (Table 23). 2'-5'A shifted the melting temperature of RNase L by 2.80 °C, while most of the small molecules did significantly stabilize RNase L. The highest shift of 0.93 °C was observed with sulfonamide **152**, a stronger stabilization than induced by C1 (**22**) and C1-3 (**24**). Additionally, **152** was shown to induce apoptosis in cellular assays, which could be an effect of RNase L activation or other cellular pathways.²²¹

Detection of RNase L dimerization was further considered as a secondary assay, since dimerization is necessary for RNase L activity. Mass photometry, which allows the determination of the protein size in buffer under non-denaturing conditions, is a useful method for the detection of protein dimerization in this case. While RNase L dimerization was observed upon the addition of 2'-5'A in the presence of ATP (Figure 26A, B), none of the hit molecules was able to induce measurable dimerization. It is noteworthy that in the sample with 2'-5'A, only very few particles corresponding to higher-order oligomers were observed, which contrasted to a study reporting that 2'-5'A induces the formation of high-order complexes of RNase L, which was presumed to be the active form of the protein.¹³³

Results and discussion

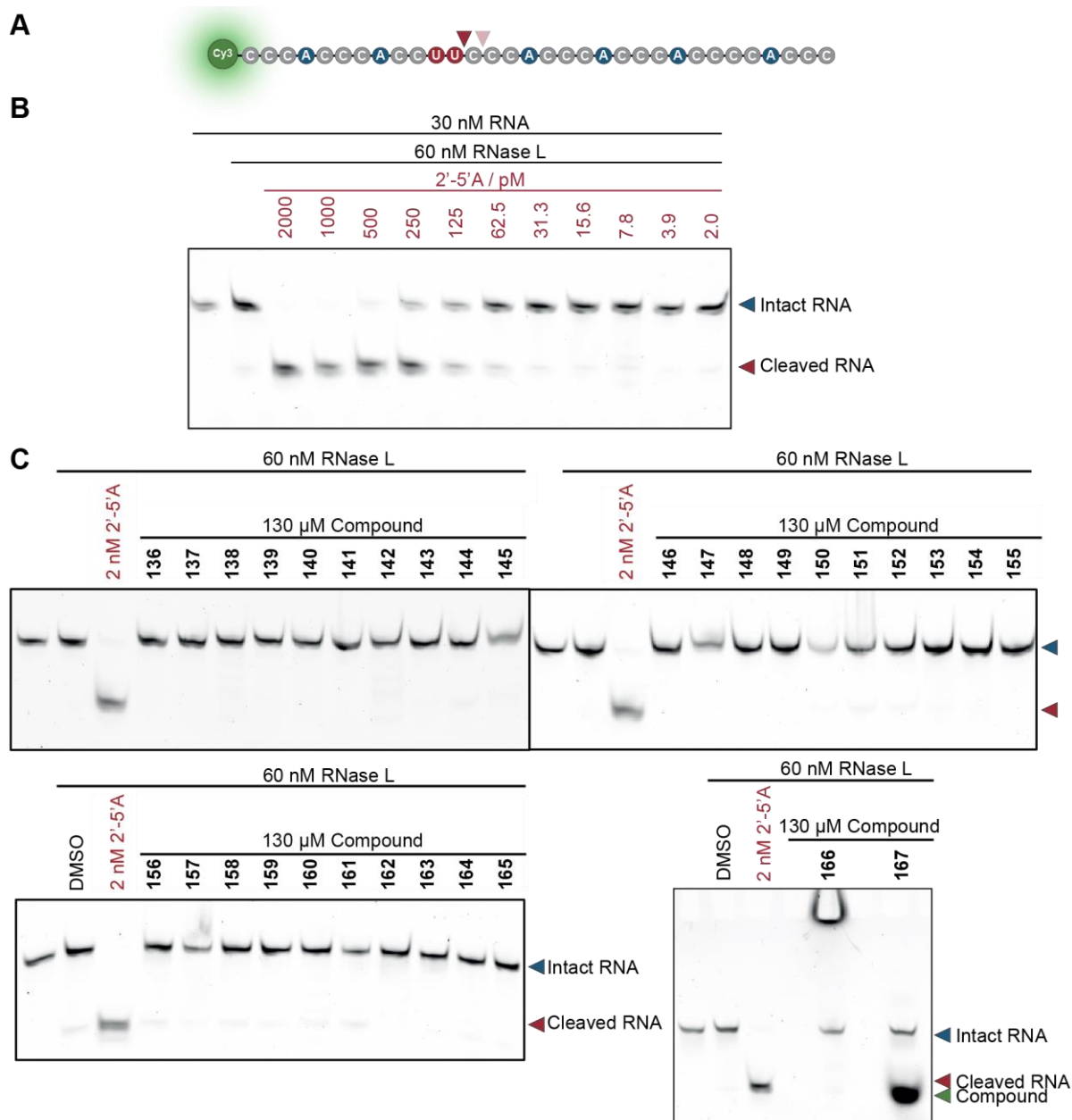


Figure 25: RNA-cleavage assay. (A) Cy-3-labeled linear RNA probe containing a central RNase L cleavage site, indicated by the red arrows. (B) Titration of 2'-5'A in gel-based RNA-cleavage assay. The blue arrow indicates the RNA probe and the red arrow indicates the cleaved RNA. The assay was performed by Neele Haacke as part of her Master thesis. (C) Evaluation of screening hits in RNA-cleavage assay. The blue arrow indicates the RNA probe, and the red arrow indicates the cleaved RNA. The green arrow indicates a fluorescent compound. The assay was performed by Neele Haacke as part of her Master thesis.

In general, only very few hits were identified from the RNase L activator screening. Among the identified hits were compounds of fluorophore structures, Michael-acceptor-containing molecules, and aryl-sulfonamides that are potential PAINS.²²³ On top of that, the extremely low hit rate of the screening indicated that RNase L is a challenging target when it comes to the search for activators and suggested that commercially available molecule libraries are not

Results and discussion

feasible for the discovery of RNase L-activating molecules. Potentially, molecules covering a new chemical space could prove to be useful to activate RNase L in the future. Nevertheless, compound **152** was shown to stabilize RNase L and is thus a possible binder which could be a useful tool compound for the design and construction of bifunctional RIBOTACs.

Table 23: Shift of melting temperature of RNase L induced by screening hits measured by nanoDSF.

Compound (60 μ M)	$\Delta T_m / ^\circ\text{C}^b$
2'-5'A	2.80 ± 0.08^a
C1 (22)	0.63 ± 0.05
C1-3 (24)	0.47 ± 0.08
138	0.47 ± 0.05
142	0.53 ± 0.05
144	0.80 ± 0.00
150	0.77 ± 0.09
151	0.13 ± 0.05
152	0.93 ± 0.05
154	0.60 ± 0.08
159	-0.50 ± 0.08
161	0.50 ± 0.00
163	0.13 ± 0.12
164	0.13 ± 0.05
166	0.00 ± 0.08

^aMeasured at 1.75 μ M. ^bThe experiment was performed in triplicates. The error values indicate the SD. The assay was performed by Neele Haacke as part of her Master thesis.

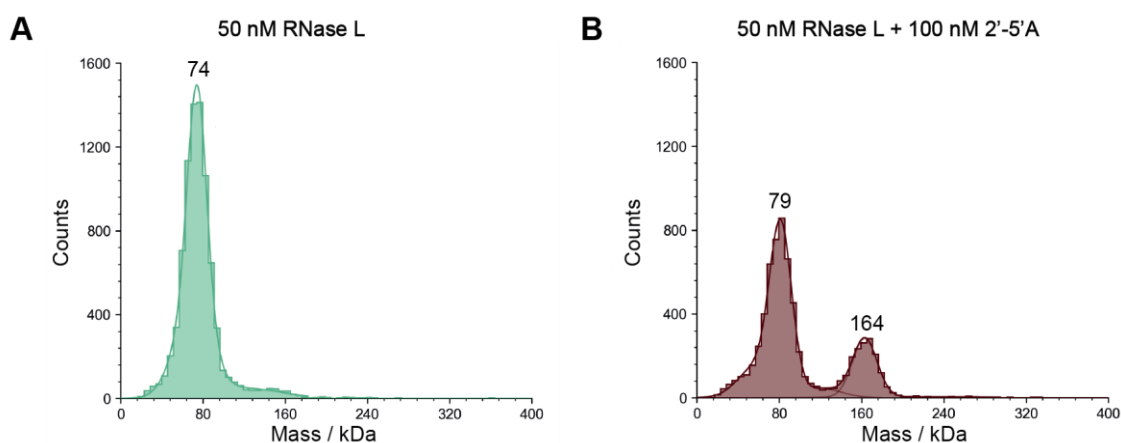


Figure 26: Mass photometry measurement of (A) RNase L and (B) RNase L with 2'-5'A. Representative results from three replicates.

4.2.3 Evaluation of 2-aminothiophenes as RNase L activators

Results from this section were published as “Synthesis and evaluation of RNase L-binding 2-aminothiophenes as anticancer agents”.²²⁴

When screening for RNase L activators, Silverman and colleagues identified the first generation of such activators in the format of 2-aminothiophene C1 (**22**) and thienopyrimidone C2 (**23**) via a FAM-based FRET assay.¹⁵⁷ Disney and colleagues applied the same assay to evaluate the SAR of both compound classes. They reported that C2 (**23**) and its analogs did not show robust RNase L-activating potency. C1 (**22**) and its derivative C1-3 (**24**) showed 24% and 48% of the fluorescence induced by 2'-5'A, respectively.¹⁶⁹ Consequently, the 2-aminothiophene scaffold was chosen for further SAR evaluation in this project. The 2-aminothiophenes modified at the 5-substituent were evaluated using the optimized FRET assay with the Alexa 647-labeled 12-mer RNA probe and a thermal shift assay (Table 24, Table 25). Additionally, the 2-aminothiophenes were modified at the 2-position and analyzed by nanoDSF and FRET (Table 26).

Table 24: Structures of aminothiophenes, normalized induced fluorescence (F_{norm}) measured by FRET, and induced shifts in melting temperatures of RNase L.

Compound	R	F_{norm} / % ^d	ΔT_m / °C ^d
2'-5'A	not applicable	100.0 ± 5.5 ^b	2.80 ± 0.08 ^c
C1 (22)	3-OH	0.2 ± 1.2 ^a	0.50 ± 0.08
C1-3 (24)	4-OMe, 3-OH	1.5 ± 0.6 ^a	0.63 ± 0.05
C1-4 (168)	3-OMe, 4-OH	0.3 ± 0.9 ^a	-1.33 ± 0.37
169	3,4-(OH) ₂	-0.3 ± 0.9 ^a	-0.13 ± 0.12
170	H	0.2 ± 0.7 ^a	0.80 ± 0.08
171	4-OMe	0.5 ± 0.5 ^a	-0.07 ± 0.25
172	3-OH, 4-NO ₂	1.0 ± 0.6 ^a	0.43 ± 0.48
173	3-OH, 4-Br	1.7 ± 0.2 ^a	0.27 ± 0.05
174	4-COOH	1.6 ± 0.3 ^a	0.30 ± 0.08
175	3-COOH	0.9 ± 0.7 ^a	0.23 ± 0.09
176	4-CF ₃	0.1 ± 1.6 ^a	0.80 ± 0.08
177	3-CN, 4-F	0.9 ± 0.5 ^a	0.83 ± 0.29
178	2,5-(OMe) ₂	1.0 ± 1.0 ^a	0.47 ± 0.05
179	2-OH	0.9 ± 0.4 ^a	-0.57 ± 0.59
180	2-CF ₃	0.8 ± 0.8 ^a	0.77 ± 0.05
181	3,5-(OMe) ₂ , 4-OH	0.9 ± 0.3 ^a	0.00 ± 0.08

^aMeasured at 130 μM. ^bMeasured at 2 nM. ^cMeasured at 1.75 μM. ^dThe experiment was performed in triplicates.

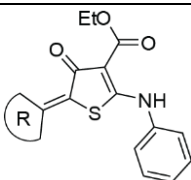
The error values indicate the SD. The assay was performed by Neele Haacke as part of her Master thesis.

Results and discussion

Table 25: Structures of aminothiophenes, normalized induced fluorescence (F_{norm}) measured by FRET, and induced shifts in melting temperatures of RNase L.

Compound	R	F_{norm} / % ^b	ΔT_m / °C ^c
182		0.4 ± 0.1^a	-0.77 ± 0.09
183		-0.3 ± 0.9^a	-1.30 ± 0.24
184		2.0 ± 0.4^a	-0.37 ± 0.09
185		1.3 ± 0.2^a	-1.63 ± 0.29
186		0.8 ± 0.3^a	0.23 ± 0.05
187		1.0 ± 0.5^a	0.97 ± 0.05
188		2.0 ± 0.2^a	0.20 ± 0.08
189		2.2 ± 0.4^a	0.03 ± 0.05
190		3.0 ± 0.3^a	-0.03 ± 0.09
Compound	Structure	F_{norm} / % ^b	ΔT_m / °C ^c
191		1.0 ± 0.2^a	1.40 ± 0.08

Results and discussion



Compound	R	$F_{\text{norm}} / \%$ ^b	$\Delta T_m / ^\circ\text{C}$ ^c
192		1.6 ± 0.2^a	0.73 ± 0.05
193		1.4 ± 0.4^a	0.10 ± 0.00
194		0.6 ± 1.4^a	0.70 ± 0.08

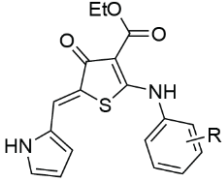
^aMeasured at 130 μM . ^bThe assay was performed by Neele Haacke as part of her Master thesis. ^cThe experiment was performed in triplicates. The error values indicate the SD. The assay was performed by Neele Haacke as part of her Master thesis.

The positive control 2'-5'A shifted the melting temperature of RNase L by 2.8 $^\circ\text{C}$ and was defined as 100% RNase L activation in the FRET assay. The reported RNase L activators C1 (**22**) and C1-3 (**24**), as well as reported negative control C1-4 (**168**) did not significantly activate RNase L in the optimized FRET assay. Similarly, all other tested analogs were no potent RNase L activators. Possibly, the initial activity in the FAM-based FRET assay could be attributed to autofluorescence since we observed fluorescence already when testing C1-3 (**24**) in buffer without RNase L. Nevertheless, compounds that did not activate RNase L could still function as binders and be useful as components of RIBOTACs.^{168,169} RNase L binding could be measured by stabilization of the RNase, which was detected for **191** with a shift of 1.40 $^\circ\text{C}$, and by **170**, **176**, **177**, and **187**, which all induced shifts between 0.80 and 0.92 $^\circ\text{C}$, which is higher than those of C1 (**22**) and C1-3 (**24**).

The discovery of RNase L activators remains a challenge to be addressed. The binding pocket naturally occupied by 2'-5'A is relevant for RNase L activation, and it is located between the ANK and PK of two RNase L monomers. The complete pocket only forms upon RNase L dimerization, which might be the reason why RNase L activation is difficult to be induced by small molecules. Additionally, 2'-5'A has a high subnanomolar potency to activate RNase L, which is a result of numerous interactions of the not small, but highly charged molecule (molecular weight 1159 g/mol) with RNase L. Nearly every functional group of 2'-5'A is involved in the interaction with the protein. Consequently, using a small molecule to mimic the extensive molecular interaction network formed between 2'-5'A and RNase L is difficult. Alternatively, oligonucleotide-based molecules or derivatives of 2'-5'A could prove to be more promising candidates for RNase L activation.

Results and discussion

Table 26: Structures of aminothiophenes, normalized induced fluorescence (F_{norm}) measured by FRET, and induced shifts in melting temperatures of RNase L.



Compound	R	F_{norm} / % ^a	ΔT_m / °C ^b
195	4-OMe	1.3 ± 0.9 ^a	-0.90 ± 0.08
196	3-OMe	1.1 ± 0.3 ^a	-0.93 ± 0.21
197	3,4-(OMe) ₂	1.0 ± 0.0 ^a	-1.17 ± 0.17
198	4-Br	1.3 ± 0.4 ^a	0.03 ± 0.05
199	2-Br	0.8 ± 0.6 ^a	0.00 ± 0.22
200	4-F	0.6 ± 0.6 ^a	0.17 ± 0.09
201	3-F	1.2 ± 0.1 ^a	0.20 ± 0.08
202	4-CF ₃	0.6 ± 0.1 ^a	0.10 ± 0.14
203	3-CF ₃	1.1 ± 0.7 ^a	0.37 ± 0.05
204	4-NO ₂	-0.2 ± 1.0 ^a	0.13 ± 0.05
205	3-NO ₂	0.7 ± 0.2 ^a	0.13 ± 0.05
206	4-Me	0.4 ± 0.7 ^a	0.23 ± 0.05
207	4-Et	0.9 ± 0.3 ^a	0.23 ± 0.05

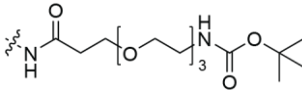
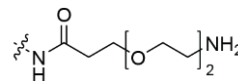
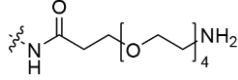
^aMeasured at 130 μM . ^bThe assay was performed by Neele Haacke as part of her Master thesis.

4.2.4 Preliminary evaluation of biphenylthiophenes as RNase L binders

The idea that RNase L binders are sufficient for successfully designing bifunctional RNA degraders was also reported by Disney and colleagues in 2022. The authors screened a DNA-encoded library (DEL) against RNase L.¹⁶⁸ The design of a DEL screening usually does not allow for the detection of the influence of a compound on the enzyme activity of a target protein. Still, it is an unbiased approach to identify binders that interact with any site of the target protein. A novel RNase L binder was identified in the study, with only moderate RNase L-activating potency. Nevertheless, the biphenylthiophene hit was successfully converted into a RIBOTAC.¹⁶⁸ Thus, it can be concluded that RNase L binders might be sufficient for the recruitment of RNase L in RIBOTACs. Biphenylthiophenes were tested for their ability to activate and to bind RNase L in this work (Table 27). In contrast to the reported hit molecule, the biphenyl was connected via the 4-position instead of the 3-position of the phenyl to the thiophene ring.

Results and discussion

Table 27: Induced shift of melting temperature of RNase L by analogs of a biphenylthiophene RNase L recruiter.

Compound	R ¹	R ²	F _{norm} / % ^{a,b}	ΔT _m / °C at 60 μM ^b
DMSO	not applicable	not applicable	0 ± 1.2	0.0 ± 0.8
208	H		0.3 ± 0.2	fluorescent ^d
209	H	NH ₂	-0.4 ± 0.3	2.0 ± 0.6
210	H		-7.2 ± 0.3	fluorescent ^d
211	H		-6.4 ± 1.8	fluorescent ^d
212	CH ₃	NH ₃ Cl	-3.5 ± 0.3	2.0 ± 0.6
2'-5'A	not applicable	not applicable	100 ± 4.6 ^c	4.9 ± 0.4 ^e

^aMeasured at 100 μM. ^bThe experiment was performed in triplicates and the SD is indicated. ^cMeasured at 12.5 nM. ^dThe compound interfered with the readout and the melting curve was shifted. A fluorescent signal was also detected without protein. ^eMeasured at 3 μM.

Although none of the molecules was able to potently activate RNase L, shifts of the melting temperature of RNase L were detected, likely indicating stabilization of the protein caused by direct binding. These preliminary results indicate that biphenylthiophene is a promising scaffold for RNase L binders. It would be interesting to clarify the binding site of the molecules, validate their activity, and possibly reprogram the compounds into RNase L activators. Although RNase L binders likely could not directly serve as antiviral drugs, they could be valuable components to build functional RIBOTACs. Therefore, future screening setups for the identification of RNase L binders, instead of activators, could be promising since it will allow more pockets to be targeted and thus theoretically will increase the number of possible hit molecules.

4.2.5 Evaluation of rationally designed 2-((pyrrol-2-yl)methylene)thiophen-4-ones as RNase L inhibitors

Results from this section were published as “Rational design and evaluation of 2-((pyrrol-2-yl)methylene)thiophen-4-ones as RNase L inhibitors.”.²²⁵

Apart from RNase L activators and binders, inhibitors of RNase L are interesting as potential drugs, for example, against autoimmune disorders such as AGS. To date, more RNase L inhibitors than activators were reported, although with limited potency and specificity. For instance, RNase L inhibitor sunitinib (**28**) was originally identified as an inhibitor of multiple receptor tyrosine kinases. In this work, we used a rational design approach to identify novel RNase L inhibitors. RNase L activator assays were thus modified to contain a minimum amount of ATP and 2'-5'A for RNase L activation, competing with the RNase L inhibitors.

RNase L inhibitor sunitinib (**28**) binds to the PK domain of RNase L by mimicking the structure of ATP (Figure 27A). 1*H*-pyrrole-3-carboxamide is a mimic of the ribose-5-phosphate, and the flat oxindole resembles the aromatic fragment of the nucleic base. The crystal structure of RNase L and sunitinib (**28**) revealed an unoccupied pocket next to the oxindole moiety that could potentially be targeted to improve potency, which inspired our efforts to perform the modification on the oxindole moiety.^{186,225} Additionally, the oxindole resembles the 2-aminothiophen-4-one-3-carboxylate (ATPC) of RNase L binder C1-3 (**24**) since both molecules carry a five-membered ring and a Michael acceptor. Further modifications based on the ATPC could potentially lead to compounds that occupy the additional RNase L PK domain pocket. Based on these considerations, the structural features of both RNase L binders were combined to give 2-((pyrrol-2-yl)methylene)thiophen-4-ones, such as **213** (Figure 27A). It is noteworthy that a thiophene substructure was also present in the DEL-screening hit DEL-2, indicating potential importance of the thiophene for RNase L binding (**25**). In total, 33 thiophenone analogs of **213** were evaluated for their ability to inhibit RNase L in an initial FRET assay (Table 28). Most molecules showed an inhibition rate comparable to that of sunitinib (**28**), except **229**, that was inactive in the FRET assay. The small molecules were further tested in the gel-based RNA cleavage assay (Figure 27B-F). Many thiophenones did not fully inhibit RNA cleavage, while a few others induced a smeared band indicating partial precipitation of the RNA, or RNA remained in the well of the gel, possibly due to precipitation. Of note, the primary amine-containing thiophenones **234**, **236**, **238**, and **240** showed complete inhibition of RNA cleavage in FRET and gel-based assay without hints towards precipitation (Table 28, Figure 27E). Initially, the primary amine was installed on the molecules as a handle for pull-down experiments. However, it seemed like the primary amine was beneficial for potency, possibly due to hydrogen bond or salt bridge formation with negatively charged amino acids.

Results and discussion

Table 28: Inhibition of RNase L by a series of 2-((pyrrol-2-yl)methylene)thiophen-4-ones.

Compound	X	R ¹	R ²	Inhibition rate /%
Sunitinib (28)	not applicable	not applicable	not applicable	83 ± 10 ^{a,c}
213	S	H	OEt	78 ± 8 ^{a,c}
214	S	4-F	OEt	80 ± 5 ^{a,c}
215	S	3-F	OEt	76 ± 8 ^{a,c}
216	S	4-CF ₃	OEt	90 ± 3 ^{a,c}
217	S	4-OMe	OEt	70 ± 7 ^{a,c}
218	S	3-OMe	OEt	78 ± 1 ^{a,c}
219	S	4-Br	OEt	90 ± 4 ^{a,c}
220	S	2-Br	OEt	85 ± 6 ^{a,c}
221	S	4-NO ₂	OEt	67 ± 3 ^{a,c}
222	S	3-NO ₂	OEt	76 ± 4 ^{a,c}
223	S	4-Me	OEt	83 ± 9 ^{a,c}
224	S	3,4-(OMe) ₂	OEt	79 ± 5 ^{a,c}
225	S	4-Et	OEt	83 ± 11 ^{a,c}
226	S	H	NHMe	67 ± 3 ^a
227	S	3-F	NHMe	58 ± 12 ^{a,c}
228	S	3-OMe	NHMe	99 ± 3 ^{a,c}
229	S	4-F	NHMe	< 5 ^{a,c}
230	S	3-Cl	NHMe	88 ± 4 ^{b,c}
231	S	3-CF ₃	NHMe	97 ± 1 ^{b,c}
232	S	3-NO ₂	NHMe	60 ± 3 ^{b,c}
233	S	3-F	NHBz	99 ± 0 ^{a,c}
234	S	H	NH-Et-NH-Boc	75 ± 7 ^{a,c}
235	S	H	NH-Et-NH ₂	101 ± 5 ^{a,c}
236	S	3-F	NH-Et-NH-Boc	100 ± 2 ^{a,c}
237	S	3-F	NH-Et-NH ₂	102 ± 2 ^{a,c}
238	S	3-Cl	NH-Et-NH-Boc	96 ± 1 ^{a,c}
239	S	3-Cl	NH-Et-NH ₂	101 ± 0 ^{a,c}
240	S	3-OMe	NH-Et-NH-Boc	49 ± 1 ^{b,c}
241	S	3-OMe	NH-Et-NH ₂	101 ± 0 ^{a,c}
242	O	H	NHMe	74 ± 7 ^a
243	O	H	NH-Et-NH-Boc	79 ± 1 ^a
244	O	H	NH-Et-NH ₂	93 ± 9 ^{a,c}
245	O	3-F	NH-Et-NH-Boc	84 ± 1 ^a
246	O	3-F	NH-Et-NH ₂	97 ± 8 ^{a,c}

^aDetermined by FRET at 250 μM. The experiment was performed in triplicates. The error values indicate the SD.

^bDetermined by FRET at 130 μM. The experiment was performed in triplicates. The error values indicate the SD.

^cMeasured by Neele Haacke as part of her Master thesis.

Results and discussion

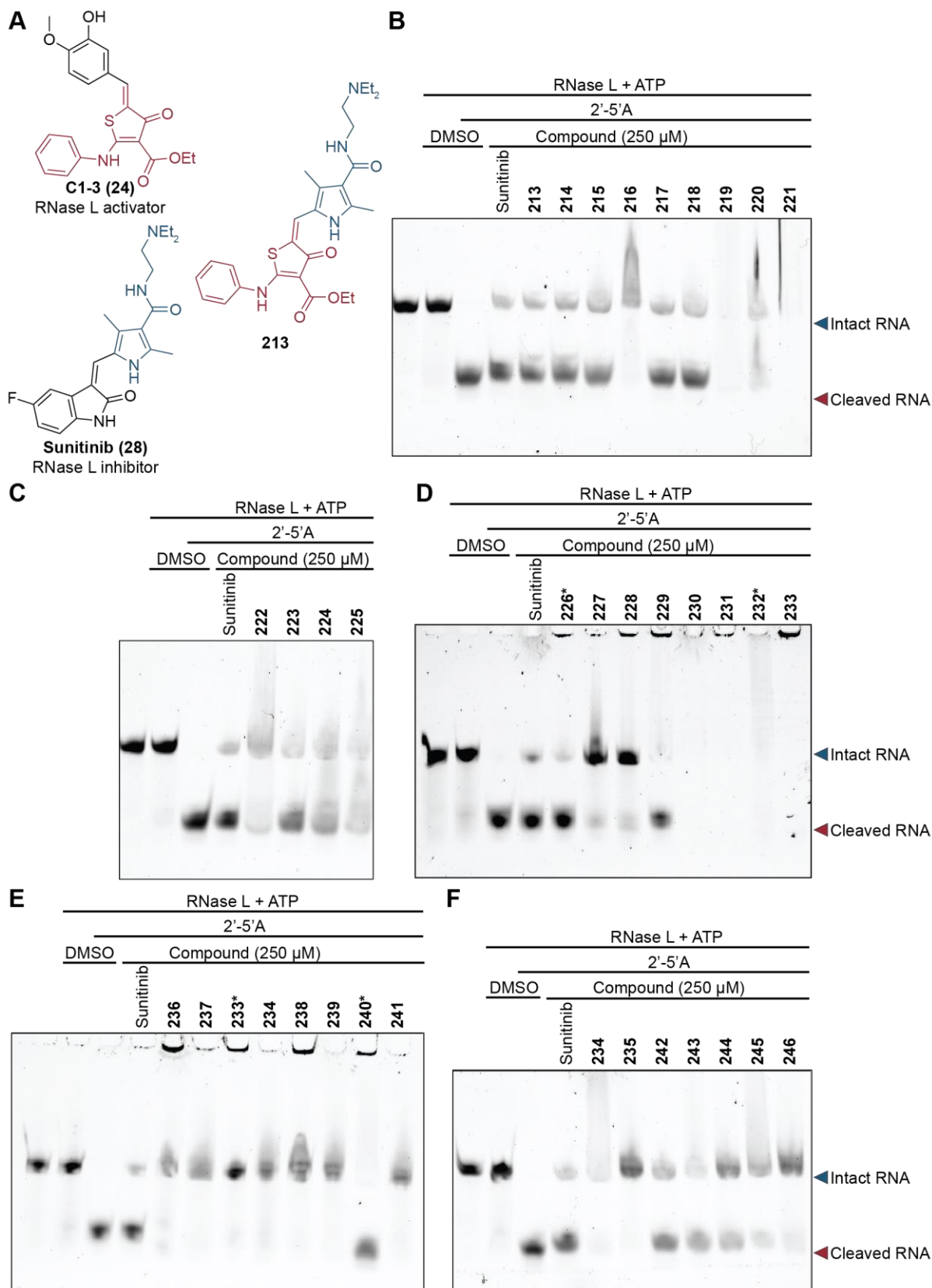


Figure 27: (A) Rational design of 2-((pyrrol-2-yl)methylene)thiophen-4-ones combining the scaffolds of C1-3 (**24**) and sunitinib (**28**). (B-F) Evaluation of 2-((pyrrol-2-yl)methylene)thiophen-4-ones in gel-based RNA cleavage assay. The asterisks highlight compounds tested at 130 μM. The assay was performed by Neele Haacke as part of her Master thesis.

Results and discussion

The four amine-containing molecules, **234**, **236**, **238**, and **240**, were further evaluated in dose-response FRET, with IC_{50} values of 15.9 μ M, 27.9 μ M, 12.4 μ M, and 12.1 μ M, respectively (Figure 28A). All four molecules performed better than sunitinib (**28**) and the recently reported PK-binding RNase L inhibitors SU11652 (**29**) and myricetin (**30**) (Figure 28A, B). The three best-performing molecules in the FRET assay were additionally tested in dose-response in the gel-based RNA cleavage assay, in which the dose-dependent inhibition of RNase L was confirmed upon treatment with the inhibitors (Figure 28C).

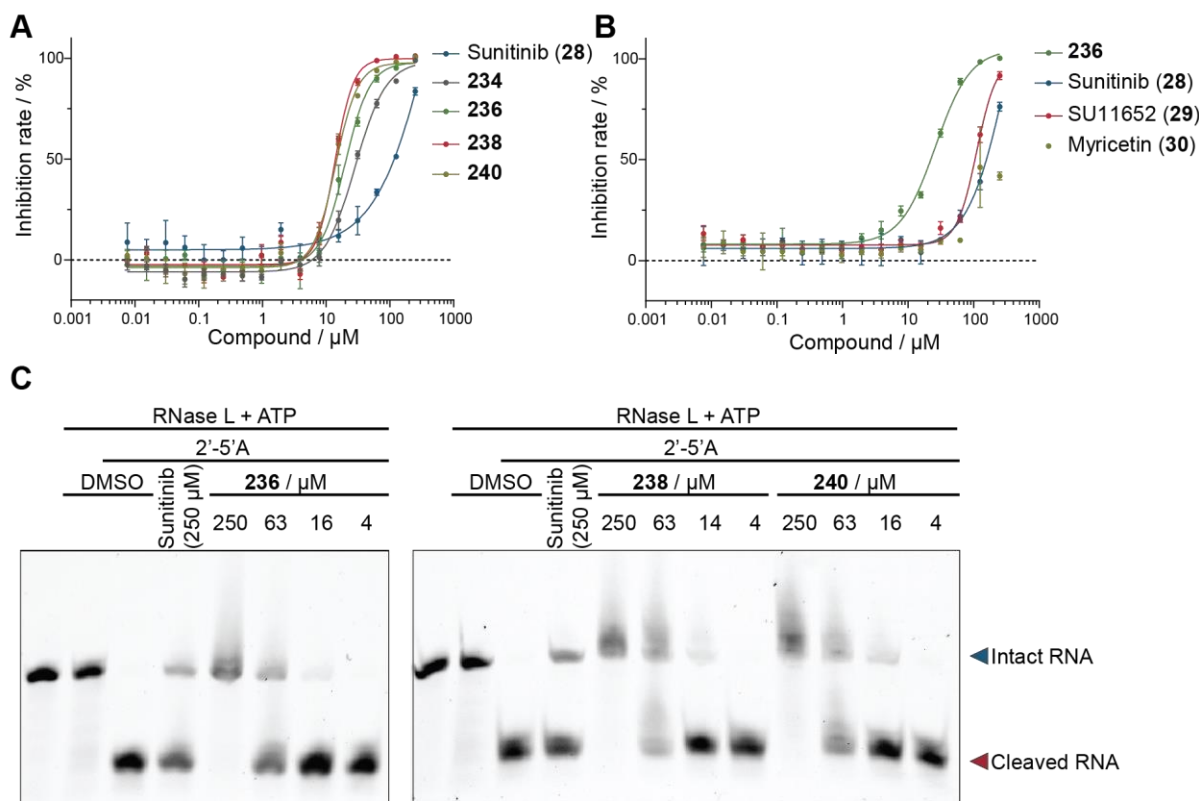


Figure 28: 2-((Pyrrol-2-yl)methylene)thiophen-4-ones as RNase L inhibitors. (A) Dose-dependent inhibition of RNase L by thiophen-4-ones compared to sunitinib (**28**) measured in FRET. The experiment was performed in triplicates. The error bars indicate the SD. The assay was performed by Neele Haacke as part of her Master thesis. (B) Dose-dependent inhibition of RNase L by **236** compared to reported RNase L inhibitors. The experiment was performed in triplicates. The error bars indicate the SD. (C) RNA-cleavage assay evaluating the inhibition of RNase L by selected thiophen-4-ones and sunitinib (**28**). The RNA probe is labeled with a blue arrow, and the cleaved RNA is labeled with a red arrow. The assay was performed by Neele Haacke as part of her Master thesis.

Further, the three thiophenones showed dose-dependent binding to RNase L in BLI (Figure 29A-D). The signal was much higher than that of sunitinib (**28**). BLI indicated that the RNase L inhibition is mediated through the direct binding of the compound with the protein.

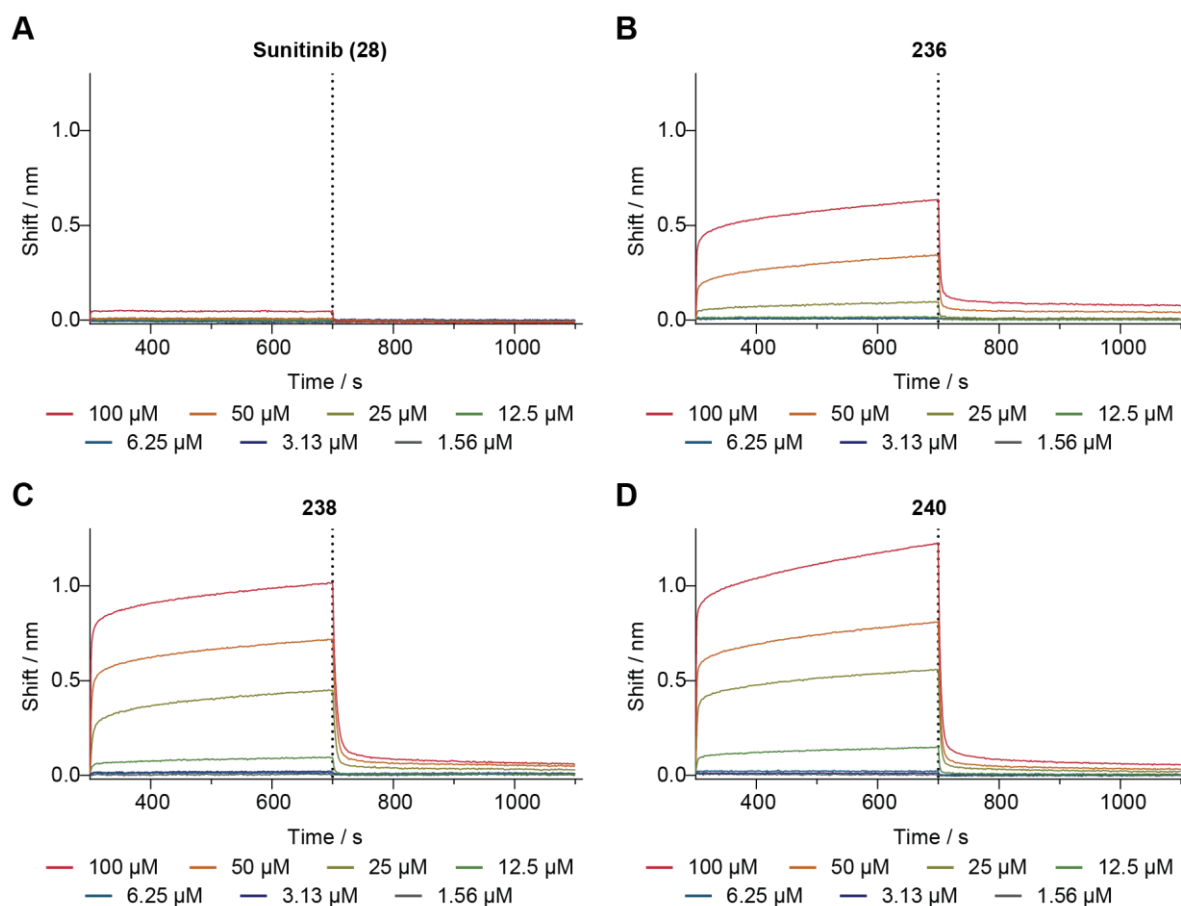


Figure 29: BLI of RNase L binding by (A) sunitinib (**28**), (B) **236**, (C) **238**, and (D) **240**. The data is representative for three replicates.

After identification of the inhibitors in biochemical and biophysical assays, the compounds' cellular activity was evaluated. First, the primary amine-containing molecule **236** was used in a pull-down experiment. The compound was immobilized via the primary amine handle and incubated with lysate of the RNase L-expressing cell line K-562.²²⁶ For comparison, C1-3 (**24**) was converted into the pull-down probe **248** and incubated with K-562-cell lysate. **247**, a phenylaminothiophenone with a minimal scaffold, served as a negative control for both pull-down probes (Figure 30A-C). In both experiments, RNase L was neither enriched compared to the negative control nor detected at all as a binder of the immobilized molecules. Since the potency of **236** was improved by the primary amine, which was also used to covalently couple the molecule to the magnetic beads, the absence of RNase L in the **236** pull-down experiment could potentially be explained by the usage of unfavorable coupling chemistry. Alternatively, it is possible that the interaction of RNase L with the compounds is transient or of low affinity, and thus RNase L is lost during the washing steps. The transient-binding hypothesis is supported by the fact that C1-3 (**24**) was successfully incorporated into various RIBOTACs, although RNase L binding was also not detected in the pull-down.

Results and discussion

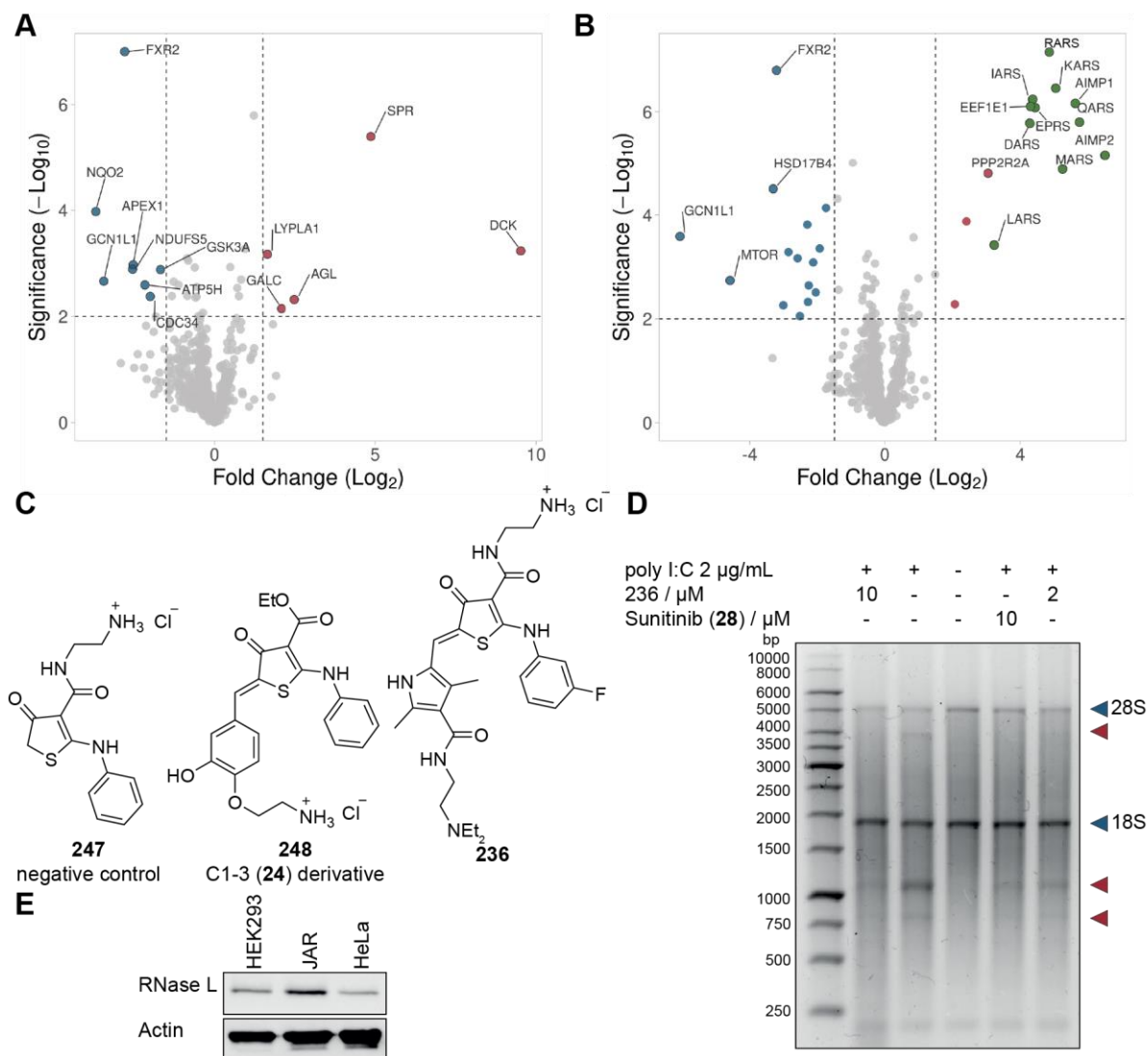


Figure 30: Cellular evaluation of thiophen-4-ones and reported RNase L binders. (A) Pull-down with C1-3 (**24**) derivative **248** incubated with K-562 cells. **247** was used as a negative control. Blue dots indicate negatively enriched proteins and positively enriched proteins are shown in red. (B) Pull-down with **236** incubated with K-562 cells. **247** was used as a negative control. Blue dots indicate negatively enriched proteins and positively enriched proteins are shown in red. Aminoacyl-tRNA synthetases and associated proteins are highlighted in green. (C) Structures of the three molecules used for pull-down. The primary amines were used for covalent immobilization. (D) Cleavage of rRNA in HeLa cells treated with **236** or sunitinib (**28**) and transfected with poly I:C. Cleavage products are highlighted with a red arrow. The size of the RNA was traced by a glyoxylated DNA ladder (left lane). The data is representative for three biological replicates. (E) Western blot detecting RNase L expression in HEK293, JAR, and HeLa cells.

Interestingly, **236** seemed to target tRNA synthesis since multiple aminoacyl tRNA synthetases and related enzymes were enriched in the pull-down samples (Figure 30B). The off-target effect of the **236** on tRNA synthesis needs to be further validated to clarify the mechanism and the importance of the interaction in the future. Second, the inhibitory effect of **236** on RNase L was evaluated in HeLa cells (Figure 30D). HeLa cells express RNase L, as

shown by western blot (Figure 30E). Cleavage of rRNA in distinct positions is a feature of RNase L activity, which could be observed after transfection of cells with the OAS activator poly I:C. The addition of **236** or sunitinib (**28**) partially inhibited the RNase L-mediated rRNA cleavage, indicating a direct or indirect inhibitory effect of the compound on RNase L activity.

4.2.6 Conclusions from targeting RNase L with small-molecule modulators

In this part, a FRET assay was successfully established for the screening of RNase L activators. Being a challenging target for small-molecule discovery, we observed an extremely low hit rate. Although no potent RNase L activators were identified in this work, the sulfonamide **152**, and the aminothiophenes **170**, **176**, **177**, **187**, and **191** stabilized RNase L to a larger extent than the positive control C1-3 (**24**) and thus are potential RNase L binders. The best RNase L stabilizing compounds additionally inhibit cell proliferation and might be useful as anticancer agents.^{221,224} Although reported RNase L activator C1-3 (**24**) did not activate RNase L in our assays and was not detected in a pull-down experiment, it could be a transient binder of RNase L. C1-3 (**24**) previously proved to be a useful component to build proximity-inducing bifunctional molecules and as such, it was successfully implemented in several RIBOTACs, for the targeted degradation of various RNAs of interest.^{169,170,179,181,227} Consequently, the identified RNase L binders from this work could be equally useful for the future development of RIBOTACs.

Besides RNase L, only one protein, IRE1, is known to have a dual kinase and ribonuclease structure. In comparison to RNase L that has a pseudo-kinase domain, IRE1 has a functional kinase domain whose active conformation mediates the dimerization and activation of the RNase domain. Thus, kinase activation could be regarded as a switch to activate the RNase activity of IRE1. The characterized structure of IRE1 facilitated the discovery of RNase activators and inhibitors, both of which were already reported. IRE1 RNase activators are generally type I kinase inhibitors that bind to the kinase domain and stabilize the active kinase conformation.^{228,229} In contrast, RNase L occupancy of the PK domain of RNase L with a nucleotide is required but is insufficient for activation. The additional 2'-5'A-mediated dimerization of the ANK domain is necessary in RNase L, while the ANK domain is absent in IRE1.¹³⁴ Therefore, it is very likely that RNase L cannot be activated by small molecules binding to the PK domain but has to be addressed at the 2'-5'A-binding site at the interface of two ANK domains and the PK domain. However, such a pocket only exists upon dimerization. Another point of concern is that 2'-5'A is a highly charged molecule that potently interacts with RNase L via a network of numerous molecular interactions. Thus, it is challenging for small molecules to potently and successfully mimic the interaction network formed between 2'-5'A and RNase L. Possibly, exploration of a novel chemical space beyond what is available in

current commercial small-molecule libraries is needed for the identification of potent RNase L activators.

Interestingly, IRE1 activator sunitinib (**28**) is an inhibitor of RNase L, underlining the thought that RNase L cannot be easily activated by small molecules via the PK domain.^{186,230} The example of sunitinib (**28**) further showed that RNase L inhibition is more feasible to be achieved than activation since the PK domain pocket can be targeted for that purpose. Indeed, **236** and analogs were identified in biochemical assays as potent RNase L inhibitors, with higher potency than all PK-targeting small molecules reported to date. Further, direct binding to RNase L and inhibition of RNase L-mediated rRNA cleavage was observed.

4.2.7 Discovery of OAS1 activators

OAS is a central component of 2'-5'A-mediated decay along the OAS–RNase L antiviral pathway. Targeting OAS with small-molecule activators is expected to yield similar effects as RNase L activation. OAS activators have the potential to serve as biochemical probes, antiviral drugs, anticancer therapeutics, and as candidates to treat CFS. Three active human isoforms of OAS are known. OAS1 is the smallest isoform consisting of a single OAS domain, while OAS2 consists of two domains and requires dimerization and glycosylation for activity.¹⁹⁴ OAS3 is formed by three consecutive OAS domains, only one of which is active. Since OAS1 carries the minimal common fold, is fully functional with a single OAS domain, and is the only isoform of which the structure of the active domain is known, the alternative splicing isoform p46 of OAS1 was chosen to be used as a model protein for all OAS family members for the identification of OAS activators.

4.2.7.1 Purification of recombinant OAS1 enzyme

In order to screen for OAS1 activators, the protein was expressed and purified. It was not possible to recombinantly express full-length OAS1 N-terminally fused to a SUMO- or maltose-binding protein tag in sufficient amounts from *E. coli*. Thus, a His₆-SUMO-OAS1 construct was expressed and purified from insect cells (Figure 31). The protein was purified by immobilized nickel affinity chromatography (Figure 31A) followed by cleavage of the tags using TEV-protease and reverse immobilized nickel affinity chromatography collecting the flow-through (Figure 31B). Since unspecific binding of the protein to the column was detected, wash fractions containing up to 10% elution buffer B were additionally collected and further purified by gel filtration (Figure 31C). The final purification step resulted in a monodisperse peak of purified OAS1 (peak 2).

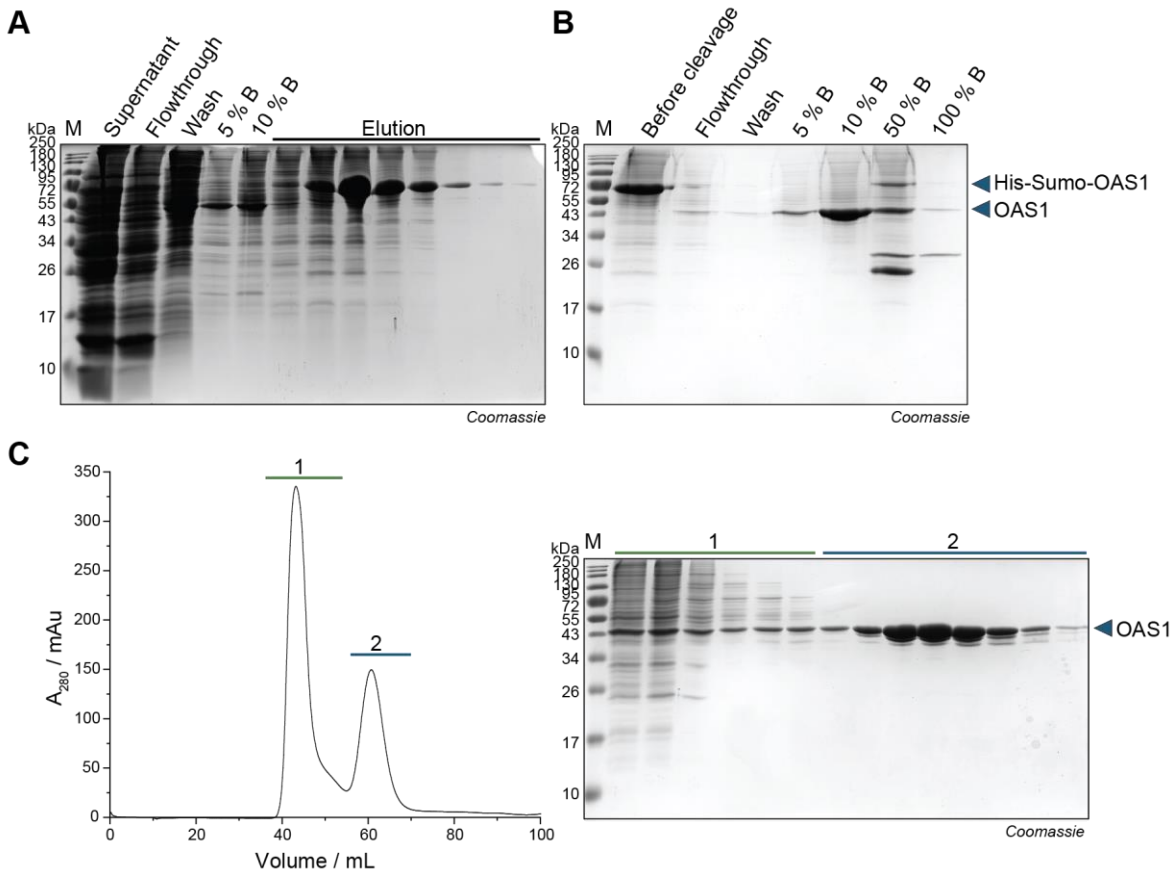


Figure 31. Purification of OAS1 from insect cells. (A) SDS-PAGE analysis of immobilized-nickel affinity chromatography purification. (B) SDS-PAGE of reverse nickel-affinity chromatography column. (C) Chromatogram and SDS-PAGE analysis of gel filtration of OAS1. The void-volume peak is labeled with 1, while the main peak containing OAS1 is labeled with 2.

4.2.7.2 Enzymatic synthesis of 2'-5'A using OAS1, and OAS1 oligomerization assay

The identity and activity of the recombinant OAS1 was confirmed by its ability to synthesize 2'-5'A. For the production of 2'-5'A, which was of use as a positive control of RNase L assays, the enzyme was immobilized on OAS1-activating dsRNA mimic poly I:C coupled to agarose beads (Figure 32A). Incubation in buffer containing ATP followed by removal of the immobilized enzyme by centrifugation resulted in a solution containing a crude mixture of ATP and 2'-5'A. The concentration of active 2'-5'A was evaluated by comparison to a 2'-5'A solution of known concentration provided by Silverman and his colleague using the same dilutions in the optimized RNase L activation FRET assay (Figure 32B, Figure S4). Both 2'-5'A solutions at the same dilutions showed comparable ability to activate RNase L, inducing RNA cleavage. Thus, the active 2'-5'A concentration of the newly synthesized solution was equivalent to that of the provided mixture. 350 μM trimeric active 2'-5'A was synthesized from 4 mM ATP. The successful enzymatic synthesis of 2'-5'A proves the identity and activity of the purified OAS1.

Results and discussion

OAS1 was previously reported to form tetramers in its active conformation.^{231,232} However, tetramerization was not confirmed by the RNA-bound crystal structure reported in literature and thus is controversial.^{130,195} Observing single particles of OAS1 in buffer by mass photometry revealed proteins with an average mass of 54 kDa, resembling monomeric OAS1 (46 kDa). The addition of a tenfold excess of dsRNA did not change the mass of OAS1 towards higher oligomerization states and no larger particles were detected (Figure 32C) hinting towards monomeric OAS1 as the active conformation. Interestingly, no shift resembling the binding of the dsRNA (13 kDa) was detected, which possibly was due to a poor sensitivity of the method to detect the expected molecular weight difference. FP and EMSA experiments later revealed that OAS1 was able to bind the used dsRNA probe (Figure 34E, F).

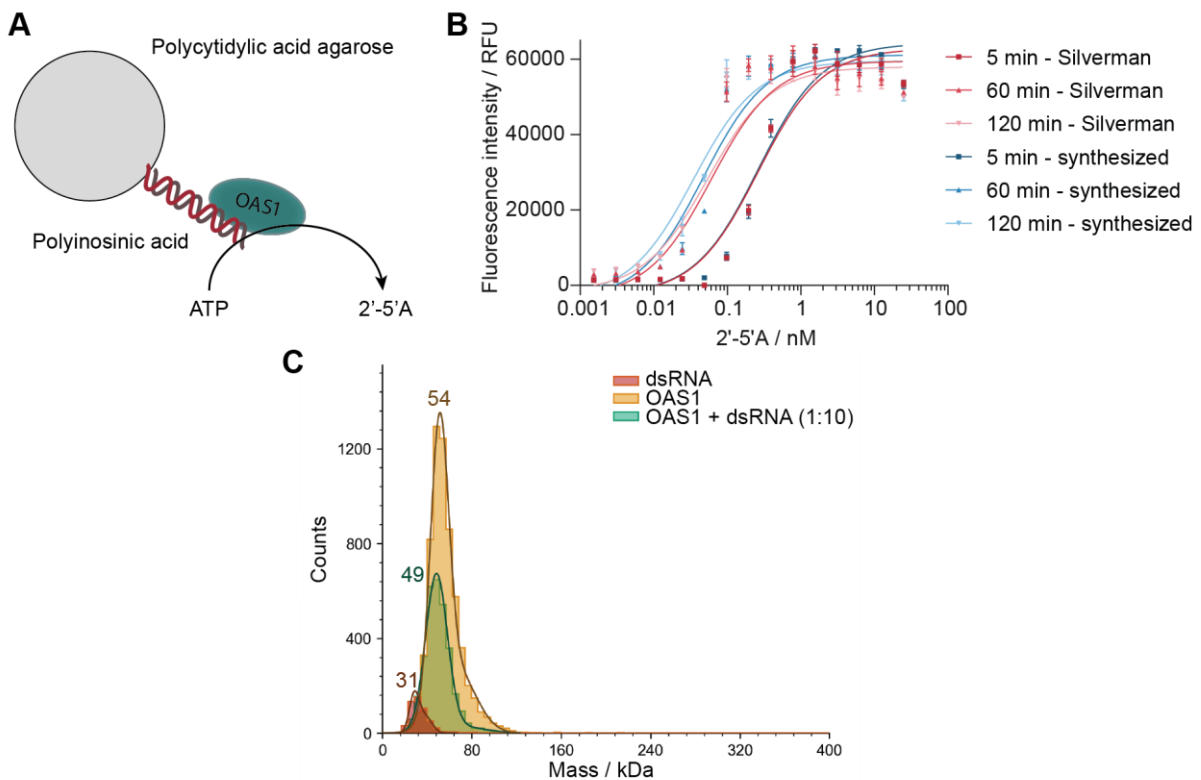


Figure 32: (A) Schematic representation of the enzymatic synthesis of 2'-5'A using recombinant OAS1. (B) FRET assay using enzymatically synthesized 2'-5'A from this work (blue) compared to 2'-5'A provided by Silverman and his co-worker (red) of known concentration to activate RNase L cleavage of RNA-5. The assay was performed in triplicates. The error bars indicate the SD. (C) Mass-photometry of recombinant OAS1 with and without dsRNA.

4.2.7.3 Optimization of the OAS1 activation assay and screening

After confirming the activity of purified OAS1, the enzyme was used to develop a screening assay for the identification of OAS1 activators. The RNase L activation FRET assay was modified by the addition of OAS1 and an increase of the concentration of ATP to allow 2'-5'A synthesis upon activation of OAS1. The product of the enzyme reaction then activates RNase L cleaving the FRET RNA-probe (Figure 33A). The dsRNA mimic poly I:C was used as a positive control OAS1 activator. Various OAS1 concentrations were tested to increase the FRET signal. The highest chosen concentration was 100 nM OAS1, producing low background fluorescence, which did not increase over the course of three hours (Figure 33B). A high enzyme concentration proved to be beneficial for a faster increase of the signal and thus 100 nM OAS1 was used for the following experiments (Figure 33C). The full signal was developed after 90 minutes with an EC₅₀ of ~0.01 µg/mL poly I:C. The assay was transferred to screening, and more than 15,000 compounds were screened for their ability to activate OAS1 at a concentration of 30 µM. Of those, 55 hits induced at least 20% fluorescence when compared to poly I:C. Comparison to the RNase L activator screening hits revealed 14 molecules that showed up in both screens and were thus excluded from further analysis since they were not expected to selectively activate OAS1. The remaining hits were evaluated in dose-response assays, and only six compounds robustly induced an increase in fluorescence. However the fluorescent signal was detected immediately after addition of the molecules, hinting towards autofluorescence. In order to verify these observations, four molecules were selected for further analysis in orthogonal assays (Figure 33D).

Results and discussion

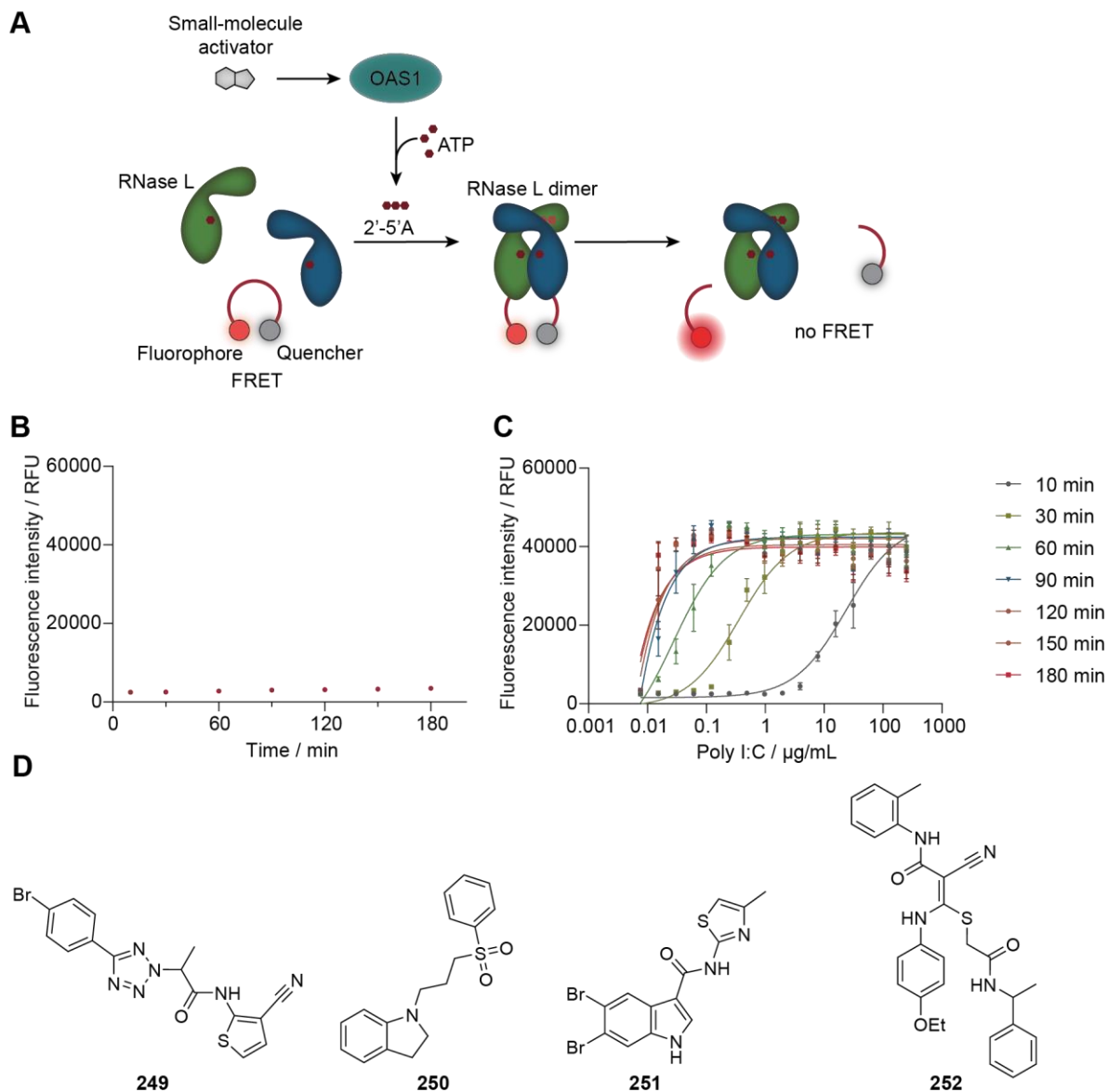


Figure 33: (A) Schematic representation of FRET assay measuring OAS1 activation. (B) Background evaluation using 100 nM OAS1 and 6 nM RNase L without poly I:C. The assay was performed in triplicates. The error bars indicate the SD. (C) Time- and concentration-dependent activation of RNA-cleavage via OAS1 activation by positive control poly I:C measured by FRET. The assay was performed in triplicates. The error bars indicate the SD. (D) Selected screening hits used for further evaluation. The screening was performed by Dr. Philipp Lampe, COMAS.

4.2.7.4 Orthogonal assays evaluating OAS1 activation

The time-dependent fluorescence signal induced by positive control poly I:C and by the screening hits is shown in Figure 34A. While poly I:C triggered an increase in fluorescence over time caused by 2'-5'A production and RNase L activation, the small molecules showed a decreasing fluorescence over time. Consequently, it seemed that the compounds do not activate OAS1 but act through autofluorescence or other assay-interfering mechanisms. Nevertheless, orthogonal assays were performed to confirm the hypothesis. A colorimetric assay detecting inorganic pyrophosphate (PP_i) via the formation of a chromophore with molybdate reagent, eikonogen reagent, and β-mercaptoethanol was conducted to measure the synthesis of the by-product of the enzymatic reaction catalyzed by OAS1 (Figure 34B).²³³ Indeed, incubation of OAS1 with poly I:C for two hours resulted in formation of PP_i, detected by a color change from yellow to blue, which could be measured as an increase in absorption at 580 nm. In comparison, the hit molecules did not induce the enzymatic reaction. A similar result was observed when measuring the ATP consumption of OAS1 using a chemiluminescent assay in which ATP was used as a substrate for the luciferase reaction of beetle luciferin to oxyluciferin, which produced a measurable luminescent signal. While poly I:C induced consumption of ATP in a dose-dependent manner (Figure 34C), the four investigated small molecules did not achieve the same effect (Figure 34D).

The future development of assays that detect binding of the RNA to OAS1, rather than enzyme activation, could be advantageous to detect competitively binding small molecules. OAS1 binders could then be further advanced into activators. An example of such an assay is an FP assay using a fluorophore-labeled 18-mer dsRNA as a probe. Binding of OAS1 increased the anisotropy with a K_d of 40 ± 6 nM (Figure 34E). Affinities of OAS1 for RNA were reported to be in the nanomolar range, which is in line with the result of the FP assay.¹⁸⁸ As a next step, the competitive binding of compounds inhibiting the interaction of RNA and OAS1 could be screened. The same RNA probe as for the FP assay was also used for EMSA, showing a shift of the RNA band caused by OAS1 binding to the dsRNA (Figure 34F). The assay could prove to be useful to evaluate OAS1 binding molecules or to study the protein–RNA interaction in more detail.

Results and discussion

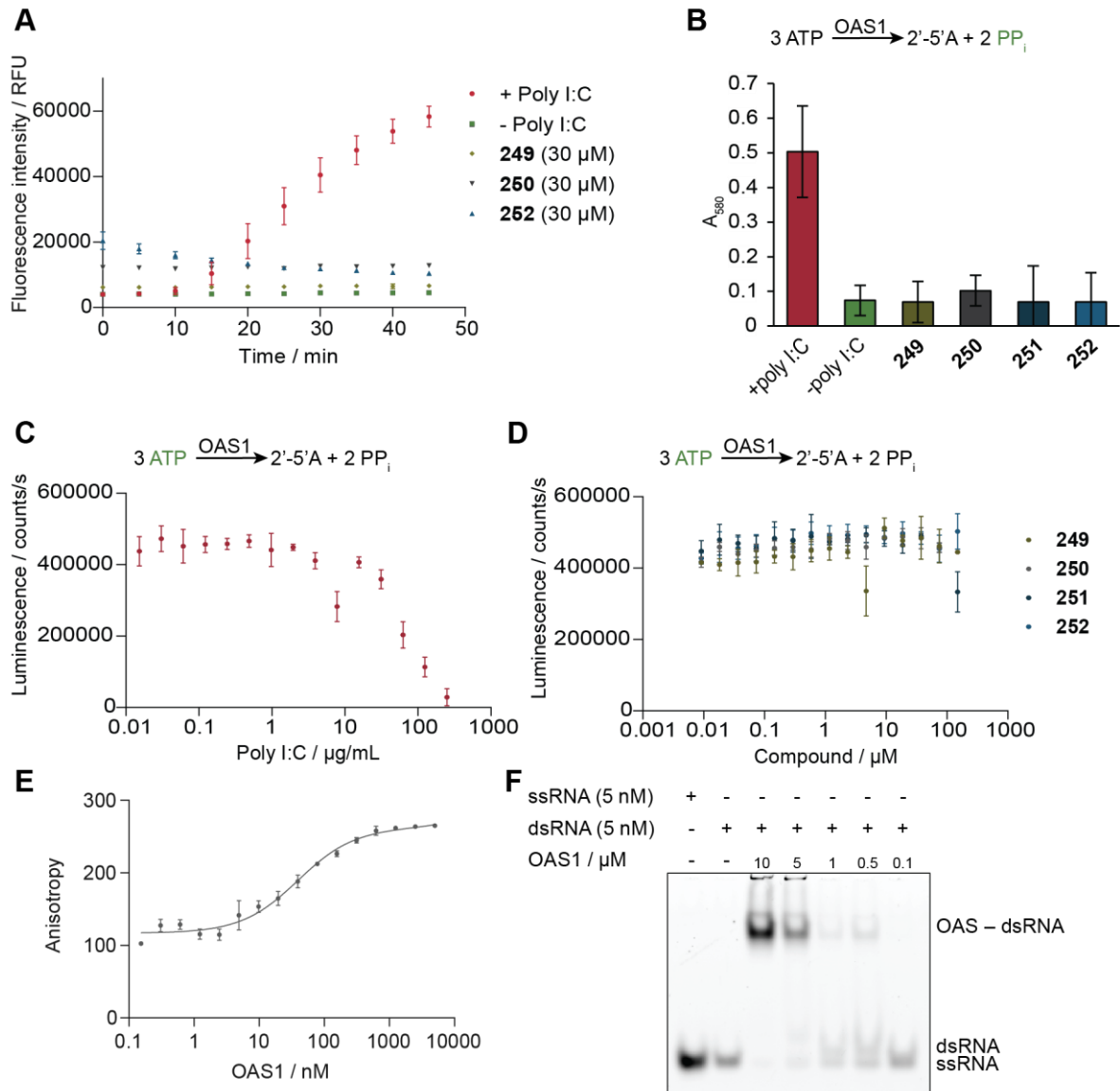


Figure 34: Orthogonal assays evaluating OAS1 activation. (A) Dose-dependent evaluation of OAS1 screening hits in FRET assay. The experiment was performed by Dr. Philipp Lampe, COMAS. (B) Evaluation of OAS1 hit molecules and positive control poly I:C in colorimetric assay measuring concentrations of pyrophosphate. (C) Positive control poly I:C activating OAS1 inducing consumption of ATP measured in Kinase-Glo luminescent assay. (D) Screening hits evaluated in Kinase-Glo assay. (E) FP assay measuring change of anisotropy of a fluorophore coupled to a dsRNA probe upon titration of OAS1. (F) EMSA evaluating binding of OAS1 to a fluorophore-labeled RNA probe. (A-E) The assays were performed in triplicates. The error bars indicate the SD.

4.2.7.5 Conclusions from the OAS1-activator screening

As a conclusion, the screening campaign in this part did not identify robust hits that activated OAS1. Screening of a larger library could potentially lead to the identification of more potent OAS1 activators. However, it has to be considered that the natural activator of OAS is dsRNA, a large molecule that interacts with OAS via surface interactions spanning a wide area of the protein. Small molecules are traditionally expected to bind to pockets of proteins, either active

sites or allosteric positions, allowing interactions of the compound with the protein in most directions of the molecule.²³⁴ When addressing a protein surface, such as the positively charged RNA-binding site of OAS, high affinities are challenging to achieve. A small molecule targeting the active site pocket of OAS, however, would most likely compete with the ATP substrate and thus inhibit the synthesis of 2'-5'A. Due to similarities of the RNA-binding surface with interaction sites of protein-protein interactions, which also often consist of large interacting surfaces with shallow pockets, one could learn from advances in the field of targeting PPIs when addressing protein-RNA interactions. It is well known that high-throughput screening targeting PPIs generally produces low hit rates.²³⁵ An alternative approach to small molecules could be the use of oligonucleotide analogues or peptides to address the surface of OAS. Both have the advantage of spanning larger areas than small molecules allowing for an increased number of interactions and rational design. The positive charge of the targeted surface of OAS1 has the drawback that binders would necessarily be negatively charged and associated with unfavorable cell permeability.

A protein with a very similar fold and function as OAS is cyclic GMP-AMP synthase (cGAS). The OAS homolog senses double-stranded DNA and synthesizes 2'-5'-linked cyclic GMP-AMP second messengers that ultimately activate the expression of antiviral genes.¹⁹⁵ Multiple cGAS inhibitors are known, many of which target the active site of the protein. However, some therapeutic molecules, such as oligodeoxynucleotides, suramin, and antimalarial drugs hydroxychloroquine and quinacrine bind to the DNA binding site of cGAS.²³⁶ These cGAS inhibitors should be tested for their ability to bind to the RNA-binding site of OAS1, for example, by FP and EMSA, where they could serve as starting points for the rational development of OAS1 inhibitors and activators. Furthermore, the existence of DNA-competitive cGAS inhibitors suggest that targeting the nucleic acid binding site of OAS should generally be possible by small molecules.

5 Conclusions and perspectives

RBPs regulate all aspects of RNA biology and metabolism, and thus targeting of RBPs with small molecules is a viable strategy to modulate pathways involving coding and non-coding RNAs. In this work, the RNA-binding proteins LIN28, which binds to miRNA, the ssRNA-cleaving protein RNase L, and the dsRNA-binding protein OAS1 were targeted using small molecules. While LIN28 is a canonical RBP consisting of two RNA-binding domains, OAS1 is a non-canonical RBP. The three RBPs were addressed using screening-based approaches aiming to identify novel small-molecule modulators and scaffold-based approaches leveraging on known RBP-targeting scaffolds.

In this work, robust fluorescence-based screening assays for all three targets were successfully established, which will be useful to enable further drug discovery efforts targeting RBPs. Trisubstituted pyrrolinones (such as **41** and **85**) and spirochromenopyrazoles (such as compound **135**) were discovered and validated as new LIN28 inhibitors targeting the CSD with micromolar potencies. For the trisubstituted pyrrolinones, the exchange of the salicylic acid substituent, which was initially thought to be essential for potency, with a biphenyl moiety led to inhibitors with significantly increased upregulation of *let-7* miRNA maturation. A possible explanation is the improved membrane permeability of the compounds.

RNase L activation proved challenging, but RNase L binders were detected in a thermal shift assay and could serve as RNase L recruiters to be used in proximity-inducing bifunctional molecules. The rational design of RNase L inhibitors led to the identification of aminothiophenones **236** and analogs carrying an ethylamine moiety. The inhibitors showed higher potency than all known small-molecule RNase L inhibitors that target the pseudokinase domain. The best-performing aminothiophenone **236** showed more than 30-fold improvement on inhibitory potency compared to the reported RNase L inhibitor sunitinib (**28**) and inhibited RNase L-mediated cleavage of rRNA.

RBPs were deemed challenging targets to be addressed by small molecules. This work showed that it is possible to target RBPs of different structures and substrates using small molecules of diverse scaffolds. However, achieving high inhibitory and activating potencies remains a challenge. One of the obstacles to overcome is the difficulty for small molecules to compete or mimic the extensive surface interactions occurring on the RNA-binding site of RBPs. Additionally, electrostatic interactions are often involved due to the negative charge of the RNA backbone, which is another obstacle for small molecules, especially if defined ligandable pockets are absent.⁹ Echoing the difficulty in RBP-targeting small molecules, screenings for PPI inhibitors were often accompanied by low hit rates and weak-potency hit molecules.²³⁵ Additionally, canonical RBPs, such as LIN28, often consist of a combination of

Conclusions and perspectives

RNA-binding domains, each of which contribute to RNA-binding.⁸ Should only one domain be targeted, the potency of the molecule remains low because only part of the RNA-binding surface or site is competed. In this context, new scaffolds harboring new chemical space likely need to be sought after to efficiently target the emerging biological space held by RBPs and RBP-RNA interactions.

6 References

1. Crick, F. Central Dogma of Molecular Biology. *Nature* **227**, 561–563 (1970).
2. Ezkurdia, I. *et al.* Multiple evidence strands suggest that there may be as few as 19 000 human protein-coding genes. *Hum. Mol. Genet.* **23**, 5866–5878 (2014).
3. Clamp, M. *et al.* Distinguishing protein-coding and noncoding genes in the human genome. *Proc. Natl. Acad. Sci. U. S. A.* **104**, 19428–19433 (2007).
4. Djebali, S. *et al.* Landscape of transcription in human cells. *Nature* **489**, 101–108 (2012).
5. Mattick, J. S. & Makunin, I. V. Non-coding RNA. *Hum. Mol. Genet.* **15 Spec No**, 17–29 (2006).
6. Warner, K. D., Hajdin, C. E. & Weeks, K. M. Principles for targeting RNA with drug-like small molecules. *Nat. Rev. Drug Discov.* **17**, 547–558 (2018).
7. Wang, F., Zuroske, T. & Watts, J. K. RNA therapeutics on the rise. *Nat. Rev. Drug Discov.* **19**, 441–442 (2020).
8. Hentze, M. W., Castello, A., Schwarzl, T. & Preiss, T. A brave new world of RNA-binding proteins. *Nat. Rev. Mol. Cell Biol.* **19**, 327–341 (2018).
9. Wu, P. Inhibition of RNA-binding proteins with small molecules. *Nat. Rev. Chem.* **4**, 441–458 (2020).
10. Gerstberger, S., Hafner, M. & Tuschl, T. A census of human RNA-binding proteins. *Nat. Rev. Genet.* **15**, 829–845 (2014).
11. Castello, A. *et al.* Insights into RNA Biology from an Atlas of Mammalian mRNA-Binding Proteins. *Cell* **149**, 1393–1406 (2012).
12. Baltz, A. G. *et al.* The mRNA-Bound Proteome and Its Global Occupancy Profile on Protein-Coding Transcripts. *Mol. Cell* **46**, 674–690 (2012).
13. Lunde, B. M., Moore, C. & Varani, G. RNA-binding proteins: Modular design for efficient function. *Nat. Rev. Mol. Cell Biol.* **8**, 479–490 (2007).
14. Smith, J. M., Sandow, J. J. & Webb, A. I. The search for RNA-binding proteins: A technical and interdisciplinary challenge. *Biochem. Soc. Trans.* **49**, 393–403 (2021).
15. Sephton, C. F. & Yu, G. The function of RNA-binding proteins at the synapse: Implications for neurodegeneration. *Cell. Mol. Life Sci.* **72**, 3621–3635 (2015).
16. Mohibi, S., Chen, X. & Zhang, J. Cancer the'RBPs'ectics–RNA-binding proteins as therapeutic targets for cancer. *Pharmacol. Ther.* **203**, 107390 (2019).
17. Julio, A. R. & Backus, K. M. New approaches to target RNA binding proteins. *Curr. Opin. Chem. Biol.* **62**, 13–23 (2021).
18. Bertoldo, J. B., Müller, S. & Hüttelmaier, S. RNA-binding proteins in cancer drug discovery. *Drug Discov. Today* **28**, 103580 (2023).
19. Crooke, S. T., Baker, B. F., Crooke, R. M. & Liang, X. hai. Antisense technology: an overview and prospectus. *Nat. Rev. Drug Discov.* **20**, 427–453 (2021).
20. Kuijper, E. C., Bergsma, A. J., Pijnappel, W. W. M. P. & Aartsma-Rus, A. Opportunities and challenges for antisense oligonucleotide therapies. *J. Inherit. Metab. Dis.* **44**, 72–87 (2021).
21. Segal, M. *et al.* Hydrophobically Modified let-7b miRNA Enhances Biodistribution to NSCLC and Downregulates HMGA2 In Vivo. *Mol. Ther. - Nucleic Acids* **19**, 267–277 (2020).
22. Lipinski, C. A. Lead- and drug-like compounds: The rule-of-five revolution. *Drug Discov. Today Technol.* **1**, 337–341 (2004).

References

23. Ambros, V. & Horvitz, H. R. Heterochronic Mutants of the Nematode *Caenorhabditis elegans*. *Science* **226**, 409–416 (1984).
24. Robinton, D. A. *et al.* The Lin28/let-7 Pathway Regulates the Mammalian Caudal Body Axis Elongation Program. *Dev. Cell* **48**, 396-405.e3 (2019).
25. Gulman, N. K., Armon, L., Shalit, T. & Urbach, A. Heterochronic regulation of lung development via the Lin28-Let-7 pathway. *FASEB J.* **33**, 12008–12018 (2019).
26. Yang, D. H. & Moss, E. G. Temporally regulated expression of Lin-28 in diverse tissues of the developing mouse. *Gene Expr. Patterns* **3**, 719–726 (2003).
27. Cao, G., Gao, Z., Jiang, Y. & Chu, M. Lin28 gene and mammalian puberty. *Mol. Reprod. Dev.* **87**, 525–533 (2020).
28. Yu, J. *et al.* Induced Pluripotent Stem Cell Lines Derived from Human Somatic Cells. *Science* **318**, 1917–1920 (2007).
29. Zhang, J. *et al.* LIN28 Regulates Stem Cell Metabolism and Conversion to Primed Pluripotency. *Cell Stem Cell* **19**, 66–80 (2016).
30. Hanna, J. *et al.* Direct cell reprogramming is a stochastic process amenable to acceleration. *Nature* **462**, 595–601 (2009).
31. Hikasa, H., Sekido, Y. & Suzuki, A. Merlin/NF2-Lin28B-let-7 Is a Tumor-Suppressive Pathway that Is Cell-Density Dependent and Hippo Independent. *Cell Rep.* **14**, 2950–2961 (2016).
32. Nam, Y., Chen, C., Gregory, R. I., Chou, J. J. & Sliz, P. Molecular basis for interaction of let-7 MicroRNAs with Lin28. *Cell* **147**, 1080–1091 (2011).
33. Lee, S. H. *et al.* The ubiquitin ligase human TRIM71 regulates let-7 microRNA biogenesis via modulation of Lin28B protein. *Biochim. Biophys. Acta - Gene Regul. Mech.* **1839**, 374–386 (2014).
34. Piskounova, E. *et al.* Lin28A and Lin28B inhibit let-7 MicroRNA biogenesis by distinct mechanisms. *Cell* **147**, 1066–1079 (2011).
35. Balzer, E. & Moss, E. G. Localization of the developmental timing regulator Lin28 to mRNP complexes, P-bodies and stress granules. *RNA Biol.* **4**, 16–25 (2007).
36. Goldstein, J., Pollitt, N. S. & Inouye, M. Major cold shock protein of *Escherichia coli*. *Proc. Natl. Acad. Sci. U. S. A.* **87**, 283–287 (1990).
37. Horn, G., Hofweber, R., Kremer, W. & Kalbitzer, H. R. Structure and function of bacterial cold shock proteins. *Cell. Mol. Life Sci.* **64**, 1457–1470 (2007).
38. Loughlin, F. E. *et al.* Structural basis of pre-let-7 miRNA recognition by the zinc knuckles of pluripotency factor Lin28. *Nat. Struct. Mol. Biol.* **19**, 84–91 (2012).
39. Zeng, Y. *et al.* Lin28A Binds Active Promoters and Recruits Tet1 to Regulate Gene Expression. *Mol. Cell* **61**, 153–160 (2016).
40. Tan, F. E., Sathe, S., Wheeler, E. C. & Yeo, G. W. Non-microRNA binding competitively inhibits LIN28 regulation. *Cell Rep.* **36**, 109517 (2021).
41. Hafner, M. *et al.* Identification of mRNAs bound and regulated by human LIN28 proteins and molecular requirements for RNA recognition. *RNA* **19**, 613–626 (2013).
42. Wilbert, M. L. *et al.* LIN28 binds messenger RNAs at GGAGA motifs and regulates splicing factor abundance. *Mol. Cell* **48**, 195–206 (2012).
43. Xu, B., Zhang, K. & Huang, Y. Lin28 modulates cell growth and associates with a subset of cell cycle regulator mRNAs in mouse embryonic stem cells. *RNA* **15**, 357–361 (2009).
44. Parisi, S. *et al.* Identification of RNA-binding proteins that partner with Lin28a to regulate Dnmt3a expression. *Sci. Rep.* **11**, 1–13 (2021).
45. Peng, S. *et al.* Genome-wide studies reveal that Lin28 enhances the translation of genes important for growth and survival of human embryonic stem cells. *Stem Cells* **29**,

References

- 496–504 (2011).
46. Shyh-Chang, N. *et al.* Lin28 enhances tissue repair by reprogramming cellular metabolism. *Cell* **155**, 778 (2013).
 47. Zhou, J., Ng, S. B. & Chng, W. J. LIN28/LIN28B: An emerging oncogenic driver in cancer stem cells. *Int. J. Biochem. Cell Biol.* **45**, 973–978 (2013).
 48. Ambros, V. The functions of animal microRNAs. *Nature* **431**, 350–355 (2004).
 49. Kozomara, A., Birgaoanu, M. & Griffiths-Jones, S. MiRBase: From microRNA sequences to function. *Nucleic Acids Res.* **47**, D155–D162 (2019).
 50. Cai, X., Hagedorn, C. H. & Cullen, B. R. Human microRNAs are processed from capped, polyadenylated transcripts that can also function as mRNAs. *Rna* **10**, 1957–1966 (2004).
 51. Lee, Y. *et al.* MicroRNA genes are transcribed by RNA polymerase II. *EMBO J.* **23**, 4051–4060 (2004).
 52. Han, J. *et al.* Molecular Basis for the Recognition of Primary microRNAs by the Drosha-DGCR8 Complex. *Cell* **125**, 887–901 (2006).
 53. Basyuk, E., Suavet, F., Doglio, A., Bordonné, R. & Bertrand, E. Human let-7 stem-loop precursors harbor features of RNase III cleavage products. *Nucleic Acids Res.* **31**, 6593–6597 (2003).
 54. Lee, Y. *et al.* The nuclear RNase III Drosha initiates microRNA processing. *Nature* **425**, 415–419 (2003).
 55. Lund, E., Güttinger, S., Calado, A., Dahlberg, J. E. & Kutay, U. Nuclear Export of MicroRNA Precursors. *Science* **303**, 95–98 (2004).
 56. Yi, R., Qin, Y., Macara, I. G. & Cullen, B. R. Exportin-5 mediates the nuclear export of pre-microRNAs and short hairpin RNAs. *Genes Dev.* **17**, 3011–3016 (2003).
 57. Liu, Z. *et al.* Cryo-EM Structure of Human Dicer and Its Complexes with a Pre-miRNA Substrate. *Cell* **173**, 1191–1203.e12 (2018).
 58. Nguyen, T. D., Trinh, T. A., Bao, S. & Nguyen, T. A. Secondary structure RNA elements control the cleavage activity of DICER. *Nat. Commun.* **13**, 1–16 (2022).
 59. Gregory, R. I., Chendrimada, T. P., Cooch, N. & Shiekhattar, R. Human RISC couples microRNA biogenesis and posttranscriptional gene silencing. *Cell* **123**, 631–640 (2005).
 60. Brennecke, J., Stark, A., Russell, R. B. & Cohen, S. M. Principles of microRNA-target recognition. *PLoS Biol.* **3**, 0404–0418 (2005).
 61. Treiber, T., Treiber, N. & Meister, G. Regulation of microRNA biogenesis and its crosstalk with other cellular pathways. *Nat. Rev. Mol. Cell Biol.* **20**, 5–20 (2019).
 62. Ha, M. & Kim, V. N. Regulation of microRNA biogenesis. *Nat. Rev. Mol. Cell Biol.* **15**, 509–524 (2014).
 63. Zheng, X. *et al.* Prediction of miRNA targets by learning from interaction sequences. *PLoS One* **15**, 1–12 (2020).
 64. Petri, R. & Jakobsson, J. Identifying miRNA Targets Using AGO-RIPseq. in *Methods in Molecular Biology* (ed. Lamandé, S. R.) vol. 1720 131–140 (Springer New York, 2018).
 65. Chen, Y. & Wang, X. miRDB: An online database for prediction of functional microRNA targets. *Nucleic Acids Res.* **48**, D127–D131 (2020).
 66. Yong, S. L. & Dutta, A. MicroRNAs in cancer. *Annu. Rev. Pathol. Mech. Dis.* **4**, 199–227 (2009).
 67. Im, H. I. & Kenny, P. J. MicroRNAs in neuronal function and dysfunction. *Trends Neurosci.* **35**, 325–334 (2012).

References

68. Büssing, I., Slack, F. J. & Großhans, H. let-7 microRNAs in development, stem cells and cancer. *Trends Mol. Med.* **14**, 400–409 (2008).
69. Reinhart, B. J. *et al.* The 21-nucleotide let-7 RNA regulates developmental timing in *Caenorhabditis elegans*. *Nature* **403**, 901–906 (2000).
70. Roush, S. & Slack, F. J. The let-7 family of microRNAs. *Trends Cell Biol.* **18**, 505–516 (2008).
71. Lee, H., Han, S., Kwon, C. S. & Lee, D. Biogenesis and regulation of the let-7 miRNAs and their functional implications. *Protein Cell* **7**, 100–113 (2016).
72. Pasquinelli, A. E. *et al.* Conservation of the sequence and temporal expression of let-7 heterochronic regulatory RNA. *Nature* **408**, 86–89 (2000).
73. Johnson, C. D. *et al.* The let-7 microRNA represses cell proliferation pathways in human cells. *Cancer Res.* **67**, 7713–7722 (2007).
74. Takamizawa, J. *et al.* Reduced expression of the let-7 microRNAs in human lung cancers in association with shortened postoperative survival. *Cancer Res.* **64**, 3753–3756 (2004).
75. Johnson, S. M. *et al.* RAS is regulated by the let-7 microRNA family. *Cell* **120**, 635–647 (2005).
76. Thomson, J. M., Parker, J., Perou, C. M. & Hammond, S. M. A custom microarray platform for analysis of microRNA gene expression. *Nat. Methods* **1**, 47–53 (2004).
77. Sempere, L. F. *et al.* Expression profiling of mammalian microRNAs uncovers a subset of brain-expressed microRNAs with possible roles in murine and human neuronal differentiation. *Genome Biol.* **5**, R13 (2004).
78. Sampson, V. B. *et al.* MicroRNA let-7a down-regulates MYC and reverts MYC-induced growth in Burkitt lymphoma cells. *Cancer Res.* **67**, 9762–9770 (2007).
79. Pobezinsky, L. A. *et al.* Let-7 microRNAs target the lineage-specific transcription factor PLZF to regulate terminal NKT cell differentiation and effector function. *Nat. Immunol.* **16**, 517–524 (2015).
80. Malumbres, M. & Barbacid, M. RAS oncogenes: The first 30 years. *Nat. Rev. Cancer* **3**, 459–465 (2003).
81. Shell, S. *et al.* Let-7 expression defines two differentiation stages of cancer. *Proc. Natl. Acad. Sci. U. S. A.* **104**, 11400–11405 (2007).
82. Yu, C. C. *et al.* MicroRNA let-7a represses chemoresistance and tumorigenicity in head and neck cancer via stem-like properties ablation. *Oral Oncol.* **47**, 202–210 (2011).
83. Yu, F. *et al.* let-7 Regulates Self Renewal and Tumorigenicity of Breast Cancer Cells. *Cell* **131**, 1109–1123 (2007).
84. Mayr, F., Schütz, A., Döge, N. & Heinemann, U. The Lin28 cold-shock domain remodels pre-let-7 microRNA. *Nucleic Acids Res.* **40**, 7492–7506 (2012).
85. Treiber, T. *et al.* A Compendium of RNA-Binding Proteins that Regulate MicroRNA Biogenesis. *Mol. Cell* **66**, 270–284.e13 (2017).
86. Heo, I. *et al.* TUT4 in Concert with Lin28 Suppresses MicroRNA Biogenesis through Pre-MicroRNA Uridylation. *Cell* **138**, 696–708 (2009).
87. Triboulet, R., Pirouz, M. & Gregory, R. I. A Single Let-7 MicroRNA Bypasses LIN28-Mediated Repression. *Cell Rep.* **13**, 260–266 (2015).
88. Wang, L. *et al.* LIN28 Zinc Knuckle Domain Is Required and Sufficient to Induce let-7 Oligouridylation. *Cell Rep.* **18**, 2664–2675 (2017).
89. Graf, R. *et al.* Identification of LIN28B-bound mRNAs reveals features of target recognition and regulation. *RNA Biol.* **10**, 1146–1159 (2013).

References

90. Ustianenko, D. *et al.* LIN28 Selectively Modulates a Subclass of Let-7 MicroRNAs. *Mol. Cell* **71**, 271-283.e5 (2018).
91. Thornton, J. E., Chang, H. M., Piskounova, E. & Gregory, R. I. Lin28-mediated control of let-7 microRNA expression by alternative TUTases Zcch85 (TUT4) and Zcchc6 (TUT7). *Rna* **18**, 1875–1885 (2012).
92. Yamashita, S., Nagaike, T. & Tomita, K. Crystal structure of the Lin28-interacting module of human terminal uridylyltransferase that regulates let-7 expression. *Nat. Commun.* **10**, 1–11 (2019).
93. Faehnle, C. R., Walleshauser, J. & Joshua-Tor, L. Multi-domain utilization by TUT4 and TUT7 in control of let-7 biogenesis. *Nat. Struct. Mol. Biol.* **24**, 658–665 (2017).
94. Heo, I. *et al.* Mono-uridylation of pre-microRNA as a key step in the biogenesis of group II let-7 microRNAs. *Cell* **151**, 521–532 (2012).
95. Yeom, K. H. *et al.* Single-molecule approach to immunoprecipitated protein complexes: Insights into miRNA uridylation. *EMBO Rep.* **12**, 690–696 (2011).
96. Chang, H. M., Triboulet, R., Thornton, J. E. & Gregory, R. I. A role for the Perlman syndrome exonuclease Dis3l2 in the Lin28-let-7 pathway. *Nature* **497**, 244–248 (2013).
97. Faehnle, C. R., Walleshauser, J. & Joshua-Tor, L. Mechanism of Dis3l2 substrate recognition in the Lin28-let-7 pathway. *Nature* **514**, 252–256 (2014).
98. Tan, F. E. *et al.* A Transcriptome-wide Translational Program Defined by LIN28B Expression Level. *Mol. Cell* **73**, 304-313.e3 (2019).
99. Shi, F., Yu, W. & Wang, X. Bistable switch in let-7 miRNA biogenesis pathway involving Lin28. *Int. J. Mol. Sci.* **15**, 19119–19133 (2014).
100. Kawahara, H. *et al.* Musashi1 cooperates in abnormal cell lineage protein 28 (Lin28)-mediated let-7 family microRNA biogenesis in early neural differentiation. *J. Biol. Chem.* **286**, 16121–16130 (2011).
101. Viswanathan, S. R. *et al.* Lin28 promotes transformation and is associated with advanced human malignancies. *Nat. Genet.* **41**, 843–848 (2009).
102. Balzeau, J., Menezes, M. R., Cao, S. & Hagan, J. P. The LIN28/let-7 Pathway in Cancer. *Front. Genet.* **8**, 1–16 (2017).
103. Hanahan, D. Hallmarks of Cancer: New Dimensions. *Cancer Discov.* **12**, 31–46 (2022).
104. Hanahan, D. & Weinberg, R. A. Hallmarks of cancer: The next generation. *Cell* **144**, 646–674 (2011).
105. Yang, X. *et al.* Double-negative feedback loop between reprogramming factor LIN28 and microRNA let-7 regulates aldehyde dehydrogenase 1-positive cancer stem cells. *Cancer Res.* **70**, 9463–9472 (2010).
106. Feng, C. *et al.* Lin28 regulates HER2 and promotes malignancy through multiple mechanisms. *Cell Cycle* **11**, 2486–2494 (2012).
107. Hamano, R. *et al.* High expression of Lin28 is associated with tumour aggressiveness and poor prognosis of patients in oesophagus cancer. *Br. J. Cancer* **106**, 1415–1423 (2012).
108. King, C. E. *et al.* LIN28B promotes colon cancer progression and metastasis. *Cancer Res.* **71**, 4260–4268 (2011).
109. Lekka, E. *et al.* Pharmacological inhibition of Lin28 promotes ketogenesis and restores lipid homeostasis in models of non-alcoholic fatty liver disease. *Nat. Commun.* **13**, 7940 (2022).
110. Chen, Y. *et al.* LIN28/let-7/PD-L1 pathway as a target for cancer immunotherapy. *Cancer Immunol. Res.* **7**, 487–497 (2019).
111. Xie, C. *et al.* Therapeutic potential of C1632 by inhibition of SARS-CoV-2 replication

References

- and viral-induced inflammation through upregulating let-7. *Signal Transduct. Target. Ther.* **6**, 84 (2021).
112. Trang, P. *et al.* Regression of murine lung tumors by the let-7 microRNA. *Oncogene* **29**, 1580–1587 (2010).
 113. Ghidini, A., Cléry, A., Halloy, F., Allain, F. H. T. & Hall, J. RNA-PROTACs: Degraders of RNA-Binding Proteins. *Angew. Chemie - Int. Ed.* **60**, 3163–3169 (2021).
 114. Békés, M., Langley, D. R. & Crews, C. M. PROTAC targeted protein degraders: the past is prologue. *Nat. Rev. Drug Discov.* **21**, 181–200 (2022).
 115. Roos, M. *et al.* A Small-Molecule Inhibitor of Lin28. *ACS Chem. Biol.* **11**, 2773–2781 (2016).
 116. Lim, D., Byun, W. G., Koo, J. Y., Park, H. & Park, S. B. Discovery of a Small-Molecule Inhibitor of Protein-MicroRNA Interaction Using Binding Assay with a Site-Specifically Labeled Lin28. *J. Am. Chem. Soc.* **138**, 13630–13638 (2016).
 117. Lightfoot, H. L., Miska, E. A. & Balasubramanian, S. Identification of small molecule inhibitors of the Lin28-mediated blockage of pre-let-7g processing. *Org. Biomol. Chem.* **14**, 10208–10216 (2016).
 118. Wang, L. *et al.* Small-Molecule Inhibitors Disrupt let-7 Oligouridylation and Release the Selective Blockade of let-7 Processing by LIN28. *Cell Rep.* **23**, 3091–3101 (2018).
 119. Lim, D., Byun, W. G. & Park, S. B. Restoring Let-7 microRNA Biogenesis Using a Small-Molecule Inhibitor of the Protein-RNA Interaction. *ACS Med. Chem. Lett.* **9**, 1181–1185 (2018).
 120. Byun, W. G., Lim, D. & Park, S. B. Discovery of Small-Molecule Modulators of Protein–RNA Interactions by Fluorescence Intensity-Based Binding Assay. *ChemBioChem* **21**, 818–824 (2020).
 121. Lorenz, D. A. *et al.* Expansion of cat-ELCCA for the Discovery of Small Molecule Inhibitors of the Pre-let-7–Lin28 RNA–Protein Interaction. *ACS Med. Chem. Lett.* **9**, 517–521 (2018).
 122. Radaeva, M. *et al.* Discovery of Novel Lin28 Inhibitors to Suppress Cancer Cell Stemness. *Cancers (Basel)*. **14**, 5687 (2022).
 123. Yu, C. *et al.* A nanobody targeting the LIN28:let-7 interaction fragment of TUT4 blocks uridylation of let-7. *Proc. Natl. Acad. Sci. U. S. A.* **117**, 4653–4663 (2020).
 124. Lin, S. & Gregory, R. I. Identification of small molecule inhibitors of Zcch85 TUTase activity. *RNA Biol.* **12**, 792–800 (2015).
 125. Cinkornpumin, J. *et al.* A small molecule screen to identify regulators of let-7 targets. *Sci. Rep.* **7**, 1–10 (2017).
 126. Roos, M. *et al.* Short loop-targeting oligoribonucleotides antagonize Lin28 and enable pre-let-7 processing and suppression of cell growth in let-7-deficient cancer cells. *Nucleic Acids Res.* **43**, e9–e9 (2015).
 127. Silverman, R. H. A scientific journey through the 2-5A/RNase L system. *Cytokine Growth Factor Rev.* **18**, 381–388 (2007).
 128. Nilsen, T. W., Maroney, P. A., Robertson, H. D. & Baglioni, C. Heterogeneous nuclear RNA promotes synthesis of (2',5')oligoadenylate and is cleaved by the (2',5')oligoadenylate-activated endoribonuclease. *Mol. Cell. Biol.* **2**, 154–160 (1982).
 129. Nilsen, T. W., Maroney, P. A. & Baglioni, C. Double-stranded RNA causes synthesis of 2',5'-oligo(A) and degradation of messenger RNA in interferon-treated cells. *J. Biol. Chem.* **256**, 7806–7811 (1981).
 130. Lohöfener, J. *et al.* The Activation Mechanism of 2'-5'-Oligoadenylate Synthetase Gives New Insights Into OAS/cGAS Triggers of Innate Immunity. *Structure* **23**, 851–862

References

- (2015).
131. Rebouillat, D., Hovnanian, A., Marié, I. & Hovanessian, A. G. The 100-kDa 2',5'-oligoadenylate synthetase catalyzing preferentially the synthesis of dimeric pppA2'p5'A molecules is composed of three homologous domains. *J. Biol. Chem.* **274**, 1557–1565 (1999).
 132. Zhou, A., Hassel, B. A. & Silverman, R. H. Expression cloning of 2-5A-dependent RNAase: A uniquely regulated mediator of interferon action. *Cell* **72**, 753–765 (1993).
 133. Han, Y., Whitney, G., Donovan, J. & Korennykh, A. Innate Immune Messenger 2-5A Tethers Human RNase L into Active High-Order Complexes. *Cell Rep.* **2**, 902–913 (2012).
 134. Huang, H. *et al.* Dimeric Structure of Pseudokinase RNase L Bound to 2-5A Reveals a Basis for Interferon-Induced Antiviral Activity. *Mol. Cell* **53**, 221–234 (2014).
 135. Han, Y. *et al.* Structure of Human RNase L Reveals the Basis for Regulated RNA Decay in the IFN Response. *Science* **343**, 1244–1248 (2014).
 136. Knight, M. *et al.* Radioimmune, radiobinding and HPLC analysis of 2-5A and related oligonucleotides from intact cells. *Nature* **288**, 189–192 (1980).
 137. Donovan, J., Rath, S., Kolet-Mandrikov, D. & Korennykh, A. Rapid RNase L–driven arrest of protein synthesis in the dsRNA response without degradation of translation machinery. *RNA* **23**, 1660–1671 (2017).
 138. Rath, S. *et al.* Concerted 2-5A-Mediated mRNA Decay and Transcription Reprogram Protein Synthesis in the dsRNA Response. *Mol. Cell* **75**, 1218-1228.e6 (2019).
 139. Chakrabarti, A. *et al.* RNase L Activates the NLRP3 Inflammasome during Viral Infections. *Cell Host Microbe* **17**, 466–477 (2015).
 140. Cooper, D. A., Jha, B. K., Silverman, R. H., Hesselberth, J. R. & Barton, D. J. Ribonuclease L and metal-ion-independent endoribonuclease cleavage sites in host and viral RNAs. *Nucleic Acids Res.* **42**, 5202–5216 (2014).
 141. Yu, G., Yang, Z., Peng, T. & Lv, Y. Circular RNAs: Rising stars in lipid metabolism and lipid disorders. *J. Cell. Physiol.* **236**, 4797–4806 (2021).
 142. Le Roy, F. *et al.* The 2-5A/RNase L/RNase L Inhibitor (RNI) Pathway Regulates Mitochondrial mRNAs Stability in Interferon α -treated H9 Cells. *J. Biol. Chem.* **276**, 48473–48482 (2001).
 143. Burke, J. M., Gilchrist, A. R., Sawyer, S. L. & Parker, R. RNase L limits host and viral protein synthesis via inhibition of mRNA export. *Sci. Adv.* **7**, eabh2479 (2021).
 144. Chitrakar, A. *et al.* Real-time 2-5A kinetics suggest that interferons β and λ evade global arrest of translation by RNase L. *Proc. Natl. Acad. Sci. U. S. A.* **116**, 2103–2111 (2019).
 145. Burke, J. M., St Clair, L. A., Perera, R. & Parker, R. Rapid decay of host basal mRNAs during SARS-CoV-2 infection perturbs host antiviral mRNA biogenesis and export. *bioRxiv Prepr. Serv. Biol.* (2021) doi:10.1101/2021.04.19.440452.
 146. Karasik, A., Jones, G. D., DePass, A. V & Guydosh, N. R. Activation of the antiviral factor RNase L triggers translation of non-coding mRNA sequences. *Nucleic Acids Res.* **58**, 7250–7257 (2021).
 147. Malathi, K., Dong, B., Gale, M. & Silverman, R. H. Small self-RNA generated by RNase L amplifies antiviral innate immunity. *Nature* **448**, 816–819 (2007).
 148. Borden, E. C. *et al.* Interferons at age 50: Past, current and future impact on biomedicine. *Nat. Rev. Drug Discov.* **6**, 975–990 (2007).
 149. Der, S. D., Zhou, A., Williams, B. R. G. & Silverman, R. H. Identification of genes differentially regulated by interferon α , β , or γ using oligonucleotide arrays. *Proc. Natl. Acad. Sci. U. S. A.* **95**, 15623–15628 (1998).

References

150. Manivannan, P., Reddy, V., Mukherjee, S., Clark, K. N. & Malathi, K. RNase L Induces Expression of A Novel Serine/Threonine Protein Kinase, DRAK1, to Promote Apoptosis. *Int. J. Mol. Sci.* **20**, 3535 (2019).
151. Castelli, J. A. C. *et al.* A study of the interferon antiviral mechanism: Apoptosis activation by the 2-5A system. *J. Exp. Med.* **186**, 967–972 (1997).
152. Zhou, A. *et al.* Impact of RNase L overexpression on viral and cellular growth and death. *J. Interf. Cytokine Res.* **18**, 953–961 (1998).
153. Burke, J. M., Lester, E. T., Tauber, D. & Parker, R. RNase L promotes the formation of unique ribonucleoprotein granules distinct from stress granules. *J. Biol. Chem.* **295**, 1426–1438 (2020).
154. Burke, J. M. Regulation of ribonucleoprotein condensates by RNase L during viral infection. *Wiley Interdiscip. Rev. RNA* e1770 (2022) doi:10.1002/wrna.1770.
155. Tanaka, N. *et al.* Structural basis for recognition of 2',5'-linked oligoadenylates by human ribonuclease L. *EMBO J.* **23**, 3929–3938 (2004).
156. Lášek, T. *et al.* 5'-Phosphonate modified oligoadenylates as potent activators of human RNase L. *Bioorg. Med. Chem.* **56**, 116632 (2022).
157. Thakur, C. S. *et al.* Small-molecule activators of RNase L with broad-spectrum antiviral activity. *Proc. Natl. Acad. Sci.* **104**, 9585–9590 (2007).
158. Silverman, R. H. *et al.* Purification and analysis of murine 2-5A-dependent RNase. *J. Biol. Chem.* **263**, 7336–7341 (1988).
159. Kubota, K. *et al.* Identification of 2'-phosphodiesterase, which plays a role in the 2-5A system regulated by interferon. *J. Biol. Chem.* **279**, 37832–37841 (2004).
160. Bisbal, C., Martinand, C., Silhol, M., Lebleu, B. & Salehzada, T. Cloning and characterization of a RNase L inhibitor. A new component of the interferon-regulated 2-5A pathway. *Journal of Biological Chemistry* vol. 270 13308–13317 (1995).
161. Li, Y. *et al.* Ribonuclease I mediates the cell-lethal phenotype of double-stranded RNA editing enzyme ADAR1 deficiency in a human cell line. *Elife* **6**, 1–18 (2017).
162. Gusho, E., Baskar, D. & Banerjee, S. New advances in our understanding of the “unique” RNase L in host pathogen interaction and immune signaling. *Cytokine* **133**, 153847 (2020).
163. Casey, G. *et al.* RNASEL Arg462Gln variant is implicated in up to 13% of prostate cancer cases. *Nat. Genet.* **32**, 581–583 (2002).
164. Banerjee, S. *et al.* RNase L is a negative regulator of cell migration. *Oncotarget* **6**, 44360–44372 (2015).
165. Nijs, J. & De Meirleir, K. Impairments of the 2-5A synthetase/RNase L pathway on chronic fatigue syndrome. *In Vivo (Brooklyn)*. **19**, 1013–1022 (2005).
166. Suhadolnik, R. J. *et al.* Biochemical evidence for a novel low molecular weight 2-5A-dependent RNase L in chronic fatigue syndrome. *J. Interf. Cytokine Res.* **17**, 377–385 (1997).
167. Prangley, E. & Korennykh, A. 2-5A-Mediated decay (2-5AMD): from antiviral defense to control of host RNA. *Crit. Rev. Biochem. Mol. Biol.* **57**, 477–491 (2022).
168. Meyer, S. M. *et al.* DNA-Encoded Library Screening To Inform Design of a Ribonuclease Targeting Chimera (RiboTAC). *J. Am. Chem. Soc.* **144**, 21096–21102 (2022).
169. Costales, M. G. *et al.* Small-molecule targeted recruitment of a nuclease to cleave an oncogenic RNA in a mouse model of metastatic cancer. *Proc. Natl. Acad. Sci.* **117**, 2406–2411 (2020).
170. Haniff, H. S. *et al.* Targeting the SARS-CoV-2 RNA Genome with Small Molecule

References

- Binders and Ribonuclease Targeting Chimera (RIBOTAC) Degraders. *ACS Cent. Sci.* **6**, 1713–1721 (2020).
171. Jha, B. K., Dong, B., Nguyen, C. T., Polyakova, I. & Silverman, R. H. Suppression of antiviral innate immunity by sunitinib enhances oncolytic virotherapy. *Mol. Ther.* **21**, 1749–1757 (2013).
172. Jha, B. K. *et al.* Inhibition of RNase L and RNA-dependent protein kinase (PKR) by sunitinib impairs antiviral innate immunity. *J. Biol. Chem.* **286**, 26319–26326 (2011).
173. Tang, J. *et al.* Identification of Small Molecule Inhibitors of RNase L by Fragment-Based Drug Discovery. *J. Med. Chem.* **65**, 1445–1457 (2022).
174. Daou, S. *et al.* A phenolic small molecule inhibitor of RNase L prevents cell death from ADAR1 deficiency. *Proc. Natl. Acad. Sci. U. S. A.* **117**, 24802–24812 (2020).
175. Torrence, P. F. *et al.* Targeting RNA for degradation with a (2'-5')oligoadenylate-antisense chimera. *Proc. Natl. Acad. Sci. U. S. A.* **90**, 1300–1304 (1993).
176. Costales, M. G., Matsumoto, Y., Velagapudi, S. P. & Disney, M. D. Small Molecule Targeted Recruitment of a Nuclease to RNA. *J. Am. Chem. Soc.* **140**, 6741–6744 (2018).
177. Zhang, P. *et al.* Reprogramming of Protein-Targeted Small-Molecule Medicines to RNA by Ribonuclease Recruitment. *J. Am. Chem. Soc.* **143**, 13044–13055 (2021).
178. Liu, X. *et al.* Targeted Degradation of the Oncogenic MicroRNA 17-92 Cluster by Structure-Targeting Ligands. *J. Am. Chem. Soc.* **142**, 6970–6982 (2020).
179. Bush, J. A. *et al.* Ribonuclease recruitment using a small molecule reduced c9ALS/FTD r(G 4 C 2) repeat expansion in vitro and in vivo ALS models. *Sci. Transl. Med.* **13**, 1–14 (2021).
180. Tong, Y. *et al.* Transcriptome-Wide Mapping of Small-Molecule RNA-Binding Sites in Cells Informs an Isoform-Specific Degradation of QSOX1 mRNA. *J. Am. Chem. Soc.* **144**, 11620–11625 (2022).
181. Tong, Y. *et al.* Programming inactive RNA-binding small molecules into bioactive degraders. *Nature* **618**, 169–179 (2023).
182. Benhamou, R. I. *et al.* Structure-Specific Cleavage of an RNA Repeat Expansion with a Dimeric Small Molecule Is Advantageous over Sequence-Specific Recognition by an Oligonucleotide. *ACS Chem. Biol.* **15**, 485–493 (2020).
183. Martin, C. *et al.* Design, Synthesis, and Evaluation of Neomycin-Imidazole Conjugates for RNA Cleavage. *Chempluschem* **87**, e202200250 (2022).
184. Mikutis, S. *et al.* Proximity-Induced Nucleic Acid Degradation (PINAD) Approach to Targeted RNA Degradation Using Small Molecules. *ACS Cent. Sci.* **9**, 892–904 (2023).
185. Heng, D. Y. C. & Kollmannsberger, C. *Small Molecules in Oncology*. vol. 184 (Springer Berlin Heidelberg, 2010).
186. Tang, J. *et al.* Sunitinib inhibits RNase L by destabilizing its active dimer conformation. *Biochem. J.* **477**, 3387–3399 (2020).
187. Donovan, J., Whitney, G., Rath, S. & Korennykh, A. Structural mechanism of sensing long dsRNA via a noncatalytic domain in human oligoadenylate synthetase 3. *Proc. Natl. Acad. Sci. U. S. A.* **112**, 3949–3954 (2015).
188. Koul, A. *et al.* Impact of double-stranded RNA characteristics on the activation of human 2'-5'-oligoadenylate synthetase 2 (OAS2). *Biochem. Cell Biol.* **98**, 70–82 (2020).
189. Hovnanian, A. *et al.* The Human 2',5'-Oligoadenylate Synthetase Locus Is Composed of Three Distinct Genes Clustered on Chromosome 12q24.2 Encoding the 100-, 69-, and 40-kDa Forms. *Genomics* **52**, 267–277 (1998).
190. Ibsen, M. S. *et al.* The 2'-5'-Oligoadenylate Synthetase 3 Enzyme Potently Synthesizes

References

- the 2'-5'-Oligoadenylates Required for RNase L Activation. *J. Virol.* **88**, 14222–14231 (2014).
191. Donovan, J., Dufner, M. & Korennykh, A. Structural basis for cytosolic double-stranded RNA surveillance by human oligoadenylate synthetase 1. *Proc. Natl. Acad. Sci. U. S. A.* **110**, 1652–1657 (2013).
 192. Sarkar, S. N., Ghosh, A., Wang, H., Sung, S. & Sen, G. C. The Nature of the Catalytic Domain of 2'-5'-Oligoadenylate Synthetases. *J. Biol. Chem.* **274**, 25535–25542 (1999).
 193. Kodym, R., Kodym, E. & Story, M. D. 2'-5'-Oligoadenylate synthetase is activated by a specific RNA sequence motif. *Biochem. Biophys. Res. Commun.* **388**, 317–322 (2009).
 194. Schwartz, S. L. & Conn, G. L. RNA regulation of the antiviral protein 2'-5'-oligoadenylate synthetase. *Wiley Interdiscip. Rev. RNA* **10**, (2019).
 195. Hornung, V., Hartmann, R., Ablasser, A. & Hopfner, K. P. OAS proteins and cGAS: Unifying concepts in sensing and responding to cytosolic nucleic acids. *Nat. Rev. Immunol.* **14**, 521–528 (2014).
 196. Gonzalez, K. J., Moncada-Giraldo, D. M. & Gutierrez, J. B. In silico identification of potential inhibitors against human 2'-5'- oligoadenylate synthetase (OAS) proteins. *Comput. Biol. Chem.* **85**, 107211 (2020).
 197. Yu, C. *et al.* Prediction of key genes and pathways involved in trastuzumab-resistant gastric cancer. 1–12 (2018).
 198. Feng, X. *et al.* Association of increased interferon-inducible gene expression with disease activity and lupus nephritis in patients with systemic lupus erythematosus. *Arthritis Rheum.* **54**, 2951–2962 (2006).
 199. Tang, J. *et al.* Increased expression of the type I interferon-inducible gene, lymphocyte antigen 6 complex locus E, in peripheral blood cells is predictive of lupus activity in a large cohort of Chinese lupus patients. *Lupus* **17**, 805–813 (2008).
 200. Hartmann, R., Walko, G. & Justesen, J. Inhibition of 2'-5' oligoadenylate synthetase by divalent metal ions. *FEBS Lett.* **507**, 54–58 (2001).
 201. Zhou, S. *et al.* A Neanderthal OAS1 isoform protects individuals of European ancestry against COVID-19 susceptibility and severity. *Nat. Med.* **27**, 659–667 (2021).
 202. Wickenhagen, A. *et al.* A prenylated dsRNA sensor protects against severe COVID-19. *Science* **374**, eabj3624 (2021).
 203. Ushijima, H. *et al.* Mode of action of the anti-AIDS compound poly(I).poly(C12U) (Ampligen): activator of 2',5'-oligoadenylate synthetase and double-stranded RNA-dependent kinase. *J. Interferon Res.* **13**, 161–71 (1993).
 204. Mitchell, W. M. Efficacy of rintatolimod in the treatment of chronic fatigue syndrome/myalgic encephalomyelitis (CFS/ME). *Expert Rev. Clin. Pharmacol.* **9**, 755–770 (2016).
 205. Li, M. Z. & Elledge, S. J. Harnessing homologous recombination in vitro to generate recombinant DNA via SLIC. *Nat. Methods* **4**, 251–256 (2007).
 206. Pattillo, R. A.; Ruckert, A.; Hussa, R. O.; Bernstein, R.; Delfs, E. The Jar cell line. Continuous human multihormone production and controls. *In Vitro* **6**, 398–399 (1971).
 207. Livak, K. J. & Schmittgen, T. D. Analysis of relative gene expression data using real-time quantitative PCR and the 2- $\Delta\Delta$ CT method. *Methods* **25**, 402–408 (2001).
 208. Reckzeh, E. S., Brockmeyer, A., Metz, M., Waldmann, H. & Janning, P. Target engagement of small molecules: Thermal profiling approaches on different levels. *Methods Mol. Biol.* **1888**, 73–98 (2019).
 209. Thakur, C. S., Xu, Z., Wang, Z., Novince, Z. & Silverman, R. H. A Convenient and Sensitive Fluorescence Resonance Energy Transfer Assay for RNase L and 2',5'

References

- Oligoadenylates. in *Interferon Methods and Protocols* (ed. Carr, D. J.) vol. 3 103–113 (Humana Press, 2005).
210. Vachon, V. K., Calderon, B. M. & Conn, G. L. A novel RNA molecular signature for activation of 2'-5' oligoadenylate synthetase-1. *Nucleic Acids Res.* **43**, 544–552 (2015).
211. Borgelt, L. *et al.* Trisubstituted Pyrrolinones as Small-Molecule Inhibitors Disrupting the Protein–RNA Interaction of LIN28 and Let-7. *ACS Med. Chem. Lett.* **12**, 893–898 (2021).
212. Richter, A., Rose, R., Hedberg, C., Waldmann, H. & Ottmann, C. An optimised small-molecule stabiliser of the 14-3-3-PMA2 protein-protein interaction. *Chem. - A Eur. J.* **18**, 6520–6527 (2012).
213. Ballatore, C., Hury, D. M. & Smith, A. B. Carboxylic Acid (Bio)Isosteres in Drug Design. *ChemMedChem* **8**, 385–395 (2013).
214. Bosica, F. *et al.* Design of Drug-Like Protein–Protein Interaction Stabilizers Guided By Chelation-Controlled Bioactive Conformation Stabilization. *Chem. - A Eur. J.* **26**, 7131–7139 (2020).
215. Borgelt, L. *et al.* Spirocyclic Chromenopyrazole Inhibitors Disrupting the Interaction between the RNA-binding protein LIN28 and Let-7. *Chembiochem* e202300168 (2023) doi:10.1002/cbic.202300168.
216. Hommen, P. *et al.* Chromenopyrazole–peptide conjugates as small-molecule based inhibitors disrupting the protein–RNA interaction of LIN28–let-7. *ChemBioChem* e202300376 (2023) doi:10.1002/cbic.202300376.
217. Goebel, G. L. *et al.* Small molecules with tetrahydroquinoline-containing Povarov scaffolds as inhibitors disrupting the Protein–RNA interaction of LIN28–let-7. *Eur. J. Med. Chem.* **228**, 114014 (2022).
218. Talele, T. T. Opportunities for Tapping into Three-Dimensional Chemical Space through a Quaternary Carbon. *J. Med. Chem.* **63**, 13291–13315 (2020).
219. Zheng, Y., Tice, C. M. & Singh, S. B. The use of spirocyclic scaffolds in drug discovery. *Bioorganic Med. Chem. Lett.* **24**, 3673–3682 (2014).
220. Hiesinger, K., Dar'In, D., Proschak, E. & Krasavin, M. Spirocyclic Scaffolds in Medicinal Chemistry. *J. Med. Chem.* **64**, 150–183 (2021).
221. Borgelt, L. *et al.* Small-molecule screening of ribonuclease L binders for RNA degradation. *Biomed. Pharmacother.* **154**, 113589 (2022).
222. Simeonov, A. *et al.* Fluorescence spectroscopic profiling of compound libraries. *J. Med. Chem.* **51**, 2363–2371 (2008).
223. Baell, J. B. & Holloway, G. A. New substructure filters for removal of pan assay interference compounds (PAINS) from screening libraries and for their exclusion in bioassays. *J. Med. Chem.* **53**, 2719–2740 (2010).
224. Hwang, J. *et al.* Synthesis and evaluation of RNase L-binding 2-aminothiophenes as anticancer agents. *Bioorg. Med. Chem.* **58**, 116653 (2022).
225. Hwang, J. *et al.* Rational design and evaluation of 2-((pyrrol-2-yl)methylene)thiophen-4-ones as RNase L inhibitors. *Eur. J. Med. Chem.* **256**, 115439 (2023).
226. Lee, T. Y. *et al.* Regulation of human RNase-L by the miR-29 family reveals a novel oncogenic role in chronic myelogenous leukemia. *J. Interf. Cytokine Res.* **33**, 34–42 (2013).
227. Zhang, P. *et al.* Reprogramming of Protein-Targeted Small-Molecule Medicines to RNA by Ribonuclease Recruitment. *J. Am. Chem. Soc.* **143**, 13044–13055 (2021).
228. Wang, L. *et al.* Divergent allosteric control of the IRE1 α endoribonuclease using kinase inhibitors. *Nat. Chem. Biol.* **8**, 982–989 (2012).

References

229. Feldman, H. C. *et al.* Structural and Functional Analysis of the Allosteric Inhibition of IRE1 α with ATP-Competitive Ligands. *ACS Chem. Biol.* **11**, 2195–2205 (2016).
230. Korennykh, A. V. *et al.* The unfolded protein response signals through high-order assembly of Ire1. *Nature* **457**, 687–693 (2009).
231. Marie, I., Svab, J., Robert, N., Galabru, J. & Hovanessian, A. G. Differential expression and distinct structure of 69- and 100-kDa forms of 2-5A synthetase in human cells treated with interferon. *J. Biol. Chem.* **265**, 18601–18607 (1990).
232. Ghosh, A., Sarkar, S. N., Guo, W., Bandyopadhyay, S. & Sen, G. C. Enzymatic activity of 2'-5'-oligoadenylate synthetase is impaired by specific mutations that affect oligomerization of the protein. *J. Biol. Chem.* **272**, 33220–33226 (1997).
233. Putnins, R. F. & Yamada, E. W. Colorimetric determination of inorganic pyrophosphate by a manual or automated method. *Anal. Biochem.* **68**, 185–195 (1975).
234. Dang, C. V., Reddy, E. P., Shokat, K. M. & Soucek, L. Drugging the 'undruggable' cancer targets. *Nat. Rev. Cancer* **17**, 502–508 (2017).
235. Scott, D. E., Bayly, A. R., Abell, C. & Skidmore, J. Small molecules, big targets: Drug discovery faces the protein-protein interaction challenge. *Nat. Rev. Drug Discov.* **15**, 533–550 (2016).
236. Decout, A., Katz, J. D., Venkatraman, S. & Ablasser, A. The cGAS–STING pathway as a therapeutic target in inflammatory diseases. *Nat. Rev. Immunol.* **21**, 548–569 (2021).

7 Abbreviations

Abbreviation	Explanation
2'-5'A	5'-phosphorylated 2',5'-linked oligoadenylates
ABCE1	ATP-binding cassette sub-family E member 1
ADAR1	Double-stranded RNA-specific adenosine deaminase
ADME	Absorption, distribution, metabolism and excretion
ADP	Adenosine diphosphate
AGO	Argonaute
AGS	Aicardi-Goutières syndrome
ANK	Ankyrin repeat domain
APS	Ammonium persulfate
ATP	Adenosine triphosphate
ATPC	2-Aminothiophen-4-one-3-carboxylate
Bis-Tris	2,2-Bis(hydroxymethyl)-2,2',2''-nitrilotriethanol
BLI	Bio-layer interferometry
BSA	Bovine serum albumin
cat-ELCCA	Catalytic enzyme-linked click chemistry assay
CDC25A	M-phase inducer phosphatase 1
CDK6	Cyclin-dependent kinase 6
CETSA	Cellular thermal shift assay
CFS	Chronic fatigue syndrome
cGAS	Cyclic GMP-AMP synthase
circRNA	Circular RNA
CLIP	cross-linking and immunoprecipitation
COMAS	Compound Management and Screening Center
COVID	Coronavirus disease
CSD	Cold shock domain
CSD ⁻	miRNA without (U)GAU motif
CSD ⁺	miRNA containing (U)GAU motif
Cy3	Cyanine3 dye
Cy5	Cyanine5 dye
Da	Dalton
DEL	DNA-encoded library
DEPC	Diethyl pyrocarbonate
DIS3L2	DIS3-like exonuclease 2
DMSO	Dimethyl sulfoxide
DNA	Deoxyribonucleic acid
dsDNA	Double-stranded DNA
dsRNA	Double-stranded RNA
DTT	Dithiothreitol
EC ₅₀	Half maximal effective concentration
EDTA	Ethylenediaminetetraacetic acid
EGFP	Enhanced green fluorescent protein

Abbreviations

eIF4A	Eukaryotic initiation factor 4A
eIF4G	Eukaryotic translation initiation factor 4 gamma
ELAV1	ELAV-like protein 1
ELISA	Enzyme-linked immunosorbent assay
EMSA	Electrophoretic mobility shift assay
ENCODE	Encyclopedia of DNA Elements
FAM	6-Carboxyfluorescein
FBS	Fetal bovine serum
FDA	United States food and drug administration
FI	Fluorescence intensity
FP	Fluorescence polarization
FRET	Förster resonance energy transfer
GTP	Guanosine 5'-triphosphate
HEPES	4-(2-hydroxyethyl)-1-piperazineethanesulfonic acid
HER2	Receptor tyrosine-protein kinase erbB-2
His ₆	Hexahistidine
HIV	Human immunodeficiency virus
HRP	Horseradish peroxidase
IC ₅₀	Half maximal inhibitory concentration
IFN	Interferon
IGF2BP1/2	Insulin-like growth factor 2 mRNA-binding protein 1/2
IPTG	Isopropyl β-D-1-thiogalactopyranoside
IRE1	Serine/threonine-protein kinase/endoribonuclease IRE1
KEN	Kinase-extension nuclease domain
LB	Lysogeny broth
<i>let-7</i>	<i>Lethal-7</i>
LIN28	Protein lin-28
LIN28A	Protein lin-28 homolog A
LIN28B	Protein lin-28 homolog B
MDA5	Melanoma differentiation-associated protein 5 / Interferon-induced helicase C domain-containing protein 1
METTL3	N6-adenosine-methyltransferase catalytic subunit
miRNA	Micro ribonucleic acid
mRNA	Messenger ribonucleic acid
MSI1/2	RNA-binding protein Musashi homolog 1/2
MST	Microscale Thermophoresis
MWCO	Molecular weight cut-off
MYC	Myc proto-oncogene protein
nanoDSF	Nano differential scanning fluorimetry
NHS	N-Hydroxysuccinimide
OAS	2'-5'-oligoadenylate synthase
OD	Optical density
PAGE	Polyacrylamide gel electrophoresis
PAINS	Pan-assay interference compounds

Abbreviations

PAMP	Pathogen associated molecular pattern
PAR-CLIP	Photoactivatable-ribonucleoside- enhanced crosslinking and immunoprecipitation
PBS	Phosphate buffered saline
PCR	Polymerase chain reaction
PEG	Polyethylene glycol
PIPES	1,4-Piperazinediethanesulfonic acid
PK	Pseudokinase domain
PMSF	Phenylmethanesulfonyl fluoride
Poly I:C	Polyinosinic-polycytidylic acid
PP _i	Inorganic pyrophosphate
PPI	Protein–protein interaction
preE	Precursor element
pre-miRNA	Precursor micro RNA
pri-miRNA	Primary transcript micro RNA
PROTAC	Proteolysis-targeting chimera
qPCR	Quantitative polymerase chain reaction
RAN	GTP-binding nuclear protein Ran
RBP	RNA-binding protein
RIBOTAC	Ribonuclease targeting chimera
RIG-I	Antiviral innate immune response receptor RIG-I
RIPA	Radioimmunoprecipitation assay
RISC	RNA-induced silencing complex
RMSD	Root-mean square deviation
RNA	Ribonucleic acid
RNase	Ribonuclease
RNase L	Ribonuclease L / 2-5A-dependent ribonuclease
rpm	Revolutions per minute
rRNA	Ribosomal ribonucleic acid
SAR	Structure–activity relationship
SARS-CoV-2	Severe acute respiratory syndrome coronavirus 2
SD	Standard deviation
SDS	Sodium dodecyl sulfate
SLIC	Sequence and ligation independent cloning
SPR	Surface plasmon resonance
ssDNA	Single-stranded DNA
ssRNA	Single-stranded RNA
SUMO	Small ubiquitin-related modifier
TAMRA	5-Carboxytetramethylrhodamin
TARBP2	RISC-loading complex subunit TARBP2
TCEP	Tris(2-carboxyethyl)phosphine
TEMED	N,N,N',N'-Tetramethylethylenediamine
TEV protease	Tobacco Etch Virus nuclear-inclusion-a endopeptidase
TFA	Trifluoroacetic Acid
Tris	Tris(hydroxymethyl)aminomethane

Abbreviations

tRNA	Transfer ribonucleic acid
TUT4	Terminal uridylyltransferase 4
TUT7	Terminal uridylyltransferase 7
UBL	Ubiquitin-like domain
VHL	Von Hippel-Lindau
YTHDF1/2	YTH domain-containing family protein 1/2
ZBTB16	Zinc finger and BTB domain-containing protein 16
ZKD	Zinc knuckle domain
β-ME	β-Mercaptoethanol

8 Appendix

8.1 Plasmid maps



pET19a-His-TEV-LIN28A(16-187)

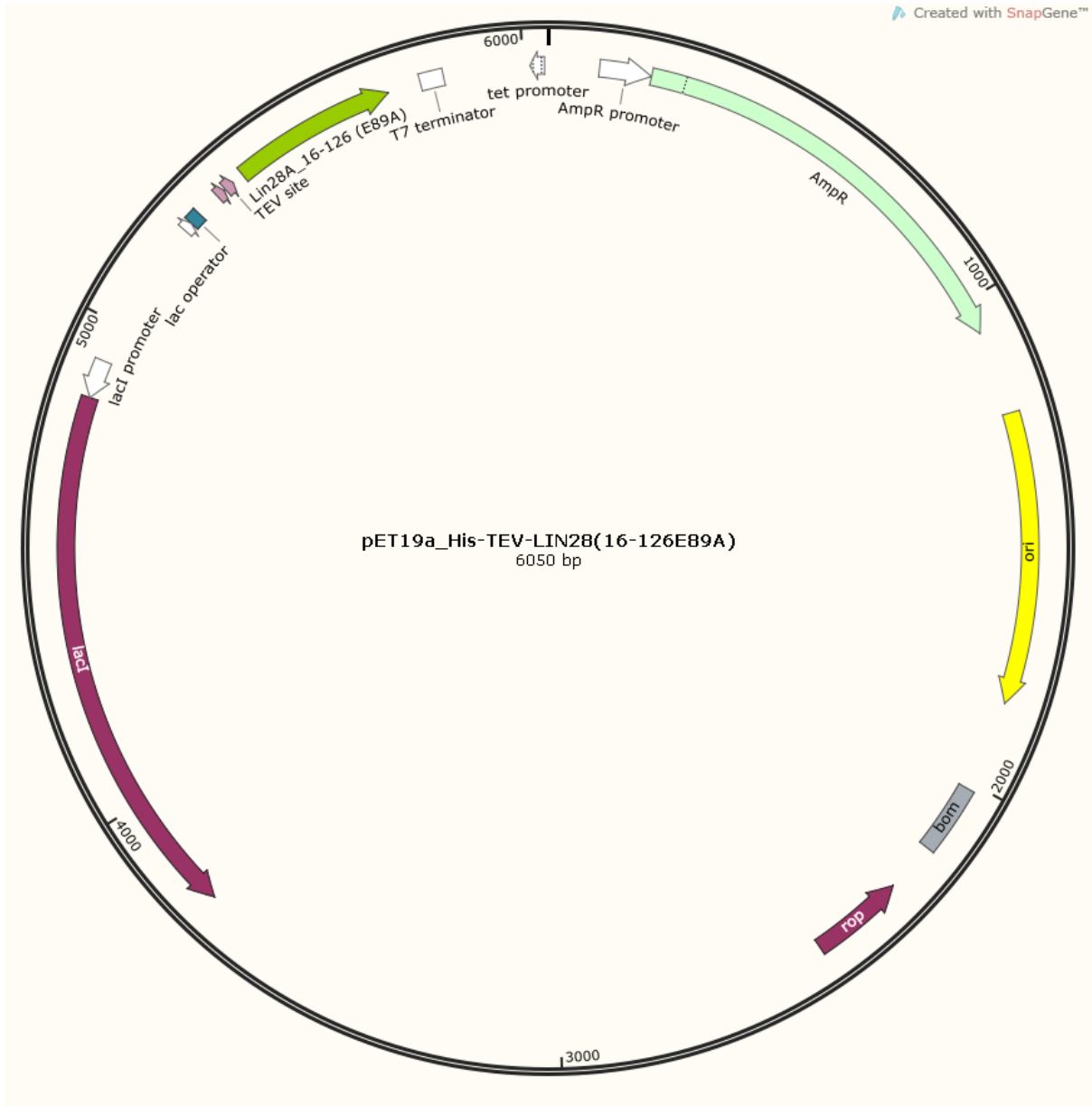
The plasmid was cloned by Dr. Fu Li at the CGC in Dortmund.

Appendix



pET19a-His-TEV-LIN28A(16-126)

Appendix



pET19a_His-TEV-LIN28(16-126E89A)

Appendix



pMAL_His-MBP-LIN28B(24-111)

Appendix



pET19a_His-TEV-XtrLIN28B(27-114)

Appendix



pET19a-His-TEV-RNaseL

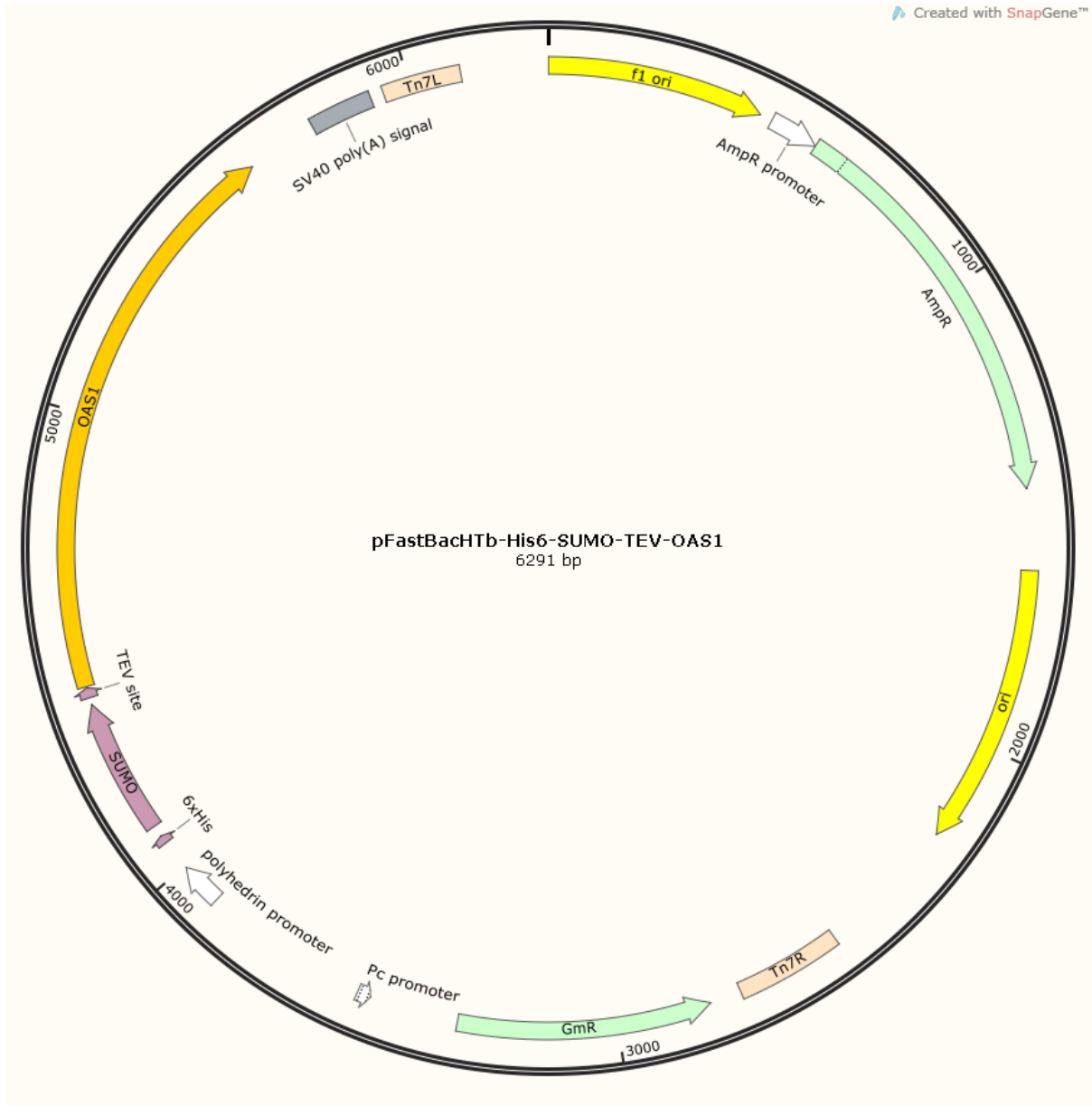
Appendix



pFastBachTb-his6-RNaseL

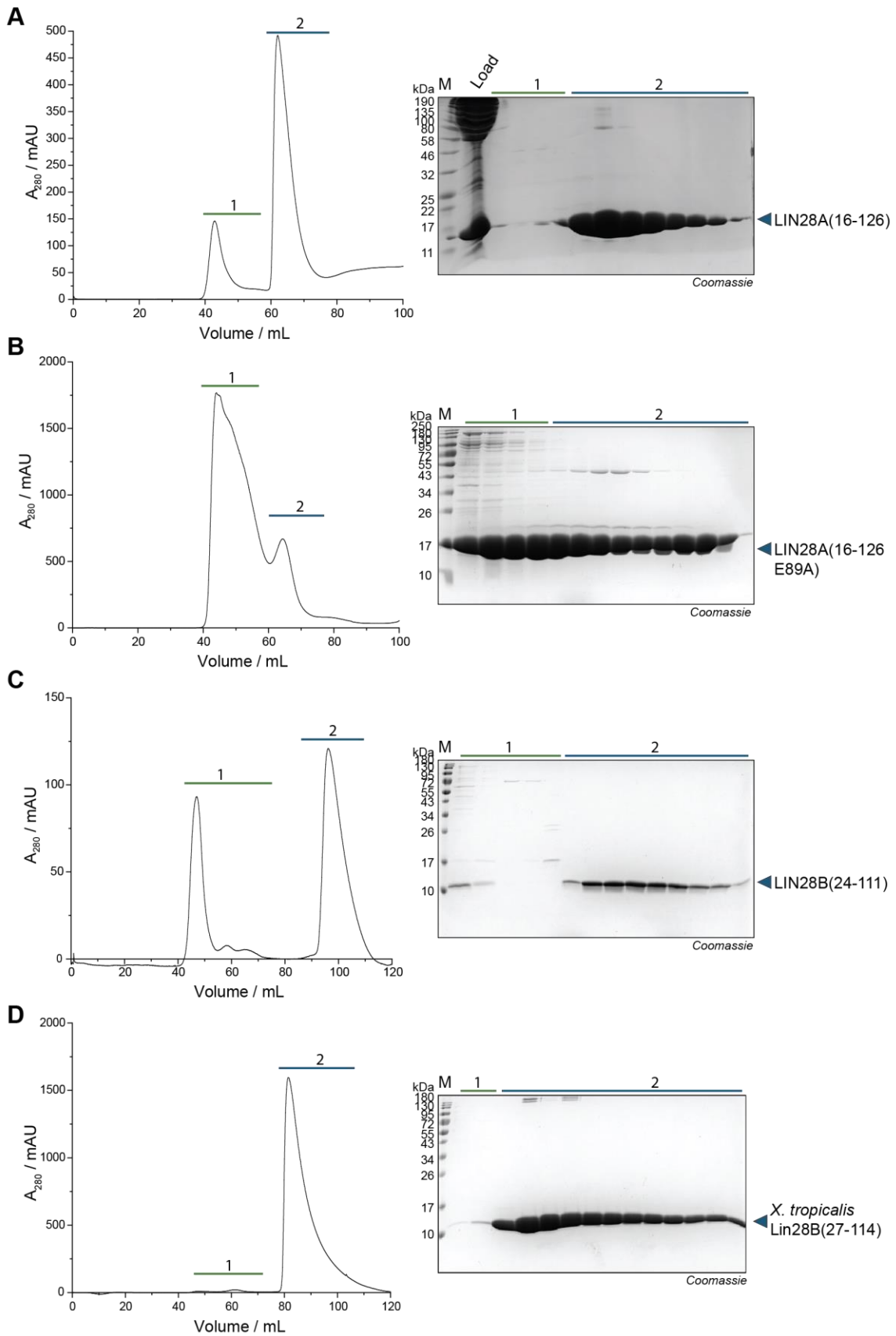
The plasmid was cloned by Dr. Fu Li at the CGC Dortmund.

Appendix



pFastBachTb-His6-SUMO-TEV-OAS1

8.2 Supplementary figures



Appendix

Figure S1: Chromatograms and SDS-PAGEs of final gel filtrations of purifications of (A) the LIN28A CSD, (B) the E89A mutant of the LIN28A cold shock domain, (C) a crystallization construct of the LIN28B CSD and (D) a *X. tropicalis* Lin28B CSD crystallization construct. The peaks from the gel filtration are labeled in chromatogram and SDS-PAGE with matching numbers.

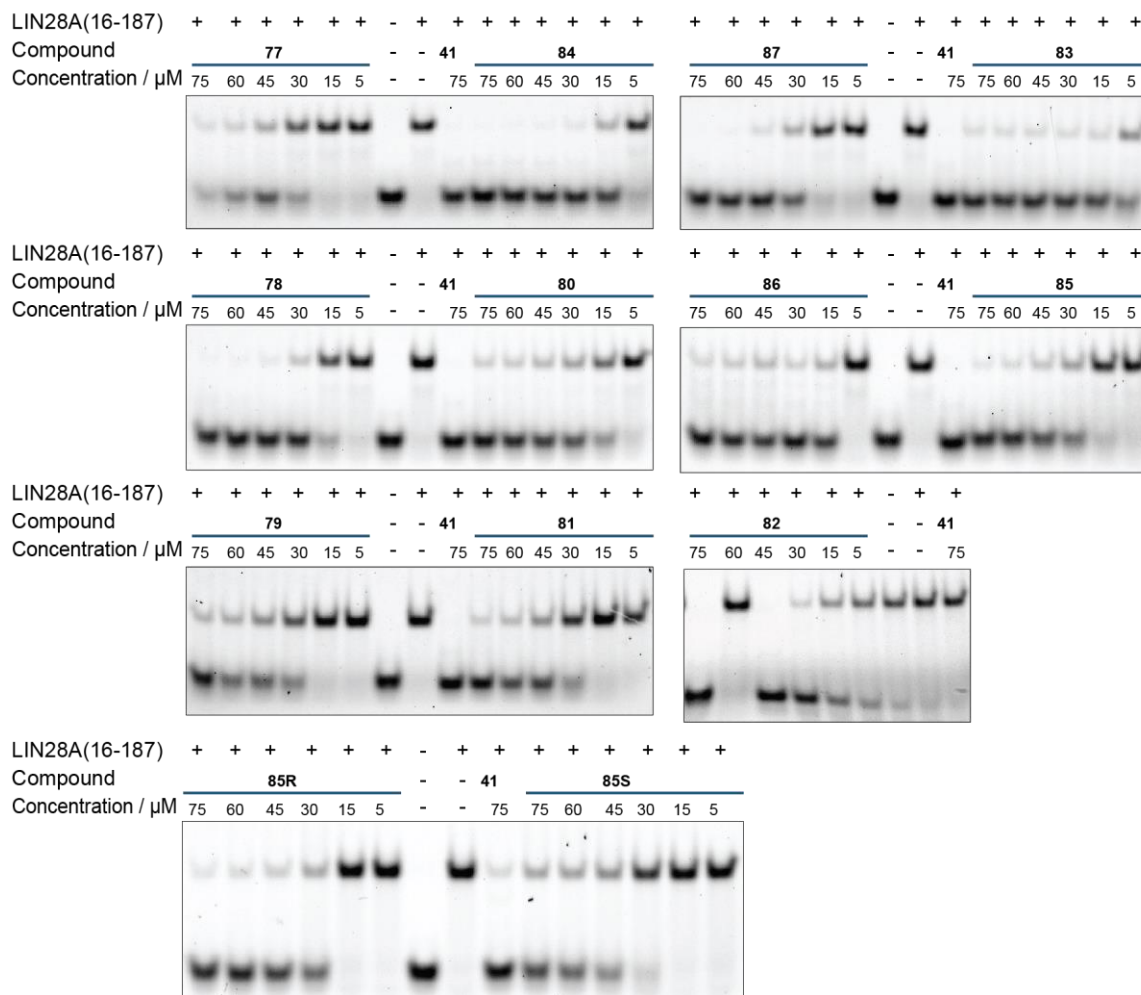


Figure S2: Dose-response EMSAs of trisubstituted pyrrolinones from Table 16. The experiment was performed by Lisa Hohnen as part of her Master thesis. The data was replicated as part of this work.

Appendix

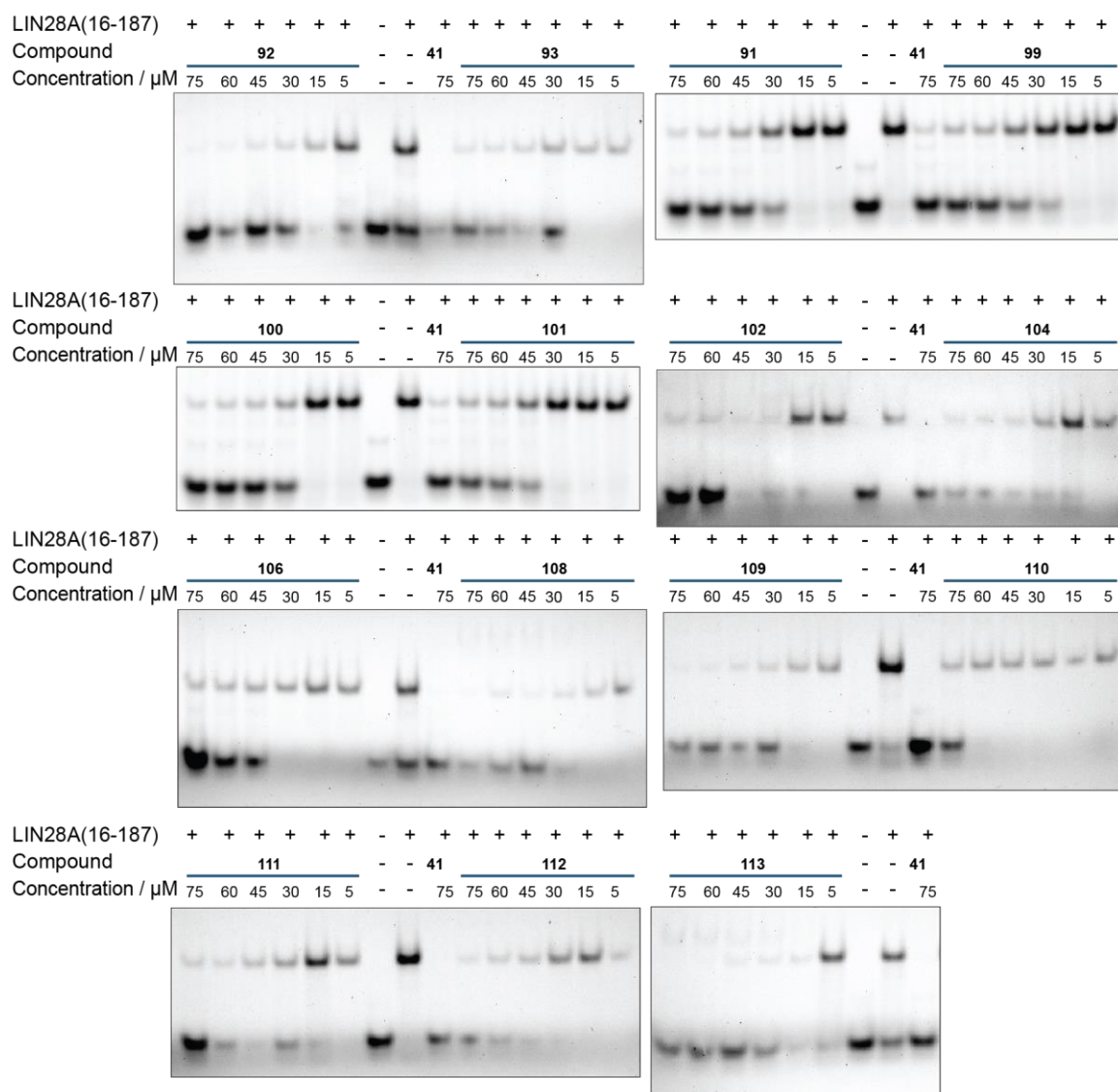


Figure S3: Dose-response EMSAs of active trisubstituted pyrrolinones from Table 18 and Table 19. Measurements of **91** and **99-101** were performed by Lisa Hohnen as part of her Master thesis. The data was replicated as part of this work.

Appendix

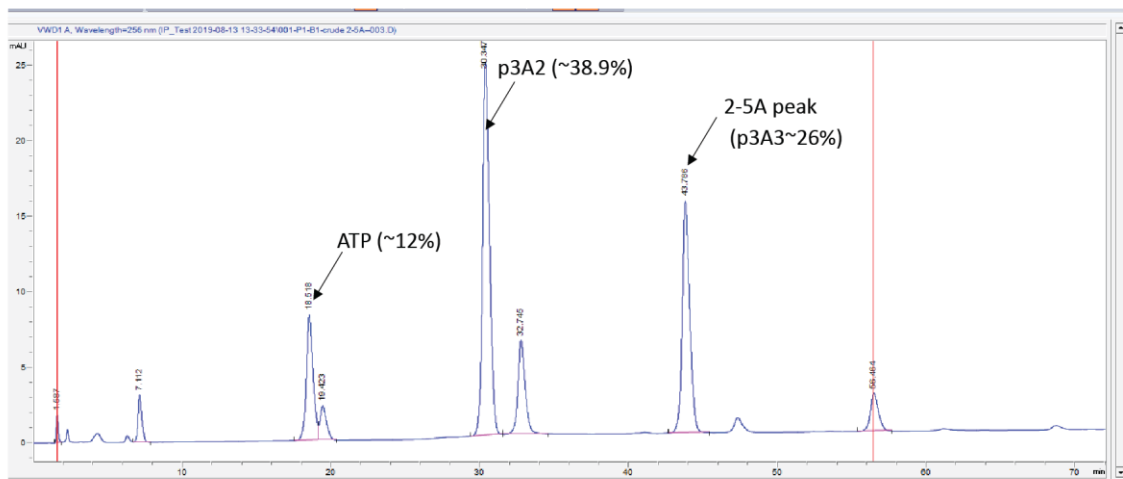


Figure S4: LC-MS analysis of crude 2'-5'A provided by Dr. Abhishek Asthana and Prof. Robert H. Silverman.

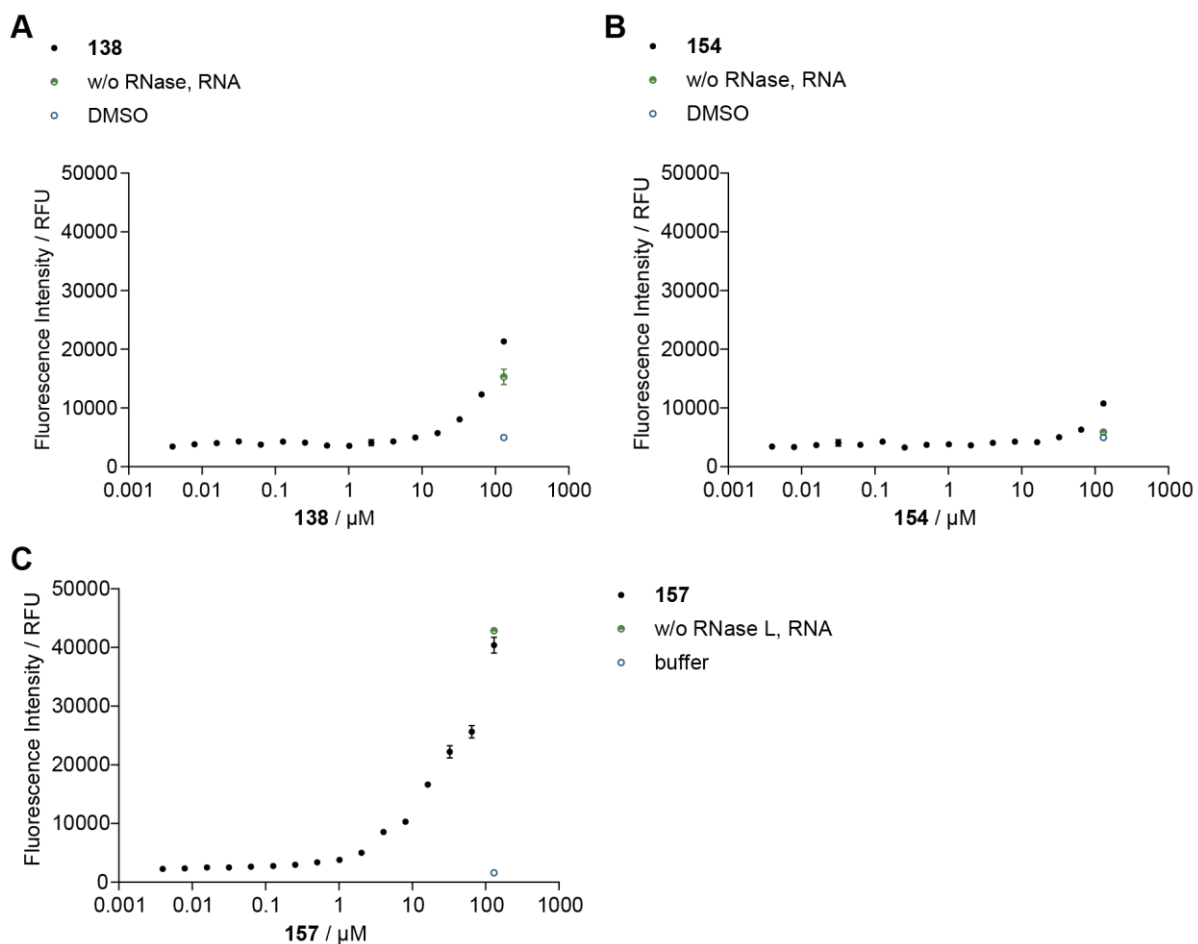


Figure S5: Dose-dependent FRET assay and autofluorescence of the tested molecules (green) of (A) **138**, (B) **154** and (C) **157**. The assay was performed by Neele Haacke as part of her Master thesis.

Eidesstattliche Versicherung

Eidesstattliche Versicherung (Affidavit)

Borgelt, Lydia

Name, Vorname
(Surname, first name)

168557

Matrikel-Nr.
(Enrolment number)

Belehrung:

Wer vorsätzlich gegen eine die Täuschung über Prüfungsleistungen betreffende Regelung einer Hochschulprüfungsordnung verstößt, handelt ordnungswidrig. Die Ordnungswidrigkeit kann mit einer Geldbuße von bis zu 50.000,00 € geahndet werden. Zuständige Verwaltungsbehörde für die Verfolgung und Ahndung von Ordnungswidrigkeiten ist der Kanzler/die Kanzlerin der Technischen Universität Dortmund. Im Falle eines mehrfachen oder sonstigen schwerwiegenden Täuschungsversuches kann der Prüfling zudem exmatrikuliert werden, § 63 Abs. 5 Hochschulgesetz NRW.

Die Abgabe einer falschen Versicherung an Eides statt ist strafbar.

Wer vorsätzlich eine falsche Versicherung an Eides statt abgibt, kann mit einer Freiheitsstrafe bis zu drei Jahren oder mit Geldstrafe bestraft werden, § 156 StGB. Die fahrlässige Abgabe einer falschen Versicherung an Eides statt kann mit einer Freiheitsstrafe bis zu einem Jahr oder Geldstrafe bestraft werden, § 161 StGB.

Die oben stehende Belehrung habe ich zur Kenntnis genommen:

Official notification:

Any person who intentionally breaches any regulation of university examination regulations relating to deception in examination performance is acting improperly. This offence can be punished with a fine of up to EUR 50,000.00. The competent administrative authority for the pursuit and prosecution of offences of this type is the chancellor of the TU Dortmund University. In the case of multiple or other serious attempts at deception, the candidate can also be unenrolled, Section 63, paragraph 5 of the Universities Act of North Rhine-Westphalia.

The submission of a false affidavit is punishable.

Any person who intentionally submits a false affidavit can be punished with a prison sentence of up to three years or a fine, Section 156 of the Criminal Code. The negligent submission of a false affidavit can be punished with a prison sentence of up to one year or a fine, Section 161 of the Criminal Code.

I have taken note of the above official notification.

Dortmund,

Ort, Datum
(Place, date)Unterschrift
(Signature)Titel der Dissertation:
(Title of the thesis):

Discovery of Small-Molecule Modulators of RNA-Binding Proteins LIN28 and RNase L

Ich versichere hiermit an Eides statt, dass ich die vorliegende Dissertation mit dem Titel selbstständig und ohne unzulässige fremde Hilfe angefertigt habe. Ich habe keine anderen als die angegebenen Quellen und Hilfsmittel benutzt sowie wörtliche und sinngemäße Zitate kenntlich gemacht.

Die Arbeit hat in gegenwärtiger oder in einer anderen Fassung weder der TU Dortmund noch einer anderen Hochschule im Zusammenhang mit einer staatlichen oder akademischen Prüfung vorgelegen.

I hereby swear that I have completed the present dissertation independently and without inadmissible external support. I have not used any sources or tools other than those indicated and have identified literal and analogous quotations.

The thesis in its current version or another version has not been presented to the TU Dortmund University or another university in connection with a state or academic examination.*

*Please be aware that solely the German version of the affidavit ("Eidesstattliche Versicherung") for the PhD thesis is the official and legally binding version.

Dortmund,

Ort, Datum
(Place, date)Unterschrift
(Signature)